

# **BULGARIAN CHEMICAL COMMUNICATIONS**

2011 Volume 43 / Number 1

*Journal of the Chemical Institutes  
of the Bulgarian Academy of Sciences  
and of the Union of Chemists in Bulgaria*



## IN MEMORIAM

To the memory of Academician EVGENI B. BUDEVSKI  
(1922-2008)



On October 13, 2008 the Academician Evgeni Budevski, the founding father of the Bulgarian Electrochemical School, passed away following a sudden illness.

Acad. Budevski started his research work in the field of the electrocrystallization in 1949 following his graduation from Sofia University “Sveti Kliment Ohridski” with a degree in Chemistry. He gained scientific recognition with the development of the original capillary method for preparation of dislocation-free faces of Ag single crystals. He was instrumental in the confirmation of the 2D theory of crystal growth, introduced by Stranski and Kaischew in the 1930s, as well as in the supplementation of Frank’s theory with quantitatively validated theoretical calculations, related to the growth of polygonized spirals.

As a founder and the first Director of the Central Laboratory of Electrochemical Power Sources, now the Institute of Electrochemistry and Energy Systems, Prof. Budevski was a major driving force behind the research and development of the electrochemical power sources. In 1971 CLEPS’ electric car, driven by primary Zn-air batteries, made a world record of a 220-kilometer run.

In the latter part of his scientific career, which was cut short by his untimely death, Evgeni Budevski tirelessly promoted the Hydrogen economy concept, championed renewable energy, and actively worked on PEMFC. He left more than 150 publications and 40 patents with a high impact on the scientific world.

During his distinguished career Evgeni Budevski received numerous national and international awards: the Dimitrov State Prize (the most prestigious Bulgarian award for that time), the prize of the Electrodeposition Division of The Electrochemical Society, the Marin Drinov Medal of the Bulgarian Academy of Sciences. He was the Vice-President of the International Society for Electrochemistry, ISE (1874-1978), Foreign Member of the Saxonian Academy of Sciences – 1974, member of the IUPAC Committee of Electrochemistry (1980-1987), member of the editorial boards of the *Ectrochimica Acta*, *J. Applied Electrochemistry* and *J. Power Sources*, member of the Advisory Committee of UNESCO-EPS on Energy Saving and Storage, Member of the Advisory Committee of the President of the Republic of Bulgaria (1997-2001).

Evgeni Budevski will be remembered with his vital and original scientific and personal philosophy, which did not leave him until his final breath. He loved nature, the outdoors, and the camping lifestyle. A keen skier and yachtsman, he passed on the passion for his hobbies to his co-workers. Together with his loving wife Lily, he enjoyed spending the weekends in their mountain house, where he entertained his numerous friends until his last days.

*On behalf of the Bulgarian Electrochemical Society*

## EDITORIAL

### National Conference “Sofia Electrochemical Days 2010” (SED 2010)

The current issue of the *Bulgarian Chemical Communications* consists of the papers, presented as lectures and posters at the “Sofia Electrochemical Days” National Conference (SED 2010), having international participants present, and held in Sofia in 11 to 13 May 2010. “Sofia Electrochemical Days” is establishing itself as an important national forum for exchanging of information on the latest scientific and technical developments in the field of the electrochemical science and technology.

“Sofia Electrochemical Days 2010” was organized by the Institute of Electrochemistry and Energy Systems under the Bulgarian Academy of Sciences (BAS) in collaboration with the Rostislav Kaishev Institute of Physical Chemistry (BAS), the Department of Inorganic and Electrochemical Production at the University of Chemical Technology and Metallurgy, and the Centre of Innovation (BAS), and was held in the memory of Academician Evgeni Budevski – a world-renown scientist and the founder of the Bulgarian Electrochemical School. The SED 2010 provided the opportunity to bring together both, the young and the experienced scientists, and engineers, researchers from the universities, the industry and the institutes of BAS, to share results and discuss issues on a wide range of electrochemical fields: fundamental electrochemistry, hydrogen energy, fuel cells, batteries, electroplating, industrial electrolysis, corrosion and protection electrochemical methods and instrumentation. Nine plenary lectures, thirteen keynote lectures, forty-four posters and two technical exhibitions, including five firm presentations, were presented at the SED 2010.

We would like to thank the SED 2010 participants for their contribution to the conference success as well as for the warm and collaborative atmosphere they created. We express our sincere gratitude to the SED Organizing Committee, as well as to the authors for their incentive presentations, to the referees for their efforts in reviewing the submitted manuscripts and the Editorial Board of the *Bulgarian Chemical Communications* for the publication of this issue.

*Guest Editors:*

*Raicho Raicheff  
Victor Boev  
Institute of Electrochemistry  
and Energy Systems  
Bulgarian Academy of Sciences*

## Environmentally friendly cathode materials for Li-ion batteries

B. I. Banov\*, H. C. Vasilchina

*Institute of Electrochemistry and Energy Systems, Bulgarian Academy of Sciences, Acad. G. Bonchev St., Bl №:10, 1113 Sofia, Bulgaria*

Received June 28, 2010; accepted October 4, 2010

Lithium cobaltate, used in commercial rechargeable lithium ion batteries, possesses good cyclability, high discharge potential, and acceptable energy density. Its synthesis is easy and can be applied on a large industrial scale. However, the price of cobalt is very high, and determines the end user price of the lithium battery. Cobalt and its oxides are very toxic. Lithium manganese dioxide spinel combines high specific energy density, volumetric and gravimetric, high Coulombic efficiency, close to the theoretical, and long cycle life. It is non-toxic, environmentally friendly, and low cost, but possesses some disadvantages such as low starting capacity and low stability at elevated temperatures. Optimising the synthesis methods and elucidating the factors influencing the electrochemical stability, we have obtained manganese dioxide spinel, which is very attractive, and a prospective cathode material for large-scale application. Cathode materials are presented based on manganese dioxide spinel with high Coulomb efficiency close to 90% at temperatures of 55°C, discharge rates of 4C and cycle life up to 500 cycles. The obtained results show that our approach could also be applied for enhancing the efficiency of other active electrode materials.

**Keywords:** Highly efficient lithium batteries, manganese dioxide spinel, elevated temperature stability, high rates, coating

### 1. INTRODUCTION

Commercially available rechargeable lithium batteries refer to the Li-Ion battery, which uses carbon powder as negative active electrode material and lithiated metallic oxides as cobaltate and nickelate for positive active electrode material. For the moment only LiCoO<sub>2</sub> (lithium cobaltate) is present at the market as a positive electrode material. However, the cost of this material is so high that it would take up too much of the battery cost and its specific energy density is not of the highest. Therefore, it may be replaced by the competitive LiNiO<sub>2</sub>. The price of the LiNiO<sub>2</sub> (lithium nikelate) is less due to the highest specific gravimetric capacity but the LiNiO<sub>2</sub> (lithium nikelate) is difficult for synthesis and treatment. Both materials are not environmentally friendly. Thus the nearest future is devoted to the development of positive electrode materials with the following features:

- ✓ *High specific energy density – volumetric and gravimetric;*
- ✓ *Improved Coulombic efficiency close to the theoretical;*
- ✓ *Cycle life, meeting the requirements;*

- ✓ *Easy for synthesis and treatment;*
- ✓ *Non-toxic and environmentally friendly;*
- ✓ *Low cost.*

There is only one group of candidates that can meet these requirements, the cathode materials which are based on manganese dioxide, working in the 4 volt range – the manganese spinel.

### 2. MANGANESE DIOXIDE SPINEL

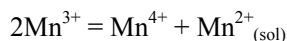
During the last 10 years a high-energy demand has existed at the lithium battery market. Lithium cobaltate and lithium nickelate have successfully found a niche in this growing market. Some non-toxic, environmentally friendly, low cost candidates with specific energy density, close to 450 Wh.g<sup>-1</sup>, are under intensive investigation for replacement of the cathode materials, based on Ni and Co. Lithium manganese spinel, LiMn<sub>2</sub>O<sub>4</sub>, is very attractive and prospective cathode material, combining the advantages to be non-toxic, environmentally friendly, with low cost and of theoretical specific energy density of 475 Wh.g<sup>-1</sup>. It has been under investigation since the beginning of the new century, but displays the big disadvantage of premature capacity loss, especially in the high temperature range of 30–60°C [1–8].

The same problem also exists in regard to the cathode materials, based on lithiated nickel and cobalt oxides. It is, however, less pronounced. The

---

\* To whom all correspondence should be sent:  
E-mail: bbanov@dir.bg

solubility of those active cathode materials is increased at elevated temperatures, and the cathodes dissolve in the electrolyte during storage and long time cycling. The main instability of  $\text{LiMn}_2\text{O}_4$  is due to the so-called  $\text{Mn}^{3+}$  disproportion, described by the equation:



The increased lithium content in the overlithiated manganese dioxide spinel of  $\text{Li}_{1+x}\text{Mn}_{2-x}\text{O}_4$  type stabilizes the crystal structure and suppresses the dissolution of  $\text{Mn}^{3+}$ . This reflects in increased stability during cycling at elevated temperatures. However, the gain in cycleability is accompanied by diminishing of the delivered reversible capacity.

Another way to solve the problem is to envelop the active electrode material with metal oxides in order to prevent the  $\text{Mn}^{3+}$  dissolution. In this way the high temperature characteristics of the  $\text{LiMn}_2\text{O}_4$  spinel are enhanced but the lithium diffusion coefficient is reduced, which reflects in deterioration of the overall electrochemical behaviour of the lithium cell. In the literature [4] the  $\text{MgO}$  is proposed as an almost universal coating agent for  $\text{LiCoO}_2$  and  $\text{LiNiO}_2$ , which are from the same-layered crystallographic group. The manganese dioxide spinel belongs to the *Fd3m* crystallographic space group, so it is difficult to apply the same method of stabilization.

The third option is to substitute small amount of  $\text{Mn}^{3+}$  ions by another metal ion. Some authors [2, 3] propose stabilization of the structure by partially replacing  $\text{Mn}^{3+}$  ions by Ni or Co ions. We have also piled up experience in this regard. The obtained stability of Co doped spinel with chemical formula of  $\text{LiCo}_{0.1}\text{Mn}_{1.9}\text{O}_4$  is excellent during long term cycling at room temperature [18–19] but it is not satisfactory at elevated temperatures. This substitution can also be performed using Mg and Al. The result is an improved cycleability but a reduced initial reversible capacity.

In a series of papers [10–18] we have demonstrated that if an appropriate method and manner of synthesis are applied, it is possible to obtain  $\text{LiMn}_2\text{O}_4$ , delivering up to 80% of the theoretical capacity in the 4 volt region during long term cycling at high charge/discharge rate (C/3) and room temperature. The techniques of preparation, sol-gel or solid-state syntheses, the influence of the initial compounds on the obtained precursor and the final product, the thermal treatment, the physicochemical properties and the electrochemical behaviour of the active electrode materials (AEM)

have been largely discussed in our previous papers [10–19].

The general principles to overcome the problems, concerning the stability of manganese dioxide spinel, numbered below, are illustrated by the next three possible steps:

- Overlithiated Manganese Dioxide Spinels,  $\text{Li}_{1+x}\text{Mn}_{2-x}\text{O}_4$
- Foreign ions substituted manganese dioxide spinel,  $\text{Li}_{1+x}\text{Me}_y\text{Mn}_{2-x-y}\text{O}_4$
- Coated Manganese Dioxide Spinel
- $\text{LiMn}_2\text{O}_4$  coated with inactive metal oxide –  $\text{ZnO}$
- $\text{LiMn}_2\text{O}_4$  coated with active lithiated metal oxide –  $\text{LiMeO}_2$ .

The typical physicochemical properties of active electrode materials also affect the material electrochemical behaviour:

- Specific Surface Area - the higher the SSA is, the lower polarization; higher delivered capacity; improved reversibility, and long cycle life are;
- Particle size – nanoparticles – balance of size depending on the specific application (the smaller the particle size is the higher discharge rate and longer cycle life are);
- Porosity of the particles and pore distribution – suitable micro and macro pore ratio;
- Conductive binder ensuring an appropriate porosity and suitable electronic conductivity.

The role of all chemical and physicochemical parameters which influence the electrochemical performance is elucidated hereafter by simple examples, and the obtained results are discussed.

### 3. OVER-LITHIATED MANGANESE DIOXIDE SPINELS

Manganese dioxide spinels of the type  $\text{Li}_{1+x}\text{Mn}_{2-x}\text{O}_4$  are regarded with the following expected results:

- Starting capacity of  $100 - 135\text{mAh.g}^{-1}$  (65-90%  $Q_{\text{th}}$ );
- Cycleability of 300 cycles at RT ;
- Improved cycleability at elevated temperatures (55°C).

The over-lithiation of manganese dioxide spinel is the simplest way to increase the stability of the active electrode material at elevated temperatures. We have prepared a series of over-lithiated manganese dioxide and subjected it to high temperature tests (cf. Table 1).

As already mentioned, this approach offers reduced reversible capacity but the cycle life is

improved significantly. The capacity fades at room temperature (RT), decreased from 0.4% to 0.032% per cycle – more than ten times. On the other hand the starting delivered capacity was reduced from 135 mAh.g<sup>-1</sup> to 101 mAh.g<sup>-1</sup>. The capacity fades at elevated temperatures (55°C), starting from 1.3%

**Table 1.** Theoretical and observed capacity dependence on extra lithium content in over-lithiated manganese spinel

Spinel	RT	Fade	55° C	Fade
Formula	Initial	%/cyc.	Initial	%/cyc.
	Cap	at 50 <sup>th</sup>	Cap	at 50 <sup>th</sup>
Li <sub>1+x</sub> Mn <sub>2-x</sub> O <sub>4</sub>	mAh/g	cycle	mAh/g	cycle
LiMn <sub>2</sub> O <sub>4</sub>	135	0.42	135	1.40
Li <sub>1.02</sub> Mn <sub>1.98</sub> O <sub>4</sub>	125	0.13	125	0.75
Li <sub>1.05</sub> Mn <sub>1.95</sub> O <sub>4</sub>	123	0.12	123	0.45
Li <sub>1.07</sub> Mn <sub>1.93</sub> O <sub>4</sub>	121	0.11	120	0.27
Li <sub>1.09</sub> Mn <sub>1.91</sub> O <sub>4</sub>	118	0.08	118	0.18
Li <sub>1.11</sub> Mn <sub>1.89</sub> O <sub>4</sub>	101	0.05	101	0.08
Li <sub>1.13</sub> Mn <sub>1.87</sub> O <sub>4</sub>	100	0.04	101	0.07

(three times higher than at RT) per cycle and drops to 0.067%, which is very close to the value, displayed at RT for the spinel with the chemical formula of Li<sub>1.11</sub>Mn<sub>1.89</sub>O<sub>4</sub>. The graphical presentation of the capacity changes at long term cycling for the investigated overlithiated samples is given in Fig. 1. Taking into account the so-called

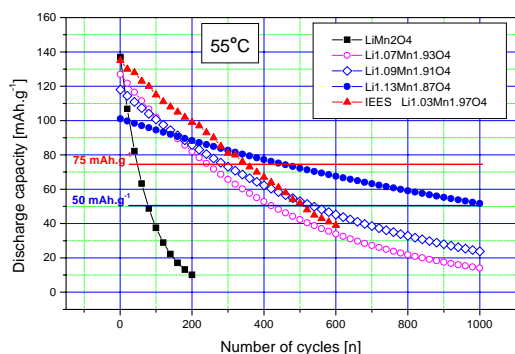


**Fig. 1.** Discharge capacity at long term cycling of overlithiated samples at elevated temperature.

‘accumulated capacity’, the best choice would be the ‘IEES’ sample because the accumulated capacity, graphically represented by the area limited by the cycling curve, is the biggest one. If the cycle life is set to 1000 cycles, the leader would be the sample with the chemical formula of Li<sub>1.13</sub>Mn<sub>1.87</sub>O<sub>4</sub>. There is no best choice for the middle cycle life (for example 400 cycles) because all tested samples offer nearly the same accumulated capacity, excluding the

spinel with maximum lithium content - Li<sub>1.13</sub>Mn<sub>1.87</sub>O<sub>4</sub>.

## CONCLUSIONS

- Small amount of extra lithium, incorporated in the initial crystal structure, stabilizes the spinel during cycling and suppresses the Mn<sup>3+</sup> dissolution;
- The cycleability of over-lithiated samples is improved by more than 50% but the reversible capacities are lower;

The capacity of the over-lithiated samples fade at room temperatures, drastically reduces at elevated temperatures.

## 4. MANGANESE DIOXIDE SPINEL

Li Me<sub>x</sub>Mn<sub>2-x</sub>O<sub>4</sub> (0.01<X<0.20) MODIFIED WITH FOREIGN IONS (Me = Mg, Al)

*Expected features:*

- Starting capacity of 100 – 120 mAh.g<sup>-1</sup> (65 – 80% Q<sub>th</sub>);
- Improved thermal stability & electrochemical futures;
- Improved cycleability of up to 700 cycles;
- Target: batteries for EV&HEV.

The advantages of doping with foreign ions are investigated on manganese dioxide spinel, LiMg<sub>0.05</sub>Mn<sub>1.95</sub>O<sub>4</sub>, i.e. the selected doping ion is the Mg.

Based on our previous investigations, lithium acetate and manganese carbonate have been chosen as lithium and manganese source, and magnesium nitrate as Mg doping agent (CH<sub>3</sub>COOLi.2H<sub>2</sub>O, MnCO<sub>3</sub>, Mg(NO<sub>3</sub>)<sub>2</sub>·6H<sub>2</sub>O). The optimal conditions to obtain a high quality active cathode material for lithium batteries, operating in the 4 volt region, are published in [10]. The AEM should be optimized specifically for reaching maximum efficiency [10–14]. The dissolution of manganese ions in the electrolyte can be reduced by diminishing the specific surface area (SSA) to a value of about 1–3 m<sup>2</sup>.g<sup>-1</sup>. When this approach is applied, the stability is improved but the electrochemical properties of the manganese spinel based cathode material are deteriorated. It is well known that the SSA of the active electrode material plays an important role for the electrochemical performance of the electrode [10–17]. In this work we tried to find a compromise between both parameters: the stability and the electrochemical performance using the Mg as a doping agent.

#### 4.1. Experimental

The newly proposed method of synthesis is based on two different techniques: impregnation and decomposition inside the particle.  $\text{MnCO}_3$  with mean particle size of about  $20 \mu\text{m}$  is chosen as starting compound and manganese source [10]. Magnesium nitrate is introduced in the reaction composition as an aqueous solution. Doped lithium manganese spinel with high purity and perfect crystal structure has been obtained as a result of this synthesis. In both cases, with and without doping, an active cathode material with SSA (measured by the B.E.T. method) of about  $10 \text{ m}^2\cdot\text{g}^{-1}$  is obtained [10 – 18]. The phase composition of the samples is determined by X-ray diffraction analysis using Philips APD 15 powder diffractometer with Cu-K $\alpha$  radiation. The electrochemical characteristics are tested in a three-electrode glass cell with lithium reference electrode in excess of electrolyte and with a floating test electrode, described in [12, 13]. The electrolyte consists of 1M  $\text{LiClO}_4$  solution in a mixture of EC:PC:DMC in a 1:1:2 volume ratio. The composite test electrode material is a mixture of the investigated compounds with Teflonized Acetylene Black (TAB-2) [10 – 13] at a 1:1 ratio by weight, pressed on expanded nickel grid with diameter of 15 mm. The test electrodes weight is typically 50 mg without the nickel grid.

#### 4.2. Results and Discussion

The XRD pattern of the manganese spinel, doped with 5 atomic percent Mg, is equal to those of the pure  $\text{LiMn}_2\text{O}_4$ , i.e. the phase of the doped spinel is also *Fd3m* and the crystallinity of the sample is very high. The doping agent cannot be detected on the XRD patterns of  $\text{LiMg}_{0.05}\text{Mn}_{1.95}\text{O}_4$  spinel. That confirms that the Mg occupies **16(d)** places. The obtained doped and non-doped spinels possess specific SSA of  $\sim 10 \text{ m}^2\cdot\text{g}^{-1}$ . The charge/discharge profiles of pure  $\text{LiMn}_2\text{O}_4$  active electrode material are presented in Fig. 2. The electrochemical tests are performed at different discharge rates and temperatures. The first curve (Fig. 2A) shows the pure spinel behaviour applying 4h charge/discharge (0,25C) rate at  $23^\circ\text{C}$  (RT). Due to the high SSA of the sample ( $10 \text{ m}^2\cdot\text{g}^{-1}$ ), the charge/discharge profile is very flat. The delivered capacity is  $135 \text{ mAh}\cdot\text{g}^{-1}$ . When a charge/discharge rate of 1C is applied and the temperature is increased to  $35^\circ\text{C}$ , the obtained capacity is  $105 \text{ mAh}\cdot\text{g}^{-1}$ . The discharge profile at high current density (4C) and  $35^\circ\text{C}$  is presented in Fig. 2C. In this case the exhibited discharge capacity is only of  $87 \text{ mAh}\cdot\text{g}^{-1}$ . The reduction is 35% in regard to RT and about 18% against 1C/ $35^\circ\text{C}$ . Fig.

3 shows the charge/discharge profiles of a newly prepared  $\text{LiMg}_{0.05}\text{Mn}_{1.95}\text{O}_4$  AEM. Three discharge/charge profiles: at 0.25C/RT, at 1C/ $35^\circ\text{C}$ , and at 4C/ $35^\circ\text{C}$ , are presented again for comparison with the pure spinel. There is no difference in the discharge capacity at 0.25C rate and RT due to the low discharge current and the high SSA of the sample. The sample exhibits capacity close to that of the pure material, which means that the very small amount of doping agent does not affect the discharge capacity. At elevated temperature of  $35^\circ\text{C}$  and discharge rate of 1C the delivered capacity is  $122 \text{ mAh}\cdot\text{g}^{-1}$ . The displayed reversible capacity decreases to  $105 \text{ mAh}\cdot\text{g}^{-1}$  when a high current drain and temperature are applied (4C/ $35^\circ\text{C}$ ). Compared to the tested pure spinel, the value increases with about 16% and 20%, respectively. In all of the tests the charge current rate is kept constant (0.25C) to ensure optimal conditions for low polarization charge. The obtained results confirm our assumption that it is possible to prepare a highly efficient cathode material.

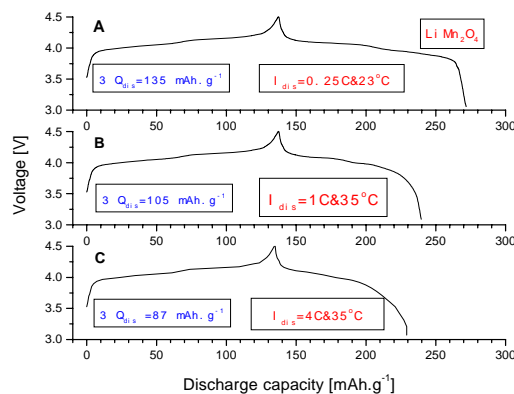


**Fig. 2.** Charge discharge profile of spinel sample at 0.25C/23°C, 1C/35°C and 4C/35°C.

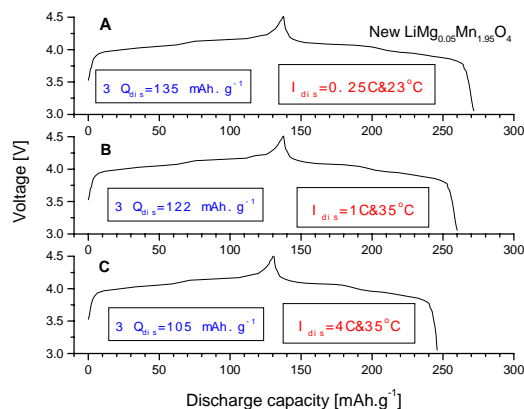


**Fig. 3.** Charge discharge profile of Mg doped spinel sample at 0.25C/23°C, 1C/35°C and 4C/35°C

## CONCLUSIONS

- $\text{LiMg}_{0.05}\text{Mn}_{1.95}\text{O}_4$  is successfully tested as cathode material with improved stability at elevated temperatures;
- A very high rate of (4C) AEM ( $\text{LiMg}_{0.05}\text{Mn}_{1.95}\text{O}_4$ ) is obtained;
- The overall efficiency of  $\text{LiMg}_{0.05}\text{Mn}_{1.95}\text{O}_4$  is enhanced by 20% at high rate (4C) and elevated temperature (35°C);

### 5. MANGANESE DIOXIDE SPINEL $\text{Li}_{1+x}\text{Al}_y\text{Mn}_{2-x-y}\text{O}_4$ MODIFIED WITH Al

#### Expected characteristics:

- Starting capacity of 100-120  $\text{mAh}\cdot\text{g}^{-1}$  (65-80%  $Q_{\text{th}}$ );
- Improved thermal stability & electrochemical features;
- Improved cycleability of up to 700 cycles;
- Target: batteries for EV&HEV.

The same procedure was applied for testing Al-doped manganese dioxide sample of the  $\text{Li}_{1+x}\text{Al}_y\text{Mn}_{2-x-y}\text{O}_4$  type. In this experiment the Al substitution was made with the same idea for improvement of the high temperature stability and the electrochemical performances of the active electrode material.

#### 5.1 Results and Discussion

The XRD patterns of pure  $\text{LiMn}_2\text{O}_4$  spinel and samples, doped with 25 atomic percent Al, do not differ from the XRD of pure manganese spinel. This is true especially in our case. Both substituting agents were especially chosen due to the fact that they make spinel of the same type,  $\text{MgAl}_2\text{O}_4$  -  $\text{Mn}_2\text{O}_4$  ( $\lambda$ - $\text{MnO}_2$ ). This is the reason that the XRD diagram of substituted spinel does not differ from the well known theoretical spinel XRD diagrams. The synthesis gives pure **Fd3m** phase (without any extra peaks). The XRD patterns of Al doped spinel,  $\text{Li}_{1.05}\text{Al}_{0.25}\text{Mn}_{1.70}\text{O}_4$ , overlap the pure one and the doping agent cannot be XRD detected. That confirms that the Al occupies **16(d)** places and the XRD pattern does not differ from the original. The obtained doped and non-doped spinels possess specific SSA of about  $\sim 10 \text{ m}^2\cdot\text{g}^{-1}$ . The samples with Al substitution show a little bit higher SSA of about  $12\text{-}15 \text{ m}^2\cdot\text{g}^{-1}$ , but in order to be accurate we chose the samples of SSA within  $10\text{-}12 \text{ m}^2\cdot\text{g}^{-1}$  for our investigation. The charge/discharge profile of the Al substituted material does not differ from the pure manganese spinel. The cycleability of the new prepared compound,  $\text{Li}_{1.05}\text{Al}_{0.25}\text{Mn}_{1.70}\text{O}_4$ , is given in Fig.4. We can see that the sample shows a very

good stability over cycling. We estimated the capacity fade based on the first 80 cycles. During cycling the samples are subjected to load tests. The results of these tests are shown in Fig.5. The plotted results are obtained on the base of 5 successive charge/discharges performed with 1-hour pause after the load discharge.

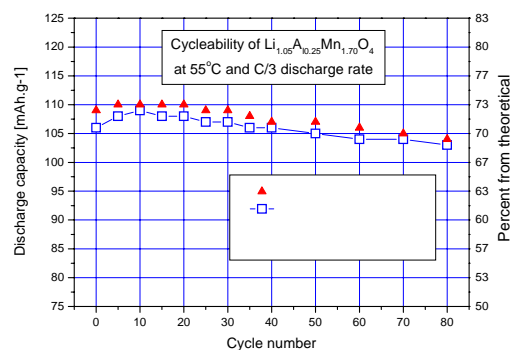


Fig. 4. Long term cycleability of Al doped spinel sample

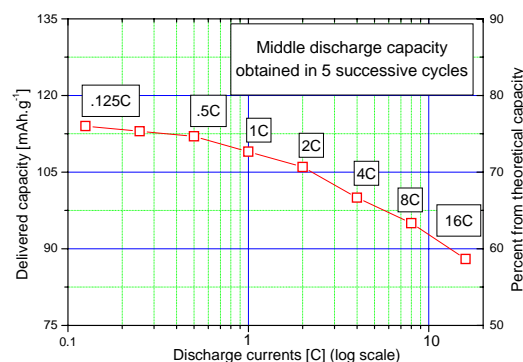


Fig. 5. Load characteristics obtained after 5 successive charge discharges and 1 hour relaxation time.

Each time the charge is effectuated with constant current of C/3. It can be seen from the graph that the aluminum-substituted material is very powerful. When a 4C discharge rate is applied, the material delivers about 90% from the base discharge capacity, delivered at C/3 (about  $110 \text{ mAh}\cdot\text{g}^{-1}$ ). Just to remind: a 4C discharge rate corresponds to starting of a car engine! At 8C the delivered capacity is 85% and even at 16C(!) the material withstands and delivers 80% from the capacity at C/3. All these results are very promising and attractive on a large-scale application. To our knowledge, by far no one has reported comparable data about power capabilities of the manganese oxide spinel. The long-term stability and cycleability at elevated temperatures (55°C) are

presented in the next Fig.6. The Figure summarizes the tests of the previously investigated and developed overlithiated manganese oxides against the winner in this experiment, the  $\text{Li}_{1.05}\text{Al}_{0.25}\text{Mn}_{1.70}\text{O}_4$ . The overall improvement in stability and cycleability is in the range of about 20-25%. The lower starting capacity leads to a very long and stable cycle life. Table 2 presents summary of both, Mg and Al doped active electrode materials, prepared and tested in the same laboratory.

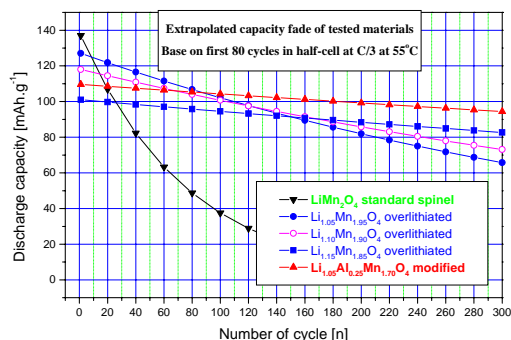


Fig. 6. Long term cycling of tested samples compared with over-lithiated ones.

**Table 2.** Reversible capacity and capacity fade at RT and elevated temperature of Mg and Al doped spinel.

Spinel Formula	RT		55° C	
	Init Cap	Fade %/c 50 <sup>th</sup> cycle	Init Cap	Fade %/c 50 <sup>th</sup> cycle
$\text{Li}_{1+x}\text{M}_y\text{Mn}_{2-x-y}\text{O}_4$	mAh/g	cycle	mAh/g	cycle
$\text{Li}_{1.05}\text{Al}_{0.1}\text{Mn}_{1.85}\text{O}_4$	119	0.04	117	0.05
$\text{Li}_{1.1}\text{Al}_{0.1}\text{Mn}_{1.8}\text{O}_4$	103	0.01	102	0.03
$\text{Li}_{1.05}\text{Al}_{0.15}\text{Mn}_{1.8}\text{O}_4$	109	0.04	109	0.06
$\text{Li}_{1.05}\text{Mg}_{0.1}\text{Mn}_{1.85}\text{O}_4$	114	0.06	112	0.08
$\text{Li}_{1.1}\text{Mg}_{0.1}\text{Mn}_{1.8}\text{O}_4$	108	0.03	108	0.07
$\text{Li}_{1.05}\text{Mg}_{0.15}\text{Mn}_{1.8}\text{O}_4$	105	0.08	105	0.09

It can be seen in the table that there are solutions which are appropriate for different cases, a high stability with low starting capacity, or higher starting capacity with acceptable cycle life. All of the above results are very interesting from theoretical point of view because they demonstrate the ability of the research group to set the requirements and to find the adequate solutions for them. Once again, the obtained result confirms our idea that it is possible to prepare cathode material, attractive for practical application by combining different techniques like over-lithiation and substitution with different starting compounds and appropriate thermal treatment (the way of synthesis).

## CONCLUSIONS

- The AEM of  $\text{Li}_{(1+X)}\text{Al}_Y\text{Mn}_{(2-X-Y)}\text{O}_4$  type is successfully synthesized and tested as a cathode material;
- The efficiency of the new prepared AEM is enhanced by 20% at high discharge rates of the 8C;
- The capacity fade at elevated temperature (55°C) of aluminum-substituted spinel is comparable with this at 25°C.

## 6. MANGANESE DIOXIDE SPINEL, $(\text{MeO})_x\text{LiMn}_2\text{O}_4$ , COATED WITH ELECTROCHEMICALLY INACTIVE MeO, IN OUR CASE (Me= Zn)

- Starting capacity of  $100 - 120\text{mAh.g}^{-1}$  (65-80%  $Q_{th}$ );
- Improved thermal stability;
- Deteriorated discharge characteristics;
- Improved cycleability, over 500 cycles;
- Best in small batteries for 3C products at RT and above.

This part of the work demonstrates the results, obtained on nanosized ZnO covered manganese spinel  $\text{LiMn}_2\text{O}_4$ . The approach for stabilization, proposed in literature, is covering of the active electrode material particles by a very thin coating, preventing the dissolution of  $\text{Mn}^{3+}$  ions. Consequently, a small deterioration of the electrochemical parameters is also expected. The aim of the study is to find a compromise between the stability and the electrochemical performance.

### 6.1. Experimental

The applied way of synthesis is based on a two-step technique: impregnation and decomposition inside the particle which was already described above. In the second step of the synthesis, the particles are covered with ZnO. Thus, two samples with thickness of the ZnO of about 30 and 50 nm (according to our calculations) are prepared.

### 6.2. Results and Discussion

The XRD pattern of the coated spinel does not differ from the theoretical. The proposed synthesis gives pure **Fd3m** phase. The ZnO cover cannot be detected by the XRD patterns, which shows that the ZnO cover is very thin and the XRD is amorphous. The presence of ZnO on the surface is proven only by Atomic Absorption Spectroscopy (AAS). The obtained spinel possesses a SSA of about  $10\text{ m}^2.\text{g}^{-1}$ . When the particles of AEM are covered with ZnO, the SSA is almost the same,  $\sim 8\text{ m}^2.\text{g}^{-1}$ . The charge/discharge profiles of the pure and ZnO

covered active electrode material are presented in Fig.7. The electrochemical tests are performed at the same charge/discharge rate (C/3) and at temperatures of 30°C and 55°C, respectively. The first curve (Fig.7A) shows the pure spinel, tested at 30°C. Due to the high SSA of the sample ( $8 \text{ m}^2 \cdot \text{g}^{-1}$ ), the charge/discharge profile is very flat. The charge/discharge profiles of the samples, covered

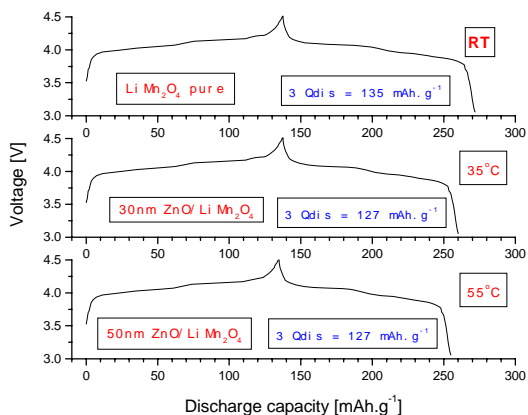


**Fig. 7.** Charge discharge profile of pure and coated with 30 and 50 nm ZnO spinel at 30 and 55°C.

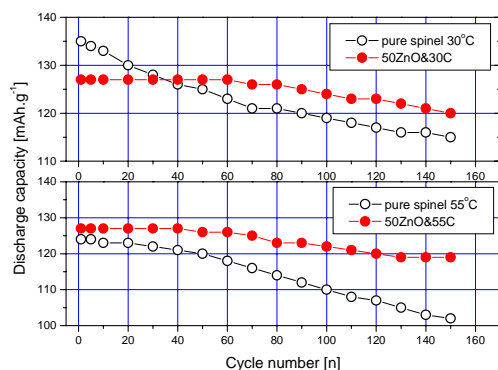


**Fig. 8.** Long term cycling test of pure and coated with 50 nm ZnO spinel at 30 and 55°C.

with 30 and 50 nm, are shown in Figs.7B and 7C. They indicate no significant difference between the discharge profiles of the pure and the coated samples. The initial discharge capacity of the pure spinel is  $135 \text{ mAh} \cdot \text{g}^{-1}$  versus  $125 \text{ mAh} \cdot \text{g}^{-1}$  for the covered one. The capacity decline versus cycle number is displayed in Fig.8. Since there is no difference in the voltage profile of both samples, covered with 30 or 50 nm of ZnO, in the next experiments only the latter is considered. Fig.8a shows the cycle life of the pure  $\text{LiMn}_2\text{O}_4$ , compared to that of the covered spinel at 30°C. The initial capacity of the pure spinel is higher and declines

slowly, reaching a value of about  $115 \text{ mAh} \cdot \text{g}^{-1}$  against  $120 \text{ mAh} \cdot \text{g}^{-1}$  for the coated material. The difference is less than 5% for 150 cycles. Fig.8b presents the same comparison for 55°C. The initial capacity of the pure spinel at 55°C is  $124 \text{ mAh} \cdot \text{g}^{-1}$ , which is close to the coated. After cycling, the difference between the two samples increases ( $102$  against  $119$  at the 150<sup>th</sup> cycle). The data show that the 50 nm ZnO coated lithium spinel is of interest for practical application in 3C products at elevated temperatures (of up to 50°C).

## CONCLUSIONS

- Manganese dioxide spinel, covered by inactive electrode material (ZnO) is successfully prepared;
- Electrochemical performances are not deteriorated;
- The stability of the cathode material is improved by 10%;
- Even very fine coating of 50 nm thickness, prevents the  $\text{Mn}^{3+}$  dissolution and stabilizes the electrochemical features at an elevated temperature.

## 7. MATERIAL PHYSICO-CHEMICAL PROPERTY EFFECT ON THE ELECTROCHEMICAL BEHAVIOUR

- SSA (the higher the SSA is, the lower the polarization is), higher delivered capacity, improved reversibility and long cycle life;
- Particles size – nanoparticles – balance of size depending on the specific application (the smaller the particle size is the higher the discharge rate and long cycle life are);
- Porosity of the particles and pore distribution – suitable micro and macro pore ratio.

The lithium manganese spinel,  $\text{LiMn}_2\text{O}_4$ , possesses two discharge plateaus, a 4 volt and a 3 volt. So far the efforts of R&D have been oriented to improve the discharge capacity and the cycleability of the high potential region, the 4 volt and the 3 volt regions have been forgotten.

We have already demonstrated [10–18] that it is possible to obtain  $\text{LiMn}_2\text{O}_4$  with 90% of the theoretical capacity in the 4 volt region during a long term cycling at high charge/discharge rate of C/3. The techniques of preparation, sol-gel or solid state syntheses, the influence of the starting compounds on the obtained precursor and the final product, and the physicochemical properties and electrochemical behaviour of the active electrode materials have been discussed [10–19]. The challenge is to improve the electrochemical

characteristics of lithium manganese spinel working in the low potential region of 3 V.

### 7.1. Experimental

Based on our previous investigations, lithium spinel is prepared by the same synthesis approach. The final thermal treatment in this case takes place at a temperature of about 550°C. The solid-state reaction synthesis, the physicochemical and electrochemical investigation procedures are described above.

### 7.2. Results and discussion

XRD patterns of both syntheses are the same, of the *Fd3m* space group, i.e. a spinel was successfully obtained at a relatively low temperature (550°C). The XRD pattern of the new synthesis shows only a little lower intensity of the peaks. The material obtained by the combined impregnation decomposition process, forms highly porous particles. The measured SSA (10 m<sup>2</sup>.g<sup>-1</sup>) is five times higher than that of the other reference materials. The discharge profile in the 3 volt region of the active electrode material, prepared by the standard synthesis, is presented in **Fig.9**. It has

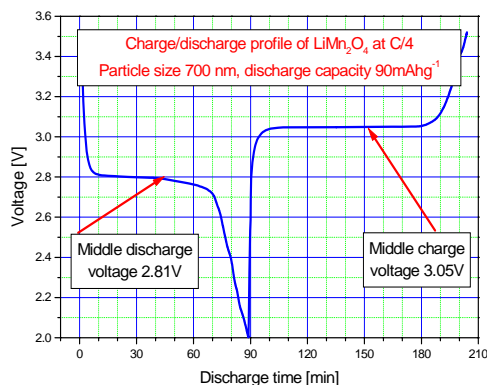


**Fig. 9.** Discharge charge profile of standard lithium spinel.

capacity of 90 mAh.g<sup>-1</sup> with a discharge plateau at 2.81 V. From a theoretical point of view, the plateau must be situated at 2.95 V. The observed difference is due to the discharge polarization. The charge plateau is at 3.05 V and the charge capacity is 115 mAh.g<sup>-1</sup>. The efficiency of the total electrochemical reaction discharge/charge is 78% and the calculated specific energy density is 253 Wh.g<sup>-1</sup>. In the 4 volt region the same active electrode material displays a reversible capacity of 135 mAh.g<sup>-1</sup> at the 3<sup>rd</sup>

cycle. The cycleability in the same region is pretty good, 115 mAh.g<sup>-1</sup> at the 100<sup>th</sup> cycle.

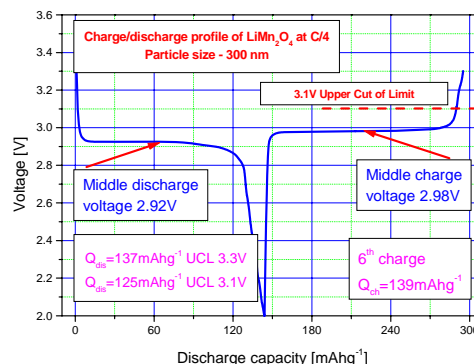


**Fig. 10.** Charge discharge profile of 3 volts spinel prepared according to new technique.

The discharge/charge profile of the active electrode material, prepared by the new synthesis process, is presented in Fig.10. The first difference between both syntheses is observed in the discharge plateau. It is situated at 2.92 V, a value very close to the theoretical one – 2.95 volts. The second difference is in the displayed discharge capacity, 131mAh.g<sup>-1</sup>. Normally, the capacity in the 3 V region is close to 60 % from the theoretical one, i.e. it is around 90 mAh.g<sup>-1</sup>. In our case the obtained value is 1.5 times higher. A specific energy density of 375 Wh.g<sup>-1</sup> is achieved. The charge plateau shows reduced polarization – the middle charge voltage is 2.98 volts. The charge capacity of the new material is 139 mAh.g<sup>-1</sup> with an efficiency of about 94%.

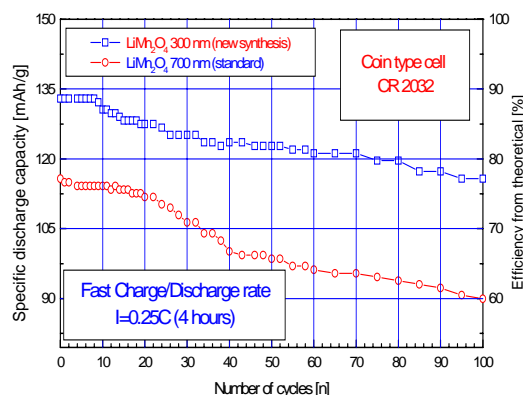


**Fig. 11.** Long term cycling of 3 volts spinel with particle size 300 and 700nm.

**Table 3.** Comparison of delivered capacity and columbic efficiency of AEM working in 3 and 4 volts range.

Cathode material	TheoCap. mAh/g	Practical Specific Capacity			CE* [%]
		5 <sup>th</sup>	25 <sup>th</sup>	50 <sup>th</sup>	
Li <sub>0.3</sub> MnO <sub>2</sub>	200	180	165	155	90-75
St LiMn <sub>2</sub> O <sub>4</sub>	148	90	75	60	60-40
New LiMn <sub>2</sub> O <sub>4</sub>	148	131	95	80	85-55
LiMn <sub>2</sub> O <sub>4</sub>	148	135	120	115	85-75
LiCoO <sub>2</sub>	275	160	155	150	60-52

According to similar investigations [5, 6], the higher SSA and porosity bring to higher discharge capacity and to lower polarization, which is in agreement with our results. They are summarized in Table 3. For comparison, the electrochemical performance of other types of active electrode materials, working in the 3-volt and the 4-volt regions, is given.

Obtained results show that the lithium spinel thus prepared is very attractive cathode material for practical use in the 3 volt region. The long-term cycleability of both samples with different particle size is presented in Fig. 11. Active electrode materials with small particle size exhibit high cycleability, good and stable electrochemical performances, and improved total efficiency. Thus, again it was demonstrated no negligible improvement of electrical characteristics by simple technique based on good knowledge of chemistry and electrochemistry of processes of tested material.

### CONCLUSIONS

Applying an appropriate synthesis method, the 3 volt region of the LiMn<sub>2</sub>O<sub>4</sub> spinel becomes very attractive for practical use, with specific energy density of more than 375Whg<sup>-1</sup>;

The charge/discharge profile of the active electrode material is improved with the SSA increase and the porosity;

The overall efficiency of manganese dioxide spinel, working in the 3 volt region, is increased up to 94%.

**Acknowledgement:** The authors acknowledge the financial support of the Bulgarian Academy of Sciences and the contribution from the German part in this project, the Karlsruhe Institute of Technology (KIT), as well as the Institute of Nanotechnology (INT) for the possibility given to the Ph.D student, Hristina Vasilchina, to work and to carry out the scientific investigation program during the period 2007–2010.

### REFERENCES

1. Y.K. Sun, K.J.Hong, J. Prakash, *J. Electrochem. Soc.* **150**, A970 (2003).
2. Y.K. Sun, Y.S.Lee, M. Yoshio, K. Amine, *Electrochem. and Solid-State Letters* **5**, A99 (2002).
3. Y.S. Lee, Y.K. Sun, S. Ota, T. Miyashita, M. Yoshio, *Electrochem. Comm.* **4**, 989 (2002).
4. M. S. Whittingham, P. Zavalij, *Solid State Ionics* **131**, 109 (2000).
5. H. Kurimoto, K. Suzuoka, T. Murakami, Y. Xia, H. Nakamura, M. Yoshio, *J. Electrochem. Soc.* **142**, 2156 (1995).
6. M. Yoshio, H. Noguchi, T. Miyashita, H. Nakamura, A. Kozawa, *J. Power Sources* **4**, 483 (1995).
7. J. Chao, Y. Kim, B. Park, *J. Electrochem. Soc.*, **149**, A127 (2002).
8. J. Chao, Y. Kim, B. Park, *J. Electrochem. Soc.* **149**, A288 (2002).
9. H. Huang, P. Bruce *J. Electrochem. Soc.* **141**, L76 (1994).
10. V. Manev, B. Banov, A. Momchilov, A. Nassalevska, *J. Power Sources* **57**, 99 (1995).
11. A. Momchilov, A. Trifonova, B. Banov, B. Puresheva, A. Kozawa, *ITE Battery Letters* **1**, 155 (1999).
12. N. Ilchev, B. Banov, *Progress in Batt. & Batt. Materials, JEC Press* **10**, 232 (1991).
13. N. Ilchev, B. Banov, *J. Power Sources* **35**, 175 (1991).
14. B. Banov, A. Momchilov, M. Massot, C. Julien, *Material Science and Engendering, B-solid state materials for advanced technology* **100**, 87 (2003).
15. B. Banov, N. Velinova, "Nanoscience and Nanotechnology", **6**, 189 (2005).
16. B. Banov, N. Velinova "Nanoscience and Nanotechnology", **5**, 131 (2005).
17. B. Banov, A. Momchilov, A. Trifonova, B. Puresheva in: C. Julien, Z. Stoynov, (Eds.), *Materials for lithium-ion batteries. Design and optimization, NATO Science Series, Kluwar Press*, **85**, 555 (2000).
18. B. Banov, Y. Todorov, A. Trofonova, A. Momchilov, V. Manev, *J. Power Sources* **68**, 578 (1997).
19. Y. Todorov, C. Wang, B. Banov, M. Yoshio, *ISE Annual Meeting Sept.*, 1997, Paris, France, Ext. Abstr. 97-18, p.176.
20. V. Manev, B. Banov, A. Momchilov, A. Nassalevska, *Proc. 9<sup>th</sup> IBA Battery Materials Symposium*, Cape Town, South Africa, 20-22 March 1995, Ext. Abstr. p.20.

## ЕКОЛОГИЧНО-СЪВМЕСТИМИ КАТОДНИ МАТЕРИАЛИ ЗА ЛИТИЕВО-ЙОННИ БАТЕРИИ

Б.И. Банов\*, Х.К. Василчина

*Институт по електрохимия и енергийни системи, Българска академия на науките, ул. Акад. Г. Бончев, бл. 10, 1113 София*

Постъпила на 26 юни, 2010 г.; приета на 4 октомври, 2010 г.

(Резюме)

Литиевият кобалтат, най-широко използвания катоден материал в произвежданите широко литиево йонни батерии, притежава добра циклируемост, високо разрядно напрежение и приемлива енергийна плътност. Неговата синтеза е лесна и може да бъде изготвян в широк промишлен мащаб. Цената обаче на кобалта е висока и е определяща за крайната цена на батерията. Кобалтът и неговите соли са високо токсични. Литиевият манганово диоксиден шпинел, притежава висока специфична тегловна и обемна енергия, висока кулонова ефективност, близка до теоретичната и добра циклируемост. Той не токсичен, не замърсява природата, цената му е ниска, но притежава някои недостатъци като нисък начален капацитет и понижена стабилност при повишена температура. Оптимизирайки методите на синтез и изяснявайки основните фактори влияещи върху електрохимичната стабилност, ние получихме литиево манганово диоксиден шпинел, притежаващ много атрактивни електрохимични характеристики, особено при широка употреба. В работата са представени изследванията на широка гама катодни материали на основата на модифицирани литиево манганово диоксидни шпинели с кулонова ефективност близка до 90% при температура от 55°C, разрядни скорости от 4С и живот над 500 цикъла. Получените резултати показват правилността на нашия подход, като методът може да бъде приложен и при други активни електродни материали за подобряване на техните електрохимични характеристики.

## Direct electrochemistry of myoglobin immobilized on non-modified and modified graphite

N. D. Dimcheva<sup>1\*</sup>, E. G. Horozova<sup>1</sup>, T. M. Dodevska<sup>2</sup>

<sup>1</sup> 'P. Hilendarski' University of Plovdiv, Department of Physical Chemistry 24 Tsar Asen St., Plovdiv 4000, Bulgaria

<sup>2</sup>University of Food Technologies, Department of Inorganic Chemistry with Physical Chemistry  
26 Maritsa Blvd., Plovdiv 4002, Bulgaria

Received: June 29, 2010; revised: September 20, 2010

Immobilization of redox protein myoglobin (Mb) through adsorption was optimized so that a direct redox transformation of the protein active site onto the surface of spectroscopic graphite was observed. The phenomenon of the direct electron transfer (DET) between the myoglobin redox centre and the electrode surface, detected both on non-modified and on graphite, patterned with gold nano-deposits, was studied using a wide range of electrochemical methods such as linear and cyclic voltammetry, square-wave voltammetry, and differential pulse voltammetry. It was shown that the immobilized Mb exhibits a high catalytic activity at the electroreduction of H<sub>2</sub>O<sub>2</sub>.

**Key words:** myoglobin, immobilized, graphite, direct electron transfer

### INTRODUCTION

The direct electron transfer (DET) between immobilized biocatalysts (redox enzymes or proteins) and the electrode surface is a key factor in the development of sensitive and fast responding electroanalytical devices (biosensors), on the one hand, and miniature electrochemical sources of electricity, the so called biofuel cells, on the other hand.

The occurrence of direct electrical communication between the immobilized biocatalyst and the electrode surface, provides a series of advantages in the designed on this basis amperometric biosensors, in terms of the: operating simplicity, cost-efficiency, high sensitivity and selectivity, relatively long linear dynamic range of the signal, and relatively good stability. The studies of DET between the proteins and the nano-modified electrode materials attracted plenty of interest [1–11] mainly because of the opportunity they provide to both, connect the biocomponent with the modifier via specific chemical interactions, and spatially orientate it on the electrode during immobilization. That is why the nanostructured materials that bind biomolecules are currently on high demand for the purposes of bioanalytical chemistry and biotechnologies.

An overview of the current state of the art in the bioelectrochemical area shows that the

development of systems based on direct bioelectrocatalysis has been achieved only for a limited number of enzymes, mainly for some heme- and Cu- containing redox enzymes (peroxidases, catalases, laccases, etc.) [12–14]. The great interest towards heme-containing redox proteins myoglobin (Mb) and hemoglobin [1–11, 15–20], is mainly due to their capabilities to perform direct electrical communication with modified electrodes, and hence to the new prospects that this type of heterogeneous bioelectrocatalysis opens up for sensor technologies. What is typical of these two redox-proteins is not only the structural similarity between their active sites but also their tendency to perform direct electron transfer (exchange) with carbonaceous electrodes, such as pyrographite [15–17], carbon paste [18] or glassy carbon [1–2]. In most of these cases myoglobin has been immobilized on electrode materials by including the redox-protein in polymer films: polyethylenimine [15], p-hydroxybutyrate (a naturally occurring lipid polymer) [16], ionomer Eastman AQ38 [17], through the formation of zol-gel [18], in a layer of hexagonal mesoporous silica (HMS) [2], in the non-toxic and possessing good biocompatibility films of histidine [19] and chitosan [20].

The purposeful building of complex electrode architecture by patterning its surface is a novel approach to immobilizing the biocomponent, aimed at achieving direct electrical communication between the biocomponent and the electrode through: 1) shortening the distance between the

\* To whom all correspondence should be sent:  
E-mail: [ninadd@uni-plovdiv.bg](mailto:ninadd@uni-plovdiv.bg)

electrode surface and the active centre; and 2) orientating the biocatalyst in a conformation favorable for DET. In this connection, the modification of electrode materials with nanoparticles of  $ZrO_2$  [1], with gold nanoparticles [3–6], carbon nanotubes (CNT) [8–10], and titanium nanotubes (TiNT) [11], prior to immobilizing myoglobin in all cases has resulted in direct bioelectrocatalysis. The capacity and possibilities of these bioelectrocatalytic systems are determined by the unique properties of the nanoparticles. They are characterized by a high surface-to-volume ratio and provide a reliable and compact surface for the oriented adsorption of biomolecules while retaining their biological activity. In most cases, the very Au-nanoparticles represent a kind of nano-wires, facilitating the electron transfer between the electrode and the protein. The employed modification approaches allow for the size and the surface morphology to be controlled through varying the conditions for depositing them. In all investigated cases, the direct bioelectrocatalysis with immobilized myoglobin offers a good basis for the development of extremely selective biosensors for qualitative determination of  $H_2O_2$ ,  $O_2$ ,  $CCl_3COOH$  and  $NaNO_2$ .

During the past decade two research streams became traditional for our group: a) studies on the electrocatalytic activity of compact carbonaceous materials, modified with biological catalysts, redox-proteins and enzymes from the group of the oxidoreductases; and b) development and characterization of electrocatalysts through electrochemical deposition of micro- and nanostructures of precious metals (Pd, Pt, Au, Ir, etc.). This study brings together to a great extent the above specified two research directions of the group, and its objective is to investigate the direct electrochemistry of myoglobin (Mb), immobilized on both, non-modified and graphite, modified with gold nanodeposits, as well as to examine its electrocatalytic activity at the reduction of  $H_2O_2$

## EXPERIMENTAL

### Materials

Myoglobin, purified from horse heart muscle, was used in this research work (myoglobin from horse heart: Fluka Biochemika).

$H_2O_2$  and the chemicals for preparing the buffer solutions ( $Na_2HPO_4 \cdot 12H_2O$ , citric acid, conc.  $H_3PO_4$  and Tris (hydroxymethyl – aminomethane), were all purchased from Fluka. Gelatin for

analytical application, manufactured by Chimtek Bulgaria, was used for the film coating of the modified electrodes as a gel (5% in phosphate-citrate buffer, pH 7.0). All solutions were prepared with double-distilled water.

The working electrode was made of spectroscopically pure graphite, in the shape of a disc with a diameter of 0.5 – 0.6 cm, pressed (extruded) together with Teflon, with a copper current lead.

### Preparation of the electrodes:

a/ the gold nanoparticles were deposited onto graphite electrode through the following procedure: mechanically cleaned and rinsed with double distilled water electrode was used as working electrode in a conventional three-electrode cell (with non-separated compartments), filled with a 2% solution of  $HAuCl_4$  + 0.1M HCl, followed by a brief electrolysis ( $t = 10$  s) at  $E_r^{dep} = +0.05V$ , vs. a reversible hydrogen electrode.

b/ both on non-modified and modified with gold nanodeposits graphite, redox protein Mb was adsorbed under static conditions from a solution containing  $2 \text{ mg} \cdot \text{ml}^{-1}$  Mb, dissolved in Tris-buffer, pH = 7. The duration of the adsorption process was from 30 to 60 min., and was followed by electrode air-drying. In addition, a drop of 20  $\mu\text{l}$  of the same Mb solution was deposited on the electrode surface and left to dry in air.

### Equipment and measurements

All electrochemical measurements were performed in a non-compartmentalized three-electrode cell with a working volume of 10–15 ml. Ag/AgCl (1M KCl) was used as a reference electrode, and a platinum wire – as an auxiliary electrode.

Cyclic, square-wave and differential pulse voltammetry were performed using Palm Sens electrochemical workstation (Palm Sens BV, the Nederland).

## RESULTS AND DISCUSSION

Fig.1 shows cyclic voltammetric curves (CVs) of the myoglobin, adsorbed on bare graphite in a background electrolyte phosphate-citrate buffer, pH = 7. The voltammograms were registered at different scan rates ranging from 1 to  $40 \text{ mV} \cdot \text{s}^{-1}$ . Fig. 1 shows diffuse maxima on the anode (over the region from – 0.05 to 0.10 V) and the cathode (at the reverse scan from –0.30 to – 0.10 V) parts of the voltammogram. Peak reversibility was established only at the lowest rate

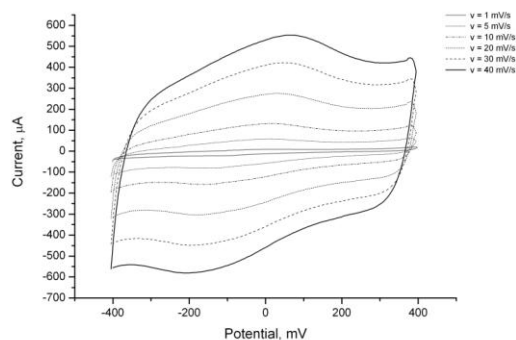


**Fig.1.** Cyclic voltammograms of adsorbed on graphite myoglobin; phosphate – citrate buffer pH 7.0 ; scan rate of 1, 5, 10, 20, 30, 40  $\text{mV}\cdot\text{s}^{-1}$  (from inner to outer) ; reference electrode Ag/AgCl, 1M KCl.

of  $1 \text{ mV}\cdot\text{s}^{-1}$ . The peaks are reversible at this rate since the following criteria applied for both maxima:

$$I_a^* / I_k^* = 1 \quad \text{and}$$

$$\Delta E = E_a^* - E_k^* = \Delta E^* = \frac{2,303RT}{nF},$$

where  $I_a^*$  and  $E_a^*$  are the values of the current and the potential of the anode peak, respectively; and  $I_k^*$  and  $E_k^*$  are the analogous values of the cathode peak.

The criterion that apply at scan rates between 5 and  $20 \text{ mV}\cdot\text{s}^{-1}$  is :

$$\Delta E = E_a^* - E_k^* = \frac{2,303RT}{\alpha nF},$$

which suggests a quasi-reversible electrochemistry of the adsorbed myoglobin. At scan rates higher than  $20 \text{ mV}\cdot\text{s}^{-1}$ , the process turns practically irreversible, as peak separation  $\Delta E^* > 200 \text{ mV}$ . Upon increasing scan rate, the anode maxima shift in a positive direction while the cathode maxima move in a negative direction. At  $v = 40 \text{ mV}\cdot\text{s}^{-1}$ , the anode maximum was found to be at a potential of

$$E_a^* = 60 \pm 5 \text{ mV},$$

and the cathode's at

$$E_k^* = -180 \pm 10 \text{ mV}.$$

Such redox maxima were not observed on the CVs of the bare graphite electrode (without adsorbed Mb, not shown in Fig.1). Therefore, their occurrence is due to the redox transformation of the myoglobin, immobilized on graphite. This transformation involves the iron in the heme of its

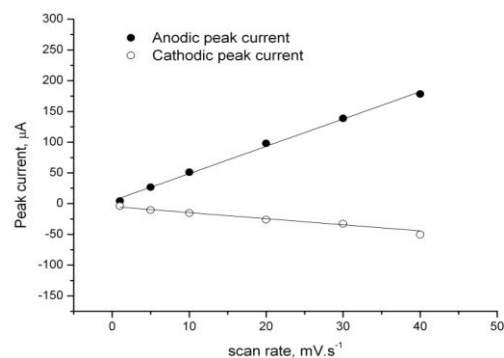


**Fig.2.** Peak current vs. scan rate of anodic (upper graph curve) and cathodic (bottom curve) peak current ( $\mu\text{A}$ ) of myoglobin adsorbed on graphite.

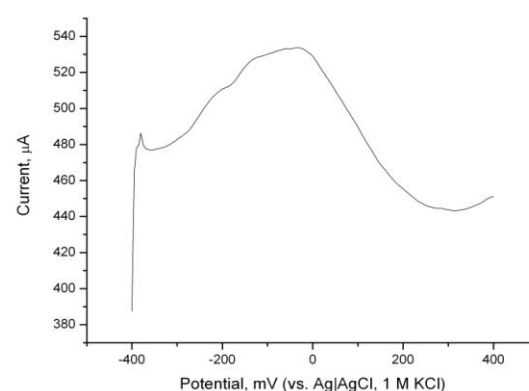


**Fig.3.** Square wave voltammetry of adsorbed on graphite myoglobin; phosphate- citrate buffer pH 7.0; reference electrode Ag /AgCl, 1 M KCl.

active centre. The number of electrons, taking part in the redox process, has been calculated on the basis of the equation

$$\Delta E^* = \frac{2,303RT}{\alpha nF},$$

assuming the transfer factor

$$\alpha = 0.5. \text{ At } \Delta E^* = 100 \text{ mV},$$

the number of electrons is  $n = 1.16$ , i.e. one electron exchanged during the redox process.

The dependence of the anode current (upper curve) and the cathode (lower curve) maxima on the scan rate is depicted in Fig.2. The linear trend of this dependence shows that the process, which takes place on the graphite, is controlled by surface chemistry, i.e. it takes place in a thin surface layer.

The electrochemistry of the myoglobin, immobilized on non-modified graphite, was also examined by means of the square-wave voltammetry (Fig.3). The formal redox potential of

the heme in the myoglobin active site was determined to be:

$$E_{red./ox.} = \frac{E_a^* + E_k^*}{2} = -30 \pm 20 \text{ mV}$$

(due to the broad maximum observed in Fig.3).

The potential, determined through the SWV method,  $E_{red./ox.}$ , is completely consistent with the data presented, which were obtained by cyclic voltammetry (see Fig.1).

Fig.4 shows the cyclic voltammogram of myoglobin, adsorbed on graphite modified with gold nanoparticles. Reversible anode and cathode maxima can be observed on the CV, the region from  $-450 \text{ mV}$  to  $-250 \text{ mV}$  (on the anode curve) and from  $-500 \text{ mV}$  to  $-250 \text{ mV}$  (on the cathode curve). Their reversibility was examined according to the two criteria, specified above. The values of the currents  $I_a^*$  and  $I_k^*$  in applying the criteria, are determined as shown in Fig.4, subtracting the background current. This finding evidences the complete reversibility of the electrochemical reaction which takes place on the modified graphite electrode with immobilized myoglobin.

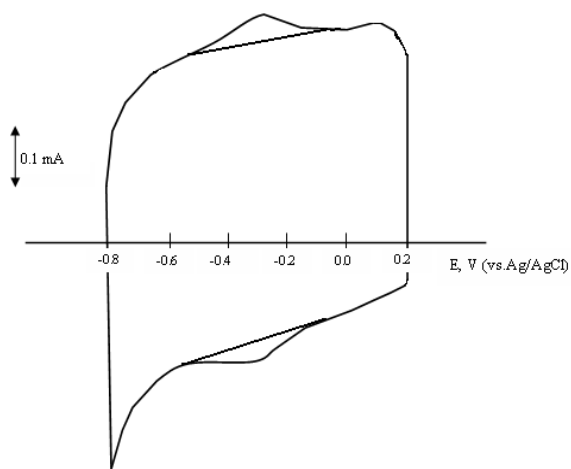


**Fig. 4.** Cyclic voltammogram of myoglobin, adsorbed on modified whit Au-nanodeposits graphite; phosphate-citrate buffer pH 7.0; scan rate  $80 \text{ mV}\cdot\text{s}^{-1}$ ; reference electrode Ag/AgCl.

The fact that it is possible to register reproducible I, E curves continuously, proves that myoglobin is adsorbed irreversibly on graphite, modified with gold nanoparticles. In addition to the high biocompatibility of the gold nanoparticles, the facilitated electron transfer between the protein redox site and the electrode surface, is also due to the specific binding of thiolated terminal groups

from the protein shell of the myoglobin with gold, i.e. this is the so called self-assembly of the protein onto the gold surface, which is a typical chemisorption process.

The atomic-force microscopy of the graphite, modified with gold nanoparticles, revealed (Fig.5) that the gold nano-wires, formed during the modification, reached a height of up to 100 nm, thus also contributing to shortening the distance between the myoglobin active site and the modified surface.

The voltammetric studies of the graphite, modified with immobilized myoglobin (Fig.4), shows that oxidation and reduction of the protein take place at a potential of

$$E = -300 \pm 20 \text{ mV.}$$

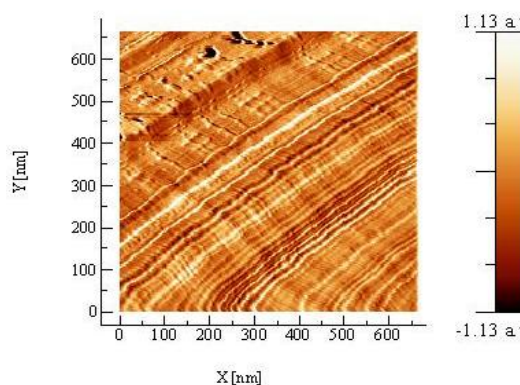


**Fig. 5a**

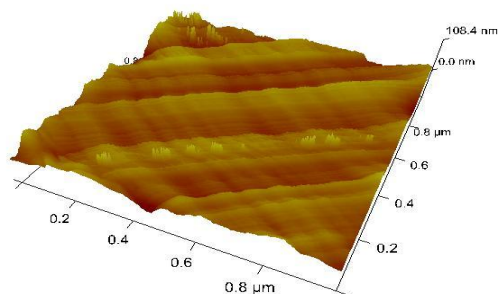


**Fig. 5b**

**Fig. 5.** 3D- topology of modified with Au-nanodeposits graphite studied whit AFM.

The number of electrons, calculated from the correlation of

$$\Delta E^* = 2,303 \frac{RT}{nF},$$

is also one. Therefore, the redox transformation of the myoglobin, adsorbed on modified graphite, also affects the iron in the heme of the protein active centre, and proceeds with the transfer of one electron. The voltammetric curves of the

myoglobin, adsorbed on modified graphite, are characterized by sharper and more clearly defined maxima (Fig.4) as compared to the curves of the myoglobin, adsorbed on bare graphite (Fig.1). Similarly to the electrochemical behavior of the protein, adsorbed on bare graphite, the cathode peaks, observed on modified graphite, also shift negatively with increasing scan rate (Fig.6).

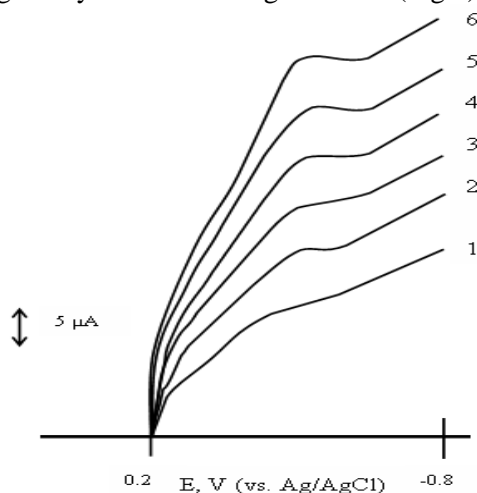


**Fig.6.** Cathodic linear sweep voltammograms of myoglobin, adsorbed on modified with Au-nanodeposits graphite; phosphate-citrate buffer pH 7.0; scan rate: 10-60  $\text{mV}\cdot\text{s}^{-1}$  (1-6); reference electrode Ag/AgCl, 1M KCl.

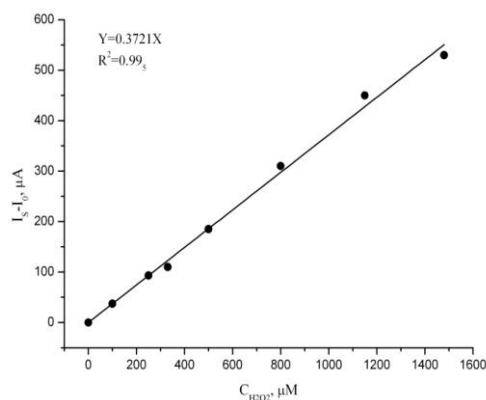


**Fig.7.** The linear regression of the reduction peak current as dependent on increased  $\text{H}_2\text{O}_2$  concentration.

The catalytic activity of myoglobin, adsorbed on graphite, modified with gold nanoparticles, was also examined at the electrochemical reduction of  $\text{H}_2\text{O}_2$  (Fig.7). It can be seen on this Figure that the dependence of the cathodic current on the concentration of  $\text{H}_2\text{O}_2$  is linear over one and a half orders of magnitude, ranging from  $1\times 10^{-4}$  M to  $15\times 10^{-4}$  M. The linear regression was shown to obey the equation of  $y = bx$  with a correlation factor of 0.995; the sensitivity being  $dI/dC = 0.372$

$\mu\text{A}\cdot\mu\text{M}^{-1}$ . This reaction constitutes a possibility for creating an amperometric biosensor for  $\text{H}_2\text{O}_2$ .

## CONCLUSIONS

- An optimal method for adsorption of myoglobin on both, non-modified graphite and on graphite, modified with gold nanoparticles, was found where a direct redox transformation of the protein was observed.

- The voltammetric studies show that depending on the scan rate, the electrochemical reaction of hemoglobin, adsorbed on non-modified graphite, changes from reversible through quasi-reversible to irreversible as the rate increases. This reaction is also not completely reversible on modified graphite.

- The redox transformation of the immobilized myoglobin, both, on non-modified and on modified graphite, involves the iron in the heme of the protein active centre. The redox potential of myoglobin, adsorbed on non-modified graphite, was found to be  $E = 30 \pm 20$  mV, and on modified graphite -  $E = -300 \pm 20$  mV.

- Myoglobin, adsorbed on graphite, modified with Au-nanoparticles, exhibits high electrocatalytic activity in the reduction of  $\text{H}_2\text{O}_2$ . This reaction provides a possibility for creating an amperometric biosensor for detection of  $\text{H}_2\text{O}_2$ .

**Acknowledgements:** The financial support from the University of Plovdiv Research Fund (Grant RS-X 12/09) is gratefully acknowledged. The access to the PalmSens electrochemical workstation, provided within the collaborative DO 02-145/2008 Project (with the Bulgarian National Science Foundation), is appreciated.

## REFERENCES

- 1 G. Zhao, F.J.-Ju, X.J.-Juan, C.H.-Yuan, *Electrochem. Commun.*, **7**, 724 (2005).
- 2 Z. Dai, X. Xu, H. Ju, *Anal. Bioch.*, **332**, 23 (2004).
- 3 S. Liu, H. Ju, *Electroanalysis*, **15**, 1488 (2003).
- 4 L. S Duan, Q. Xu, F. Xil, S. F. Wang, *Int. J. Electrochem. Sci*, **3**, 118, (2008).
- 5 S. Zhao, K. Zhang, Y. Bai, W. Yang, *Sun C., Bioelectrochem.*, **69**, 158, (2006).
- 6 S. Zhang, W. Yang, Y. Niu, Y. Li, M. Zhang, *Sun C., Anal. Bioanal. Chem.*, **384**, 736, (2006).
- 7 P. Yanez-Sedeno, J.M. Pingarron, *Anal. Bioanal. Chem.* **382**, 884 (2005).
- 8 W. Sun, X. Li, Y. Wang, X. Li, C. Zhao, K. Jiao, *Bioelectrochem.*, **75**, 170 (2009).

- 9 L. Zhang, G.C. Zhao, X.-W. Wei, Z.Z. Yang., *Chem. Letters*, **33**, 86 (2004).
- 10 M.G. Esplandiu, M. Pacios, L. Cydanek, J. Bartoli, M. del Valle, *Nanotechnology*, **20**, 355502 (2009).
- 11 A. Liu, M. Wei, I. Honma, H. Zhou, *Anal. Chem.* **77**, 8068 (2005).
- 12 G.K. Ahirwal, C.K. Mitra, *Sensors*, **9**, 881 (2009).
- 13 A. Christenson, N. Dimcheva, E. Ferapontova, Lo Gorton, T. Ruzgas, L. Stoica, S. Shleev, A. Yaropolov, D. Haltrich, R. Thorneley, S. Aust, *Electroanalysis*, **16**, 1074 (2004).
- 14 E. Horozova, N. Dimcheva, Z. Jordanova, *Bioelectrochem*, **53**, 11 (2001).
- 15 A. Pardo, R. Basseguy, A. Bergel, *J. Applied Electrochem.*, **36**, 835 (2006).
- 16 X. Ma, R. Yang, G. Li, *American Biochem. and Biotechn.*, **1**, 43 (2005).
- 17 N. Hu, J.F. Rusling, *Langmuir*, **13**, 4119 (1997).
- 18 Q. Wang, G. Lu, B. Yang, *Langmuir*, **20**, 1342 (2004).
- 19 G. Li, L. Chen, J. Zhu, D. Zhu, D.F. Untereker, *Electroanalysis*, **11**, 139 (1999).
- 20 X. Feng, Y. Liu, Q. Kong, J.X. Chen, J. Hu, Z. Chen, *J. Solid State Electrochem.* **4**, 923 (2009).

## ДИРЕКТНИ ЕЛЕКТРОХИМИЧНИ ОТНАСЯНИЯ НА МИОГЛОБИН, ИМОБИЛИЗИРАН ВЪРХУ НЕМОДИФИЦИРАН И МОДИФИЦИРАН ГРАФИТ

Н.Д. Димчева<sup>1</sup>, Е.Г. Хорозова<sup>1</sup>, Т.М. Додевска<sup>2</sup>

<sup>1</sup> Пловдивски университет "Паусий Хилендарски", Департамент по физикохимия, Пловдив 4000

<sup>2</sup> Университет по хранителни технологии, Департамент по неорганична химия с физикохимия, Пловдив 4002

Постъпила на 29 юни, 2010 г.; преработена на 20 септември, 2010 г.

(Резюме)

Адсорбционната имобилизация на редокс-протеина миоглобин (Mb) върху повърхността на спектрално-чист графит беше оптимизирана така, че да се осъществи директна електрохимична трансформация на активния му център върху повърхността на така получения ензимен електрод. Осъществяване на явлението директен електронен пренос (DET) между редокс-активния център на миоглобина и електродната повърхност беше наблюдавано както върху немодифицирани, така и върху модифицирани със златни нано-отложения графити и беше изследвано с разнообразни електрохимични методи: линейна и циклична волтаперометрия, волтаперометрия с квадратен импулс и диференциална импулсна волтаперометрия. Беше показано, че имобилизираният миоглобин притежава висока каталитична активност при електрохимичната редукция на H<sub>2</sub>O<sub>2</sub>.

## Effect of preliminary treatment on the superficial morphology and the corrosion behaviour of AA2024 aluminum alloy

E. A. Matter<sup>a,\*</sup>, S. V. Kozhukharov<sup>b</sup>, M. S. Machkova<sup>b</sup>

*a) Chemistry Department, Faculty of Science, Damanhour University, 22111 Damanhour, Egypt.*

*b) University of Chemical Technology and Metallurgy, 8 Kl. Ohridski St, 1756 Sofia, Bulgaria.*

Received: June 10, 2010; revised: September 27, 2010

The effect of the superficial preliminary treatment on the properties of the oxide film and its influence on the corrosion behaviour of AA 2024 aluminum alloy in 3.5% NaCl solution was investigated. It was done applying crystallographic optical and atomic force microscopic techniques, combined with electrochemical measurements - linear voltammetry (LVA) and Electrochemical Impedance Spectroscopy (EIS).

Three approaches were used for preliminary treatments of the samples, as follows: only degreasing (without removal of oxide film), mechanical polishing and a combination between mechanical polishing with etching in alkaline solutions. The parameters of the corrosion process (polarization resistance, pitting nucleation potential, impedance module and capacitance) were used as a quantitative measure for the effect of the preliminary treatment approach. It was established that the most effective pretreatment in terms of removal of the oxide layer is the mechanical polishing. The undertaken electrochemical measurements evidenced that the approach of etching in alkaline solutions, used in a large number of articles, causes a formation of a film, which could not be removed completely by desmutting with diluted solutions of HNO<sub>3</sub>. Etching procedure could be appropriate for other Al-alloys but it is not recommended for the AA2024 alloy.

**Keywords:** preliminary treatment, corrosion, aluminum alloy - AA2024, EIS.

### INTRODUCTION

The aluminum is a metal which possesses a distinguishable corrosion resistivity in a water media. It is well known that the reason for this is the formation of a natural oxide layer, which is usually present on its surface. In neutral environments, this film consists generally of boehmite  $\gamma$ -AlO(OH) mineral [1]. According to ref. [1] it has relatively low thickness (5nm), as well as low electronic conductivity, which strongly hinders the oxidation and the reduction reactions in the corrosion process. In the case of Al-alloys, due to the extended mechanical strength and the relatively lower weight, they are accompanied coincidentally by enhanced susceptibility to local corrosion impact. These alloys possess lower corrosion resistivity, due to the presence of intermetallics in the basic Al-matrix. These inclusions are in the form of particles, which become centers of nucleation and further spreading of local corrosion process. AA2024 alloy reveals peculiar aptitude to that kind of corrosion [2-5]. This alloy is generally used in the aircraft industry, but its application is possible only upon appropriate and effective anticorrosion protection [6].

In any case related to the protection methods, either by inhibitors or by protective coatings, the corresponding alloy samples undergo preliminary treatments in order to remove the superficial oxide layer. There is a large variety of methods which are based on two general approaches: a) mechanical treatment [7-9] by grinding with emery paper and b) chemical by dissolution of the film in alkaline solutions [10-12]. No description for the reasons of approach selection is found in the literature. Logically, a comparison between the above approaches and their impact over the AA2024 behavior in a corrosive medium is necessary.

It seems that one of the reasons for the contradictive results, described by different authors [3-12], as well as the unsatisfactory reproduction of such results, could be ascribed to the difference in the approaches, applied for the preliminary treatments.

The aim of the present work is to study the effect of the preliminary treatment on the superficial morphology of the AA2024 alloy which predetermines its behavior in corrosive media. In addition, a detailed description of the preliminary treatment effect on the parameters of the corrosion process and their evolution within the exposure time, for the AA2024 aluminum alloy in an aggressive Cl<sup>-</sup> ions media was done.

\* To whom all correspondence should be sent:  
E-mail: e\_a\_matter@yahoo.com

## EXPERIMENTAL

### 2.1. AA2024 aluminum alloy composition

The composition is presented in Table 1, determined by Induction Coupled Plasma (ICP–OES) analysis upon decomposition in a mixture of acids.

**Table 1.** Composition of AA2024 aluminum determined by ICP – OES analysis.

Element	Concentration (wt. %)
Al	remainder
Cu	3.716
Fe	0.404
Mg	1.259
Mn	0.537
Ni	0.055
Si	<0.01

### 2.2. Preliminary treatment of the samples

AA2024 metal plates with thickness of 2 mm underwent the following preliminary treatment procedures:

**S<sub>1</sub>**- As received, only degreasing in Ethanol/Ether 1:1 (10 min) and final washing vigorously with distilled water. It should be noticed that the natural oxide layer is not removed in this case;

**S<sub>2</sub>**- Polished, using emery paper, in the following order: 240-360-500-800 grits. Then degreased by Ethanol/Ether 1:1 (10 min) and finally washed with distilled water;

**S<sub>3</sub>**- Polished, using emery paper as described above, degreased with Ethanol/Ether 1:1 (10 min), washed with distilled water, after that chemically treated with a mixture of [NaOH (40gm/l) + Na<sub>3</sub>PO<sub>4</sub> (30gm/l) + Na<sub>2</sub>CO<sub>3</sub> (20gm/l) for 3 min at 60 °C], then desmutted by [HNO<sub>3</sub> : H<sub>2</sub>O (1:1)] solution for 2 min, at room temperature, and finally washed by distilled water.

The corresponding methods of preliminary treatment procedures either could be found in various articles [3-12] or recommended in handbooks [13, 14].

### 2.3. Superficial morphology measurements

#### a. Optical metallographic microscopy

It was carried out using BOECO metallographic microscope. The image measurements were obtained by web-camera with 600 x 800 pixel resolution at a magnification of 40X.

#### b. Atomic Force Microscopy

The observations were performed by EasyScan 2 AFM, supplied by Nanosurf,

Switzerland, supported by TAP190G cantilever, produced by Budgetsensors, Bulgaria. The measurements were done at a square area of 49.5 μm linear size. The resolution was 256 points/line, at an imaging rate of 2 seconds per line. The images were obtained in a “scan forward” mode and the scan mode was from down to up, performed in static regime.

### 2.4. Electrochemical measurements

For the purpose, three-electrode electrochemical cell with a volume of 100 ml was used. The area of each sample, serving as a working electrode, was about 2.0 cm<sup>2</sup>. A platinum net in a cylindrical form was used as counter electrode. Its surface area was relatively two orders of magnitude higher than that of the working electrode, in order to avoid the influence of its superficial capacitance on the experimental results [15, 16]. All potential values of the working electrode were measured using Ag/AgCl standard reference electrode, model 0726100, produced by Metrohm, with a potential of E(Ag<sup>+</sup>/AgCl) = 0.2224V (with 3M KCl).

AUTOLAB PGStat 30/2 potentiostat-galvanostat, produced by ECO CHEMIE B.V. in the Netherlands, with additional FRA-2 frequency response analyzer, was used for the both kinds of electrochemical measurements. Each linear voltammetric measurement was carried out after acquiring of the respective impedance spectrum in order to eliminate any possible changes of the electrode surface due to the high polarization. The measurements were performed in the following sequence: initially cathodic polarization curves were recorded in the potential range from OCP + 0.03 V to OCP – 0.40 V with a potential sweep rate of 0.001 V/s. After recuperation of the OCP, the anodic polarization curves were recorded in the range from OCP - 0.03 V to OCP + 0.50 V. At least 3 samples underwent the same test procedures in order to obtain reliable results. The results of the most representative sample of each group were selected for the needs of this research work.

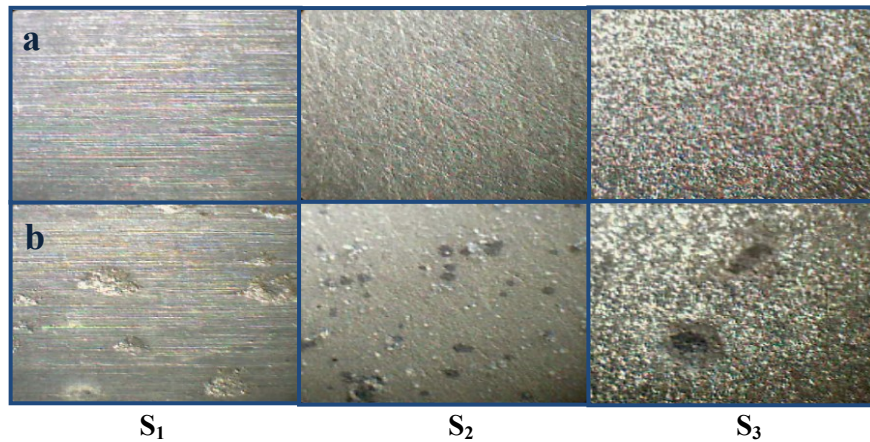
All the EISs were done at an OCP in the frequency range between 10<sup>5</sup> and 10<sup>-2</sup> Hz at 7 frequencies per decade, and signal amplitude of 20 mV from peak to peak. The entire electrochemical cell was enclosed in Faraday cage, in order to avoid any outside electromagnetic influences. The corrosive medium was a 3.5 % NaCl solution with a pH= 6.60, served as a naturally aerated model corrosive medium (electrolyte). All measurements were carried out at a room temperature.

## RESULTS AND DISCUSSION

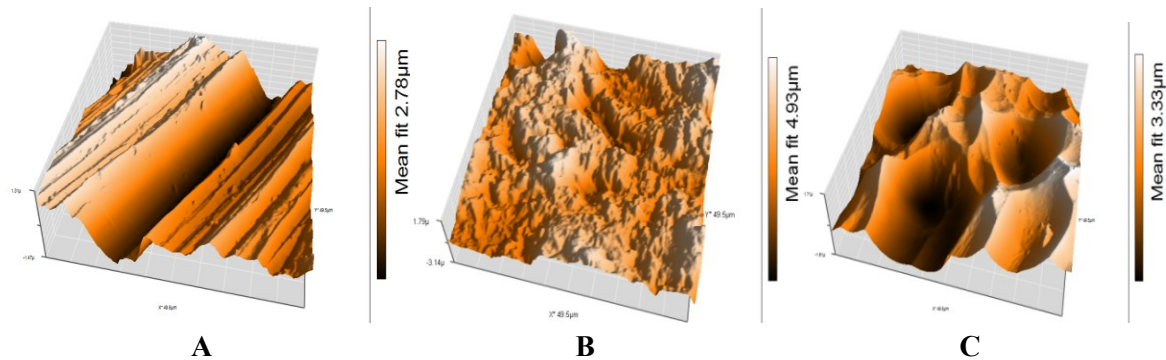
### 3.1. Surface morphology

Figure 1 shows the optical metallographic images of the sample surface upon different pre-

treatments prior to their immersion and after 24-hours of exposure into the corrosive solution. On Figure 2 are depicted the initial surface topographies obtained via AFM microscopy.



**Fig. 1.** Images obtained by Optical Metallographic Microscopy for samples  $S_1$ ,  $S_2$  and  $S_3$  after superficial pretreatment (a) - before and (b) - after 24 hours exposure into the aggressive medium and subsequent anodic polarization.



**Fig. 2.** Topographic images of the output surface obtained with AFM microscopy for A- degreased, B-mechanically polished and C-mechanical then etched with alkaline solutions samples.

One of the most interesting effects is seen in the surface morphology of the specimen after anodic polarization (Fig. 1-b). From the Figure is clear that a few corrosive spots are observed on sample surface which was only degreased ( $S_1$ -procedure). The morphology of these spots is consequence of the thicker oxide layer on this sample, which predetermines the kinetics of the pitting growth. The pitting appears on the sites of defects in the layer only. Similar behaviour was established for the  $S_3$  treatment procedure, as well. The products, of the surface etching remain in the form of insoluble layer and cannot be removed by desmutting in  $\text{HNO}_3/\text{H}_2\text{O}$  (1:1) solution.

In the case of mechanical pretreatment ( $S_2$ -procedure), the thick oxide layer, which is formed during the metallurgical production process, was removed. It was established that only very thin oxide film was formed during the exposure into the corrosive medium. The formed oxide layer was of uneven thickness and thinner in the areas where the

intermetallic particles of the alloy elements (Al, Mg, Cu) exist, as mentioned by other authors [2-6]. According to Yasakau and co-workers [5], the most predominant among the various intermetallics is the S-phase ( $\text{Al}_2\text{CuMg}$ ). The latter occupies more than 60% of all inclusions into the AA2024 alloy. Consequently, S-phase has the most significant contribution to the AA2024 behaviour. Namely, the S-phase superficial areas, possess defects in the oxide film. The chloride anions in the solution predominantly attack these areas and form pitting centers which due to their large number grow slowly and do not stimulate development of crevice corrosion.

### 3.2. Electrochemical measurements

#### a. Polarization measurements

Figure 3 shows that the variation of OCP with the exposure time is remarkably different depending on the technique, applied in the preliminary

treatment. OCP of the  $S_1$  sample oscillates around a defined value, remaining almost unchanged even after 24 hours. Similar behaviour is observed also in the case of the sample, etched by the  $S_3$  procedure. Similar oscillations of OCP are also described by Schem and co-authors [10]. According to them, these oscillations are indicative for permanent nucleation and repassivation of pitting.

The observed differences of the shapes of OCP-time curves of all samples could be explained by the Yasakau concepts [5]. Intermetallics are formed in the AA2024 structure as particles with different size and composition. The most widespread among them is named "S-phase" with  $Al_2CuMg$  composition. Al is presented consequently in both, the basic matrix and the intermetallics. The corrosion mechanism of the AA2024 alloy is described in details by Yasakau and co-workers [5].

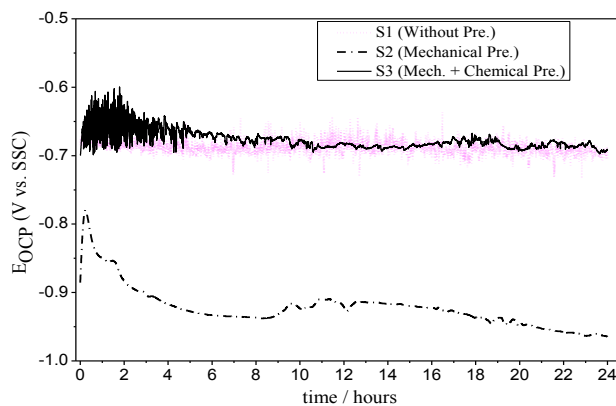


**Fig. 3.** Open Circuit Potential - time curves of samples prepared with different approaches of preliminary treatment during the exposure to 3.5 % NaCl.

When the polished sample ( $S_2$ ) is exposed into the model corrosive medium, *chemical selective dissolution* of Al and Mg from the S-phase begins, causing enrichment of the surface by copper remnants. The latter, shift the OCP to more positive values (Fig. 3, curve  $S_2$ ). The copper enriched remnants become cathodic areas, relative to the aluminum matrix, which in that case reveals anodic behaviour. As a consequence, galvanic couples appear, promoting *electrochemical dissolution* of Al from the anodic zones. After that moment, accelerated rate of the anodic reaction causes shift of the OCP values towards the negative direction. Moreover, the evolution of the OCP values in the case of  $S_3$  and  $S_1$  is similar due to the fact that the surfaces of both are covered by oxide film.

Figure 4 shows the cathodic and anodic potentiodynamic polarization curves of the samples upon different superficial treatments and different duration of exposition to corrosive medium (3.5 % NaCl). It could be seen that the sample with a

natural oxide layer ( $S_1$ ), compared to the rest of the samples, shows the lowest cathodic currents (Fig. 4-a). Evidently is that the cathodic partial reaction is more remarkably hindered by both, the higher thickness and the lower electronic conductivity. This film is removed afterwards, either by mechanical polishing ( $S_2$ ) or by etching in alkaline solutions ( $S_3$ ). Cathode currents increase with one order of magnitude, achieving almost the same values.

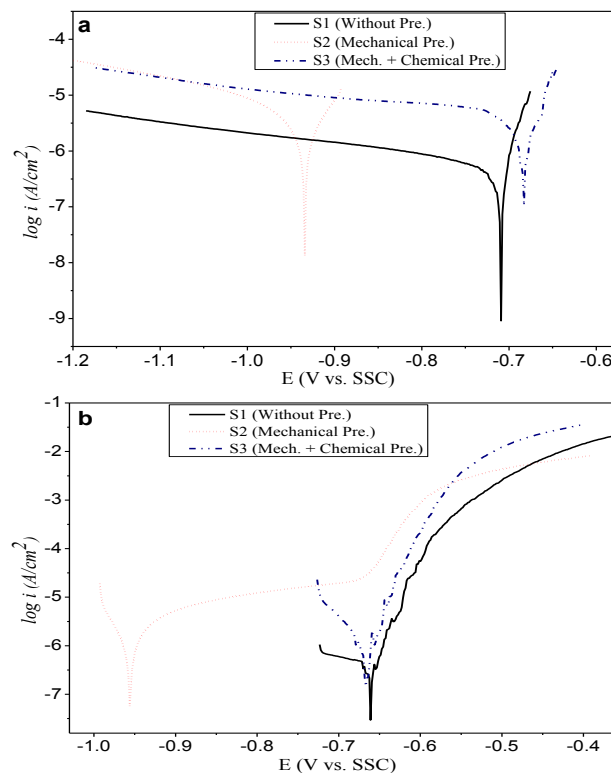


**Fig. 4.** Potentiodynamic cathodic- (a) and anodic- (b) polarization curves of samples prepared with different approaches of preliminary treatment after 4h exposure to 3.5% NaCl solution.

It seems that the superficial sediments, formed during etching, possess relatively high electronic conductivity because it does not suppress the cathode partial reaction of oxygen reduction. The anodic partial polarization curves of  $S_1$  and  $S_3$  treatments (Fig. 4-b) after 4 hours of exposure are almost identical and they have not got any passive region. The absence of such region means that there is overlapping between the corrosion potential and the potential of pitting nucleation [17].

The shape of the anodic polarization curve of the mechanically treated sample ( $S_2$ ) is quite different. The corrosion potential of this sample is shifted into a negative direction as a result of acceleration of the anodic polarization reaction. The corrosion products, formed on the surface of the

samples, cause the appearance of anodic current plateau. At higher polarization, when the pitting formation potential is reached, a sharp rise of the current density begins and becomes almost equal to the current values of the  $S_1$  and  $S_3$  samples.

*b. EIS measurements*

The application of this method gives a possibility to clarify the nature of the physical and chemical processes in the bulk of the individual phases and their boundaries in the entire metal/electrolyte system. Figure 5 shows the impedance spectra in Bode and Nyquist plots for the samples after 2 hours of exposure to a corrosive medium. Clearly defined maximum at the average frequency range (from  $10^2$  to 0.5 Hz) is observed in the spectra of all samples. This maximum is related to the time-constant  $\tau = RC$ , originated from the parallel connection between the resistance R and the capacitance C.

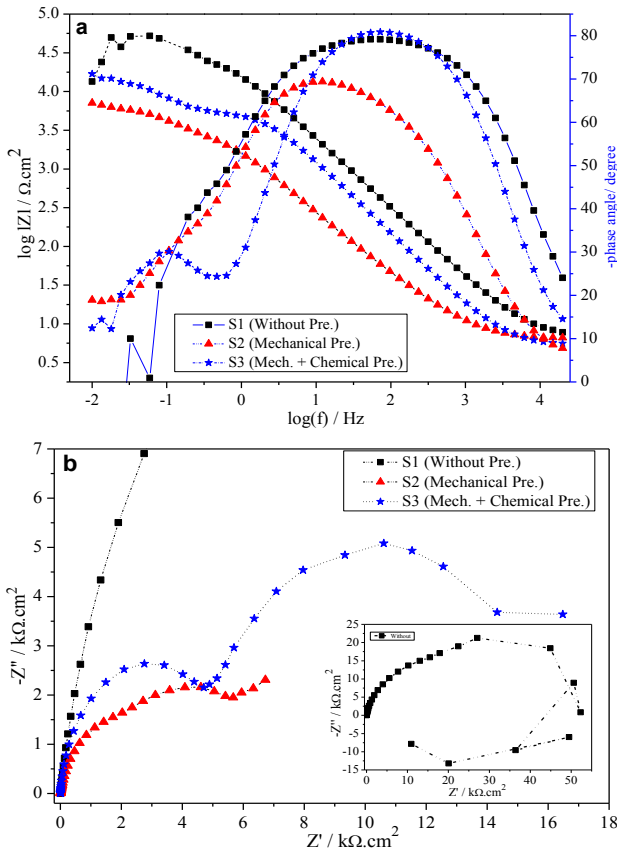


**Fig. 5.** Bode (a) and Nyquist (b) plots of samples after different approaches of preliminary treatment and after 2h exposure into 3.5% NaCl solution.

In this particular case R and C correspond to resistance and capacitance of the superficial oxide layer,  $R_{oxy}$ , and its capacitance,  $C_{oxy}$ . Thus, the development of this time constant for the degreased  $S_1$  sample is extremely interesting. The comparison of spectra of  $S_1$  with different exposure times reveals that the medium frequency maximum range

increases after a prolonged time of exposure. This phenomenon is particularly expressed after a 24-hour exposure (Fig. 6).

The evolution of the dependence of the phase shift-  $\varphi$  versus the frequency- f, suggests that during the exposure to the corrosive medium, the electrolyte penetrates the oxide film and as a consequence two noticeable oxide layers appear. Both layers are represented in the impedance spectrum by one joined double time-constant. Both layers could be ascribed to the natural oxide film and to the additionally formed oxide film due to the hot-rolling process during production of the said Al-sheets.

The impedance behaviour is rather different at the lowest frequencies. Pseudo inductance appears when the thick oxide layer is not removed in the case of  $S_1$ . It is expressed in positive values of both, the imaginary component of the impedance Z and the phase shift  $\varphi$ . This behaviour, according to ref.

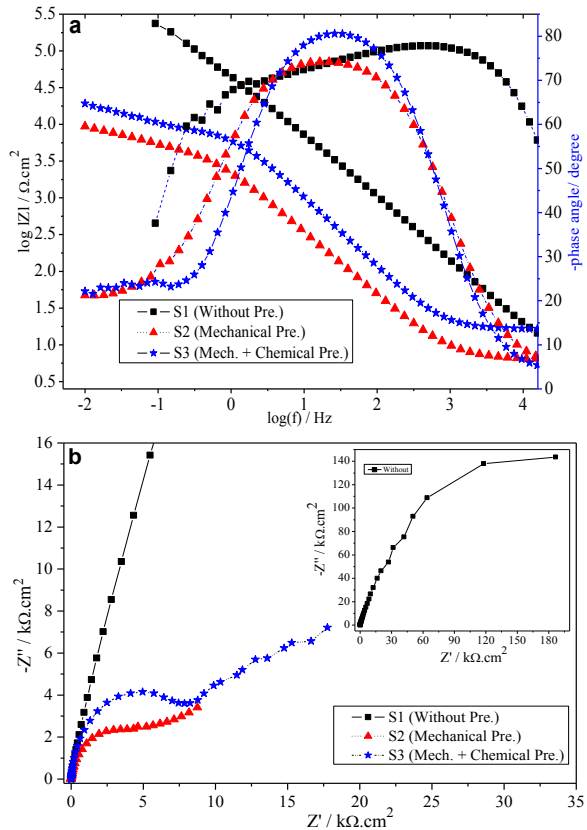


**Fig. 6.** Bode -(a) and Nyquist -(b) plots of samples after different approaches of preliminary treatment and after 24h exposure to 3.5% NaCl solution.

[18], owes its origin to pitting nucleation in the oxide layer. Other authors [19] suggest that this behaviour is a consequence of particle involvement in the oxide layer. The inductance completely disappears after achievement of a stationary state (Fig. 6-a).

The samples, treated using different approaches, reveal different values of the total impedance (impedance modulus) at a frequency of  $10^{-2}$  Hz. Usually, these values are related to the protective properties of the oxide film. Figures 5 and 6 undoubtedly demonstrate that the impedance module ( $Z$ ) value for  $S_1$  is in orders of magnitude higher than those of the remaining samples. It is due to the formation of two oxide layers. On the other hand, the impedance module  $Z$  for  $S_2$  possesses the lowest value because of the complete removal of the superficial oxide layer, which is actually the main aim of each pretreatment. In addition, the values of the impedance modulus are relatively higher for the etched  $S_3$  sample, compared to the mechanically treated  $S_2$  sample. This fact confirms the observation that the etching in alkaline media leads to formation of an insoluble film, thus increasing the total resistance at an alternate current.

Structural Impedance Modeling was carried out in order to obtain numeric values for the corrosion parameters of the samples presented in Table 2. This procedure allows the electrochemical system to give all resistive (R) and capacitive (C) response by fitting it to the appropriate equivalent circuit.

For the purposes of the present study an appropriate equivalent circuit was chosen. According to Boukamp [20], it could be described as follows:  $R_{el}(Q_{oxy}[R_{oxy}(Q_{dl} R_p)])$ , where  $R_{el}$ ,  $R_{oxy}$ , and  $R_p$  are the resistances of the electrolyte, the oxide layer, and the charge transfer at the interface metal-oxide (also known as a polarization resistance).  $Q_{oxy}$  and  $Q_{dl}$  are the Constant Phase Elements (CPE) used to approximate the values of the respective capacitances of the oxide layer and the double electric layer. The mentioned approximation is always used when the phase shift of the electric current sinusoid is less than  $90^\circ$  with respect to the potential. The impedance of the constant phase element depends on the frequency, like the capacitance. Therefore, it could be presented by the following equation:

$$Q = Y_0^{-1}(j\omega)^{-n}$$

where  $Y_0$  and  $n$  are frequency independent constants,  $\omega$  – angular frequency and  $j$ - imaginary unite. Once the constant-  $n$  has values in the range of 0.8 to 1, the respective CPE could be accepted as capacitance. Straight tails appear at the lowest frequency range in the Nyquist plots for some of the samples revealing the presence of diffusion process.

**Table 2.** Corrosion parameters for  $S_1$ ,  $S_2$  and  $S_3$  samples vs. time treatment.

PARAMETERS	The equivalent circuit: $R_{el}(Q_{oxy}[R_{oxy}(Q_{dl} R_p)])$									
	$S_1$			$S_2$			$S_3$			
	2 h	4 h	24 h	2 h	4 h	24 h	2 h	4 h	24 h	
$R_L$ ( $\Omega.cm^2$ )	6.67 ± 0.077	5.24 ± 0.10	5.71 ± 0.18	6.35 ± 0.1	11.7 ± 0.04	6.32 ± 0.037	5.31 ± 0.067	5.4 ± 0.089	16.5 ± 0.08	
$R_{oxy}$ (k $\Omega.cm^2$ )	33.7 ± 1.23	35 ± 1.87	22.01 ± 3.97	4.38 ± 0.42	3.5 ± 0.05	5.22 ± 0.14	5.68 ± 0.09	3.5 ± 0.06	8.33 ± 0.13	
$Q_{oxy}$	$Y_0$ $S^n \Omega^{-n} cm^{-2}$	9.8E-6 ± 1.1E-7	1.6E-5 ± 2.5E-7	3.1E-6 ± 8.1E-8	1.2E-4 ± 3.5E-6	1E-4 ± 8.2E-7	7.7E-5 ± 8.0E-7	1.6E-5 ± 2.8E-7	1.7E-5 ± 4.5E-7	1.9E-5 ± 2E-7
	$n$	0.89 ± 0.01	0.84 ± 0.002	0.89 ± 0.003	0.8 ± 0.004	0.83 ± 0.001	0.87 ± 0.002	0.93 ± 0.002	0.95 ± 0.004	0.95 ± 0.002
$R_p$ (k $\Omega.cm^2$ )	30.46 ± 9.08	13.96 ± 2.67	391 ± 22.44	5.62 ± 2.04	1.1 ± 0.12	10.93 ± 1.66	11.04 ± 0.42	10.06 ± 0.63	21.92 ± 1.59	
$Q_{dl}$	$Y_0$ $S^n \Omega^{-n} cm^{-2}$	4.1E-5 ± 2.9E-6	7.6E-5 ± 2.1E-5	2.0E-6 ± 1.1E-7	8.7E-4 ± 3.3E-4	0.001 ± 1.8E-4	7.7E-4 ± 7.4E-5	3.1E-4 ± 1.2E-5	5.6E-4 ± 2.5E-5	3.3E-4 ± 1.5E-5
	$n$	1 ± 0.11	1 ± 0.13	0.73 ± 0.024	0.621 ± 0.15	1 ± 0.06	0.638 ± 0.04	0.915 ± 0.02	0.947 ± 0.03	0.683 ± 0.02
$S^{0.5} \Omega^{-1}$	-	-	-	-	0.003 ± 2.1E-4	-	-	-	-	

For these cases, supplementary Warburg element was added to the equivalent circuit. Table 2 presents values of the corrosion parameters, obtained by spectra fitting procedure to the equivalent circuits.

## CONCLUSIONS

The influence of the AA 2024 aluminum alloy specimen superficial preliminary treatment over its morphology and corrosion behaviour in a 3.5% NaCl solution was studied. Three different approaches for a preliminary treatment of AA2024 metal plates were applied: S<sub>1</sub> - just degreased, S<sub>2</sub> - mechanically polished, and S<sub>3</sub> - mechanically treated and etched in alkaline solution. The investigation is done by applying crystallographic optical and atomic force microscopic techniques, combined with electrochemical measurements executed by linear voltammetry and Electrochemical Impedance Spectroscopy.

The analysis of the impedance spectra of the not treated samples (only degreased), reveals that they are covered by oxide film, consisting of two layers, a natural oxide layer, and a layer of additionally formed oxide during the metallurgical production process of the alloy. These samples show the highest impedance modulus, the highest polarization resistance, and respectively the lowest corrosion rate. It is established that they are not protected from the pitting corrosion process. The oxide layer possesses low number of defects and consequently, low number of pittings is formed during the exposure of the samples to the corrosion medium. These pittings are converted to crevice corrosion sites with a remarkable size. The reason for this phenomenon is that the pitting growth rate exceeds their nucleation rate.

The etching procedure in the alkaline solutions causes sediment coverage of alloy element oxides. These sediments can not be removed by desmutting with a diluted solution of HNO<sub>3</sub>. The presence of these sediments is confirmed by the OCP behaviour within the exposure time in the corrosive medium.

It is established that the mechanically polished samples are always covered with a natural oxide layer after exposure in the corrosive medium. This film has the highest number of defects combined by the lowest values of impedance modulus, polarization and capacitive resistances. By this approach of preliminary treatment the oxide layer is almost completely removed, which is the purpose of the superficial treatment.

The following general conclusion with a significant importance for the practice could be made: the etching in alkaline solutions, used in a large number of articles referring various aspects of the corrosion of AA2024 alloy, is not recommended. However, it could be appropriate for alloys with other compositions. In the particular case of the AA2024 alloy, mechanical polishing could be recommended because the sample surfaces achieved a state close to the complete absence of an oxide layer.

**Acknowledgement.** *The authors would like to thank to Assoc. Prof. I. Nenov for his valuable assistance during the experiments carried out and preparation procedure of the present paper.*

## REFERENCES

1. H. Kaesh, *Die Korrosion der metalle*, Springer-Verlag, Berlin, 1979.
2. M. Iannuzzi, G. S. Frankel, *Corr. Sci.* **49**, 2371 (2007).
3. J. R. Davis, *ASM Specialty Handbook: Aluminum and Aluminum Alloys*, ASM International, Chapter 2, 1993, pp.31–35.
4. C. Kammer, *Aluminum Handbook first ed. Vol. Aluminum - Verlag 1999* (Chapter 4) pp. 125-143.
5. K. A. Yasakau, M. L. Zheludkevich, S. V. Lamaka, M. G. Ferreira, *J. Phys. Chem. B*, **110**, 5515 (2006).
6. G. S. Tsaneva, V. S. Kozhukharov, S. V. Kozhukharov, M. E. Ivanova, J. Gervann, M. Schem, T. Schimdt, *J. Univ. Chem. Techn. Met.* **43**, 231 (2008).
7. F. M. Queiroz, M. Magnani, I. Costa, H. G. De Melo, *Corr. Sci.* **50**, 2646 (2008).
8. M. Bethencourt, F.J. Botana, M. J. Cano, M. Marcos, J. M. Sanchez-Amaya, L. Gonzalez-Rovira, *Corr. Sci.* **51**, 518 (2009).
9. S. M. Tamborin, A. P. Maisonnave, D. S. Azambuja, G. E. Englerd, *Surf. Coat. Techn.* **202**, 2304 (2008).
10. M. Schem, T. Schmidt, J. Gerwann, M. Wittmar, M. Veith, G. E. Thompson, Ls. Molchan, T. Hashimoto, P. Skeldon, A. R. Phani, S. Santucci and M. L. Zheludkevich, *Corr. Sci.* **51**, 2304 (2009).
11. O. Lunder, J. C. Walmsley, P. Mack, K. Nisancioglu, *Corr. Sci.* **47**, 1604 (2005).
12. S. V. Kozhukharov, G. S. Tsaneva, V. S. Kozhukharov, J. Gerwann, M. Schem, T. Schmidt, M. Veith, *J. Univ. Chem. Techn. Met.* **43**, 73 (2008).
13. B. Pentchev, S. Detchev, *Manual of Galvanotechniques*, Technika, Sofia 1982.
14. L.Y. Kadaner, *Manual of Galvanostegy*, Technika Gov. Ed., Kiev, 1976.
15. B. B. Damaskin, O. A. Petrii, *Fundamentals of theoretical Electrochemistry*, Superior School, Moscow, 1978.

16. B. V. Damaskin, O. A. Petrii, Introduction to electrochemical kinetics, Superior School, Moscow, 1975.
17. M. Bethencourt, F. J. Botana, J. J. Calvino, M. Marco, M. A. Rodriguez-Cachon, *Corr. Sci.* **40**, 1803 (1998).
18. Li Song-mei, Zhang Hong-rui, Liu Jian-hua, *Trans. Nonferrous Met. SOC. China* **17**, 318 (2007).
19. S. A. Rehim, H. H. Hassan, M. A. Amin, *Appl. Surf. Sci.* **187**, 279 (2002).
20. B. A. Boukamp, *Solid State Ionics*, **20**, 31 (1986).

## ЕФЕКТ НА ПРЕДВАРИТЕЛНАТА ПОДГОТОВКА ВЪРХУ ПОВЪРХНОСТНАТА МОРФОЛОГИЯ И КОРОЗИОННОТО ПОВЕДЕНИЕ НА АЛУМИНИЕВА СПЛАВ АА 2024

Е.А. Матер<sup>a,\*</sup>, С.В. Кожухаров<sup>b</sup>, М.С. Мачкова<sup>b</sup>

*a) Департамент по химия, Научен факултет, Университет в Даманхур, 22111 Даманхур, Египет*

*b) Химико-технологичен и металургичен университет, бул. Кл. Охридски, 8, 1756 София*

Постъпила на 10 юни, 2010 г.; преработена на 27 септември, 2010 г.

(Резюме)

Изследван е ефектът на повърхностната предварителна подготовка върху свойствата на оксидния филм и нейното влияние върху корозионното поведение на алуминиева сплав АА 2024 в 3.5% NaCl разтвор. Изследването е проведено, чрез оптична и атомно – силова микроскопски техники, съчетани с електрохимични изследвания - линейна волтаперометрия (ЛВА) и електрохимична импедансна спектроскопия (ЕИС).

За предварителна обработка на образците са използвани три подхода, както следва: само обезмасляване и промиване (без отстраняване на оксидния филм), механично полиране и комбинация между механично полиране с ецване в алкални разтвори. Параметрите на корозионния процес (поляризационно съпротивление, потенциал на питингообразуване и импедансен модул и капацитет) са използвани за количествено определяне на ефекта от предварителната подготовка. Установено е, че най-ефективната предварителна повърхностна обработка по отношение на премахването на оксидния слой е механичното полиране. Проведените електрохимични изследвания доказваха, че подходът на ецване в алкални разтвори, използван най-често, съгласно голям брой статии, причинява образуването на филм, който не може да бъде премахнат, чрез просветляване в разредени разтвори на HNO<sub>3</sub>. Процедурата на ецване би могла да е подходяща за други алуминиеви сплави, но не е препоръчителна за сплавта АА2024.

## Auger analysis of plasma treated ultrananocrystalline diamond films

G. S. Spasov<sup>1\*</sup>, C. Popov<sup>2</sup>

<sup>1)</sup>Central Laboratory of Photoprocesses, Bulgarian Academy of Sciences, Acad. G. Bonchev St., Building 109, 1113 Sofia, Bulgaria

<sup>2)</sup>Institute of Nanostructure Technologies and Analytics, University of Kassel, Heinrich-Plett-St. 40, 34132 Kassel, Germany

Received: July 1, 2010; accepted: September 20, 2010

Ultrananocrystalline diamond films have attracted great research interest due to their properties approaching those of diamond. In a cycle of works we study the treatment of such layers in oxygen or ammonia plasma. In the first case the treatment time is tracked; and in the second one we monitor the influence of different additions (fluorophore, maleimide, etc.). In the current work the accent falls on the Auger analysis (AES). With a view to the electronic spectroscopies, this is a research of the partial monoatomic overlayer. Since there is more than one adsorbate, it suggests a solution for the general case of  $n$  adsorbed elements giving their fractional monolayer coverage. This solution is an approximation for energy above 150 eV, however, it is exact in respect of the magnitude of the fractional monolayer coverage.

The research showed a significant surface modification of the ultrananocrystalline diamond films in oxygen and ammonia plasma. The fractional monolayer coverage is in the range of dozens of percentages. The monolayer coverage model gives values for the adsorbed quantities about 1.9 times higher as compared to the values, obtained by the homogeneous one. The comparison between AES and X-ray photoelectron spectroscopy (XPS) results for the coverages, shows qualitative similarity.

The usage of realistic model of the adsorbed layer is crucial for the quantification.

**Key words:** ultrananocrystalline diamond films, Auger analysis, monolayer coverage

### INTRODUCTION

All types of diamond films (single-, poly- (PCD), nano- (NCD), and ultrananocrystalline (UNCD) [1, 2]) have recently attracted an increasing interest for applications in biotechnologies, especially as a template for the functionalization with biomolecules, e.g. for biosensors or DNA chips [3–5]. Besides the intrinsic extreme properties of the diamond films such as the high hardness, the chemical inertness, the high thermal conductivity, and the high optical transparency which are to a large extent preserved in the diamond films, and their general bioproperties such as biocompatibility, bioinertness, and non-fouling character, there are a number of surface properties making the diamond films extremely attractive for such applications. They can be prepared either H- or O-terminated, giving a way to either hydrophobic or hydrophilic chemistries. Almost all diamond surfaces are H-terminated after the growth, and these surfaces are

rather stable [3, 4, 6], i.e. they can not be easily modified by simple chemical treatment in order to achieve, for example, O- or NH<sub>2</sub>-termination, but require photo-, thermo- or electrochemical processes. Another possibility is the application of plasmas, making use of their non-equilibrium character, and the presence of highly excited species.

In a cycle of works we report on the investigation of the surface modification of UNCD films by oxygen and ammonia plasmas by means of surface sensitive analytical techniques, namely Auger electron spectroscopy (AES) and X-ray photoelectron spectroscopy (XPS). With a view to the electronic spectroscopies, this is a research of the partial monoatomic overlayer. In the current work the accent falls on the Auger analysis.

### Theory

Seah [7] is the first to give accurate expressions for the Auger signals in the monolayer coverage. The model for substrate from element B with coverage from the element A, considers Auger signal from the substrate with two components: the first from the non-covered ( $1 - \Phi_A$ ) part and the

\*To whom all correspondence should be sent:  
E-mail: gspasov@clf.bas.bg

second from beneath the covered part,  $\Phi_A$ . Analytic expression binds the fractional monolayer coverage,  $\Phi_A$ , with the Auger intensities  $I_A$  and  $I_B$ .

For  $\Phi_A$  the equation [7, 8] is obtained:

$$\frac{\Phi_A \{1 - \exp[-a_A / \lambda_A(E_A) \cos \theta]\}}{1 - \Phi_A \{1 - \exp[-a_A / \lambda_A(E_B) \cos \theta]\}} = \left[ \frac{1 + r_A(E_A)}{1 + r_B(E_A)} \right] \frac{I_A / I_A^\infty}{I_B / I_B^\infty} \quad (1)$$

in which  $a_A$  means characteristic linear size of the atom  $A$ ;  $\lambda_M(E_i)$  and  $r_M(E_i)$  – respectively, the length of the attenuation and the back-scattering term of the electrons with energy  $E_i$  in matrix  $M$ ;  $I_i^\infty$  – the Auger signal from a pure sample of the element  $i$ , and  $\cos \theta$  has typical value of 0.74 for the cylindrical mirror analyser. For energy above 150 eV and if  $\Phi_A$  is small, Eqns. (1) is reduced to:

$$\Phi_A = Q_{AB} \frac{I_A / I_A^\infty}{I_B / I_B^\infty} \quad (2)$$

with a symbol  $Q$  for the matrix factor of the monolayer coverage:

$$Q_{AB} = \left[ \frac{\lambda_A(E_A) \cos \theta}{a_A} \right] \left[ \frac{1 + r_A(E_A)}{1 + r_B(E_A)} \right] \quad (3)$$

We will point out that Eqns. (1), (2) and (3) are relevant for quantification of XPS data too, with the only difference that in this case  $r_M(E_i) = 0$ .

## EXPERIMENTAL

The ultrananocrystalline diamond films were prepared by microwave plasma chemical vapor deposition from  $\text{CH}_4/\text{N}_2$  gas mixture with 17% methane. UNCD films consist of diamond nanocrystallites with diameters of 3–5 nm, embedded in an amorphous carbon matrix with grain boundary width of 1–1.5 nm. The volume ratio between the two phases, the crystalline and the amorphous, is close to one.

In the experiments with oxygen-plasma treatment it changes the exposition time. In the others we examine the influence of the combination of  $\text{O}_2$ - and  $\text{NH}_3$ -plasma treatment with several technologies. 1.  $\text{NH}_3/\text{N}_2$ -plasma treatment (for 10 min.), marked in the text as “ $\text{NH}_3$ ” (gas flows of 50 sccm of  $\text{NH}_3$  and 950 sccm of  $\text{N}_2$ ); 2. SAMSA attachment (SAMSA concentration of 2 mM, for 15 h), marked in the text as “FI” (the thiol-bearing SAMSA fluorescein is prepared from 5-((2-(and-3)-S-(acetylmercapto)succinoyl) amino) fluorescein, A-685, Invitrogen, dissolved in NaOH, neutralized with concentrated HCl, and buffered with sodium phosphate); 3. Mitsunobu reaction after  $\text{O}_2$ -plasma

treatment, marked in the text as “ $\text{O}_2 + \text{M}$ ” (Triphenylphosphane  $\text{Ph}_3\text{P}$  was diluted with tetrahydrofuran (anhydrous) THF. Di-isopropyl-azodicarboxylate DIAD was added at 0 °C and the samples with oxygen terminated UNCD/a-C composite films were immersed into the mixture for 1 min, and stirred for 5 min. Then, N-substituted maleimide (0,029 g) was added as a solid to the reaction mixture. It was kept for about 5 min at low temperature for maleimide dissolving. The reaction mixture was stirred overnight at ambient temperature); 4. Mitsunobu reaction and SAMSA attachment after  $\text{O}_2$ -plasma treatment, marked in the text as “ $\text{O}_2 + \text{M} + \text{FI}$ ”; 5. SSMCC attachment after  $\text{NH}_3/\text{N}_2$ -plasma treatment (1.5 mM SSMCC solution, for 24 h), marked in the text as “ $\text{NH}_3 + \text{SSMCC}$ ” (SSMCC (sulfosuccinimidyl 4-(N-maleimidomethyl) cyclohexane-1-carboxylate) dissolved in TEA solution (150 nM solution of triethanolamine (TEA) in deionized water)).

More details for the experiment and for the results from it can be found in our work [9].

The Auger analysis was performed in the differential mode at primary electron energy  $E_p = 3$  keV ( $I_E = 0.07 \mu\text{A}$ ,  $V_{\text{mod}} = 4 \text{ V}_{\text{ptp}}$ ,  $\Delta E/E = 0.3\%$ ). The most intense Auger peaks of C (272 eV), N (381 eV), and O (510 eV) were monitored, as well as those of Si (92 eV), S (152 eV), and F (650 eV); the concentration of the last 3 elements was below the sensitivity of our analysis. (Ion milling of the surface was not performed in order to prevent its amorphisation and/or graphitisation.) The analyzed area is with a spot size of  $\sim 5 \mu\text{m}$ . Usually, the analysis is performed in 5 points from the sample surface, after which the values of the measured intensities are averaged, if there are not any major differences between them. Otherwise, more analyses are made, up to 20. The intensity is measured “peak to peak”. The quantification is made by comparison with the standard samples of  $\text{SiO}_2$ , AlN, and graphite.

## RESULTS

### *Generalized formulae for monolayer coverage in the case of several adsorbates*

In the case of  $n$  adsorbates of the elements  $A_k$ , covering the substrate (B), analogically to the reasoning [8] behind the deduction of Eqns. (1), we reach a system of  $N$  equations for the degree of coverage  $\Phi_k$ . For energy above 120 eV, the system becomes linear. Its solution is:

$$\Phi_{A_k} = \left[ \frac{\lambda_{A_k}(E_{A_k}) \cos \theta}{a_{A_k}} \right] \left[ \frac{1 + r_{A_k}(E_{A_k})}{1 + r_B(E_{A_k})} \right] \frac{I_{A_k}/I_{A_k}^\infty}{I_B/I_B^\infty} \left\{ 1 + \sum_i \frac{\lambda_{A_i}(E_{A_i})}{\lambda_{A_i}(E_B)} \cdot \frac{1 + r_{A_i}(E_{A_i})}{1 + r_B(E_{A_i})} \cdot \frac{I_{A_i}/I_{A_i}^\infty}{I_B/I_B^\infty} \right\}^{-1} \quad (4)$$

Here  $\Phi_k$  is the fractional monolayer coverage of the element  $A_k$ , while the other symbols are as in Eqns. (1), juxtaposed to the element with the corresponding index.

In our case of three elements (O and N above C), the common denominator in the matrix factor of Eqns. (4) is:

$$Q = \left[ 1 + \frac{\lambda_O(E_O)}{\lambda_O(E_C)} \cdot \frac{1 + r_O(E_O)}{1 + r_O(E_C)} \cdot \frac{I_O/I_O^\infty}{I_C/I_C^\infty} + \frac{\lambda_N(E_N)}{\lambda_N(E_C)} \cdot \frac{1 + r_N(E_N)}{1 + r_N(E_C)} \cdot \frac{I_N/I_N^\infty}{I_C/I_C^\infty} \right]^{-1} \quad (5)$$

### Experimental Auger data

The measured relative intensities from the experiments with an oxygen-plasma treatment are shown in Fig. 1, while those with an  $NH_3$ -plasma treatment in Fig. 2.

### Quantification

The data from Fig. 1, quantificated by Eqns. (2) and (3), are presented in Table 1, while those from Fig. 2, quantificated by Eqns. (4) and (5), are presented in Table 2. In the tables  $\Phi_k$  is a symbol for the degree of coverage with the element  $k$ , normalized to the area of the atom (In terms of the model, this is the square of his covalent diameter.). The symbol  $\Phi_{k/C}$  is for degree of coverage, defined as ‘number of adsorbed atoms on atom from the substrate’.

The data from the XPS analysis are presented in the last column of Tables 1 and 2.

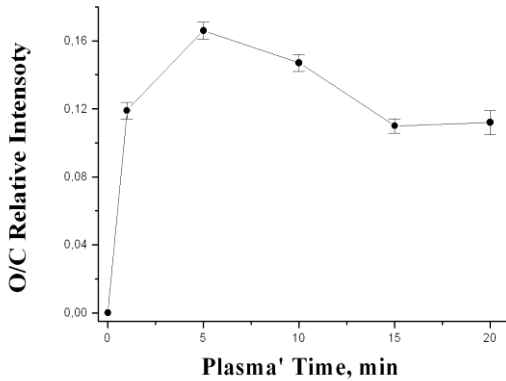


**Fig.1.** Dependence of the relative intensity of the oxygen Auger signal (towards the carbon) from the time of treatment with oxygen plasma.

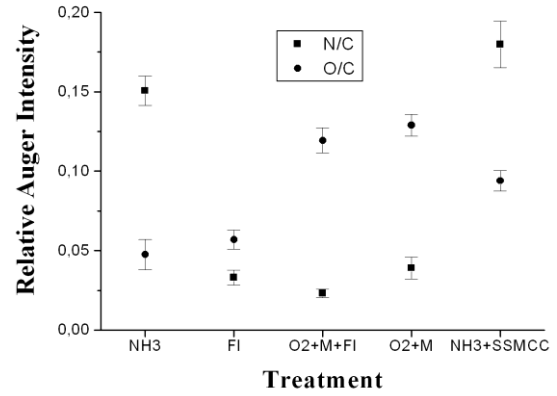


**Fig. 2.** Relative intensity of the oxygen and nitrogen Auger signal (towards the carbon) for different treatments with ammonium plasma.

The attenuation lengths, appearing in the formulas, are obtained from a predictive formula of TPP-2M in the database [10]. The covalent atomic radiuses of oxygen and nitrogen are taken from the NIST database. The back-scattering term calculation, necessary for the matrix correction, is done according to [11]. More procedure details are presented in section ‘Discussion’.

**Table 1.** AES data quantification of the oxygen-plasma experiments (The notation is in the text).

Time, min	$\Phi_O$ , %	$C_O$ , at. %	O/C-atom	OIs, at. % (XPS)
1	7.6	4.5	0.14	15.45
5	10.6	6.2	0.20	14.10
10	9.4	5.5	0.18	15.07
15	7.1	4.2	0.13	16.00
20	7.2	4.2	0.14	15.02

**Table 2.** AES data quantification of the experiments combined  $O_2$ - and  $NH_3$ -plasma treatment with several technologies (The notation is in the text).

Treatment	Adsorbed Oxygen				Adsorbed Nitrogen			
	$\Phi_{O_2}$ , %	$C_{O_2}$ , at. %	O/C-atom	OIs, at. % (XPS)	$\Phi_{N_2}$ , %	$C_{N_2}$ , at. %	N/C-atom	NIs, at. % (XPS)
$NH_3$ PI (10 min)	2.8	1.8	0.05	3.12	10	4.8	0.17	7.39
FI	3.5	2.2	0.07	5.97	2.4	1.1	0.04	1.35
$O_2$ PI + M + FI	7.2	4.5	0.14	12.30	1.6	0.74	0.03	1.21
$O_2$ PI (10 min) + M	7.7	4.8	0.14	–	2.7	1.3	0.04	–
$NH_3$ PI + SSMCC	5.5	3.4	0.10	8.18	12	5.6	0.20	7.34

## DISCUSSION

Although it remains semi-quantitative, the surface evaluation, done by this method, is much more accurate compared to that of the homogeneous model of the surface (where the matrix correction is disregarded). The obtained numerical result of the surface is 2 to 8 times bigger [7] (we have an average of 1.9 in our case). By reason of interpretation through ‘the common’ Auger quantification, the atoms from the monolayer coverage are looked at as distributed in greater volume (determined from the information depth), apparently their concentration is lower.

We would like to highlight, that the formula derivation (4) is not linked with the magnitude  $\Phi_i$ , i.e. Eqns. (4) are always valid, and are not approximated to  $\Phi_i$ . This is important because in the case of heterogeneous coverage, it can turn out that the total degree of the coverage is not small, although every of its components is small (i.e.,  $\Phi_i \ll 1$ , but not  $\sum \Phi_i \sim 1$ ).

The used model suggests covering the substrate with the material from the standard sample (‘overlayer’ experiment). The calculated degree of coverage measure is the average atom size from the standard,  $a$ . All of this is clearly defined in the deposition of metal over metal. The adsorption of an element, for which there is no elemental standard (usually metalloid or gas), requires a comment. The formal approach is to assume coverage of hypothetical substance which has the same structure as the standard but consists of adsorbate atoms only. However, we now have  $\Phi$  depending on the standard which is disturbing at first sight. But if we take in consideration that in the case of other standard we have to introduce matrix

correction too, the detailed deduction according to the model gives us that  $\Phi \sim a^2$ .  $a$  reflects the atom density (in the volume  $a^3$  there is one atom). The actually covered area  $a^2$  (‘occupied’ by single adsorbed atom), is the  $S/a^2$ -part, where  $S$  the actual size of the atom, calculated with the corresponding atom radius. That is to say that in such normalization of the atom area,  $\Phi$  depends on the type of the adsorbed atom only, but not on the used standard.

In the discussed case (of adsorption of an element, which does not have elemental standard), the maximum degree of coverage depends on the system (A, B) and the conditions, in which the process takes place. Maximum coverage is attainable in the case of chemisorption, and it could be less than the determined coverage through the atomic radius (considered as 100%). If the object of the experimental study is not the adsorption itself, additional data for the physical chemistry of the surface are necessary for the determination of  $\Phi_{max}$  [12]. It may turn out to be more useful if the result is presented as a ‘number of adsorbed atoms on atom from the substrate’. In the studied case, the adsorption of non-activated gas (oxygen or nitrogen) is not present even in the case of atmospheric pressure. Apparently, the plasma activates the chemisorption. But a C-atom from the surface has one free valance bond with which it can connect to the adsorbed species. The maximum degree of coverage can be achieved if every atom from the surface joins one adsorbed particle. For example, for the last sample in Table 2 there is a particle at three of every 10 surface atoms (two particles, including oxygen atom and one, including nitrogen atom).

Main requirement for the accuracy in the determination of degree of coverage is to know the attenuation length of the electrons,  $\lambda$ . It would be best if reliable experimental data are used. The lack of such for the nitrogen standard used by us, made us use the both standards with the same priority, i.e. predictive formulae. (For instance, in [13] through Elastic peak and reflected electron loss spectrum (REELS) measurements 1.75 nm are obtained for SiO<sub>2</sub>; and 1.77 nm are obtained through TPP-2. For Si<sub>3</sub>N<sub>4</sub>; however, the respective figures are 1.12 nm and 1.41 nm). In the case of metal over metal deposition,  $\lambda$  can be determined by overlayer experiment, too.

The comparison between AES and XPS results on the coverages shows similar quality behavior. The quantity difference in the results suggests for a systematical error. The probable reason for this is the difference in the readings of the surface carbon contamination of both of the spectroscopic methods [8]. The different composition of standards, as well as the area and the place of the analysis, may have significant contribution. (In the case of XPS, the area is 400 × 700 μm but the analysis is in three points).

## CONCLUSIONS

The research showed a significant surface modification of the ultrananocrystalline diamond films in oxygen and ammonia plasma. Chemisorbed oxygen and nitrogen are observed. The fractional monolayer coverage is of order of about ten per cent. The comparison between AES and XPS results for the coverages shows qualitative similarity.

Oxygen and nitrogen content, calculated by the model of the monolayer coverage, is about 1.9 times bigger, compared to the same obtained by using homogeneous model of the surface.

The usage of realistic model of the adsorbed layer is crucial for the quantification.

## REFERENCES

1. J. Butler, *Electrochem. Soc. Interface* **12**, 22 (2003).
2. O. A. Williams, M. Daenen, J. D'Haen, K. Haenen, J. Maes, V. V. Moshchalkov, M. Nesladek, D. M. Gruen, *Diamond Relat. Mater.* **15**, 654 (2006).
3. C. E. Nebel, B. Rezek, D. Shin, H. Uetsuka, N. Yang, *J. Phys. D* **40**, 6443 (2007).
4. S. Szunerits, R. Boukherroub, *J. Solid State Electrochem.* **12**, 1205 (2008).
5. W. Yang, O. Auciello, J. E. Butler, W. Cai, J. A. Carlisle, J. E. Gerbi, D. M. Gruen, T. Knickerbocker, T. L. Lasseter, J. N. Russell Jr, L. M. Smith, R. J. Hamers, *Nature Mater.* **1**, 294 (2002).
6. W. Kulisch, T. Sasaki, F. Rossi, C. Popov, C. Sippel, D. Grambole, *Phys. Stat. Sol. (RRL)* **2**, 77 (2008).
7. M. P. Seah, *J. Vac. Sci. Technol.* **17**, 16 (1980).
8. M. P. Seah, in: *Practical Surface Analysis*, D. Briggs, M. P. Seah (eds), 2<sup>nd</sup> ed, vol. 1, Wiley, 1990, p. 245.
9. C. Popov, H. Koch, W. Kulisch, M. Kopnarski, G. Ceccone, G. Spasov, J.P. Reithmaier, Tailoring of the Surface Properties of Ultrananocrystalline Diamond/Amorphous Carbon Composite Films by Plasma Modifications, 4th International Conference on New Diamond and Nanocarbons (NDNC 2010), Suzhou, China, 2010.
10. C.J. Powell, A. Jablonski, NIST Electron Inelastic-Mean-Free-Path Database - Version 1.1, National Institute of Standards and Technology, Gaithersburg, 2000.
11. R. Shimizu, *Jap. J. Appl. Phys.* **22**, 1631 (1983).
12. S. Bouquet, G. Lorang, J.P. Langeron, P. Marcus, *J. Microsc. Spectrosc. Electron.* **7**, 447 (1982)
13. R. Jung, J. C. Lee, G. T. Orosz, A. Sulyok, G. Zsolt, M. Menyhard, *Surf. Sci.* **543**, 153 (2003).

## ОЖЕ-АНАЛИЗ НА ПЛАЗМЕНО ТРЕТИРАНИ УЛТРАНАНОКРИСТАЛНИ ДИАМАНТЕНИ СЛОЕВЕ

Г. С. Спасов<sup>1\*</sup>, К. Попов<sup>2</sup>

<sup>1)</sup> Централна лаборатория по фотопроцеси, Българска академия на науките, ул. Акад. Г. Бончев, блок 109, София 1113; \* E mail: gspasov@clf.bas.bg

<sup>2)</sup> Институт по наноструктурни технологии и анализи, Каселски университет, ул. Хайнрих-Плет, 40, Касел 34132, Германия

Постъпила на 1 юли, 2010 г.; приета на 20 септември, 2010 г.

(Резюме)

Ултра-нанокристалните диамантени слоеве привличат голям изследователски интерес, поради свойствата им, близки до тези на диаманта. В цикъл научни трудове изследваме третирането на такива слоеве с кислородна и амонячна плазма; в първия случай – от продължителността на третирането, а във втория – влиянието на различни добавки (флуорофор, малеимид и т.н.). В настоящата работа ударението пада на Оже анализите. От гледна точка на електронните спектроскопии, това е изследване на частично покритие от моно-атомен слой. Тъй като присъстващите адсорбати са повече от един, се предлага решение за общия случай за  $n$  адсорбирани химични елемента, даващо тяхното частично от моно-слоейно покритие. Решението е в сила за енергии на следените Оже пикове над 120 eV, но то е точно спрямо степента на покритие.

Изследванията показаха значително повърхностно изменение на ултрананокристалните диамантени слоеве в кислородна и амонячна плазма. Частичното моно-слоейно покритие е от порядъка на десетиия процента. Този резултат (пресметнат по модела за моно-слоейно покритие) е около 1.9 пъти по-голям в сравнение с резултата, използващ хомогенен модел на повърхността. Сравнението между Оже резултатите за покритията и тези от Рентгенова Фотоелектронна Спектроскопия (РФС) показва качествено подобие.

Използването на реалистичен модел за адсорбирания слой е решаващо за количествения анализ.

## Zinc recovery from sulphate electrolytes, containing copper and ferrous ions

G. Hodjaoglu, I. Ivanov\*

*Institute of Physical Chemistry, Bulgarian Academy of Sciences, Acad.G.Bonchev St., Building 11, 1113 Sofia, Bulgaria*

Received: June 7, 2010; revised: October 29, 2010

The influence of copper and ferrous ions on zinc recovery from sulphate electrolytes is investigated. It is found, using cyclic voltammetry that simultaneous deposition of Zn and Cu begins at a potential (*vs.* SSE) of  $-1.450$  V. Simultaneous deposition of Zn, Fe, and Cu begins at a potential of  $-1.500$  V. Deposition of Cu solely, takes place at more positive potentials. The presence of  $\text{Cu}^{2+}$  and  $\text{Fe}^{2+}$  ions results in Zn redissolution, decreasing the current efficiency of Zn electroextraction. Zn deposit, which contains 2.4 wt.% Cu and 0.25 wt.% Fe, is obtained upon 60 min deposition at  $-1.600$  V in an electrolyte containing  $\text{Zn}^{2+} - 50$  g/L,  $\text{H}_2\text{SO}_4 - 130$ g/L,  $\text{Cu}^{2+} - 200$  mg/L, and  $\text{Fe}^{2+} - 200$  mg/L .

**Keywords:** copper; deposition; iron; potentiodynamic scan; zinc electrowinning; zinc recovery.

### 1. INTRODUCTION

A major problem during the Zn electrowinning from waste streams is the harmful effect exerted by metallic impurities such as Ni, Co, Fe, Cu, Cd, Sb, Ge, Bi, etc. By advanced purification of the electrolyte, the concentration of metallic ions is decreased below limit, where their harmful effects are no longer present. Another possibility is the addition of various organic and inorganic substances to the electrolyte in order to improve the deposit structure and to inhibit the discharge of  $\text{H}^+$  or the Zn redissolution process, and thus to increase the current efficiency.

Stender et al. [1–2] established that the  $\text{Cu}^{2+}$  (100 mg/L) decrease the potential of the Zn cathode with 50 mV (at 5 A/dm<sup>2</sup>) and the current efficiency of hydrogen evolution increases with the increase in the  $\text{Cu}^{2+}$  concentration. Because of the small overvoltage of Cu deposition on Zn, the Cu deposits on the cathode, forming numerous galvanic micropairs of intermetallic Zn–Cu compounds and the Zn cathode dissolves as a result of their action. According to Turomshina and Stender [3, 4], Cu and Fe, codeposited with Zn, act as microanodes or microcathodes in the galvanic micropairs, depending on the geometric configuration of the deposit. Thus, a small amount of Fe is able to intensify the harmful action of the noble Cu. The experiments show that such effect is observed only at increased temperatures because at a lower temperature, Fe is in passive state and acts

as a microcathode in the galvanic micropairs. As a result, the total effect of Cu and Fe on the Zn electroextraction is a sum of their partial effects. Maja et al. [5, 6] found that in the presence of 100 mg/L  $\text{Cu}^{2+}$  the current efficiency of Zn decreases from 90% to 0% after 4 h electroextraction at 60 mA/cm<sup>2</sup> and 40°C. According to Ault and Frazer [7] 5 mg/L  $\text{Cu}^{2+}$  decrease the current efficiency from 97.5 to 96.7 %. MacKinnon [8] and MacKinnon et al. [9] established that a significant difference between the cyclic voltammograms for the addition-free and  $\text{Cu}^{2+}$ -containing (1 and 5 mg/L) electrolytes is the potential at which the descending branch crosses the zero-current axis (crossover potential). The crossover potential occurs at or near the reversible potential of the system so that any departure is generally caused by impurity currents, side reactions such as  $\text{H}_2$  evolution or perhaps the dissolution of a Zn–Cu alloy phase. Analysis of the coatings confirms that Cu co-deposits with Zn. At the higher (5 mg/L)  $\text{Cu}^{2+}$  concentration the voltammogram is characterized by higher current in the potential region prior to Zn deposition. At this concentration, Cu strongly depolarizes the Zn deposition reaction because the decomposition potential for Zn occurs at a less negative cathode potential compared to the  $\text{Cu}^{2+}$ -free electrolyte. The reverse scan is characterized by an increasing cathodic current that occurs after the anodic peak for Zn dissolution. Muresan et al. studied the influence of metallic impurities and the effect of additives on Zn electrowinning from sulphate electrolytes and from industrial waste product, known as the ‘blue-powder’, containing: Zn (25–45%), Pb (20–25%),

\*To whom all correspondence should be sent:  
E-mail: [isivanov@ipc.bas.bg](mailto:isivanov@ipc.bas.bg)

Fe (3–5%), Cu (0.5–1%), Cd (0.5–1%), Sb (0.05–0.1%), and Bi (0.03%). They found that  $\text{Al}_2(\text{SO}_4)_3$ , animal glue or horse-chestnut extract (HCE) added in the electrolyte increase the cathodic polarisation and promote levelling. HCE has a beneficial influence on the deposit quality, being a good levelling agent. Aluminium sulphate influences the reduction of  $\text{Zn}^{2+}$ , increasing the nucleation overpotential and the deposition rate of Zn on the cathode. The conjoint use of the studied additives results in more uniform, slightly bright deposits [10]. They established also that the presence of  $\text{Cu}^{2+}$  leads to an acceleration of the cathodic process. Copper is deposited before Zn, as indicated by the appearance of a cathodic peak at about  $-0.4$  V vs. SCE. The height of the peak increases with  $\text{Cu}^{2+}$  concentration in the electrolyte. The corrosion potential of Zn in a Cu-containing electrolyte is more positive than in an electrolyte without the impurity and a second anodic peak, corresponding to Cu dissolution can be observed in the positive potential region during the reverse scan. The cathodic deposit, obtained in the presence of  $\text{Cu}^{2+}$  ions, is non-adherent with the substrate, and consists of porous microspheres [11].

There are numerous papers concerning the influence of the  $\text{Cu}^{2+}$  and  $\text{Fe}^{2+}$  ions on the process of Zn electroextraction such as Znamenskiy, Kardashevskiy and Stender [12]; Kiryakov [13]; Kiryakov and Baynietova [14]; Sheka and Karlishева [15]; Jurin and Pyunnenen [16]; Pahomova [17]; Jurin and Hafsi Azdin [18]; Pomosov, Krimakova and Levin [19]; Wever [20]; Akiyama, Fukushima and Higashi [21]; Ohyama and Morioka [22]. However, the simultaneous action of  $\text{Cu}^{2+}$  and  $\text{Fe}^{2+}$  ions is not well studied.

The aim of this study is to establish the influence of  $\text{Cu}^{2+}$  ions and the common action of the  $\text{Cu}^{2+}$  and  $\text{Fe}^{2+}$  ions on the Zn electroextraction, as well as the possibility of separate deposition of Zn, Cu or Fe.

## 2. EXPERIMENTAL

The experiments were carried out in a thermostated ( $37 \pm 1^\circ\text{C}$ ), three-electrode glass cell without stirring of the electrolyte. The cathode was of Al, containing 0.2% Fe, manufactured by the Riedel de Haen (RdH-Al) with an effective area of  $1.0 \text{ cm}^2$ . It was placed vertical and parallel to the symmetry axis of the cell. Both counter anodes were Pt plates of  $8.0 \text{ cm}^2$  total area. The reference electrode (SSE) consisted of a mercury/mercurous sulphate electrode in  $0.5 \text{ M H}_2\text{SO}_4$  (SSE), its potential being  $+0.655 \text{ V}$  (NHE).

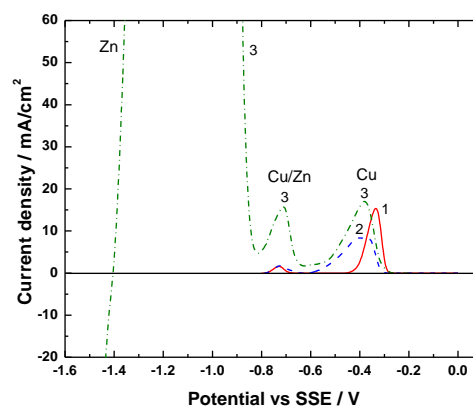
The studies were carried out using a cyclic potentiodynamic technique. Potential scanning at a rate of  $10 \text{ mV/s}$  was performed with an EP 20A Elpan potentiostat (equipped with an IR compensator) and an EG 20 Elpan scanner. The cyclic voltammograms (CVAGs), were carried out in the range of  $0.000 \text{ V}$  to  $-1.650 \text{ V}$ , and were recorded by Endim 622.01 X–Y chart recorder.

The composition of the base electrolyte (BE) was:  $130 \text{ g/L H}_2\text{SO}_4$ , and  $220 \text{ g/L ZnSO}_4 \cdot 7\text{H}_2\text{O}$  ( $50 \text{ g/L Zn}^{2+}$ ).  $\text{Cu}^{2+}$  ions were added in the form of  $\text{CuSO}_4 \cdot 5\text{H}_2\text{O}$  to the base electrolyte in concentrations of  $50, 100, \text{ and } 200 \text{ mg/L}$ .  $\text{Fe}^{2+}$  ions were added as  $\text{FeSO}_4 \cdot 5\text{H}_2\text{O}$  to the electrolyte in concentrations of  $50, 100, \text{ and } 200 \text{ mg/L}$ .

The quantity of electricity ( $q$  – in Coulombs), required for the dissolution of Zn or Cu, deposited during the cathodic process, was determined by graphical integration of the respective anodic peak on the CVAG. The deposition of Zn was carried out at a potential of  $-1.600 \text{ V}$  vs. SSE, and of Cu at potentials between  $-1.010 \text{ V}$  and  $-1.470 \text{ V}$  vs. SSE.

## 2. RESULTS AND DISCUSSION

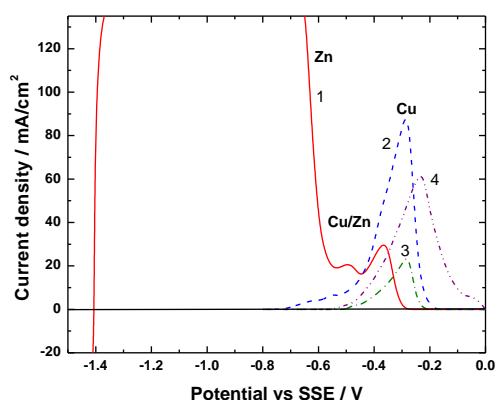
### 2.1. Separate deposition of zinc and copper



**Figure 1.** Anodic peaks of dissolution of Cu layers, deposited in an electrolyte, containing  $\text{Zn}^{2+} - 50 \text{ g/L}$ ,  $\text{H}_2\text{SO}_4 - 130 \text{ g/L}$  and  $\text{Cu}^{2+} - 50 \text{ mg/L}$  on an Al cathode at potentials (vs. SSE): 1)  $-1.330 \text{ V}$ , 2)  $-1.430 \text{ V}$ , 3)  $-1.470 \text{ V}$ . Time of deposition -  $15 \text{ min}$ . Scan rate -  $10 \text{ mV/s}$ .

Figure 1 shows the anodic peaks of dissolution of Cu layers, deposited for  $15 \text{ min}$  in the base electrolyte, containing  $50 \text{ mg/L Cu}^{2+}$  at potentials of  $-1.330 \text{ V}$  (curve 1),  $-1.430 \text{ V}$  (curve 2), and  $-1.470 \text{ V}$  (curve 3). A little peak at  $-0.725 \text{ V}$  and large peaks at potentials (vs. SSE) between  $-0.300$  and  $-0.400 \text{ V}$  are observed on the curves 1 and 2. The more negative peak ( $2-7 \text{ mA}$ ) is, perhaps, a peak of dissolution of an alloy Zn-Cu phase. The more

positive peaks at potentials (vs. NHE) between +0.255 V and +0.355 V are close to the reversible potential of oxidation of Cu to  $\text{Cu}^{2+}$  (+0.337 V vs. NHE). In all cases the cathodic Cu deposits are non-adherent with the substrate, and are easily wiped and rinsed with water. The simultaneous deposition of Zn and Cu begins at a potential of -1.450 V (vs. SSE). Zn dissolution peak appears after deposition at more negative (-1.470 V) potential, and is much larger than the peaks of Cu dissolution (curve 3). The peak of Zn-Cu alloy dissolution is much higher (20 mA) than the peaks, obtained at the lower cathodic potentials because of the larger alloy amount.



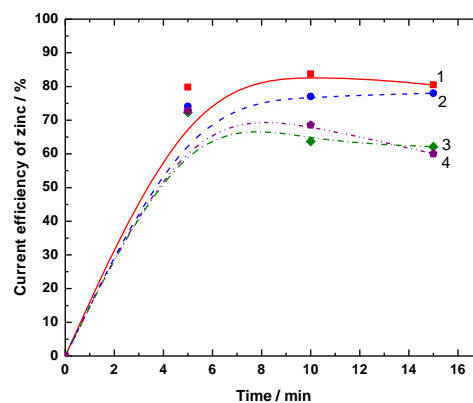
**Figure 2.** Anodic peaks of dissolution of Cu and Zn deposits. Scan rate - 10 mV/s. Deposition potential (vs. SSE): -1.470 V. Time of deposition - 30 min. 1)  $\text{Zn}^{2+}$  - 50 g/L,  $\text{H}_2\text{SO}_4$ -130 g/L and  $\text{Cu}^{2+}$ -100 mg/L, 2)  $\text{Zn}^{2+}$ -50 g/L,  $\text{H}_2\text{SO}_4$ -130 g/L,  $\text{Cu}^{2+}$ -100 mg/L and  $\text{Fe}^{2+}$ -50 mg/L, 3)  $\text{Zn}^{2+}$ -50 g/L,  $\text{H}_2\text{SO}_4$ -130 g/L,  $\text{Cu}^{2+}$ -100 mg/L and  $\text{Fe}^{2+}$ -100 mg/L, 4)  $\text{Zn}^{2+}$ -50 g/L,  $\text{H}_2\text{SO}_4$ -130 g/L,  $\text{Cu}^{2+}$ -200 mg/L and  $\text{Fe}^{2+}$ -200 mg/L.

Figure 2 shows the anodic peaks of dissolution of coatings, deposited for 30 minutes at a potential of -1.470 V. Only one peak at potentials between -0.200 and -0.400 V vs. SSE (+0.455 and +0.255 V vs. NHE) is observed on the curves, obtained in the presence of both,  $\text{Cu}^{2+}$  and  $\text{Fe}^{2+}$  ions in the base electrolyte (curves 2, 3 and 4) which is close to the reversible potential of the oxidation of Cu to  $\text{Cu}^{2+}$  (+0.337 V vs. NHE). In all cases this peak is higher and appears at more positive potentials than the peak obtained in the presence of only  $\text{Cu}^{2+}$  ions in the base electrolyte (curve 1). The more negative peak at -0.500 (curve 1) observed in the presence of  $\text{Cu}^{2+}$  only (and due to the dissolution of Zn-Cu phase) is absent in the presence of both, the  $\text{Cu}^{2+}$  and  $\text{Fe}^{2+}$  ions (curves 2, 3 and 4). Peaks of Fe dissolution are not observed in all cases. Obviously, the potential of Fe dissolution is very close to the

potential of Zn dissolution. Because the reversible potential of Fe dissolution to  $\text{Fe}^{2+}$  is -1.100 V vs. SSE (-0.440 V vs. NHE), it can be supposed that at this potential the  $\text{H}_2$  evolution takes place. Zn dissolution is taking place at this potential, too (Figure 1). Thus, the anodic peak of the Fe dissolution is masked by the cathodic peak of the  $\text{H}_2$  evolution or by the anodic peak of Zn dissolution. The deposition of Zn in the presence solely of  $\text{Cu}^{2+}$  begins at a potential of -1.450 V, and in the presence of both,  $\text{Cu}^{2+}$  and  $\text{Fe}^{2+}$ , at -1.500 V. For this reason, the peak of Zn dissolution appears only on the curve, obtained at -1.470 V in the presence solely of  $\text{Cu}^{2+}$  (curve 1).

## 2.2. Influence of $\text{Cu}^{2+}$ and $\text{Fe}^{2+}$ ions on zinc deposition

Figure 3 shows the current efficiency of Zn (CEZn) deposition in the presence of  $\text{Cu}^{2+}$  and  $\text{Fe}^{2+}$  as a function of time. The current efficiency is 2% smaller (in the presence of 50 mg/L  $\text{Cu}^{2+}$ ), and about 20% smaller (in the presence of 100 mg/L



**Figure 3.** Current efficiency of Zn deposition at potential (vs. SSE): -1.600 V as a function of time: 1)  $\text{Zn}^{2+}$ -50 g/L and  $\text{H}_2\text{SO}_4$ -130 g/L, 2)  $\text{Zn}^{2+}$ -50 g/L,  $\text{H}_2\text{SO}_4$ -130 g/L and  $\text{Cu}^{2+}$ -50 mg/L, 3)  $\text{Zn}^{2+}$ -50 g/L,  $\text{H}_2\text{SO}_4$ -130 g/L and  $\text{Cu}^{2+}$ -100 mg/L, 4)  $\text{Zn}^{2+}$ -50 g/L,  $\text{H}_2\text{SO}_4$ -130 g/L,  $\text{Cu}^{2+}$ -100 mg/L and  $\text{Fe}^{2+}$ -100 mg/L.

$\text{Cu}^{2+}$ , and 100 mg/L  $\text{Cu}^{2+}$  and 100 mg/L  $\text{Fe}^{2+}$  simultaneously) than the CEZn obtained during deposition in the base electrolyte.

Copper content in the Zn coatings, obtained after one hour deposition at -1.600 V, is 1.75 wt.% (in the presence of 50 mg/L  $\text{Cu}^{2+}$ ) and 2.70 wt.% (in the presence of 100 mg/L  $\text{Cu}^{2+}$ ). The impurity content in the coatings, obtained from the electrolyte containing 100 mg/L  $\text{Cu}^{2+}$  and 100 mg/L  $\text{Fe}^{2+}$ , is 2.5 wt.% Cu and 0.1 wt.% Fe. The impurity content from electrolyte, containing 200 mg/L  $\text{Cu}^{2+}$  and 200 mg/L  $\text{Fe}^{2+}$ , is 2.4 wt.% Cu and 0.25 wt.%

Fe. In all cases the deposits of Zn are mat, grey in color, rough, and with dendrites on the edges.

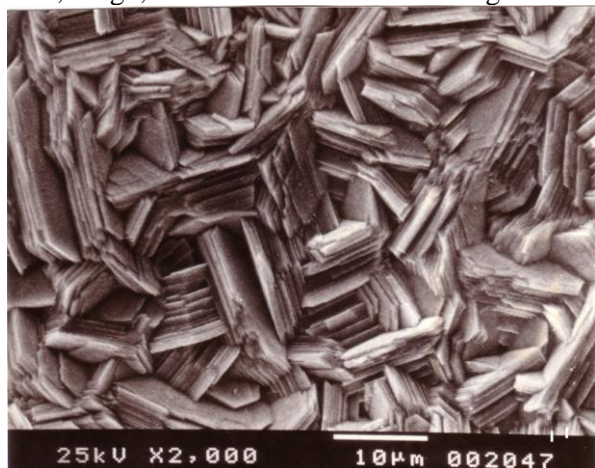


**Figure 4.** SEM micrograph of pure Zn. Deposition potential (vs. SSE): -1.600 V. Deposition time - 60 min.

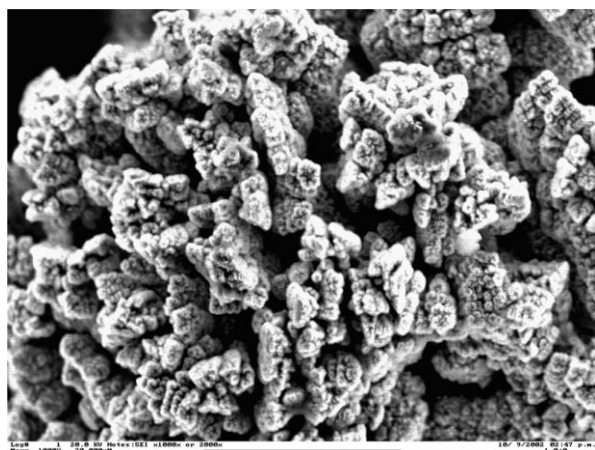


**Figure 5.** SEM micrograph of Zn, containing 2.4 wt.% Cu and 0.25 wt.% Fe. Electrolyte: Zn<sup>2+</sup> - 50 g/L, H<sub>2</sub>SO<sub>4</sub> - 130 g/L, Cu<sup>2+</sup> - 200 mg/L and Fe<sup>2+</sup> - 200 mg/L. Deposition potential (vs. SSE): -1.600 V. Deposition time - 60 min.

Figures 4 and 5 show SEM micrographs of Zn deposits, obtained in pure (base) electrolyte (Figure 4) and in an electrolyte, containing 200 mg/L Cu<sup>2+</sup> and 200 mg/L Fe<sup>2+</sup> (Figure 5). It can be seen that Cu (2.4 wt.%) and Fe (0.25 wt.%) change the Zn morphology and that dissolution takes place at the edges of the crystal grains.

### CONCLUSIONS

1. Simultaneous deposition of Zn and Cu begins at a potential of -1.450 V (vs. SSE).
2. Simultaneous deposition of Zn, Fe, and Cu begins at a potential of -1.500 V vs. SSE. At potentials more positive than -1.500 V vs. SSE, deposition of Cu solely, takes place.
3. The current efficiency of Zn deposition decreases with the time due to the Zn redissolution

which takes place in the presence of Cu<sup>2+</sup> and Fe<sup>2+</sup> ions. This process is a result of occurrence of Zn/Cu and Zn/Fe galvanic microelements, formed during simultaneous deposition of Zn, Cu, and Fe. Zn dissolves because it is more electronegative element than Cu and Fe.

4. Copper and iron, codeposited with zinc, change the deposit morphology and deteriorate the quality of the zinc produced.

### REFERENCES

1. A.G. Pecherskaya, V.V. Stender, *J. Appl. Chem.* (in Russian), **23**, 920 (1950).
2. V.V. Stender, A.G. Pecherskaya, *Non-Ferrous metals* (in Russian), **4**, 45 (1950).
3. U.F. Turomshina, V.V. Stender, *J. Appl. Chem.* (in Russian), **28**, 372 (1955).
4. U.F. Turomshina, V.V. Stender, *J. Appl. Chem.* (in Russian), **28** (5), 467 (1955).
5. M. Maya, N. Penazzi, R. Fratesi, G. Roventi, *J. Electrochem. Soc.*, **129**, 2695 (1982).
6. M. Maya, N. Penazzi, R. Fratesi, G. Roventi, *Oberfläche-Surfaces*, **24**, 234 (1983).
7. A.R. Ault, E.J. Frazer, *J. Appl. Electrochem.*, **18**, 583 (1988).
8. D.J. MacKinnon, *J. Appl. Electrochem.*, **15**, 953 (1985).
9. D.J. MacKinnon, J.M. Brannen, P.L. Fenn, *J. Appl. Electrochem.*, **17**, 1129 (1987).
10. L. Muresan, G. Maurin, L. Oniciu, S. Avram, *Hydrometallurgy*, **40**, 335 (1996).
11. L. Muresan, G. Maurin, L. Oniciu, D. Gaga, *Hydrometallurgy*, **43**, 345 (1996).
12. G.N. Znamenskiy, V.V. Kardashevskiy, V.V. Stender, *J. Appl. Chem.* (in Russian), **34** (6), (1961).
13. G.Z. Kiryakov, *J. Phys. Chem.* (in Russian), **32** (11), 2561 (1958).
14. G.Z. Kiryakov, F.K. Baynietova, *Akad. Nauk. Kazah. SSR, Trudi Inst. Chim. Nauk* (in Russian), **3**, 64 (1958).
15. Z.A. Sheka, K.F. Karlisheva, *Dokladi Akad. Nauk SSSR*, **108** (1), 126 (1956).
16. A.I. Jurin, S.P. Pyunnenen, *Trudi Leningradskogo Politehn. Inst.* (in Russian), **188**, 204 (1957).
17. G.N. Pahomova, *Non-Ferrous metals* (in Russian), **9**, 33 (1965).
18. A.I. Jurin, H. Azdin, *J. Appl. Chem.* (in Russian), **52** (8), 1763 (1979).
19. A.V. Pomosov, E.E. Krimakova, A.I. Levin, *J. Appl. Chem.* (in Russian), **31** (5), 734 (1958).
20. G.T. Wever, *J. of Metals*, **11**, 130 (1959).
21. T. Akiyama, H. Fukushima, K. Higashi, Proc. Intern. Simp. on Extractive Metallurgy of Zinc, Tokyo, Japan, Chapter **9**, 141 (1985).
22. S. Ohyama, S. Morioka, 1985. Proc. Intern. Simp. on Extractive Metallurgy of Zinc, Tokyo, Japan, Chapter **14**, 219 (1985).

## ИЗВЛИЧАНЕ НА ЦИНК ОТ СУЛФАТНИ ЕЛЕКТРОЛИТИ, СЪДЪРЖАЩИ МЕДНИ И ФЕРОЙОНИ

Г. Ходжаоглу, Ив. Иванов

*Институт по физикохимия, Българска академия на науките, ул. „Акад. Г. Бончев”, бл. 11, 1113 София, България*

Постъпила на 7 юни, 2010 г.; преработена на 29 октомври, 2010 г.

(Резюме)

Изследвано е влиянието на медните и феройоните върху извличането на цинк от сулфатни електролити. С използването на циклична волтаперометрия е установено, че едновременното отлагане на Zn и Cu започва при потенциал  $-1.450\text{ V}$  (спрямо SSE). Едновременното отлагане на Zn, Fe и Cu започва при потенциал  $-1.500\text{ V}$ . При по-положителни потенциали се отлага само Cu. В резултат на наличието на  $\text{Cu}^{2+}$  и  $\text{Fe}^{2+}$  йони протича процес на обратно разтваряне на отложения Zn, което понижава добива му по ток. Отлагането в продължение на 60 мин. при  $-1.600\text{ V}$  в електролит, съдържащ  $\text{Zn}^{2+} - 50\text{ g/L}$ ,  $\text{H}_2\text{SO}_4 - 130\text{ g/L}$ ,  $\text{Cu}^{2+} - 200\text{ mg/L}$  и  $\text{Fe}^{2+} - 200\text{ mg/L}$  води до получаването на Zn покритие, съдържащо 2.4 тегл.% Cu и 0.25 тегл.% Fe.

## Environmentally-clean Mg-air electrochemical power sources

Y.D. Milusheva<sup>\*</sup>, R.I. Boukoureshlieva, S.M. Hristov, A.R. Kaisheva

*Institute of Electrochemistry and Energy Systems, BAS, Sofia 1113, Acad. G. Bonchev St., Building 10*

Received: July 7, 2010; accepted September 13, 2010

The main aim of this work is investigation, development, and implementation of electrochemical systems of the Mg-Air type with salt electrolytes. The fulfilment of this primary aim will result on one hand in the construction of a comparatively simple and easy to use emergency power source, and on the other, in the development of demo models for training and popularization of the technology for obtaining of ecologically-clean energy.

This research covers:

- Selection of a hydrophobic material with optimal physical, chemical and electrochemical characteristics for the gas layer of the air gas-diffusion electrode;
- Research and selection of a suitable catalyst for the electrochemical reduction of oxygen that occurs on the air gas-diffusion electrode;
- Characterization of various Mg alloys as potential anode material in the Mg-Air system;
- Selection of a non-aggressive salt electrolyte with high ionic conductivity, operational stability, and comparatively low corrosion activity. Design and test of apt constructions for emergency and demo Mg-Air cells.

**Key-words:** Mg-air cells, air gas-diffusion electrodes, environmentally-clean energy

### INTRODUCTION

In the recent years a significant worldwide attention has been paid to the development of new types and novel generations of Electrochemical Power Sources. The interest is mainly due to the extensive search for efficient and ecologically-friendly renewable power sources. The needs for autonomous supply and quick reaction in emergency situations predetermine the extensive use of Chemical Power Sources (CPS) in almost every technical field. Many different types of Metal-Air batteries, like primary, reserve, electrically or mechanically rechargeable battery configurations, have been explored and developed over the last decades. Several metals such as Li, Ca, Mg, Al, Zn, Fe, etc, have been considered for use in the Metal-Air batteries. [1].

Generally the Metal-Air power source comprises of an air gas-diffusion electrode and a metal anode separated by electrolyte. The Metal-Air elements can be viewed as hybrid systems. Their metal anode works as the anodes in the conventional Me/MeO elements, while the cathode operates as a fuel cell. The electrochemical

reduction of oxygen upon an inert air electrode, which is thin and light, results in significantly higher values of the specific characteristics (Wh/kg and Ah/kg) of the Metal-Air element, compared to those, exhibited by conventional elements with an identical metal electrode. The development of Metal-Air systems, operating with non-aggressive, safe and environmentally-friendly salt electrolyte (NaCl, KCl, sea water and others), is of immense practical importance. Despic et al. [2] were the first to investigate Al-Air batteries using physiological electrolytes. Promising results were obtained with primary Al-Air cells in NaCl solution [3]. Despite the good characteristics of the Al in the system, some unsolved problems remained. These problems are related to the high internal resistance of the electrolyte, the formation of a gel of Al hydroxide, and the anode passivation, which made the cleaning of the cell difficult.

The concept of cells, working with sea water, is well-known and has been covered by a number of patents [4–10]. Cells with high energy density and sea water electrolyte involved the use of alloys of the Mg-Hg-Ga type [11]. Shinohara et al [12] reported on the development of a system with sea water for practical application in deep water tanks. The advantages, according to [13], are high energy density, low price, and long storage potential. A joint research project between DGA/BEC (France) and FFI (Norway) focused on the design of autonomous vehicles, powered by semi-fuel cell

---

<sup>\*</sup>To whom all correspondence should be sent:  
E-mail: joschi@abv.bg

with oxygen as an oxidant, sea water as an electrolyte, and Mg as fuel [14].

Promising results have been obtained with Magnesium-Air cells. The Mg-Air system possesses a number of significant advantages. The use of salt electrolyte is of immense importance for preservation of the environment. The Mg-Air cells are ecologically clean, Mg is non-toxic, no toxic substances are generated during the operation, and the salt electrolyte is chemically non-aggressive. What is more, the Mg-Air cell has practically unlimited storage life. The salt electrolyte can be removed from the cell storage and when necessary, it can be put back, thus making it instantly operational. All of the above, along with the good electrochemical characteristics and the comparatively low price, turns the Mg-Air cell into a very suitable emergency electrochemical power source not only to suit our every-day life needs, but also for application in both, the commercial and the industrial fields. The fact that all components of the cell are harmless and safe, makes the Mg-Air system suitable for demonstration aims (children included) in school labs, for training of students, for specialized university courses, etc.

The Magnesium-Air cell is a conventional electrochemical cell, containing one or two flat air gas-diffusion cathodes, and a magnesium anode, placed in NaCl-solution as an electrolyte. The air gas-diffusion electrode for Metal-Air cell separates the electrolyte from the surrounding air. The electrode, developed in the IEEC, is a double layer tablet, consisting of a porous hydrophobic layer and an active layer, containing porous catalyst. A special highly hydrophobic, electrically conductive material is used to form the gas layer of the electrodes [15, 16].

One of the most important tasks in the development of air gas-diffusion electrodes is to find proper catalysts for the electrochemical reduction of oxygen, which ensures high electrochemical characteristics and long exploitation time of the electrodes. In this respect, the development of non-platinum catalysts for the electrochemical reduction of oxygen is of great interest. Various porous catalysts are tested in air gas-diffusion electrodes, operating in saline electrolytes. The carbon-supported pyrolyzed macrocycles show good oxygen reduction reaction (ORR) activity in alkaline electrolytes, and are currently used in mechanically rechargeable Metal-Air batteries [17–23]. One popular non-noble air cathode is based on cobalt and iron tetramethoxyphenylporphyrine (CoTMPP and FeTMPP). CoTMPP has higher electrochemical

stability and promotes the two-electron ORR pathway, while FeTMPP has inferior ORR activity and promotes direct four-electron oxidation. The stability of the metal macrocyclic complex depends on the metal, and it decreases accordingly:  $\text{Co} > \text{Fe} > \text{Mn}$ . One common approach to combine the advantages of a more stable CoTMPP and a more ORR active FeTMPP is to fabricate a mixture, FeTMPP/CoTMPP [24]. The ORR activity increases due to the formation of a face-to-face structure, accelerating the destruction of the O–O bond in the oxygen molecule [25–28]. The effect of heat treatment on the N4-chelate stability increase, discovered by Jahnke et al. [29] in 1976, is currently a very popular method for increasing the stability of Co/FeTMPP-based catalysts.

The silver is a typical O<sub>2</sub> reduction catalyst, and has a reasonable high catalytic activity for O<sub>2</sub> reduction, competitive to platinum in alkaline electrolyte [30].

Catalysts, containing mixed Ni-Co oxides, prepared by impregnating active carbon with solution of Ni-acetate and Co-acetate and subsequent heat treatment, are investigated [31].

## EXPERIMENTAL

Catalysts, based on different kinds of active carbons, used as carriers, were investigated.

Four types of additional catalysts, introduced into the active carbon, were studied.

VS50–CoTMPP–700 type was prepared while dispersed SiO<sub>2</sub> (VS) was impregnated with a solution of CoTMPP, and after removing the solvent and drying, the material was treated at 700 °C in argon.

Pyrolysed CoTMPP catalyst is produced by impregnation of a dispersed carbon material with a solution of CoTMPP, drying and subsequent heat treatment in Ar at 800 °C. The pyrolysis in Ar of the pure compound of CoTMPP, results in a hard, glassy-like product that practically could not be used as catalyst, so that the presence of a highly dispersed carrier in the production of catalyst seems indispensable. During the heat treatment, the CoTMPP-molecule is decomposed and the pyrolysis residual products are formed in the porous structure of the carbon support and are responsible for the observed high electrochemical activity of the catalyst.

ACCoNi catalyst was prepared by impregnation of the NORIT NK active carbon with a solution, containing both, the Co- and the Ni-acetates, dried and heat treated at 300 °C in open air.

Magnesium possesses a comparatively high

energy density and low specific gravity; its price is not very high, so it could be used as a primary anode in metal-air systems. Sheets of Mg or magnesium alloys are used as anodes in the developed Magnesium-Air cells. The behavior of the air gas diffusion electrode is investigated in a half-cell arrangement, when operating in solutions of NaCl with different concentrations.

## RESULTS AND DISCUSSION

### Air Gas-Diffusion Electrode

The air electrode, used in the magnesium-air cell, is a double layer electrode, consisting of a gas layer made from a hydrophobic carbon/PTFE material and a catalytic layer, made from mixture of catalyst and the same hydrophobic material.

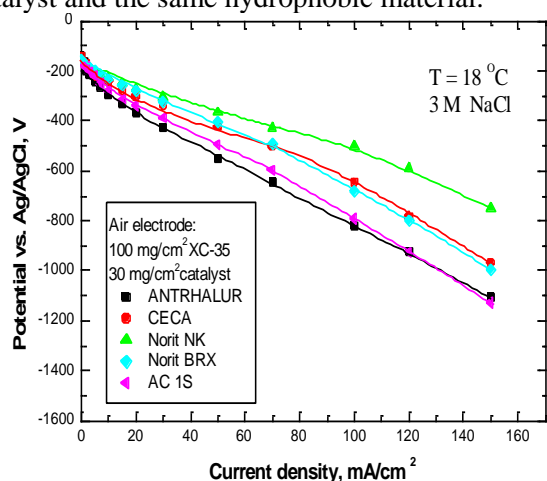


Fig. 1. Polarization curves of air electrodes with different types active carbon catalysts

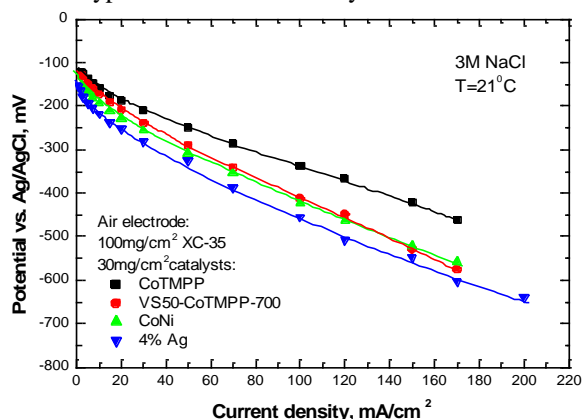


Fig. 2. Polarization curves of air electrodes with different catalysts in 3 M NaCl

Fig. 1 shows the polarization characteristics of air gas diffusion electrodes in 3 M NaCl with catalysts from different kinds of active carbon. It is seen that pure active carbon can be used as catalyst in air electrodes in saline solutions, but the polarization of the electrode in this case is quite high. On the other hand, the active carbon is

suitable to be additionally activated with some suitable compounds.

Four types of catalysts were used for the catalytic layer: pyrolyzed CoTMPP, VS50-CoTMPP-700, active carbon with Co and Ni (ACCoNi), and AC with 4 % Ag. Fig. 2 represents a comparison between the polarization curves of the air electrodes and the investigated types of catalysts when operating in 3 M NaCl. The comparison with the polarization curve for the electrodes with CoTMPP catalyst shows that the chelate-promoted electrodes have also better current-voltage characteristic.

The behaviour of one and the same electrode with a pyrolyzed CoTMPP catalyst, is investigated in a half-cell arrangement, when operating in

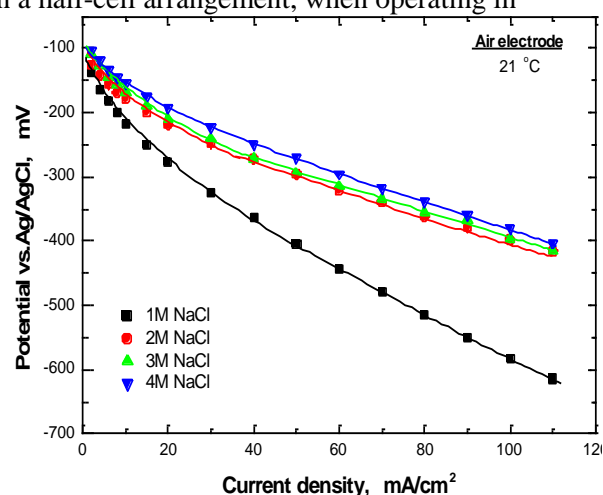


Fig. 3. Current-voltage curves of the air-electrode operating in NaCl solution with different concentrations.

solutions of NaCl with different concentrations (Fig. 3). The difference in the obtained curves, in this case, is probably and mainly due to the difference in the conductivity of the NaCl solution of different concentrations  $k = 0,074-0,217 [\Omega^{-1} \cdot \text{cm}^{-1}]$ .

### Magnesium anodes

Several types of magnesium alloys are tested: pure Mg (99,99 %), MgAM60 (94 % Mg, 6 % Al), MgAM50 (95 % Mg, 5 % Al), MgAZ91(90 % Mg, 9 % Al, 1 % Zn), and MA8M06 (~ 97 % Mg, 0,2 % Fe, 0,12 % Zn, 1,3 % Mn, 0,01 % Si, 0,12 % Al). The testing of the different magnesium anodes is performed in Mg-Air cells with two air electrodes with pyrolyzed CoTMPP catalyst ( $S = 65 \text{ cm}^2$ ). The electrolyte is 3 M NaCl. Fig.4 illustrates a comparison between the current-voltage characteristics of the investigated Mg-Air cell and the different Mg-anodes. The

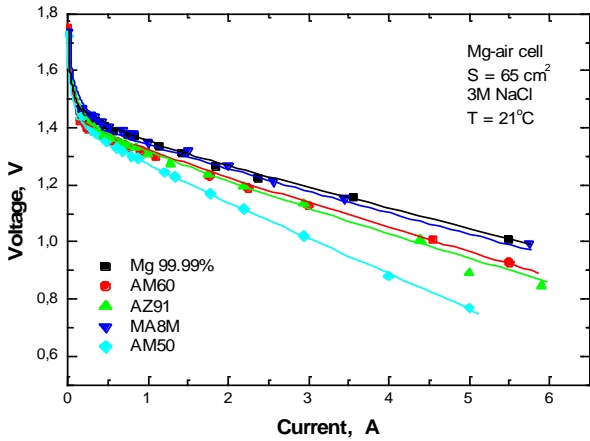


Fig. 4. Current-voltage of the Mg-Air cells with different Mg-anodes.

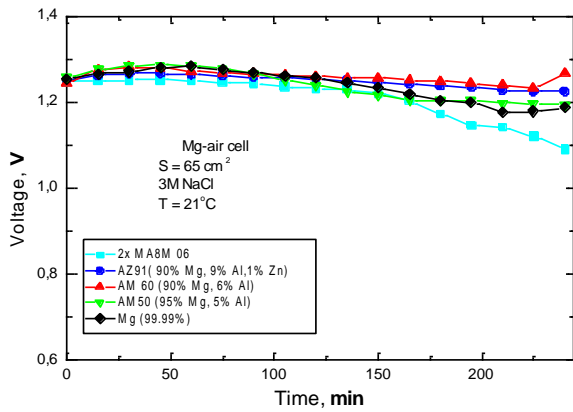


Fig. 5. Discharge curve of Mg-Air cell ( $S = 65 \text{ cm}^2$ ) with different Mg-anodes.

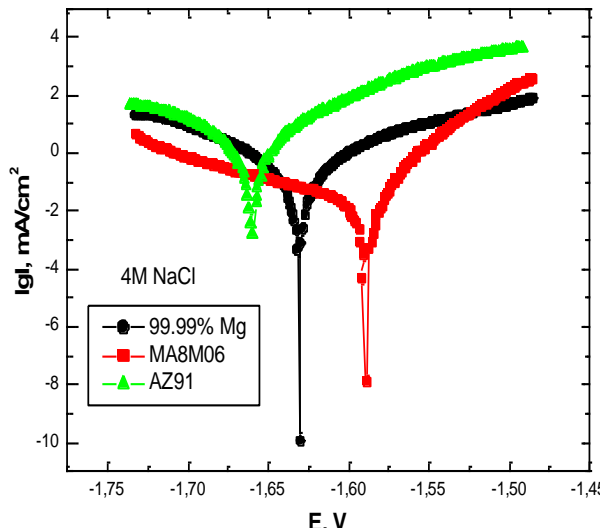


Fig. 6. Polarization curves of Mg alloys and pure magnesium in 4M NaCl.

comparison of the data shows that the Mg 99.99 % and the MA8M, which is produced especially to be used in water activated batteries, are the most suitable materials to be used as anodes. The discharge curves at  $0.6 \Omega$  constant load of the

magnesium-Air cells and different anodes are compared in Fig.5.

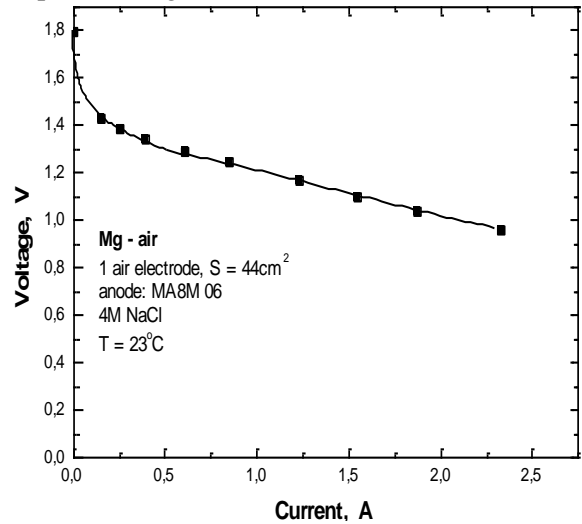


Fig.7. Current-voltage curves of Mg-Air cell ( $S = 44 \text{ cm}^2$ ).

Corrosion investigations on various types of magnesium alloys were carried out in order to optimize the performance of the mechanically rechargeable Magnesium-Air cells. The behavior of AZ 91 and MA8M 06 alloys in respect to pure Mg was under investigation. The experiments were conducted in aqueous solutions of 4M NaCl and the results are shown in Fig.6. It is obvious that corrosion stability increases in the following order: AZ91 < Mg < MA8M. The corrosion stability is described by the corrosion potential shift towards more negative values and the corrosion rate, expressed by the corrosion current.

#### Experimental Mg-air cells

Several types of experimental Mg-Air cells are tested, differing in size (working area of the air electrodes used) [32].

Fig. 7 presents the current-voltage characteristics of the magnesium-air cell with one air electrode ( $S = 44 \text{ cm}^2$ ). Magnesium MA8M 06 is used. It is covered with a protective current conductive sheet from the side opposite to the air electrode. The discharge curve of this cell at constant load ca.  $0.6 \Omega$  is presented in Fig.8.

The investigated magnesium-air cells are constructed as experimental mechanically rechargeable cells. Once the magnesium anode has been discharged, it is removed out from the cell together with the electrolyte, and a new magnesium electrode and fresh saline electrolyte are introduced in it. After this mechanical recharge, the magnesium-air cell is operational again. In this case the essential feature is that the air electrodes in the

cell are used many times. Investigation of both, the current-voltage characteristics and the power curves

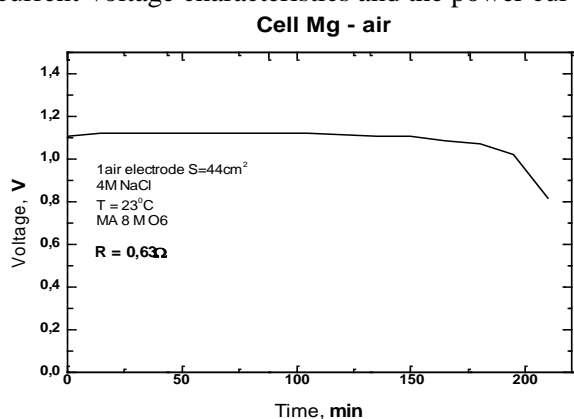


**Fig. 8.** Discharge curve of Mg-Air cell ( $S = 44\text{cm}^2$ ) at constant load  $0,63\ \Omega$ .

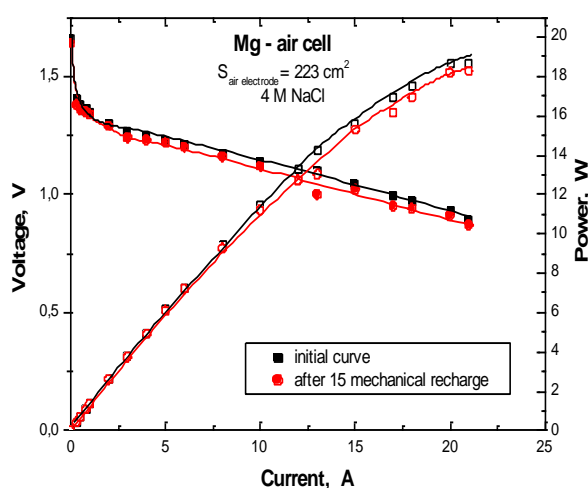


**Fig. 9.** Current-voltage and power characteristics of the Mg-Air cell ( $S = 223\ \text{cm}^2$ ): initial and after 15 mechanical recharge.

of one and the same Mg-air cell, are performed after its mechanical recharge. The cell comprises of two air electrodes with a catalyst from pyrolyzed CoTMPP (total working area of  $223\text{cm}^2$ ), and Mg anodes from the MA8M06 alloy are used. 4M NaCl solution is used as electrolyte. The initial current-voltage curve and the current-voltage curve after 15 mechanical recharges of the same Mg-Air cell are presented in **Fig. 9**. It is seen that currents up to 20 A could be obtained from this cell at voltage higher than 1 V. The specific power of this cell is ca. 20 W/kg. The results show also that the Mg-Air cell can be recharged mechanically several times without any significant loss in its performance.

More powerful Mg-Air cell with a total working area of the air electrodes of  $440\ \text{cm}^2$  and  $660\ \text{cm}^2$  are designed and investigated. They can be used as emergency energy sources.

## CONCLUSIONS

Magnesium-Air cells, operating with non-aggressive electrolyte, are developed. Air gas-diffusion electrodes, suitable for operation in NaCl-solution, are designed. Various carbon-based catalysts for the ORR are tested. Magnesium alloys suitable for use as anodes in Mg-Air cells are found.

The current-voltage and the power characteristics of various types of magnesium-air cells are investigated. The results show that the mechanically rechargeable magnesium-air cell with a NaCl-electrolyte is a prospective energy source.

The Mg-air cells are of substantially increased power output. They could be used as primary and emergency power sources for the residential, commercial, and industrial purposes. It should be noticed again that the magnesium-air cells are safe and employ environmentally friendly salt-water electrolyte, therefore, they can be used at school laboratories for experiments and demonstrations.

## REFERENCES

1. G. Koscher, K. Kordes, *J. Power Sources* **136**, 215 (2004).
2. A. Despic, D. Drazic, M. Purenovic, N. Civkovic, *J. Appl. Electrochemisry*, **6**, 652 (1976).
3. D. Drazic, A. Despic, S. Zecevic, in „Fuel cell trends in research and application“ (ed. by A. Applely), Hampshire, New York, 1987.
4. N. Lidorjenko, V. Naumjenko, A. Kopjov, L. Esajan, D. Kurygitsa, Russ. Patent SU-5, 509,307 (1976).
5. C. Opitz, US Patent 3,401,063 (1968).
6. M. Walsh, US Patent 4,522,897 (1984).
7. O. Hasvold, Norweg. Patent 164, 324 (1988).
8. E. Buzzelli, J. Jackovitz, J. Lauer, *Sea Technol.* **32**, 66 (1991).
9. B. Rao, J. Giacomo Jr., W. Kobasz, D. Hosom, R. Weller, A. Hinton, *Sea Technol.* **33**, 63 (1992).
10. P. Shen, A. Tsueng, C. Kuo, *J. Power Sources*, **47**, 119 (1994).
11. Y. Feng, R. Wang, K. Yu, C. Peng, J. Zhang, C. Zhang, *J. of Alloys and Compounds*, **473**, 215 (2009).
12. M. Shinohara, E. Araki, M. Mochizuki, T. Kanazawa, K. Sueyhiro, *J. Power Sources*, **187**, 253 (2009).
13. O. Hasvold, H. Henriksen, E. Melvæ, G. Citi, B. Johansen, T. Kjøningsen, R. Galetti, *J. Power Sources*, **65**, 253 (1997).
14. Hasvold, T. Lian, E. Haakaas, N. Storkensen, O. Perelman, S. Gordier, *J. Power Sources*, **136**, 232, (2004).
15. A. Kaisheva, I. Iiev, S. Gamburtcev, E. Vakanova, E. Budevski, US Patent No 4031033, 1972.
16. I. Iliev, A. Kaisheva, US Patent No 1392341

17. S.R. Ovshinsky, C. Fierro, B. Reichman, W. Mays, J. Strebe, M.A. Fetcenko, A. Zallen, T. Hicks, US Patent 7,097,933 (2003).
18. M. Maya, C. Oreccia, M. Strano, P. Tosco and M. Vanni, *Electrochim. Acta*, **46**, 423 (2000).
19. C. Mocci, S. Trassatti, *J. Mol. Catal. A: Chem.* **204–205**, 713 (2003).
20. X.-Y. Xie, Z.-F. Ma, X.-X. Ma, Q. Ren, V.M. Schmidt and L. Huang, *J. Electrochem. Soc.* **154**, B733 (2007).
21. S. Lj. Gojkovic, S. Gupta, R.F. Savinell, *J. Electrochem. Soc.* **145**, 3493 (1998).
22. W. Yao, T. Tsai, US Patent 6,368,751 (2002).
23. N. Naimer, E.E. Khasin, J.R. Goldstein, J. Sassen, US Patent 5,242,765 (1993)
24. R. Jiang, L. Xu, R. Jin, S. Dong, *J. Inorganic Biochemistry*, **30**, 189 (1987).
25. N. Oyama, F.C. Anson, *Anal. Chem.* **52**, 1192 (1980). J.P. Collman, P. Denisevich, Y. Konai, M. Marocco, C. Koval, *J. Am. Chem. Soc.* **102**, 6027 (1980).
26. M. Lefevre, J.P. Dodelet, P. Bertrand, *J. Phys. Chem. B* **104**, 11238 (2000).
27. F.C. Anson, *J. Am. Chem. Soc.* **102**, 6027 (1980).
28. H. Jahnke, M. Schonborn and G. Zimmermann, *Top. Curr. Chem.* **61**, 133 (1976).
29. M. Chatenet, L. Genies-Bultel, M. Aurousseau, R. Durand, F. Andolfatto, *J. Appl. Electrochem.*, **32**, 1131 (2002).
30. A. Kaisheva, I. Iliev, NATO Science Series II Mathematics, Physics and Chemistry, **229**, 105 (2006).
31. A. Kaisheva, I. Iliev, J. Milusheva, Mechanically rechargeable magnesium-air cell with non-aggressive electrolyte, Proc. International Congress for Battery Recycling, 2002, Vienna, Austria.

## ЕКОЛОГИЧНИ ЕЛЕКТРОХИМИЧНИ ИЗТОЧНИЦИ НА ЕНЕРГИЯ МАГНЕЗИЙ – ВЪЗДУХ

Й.Д. Милушева, Р.И. Букурещлиева, С.М. Христов, А.Р. Каишева

Институт по електрохимия и енергийни системи, БАН, 1113 София, ул. „Акад. Г. Бончев” бл. №10

Постъпила на 7 юли, 2010 г.; приета на 13 септември 2010 г.

(Резюме)

Основна цел на работата е разработване и реализиране на електрохимични системи Магnezий-Въздух със солеви електролити, които са подходящи за употреба като аварийни източници на енергия и демонстрационни модели за обучение и популяризиране на технология за получаване на екологично чиста енергия.

За реализиране на основната цел са решени следните основни задачи:

- избор на хидрофобен материал с оптимални физични, химични и електрохимични характеристики за газовия слой на въздушния електрод;
- изследване и подбор на подходящ катализатор за електрохимичната редукция на кислорода, протичаща върху въздушен газодифузионен електрод;
- охарактеризиране на различни Mg сплави като аноден материал;
- избор на неагресивен електролит и сепаратор;
- проектиране, изработване и тестване на аварийни и демонстрационни клетки Магnezий-Въздух.

## Study of the influence of nitrite anions on the electrode processes in ammonium electrolyte for Ag-Cu deposition

K. Ignatova<sup>1\*</sup>, D. Stoykova<sup>2</sup>

<sup>1\*)</sup>University of Chemical Technology and Metallurgy, 8 St. Kliment Ohridski Blvd., 1756 Sofia, Bulgaria

<sup>2)</sup>Mint, Sofia, Bulgaria

Received: June 16, 2010; revised: October 29, 2010

By means of the cyclic voltammetry (CV) the effect of nitrite anions (in the form of NaNO<sub>2</sub>) on the kinetics of separate and of codeposition of Ag and Cu is examined. The effect of the electrode substrate and the proportion of the basic components of the solution on the deposition kinetics and the powder formation of Ag-Cu alloys is also established. It is found that the one step process of silver deposition in the absence of nitrite anions is fully reversible. In presence of nitrite anions in the solution, the stage of reduction of the silver-ammonium complexes is preceded by reversible chemical reaction of AgNO<sub>2</sub> formation. The copper in nitrite ions absence and presence is deposited by two-stage mechanism – incomplete reduction of the cupri-ammonium ions to cupro-ammonium ions and the main process of electrodeposition of cupri-ammonium ions to elementary copper. As a whole the presence of NO<sub>2</sub><sup>-</sup> ions and the decrease of the Ag<sup>+</sup>/Cu<sup>2+</sup> - ratio in the electrolyte impedes the Ag and Cu electrodeposition and results in production of more fine dispersion Ag-Cu alloy powders.

*Key words:* electrodeposition of alloys, alloy metal powders, cyclic voltammetry

### INTRODUCTION

The alloyed Ag-Cu powders find application as components most of all in solder creams in the electronics [1] and in electro-conductive pastes in many areas of the electrical engineering [2, 3].

The electrolysis is a method which allows direct preparation of alloyed metal powders of high purity and dispersibility, controlled phase and component composition [4–6]. The application of non-stationary (impulse) current modes [7, 8], the use of complex electrolytes and the introduction of special additives [6, 8], affecting the crystal growth are becoming more and more frequently applied means in order to meet the high requirements for achievement of maximum dispersibility and morphological homogeneity of the powders.

The thorough analysis of the publications has shown that the ammonium electrolyte may be successfully applied for deposition of finely dispersed Ag-Cu powder [9]. It is well known that these electrolytes are stable during continued operation and permit easy removal of the powder coating from the cathode [9]. In most of the other complex electrolytes for Ag-Cu deposition [10, 11] the silver forms difficult to dissolve compounds, and the electrolytes on their base are unstable.

The ammonium electrolytes are also of theoretical interest for examination of the copper reduction mechanism (the oxidation, respectively) [12–16]. A previous publication of ours is related to the study of this phenomenon in amino-nitrate electrolyte [17]. There is no reference data about the NO<sub>2</sub><sup>-</sup> effect on the kinetics and mechanism of Ag and Cu deposition as well as on the structure of Ag-Cu powders. Based on the arguments, pointed out, the composition of the electrolyte, in which we have carried out the present investigations, was chosen.

The method of cyclic voltammetry with its simple qualitative and quantitative criteria [18] is particularly preferred for examination of the alloy deposition. Thus, in the chosen electrolyte composition, the kinetics of separate and codeposition of Ag and Cu on electrodes of copper and silver is examined as well as the Ag-Cu powder formation.

### 2. EXPERIMENTAL

The electrolyte in which the studies are carried out has the following composition: Ag – from 2.5 to 7.5 g dm<sup>-3</sup> in the form of AgNO<sub>3</sub>; Cu – from 2.5 to 7.5 g dm<sup>-3</sup> in the form of Cu(NO<sub>3</sub>)<sub>2</sub>; 20–40 g dm<sup>-3</sup> NH<sub>4</sub>NO<sub>3</sub>; 0–15 g.dm<sup>-3</sup> NaNO<sub>2</sub> and 25% NH<sub>3</sub> up to pH=9÷9.5. Due to the high solubility of the salts, the preparation of the solution does not give special

\* To whom all correspondence should be sent:

E-mail: E-mail: [vi21959@yahoo.com](mailto:vi21959@yahoo.com)

problems. On addition of ammonium, initially at pH 7÷8, the solution becomes cloudy but reaching pH values of 8.5-9 makes the solution transparent, coloured in blue. According to [9, 19] in excess of ammonia in the electrolyte, the silver and copper are in the form of soluble ammonium complexes:  $[\text{Ag}(\text{NH}_3)_2]^+$  and  $[\text{Cu}(\text{NH}_3)_4]^{2+}$ , respectively.

The studies are performed in thermostated, three-electrode cell with working electrodes made of copper (99.97%) and silver (96.97%) in the shape of disk with working area of 1 cm<sup>2</sup>. The counter electrode is a platinum plate with surface area 30 cm<sup>2</sup>, and the working electrode is polarized to different, constant potentials E in reference to a Hg/Hg<sub>2</sub>Cl<sub>2</sub>, sat.KCl electrode.

The cyclic voltammograms are recorded by means of potentiostat of "Wenking" type (Germany) in a potential range from 0.600 V ÷ -1.400 V. The polarization is always from the chosen initial potential in the cathode direction. The

rate of potential scanning in the presented voltammograms is varied in the range between 10 and 50 mV.s<sup>-1</sup>.

The investigation of the alloys morphology is performed by SEM of Oxford Instruments series, JSM-6390 of JEOL.

### 3. RESULTS AND DISCUSSION

#### 3.1. Voltammograms in Ag electrolyte.

Figure 1(a-c) present the cyclic voltammograms, recorded on silver electrode in an electrolyte which contains 7.5 g dm<sup>-3</sup> Ag in the presence of a background electrolyte of 40 g dm<sup>-3</sup> NH<sub>4</sub>NO<sub>3</sub> (Figure 1a) and 15 g dm<sup>-3</sup> NaNO<sub>2</sub> (Figure 1b), as well as in the parallel presence of both background additives of 40 g dm<sup>-3</sup> NH<sub>4</sub>NO<sub>3</sub> and 15 g dm<sup>-3</sup> NaNO<sub>2</sub> (Figure 1c).

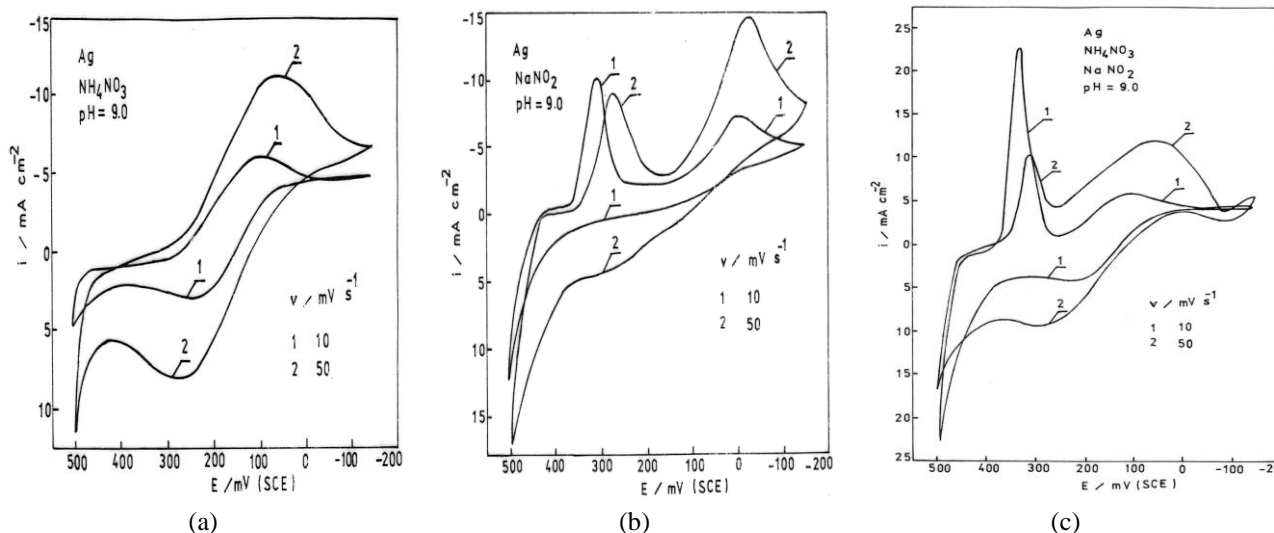
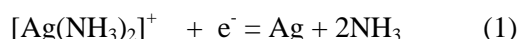


**Fig. 1.** Voltammograms on Ag electrode in (a): 7.5 g dm<sup>-3</sup> Ag and 40 g dm<sup>-3</sup> NH<sub>4</sub>NO<sub>3</sub>; (b): 7.5 g dm<sup>-3</sup> Ag and 15 g dm<sup>-3</sup> NaNO<sub>2</sub> and (c): 7.5 g dm<sup>-3</sup> Ag; 40 g dm<sup>-3</sup> NH<sub>4</sub>NO<sub>3</sub> and 15 g dm<sup>-3</sup> NaNO<sub>2</sub>, (pH=9,0).

In the presence of NH<sub>4</sub>NO<sub>3</sub> only as a background (Figure 1a), observed in the curves are cathode and the corresponding to it anode current maximums that grow proportionally to the rate of potential scanning and the silver ion concentration in the solution.

The current peaks observed are most probably connected with the reduction/oxidation of the forms of silver in accordance with the following reaction:



In the presence of NaNO<sub>2</sub> as a background, two successive cathode maximums arise, and there is no anode branch (Figure 1b). The detailed examination of the processes in solutions, containing only

NaNO<sub>2</sub> (data not shown), shows that formation of partially soluble product of AgNO<sub>2</sub> is possible at more positive potentials than the steady one, on the electrode surface in accordance with the following reaction:



According to the data of Salt Lake Metals, USA [20], the solubility product of AgNO<sub>2</sub> is  $k_{sp} = 6.0 \cdot 10^{-4}$ , and it is close to that of the AgSO<sub>4</sub>, ( $k_{sp} = 1.4 \cdot 10^{-5}$ ). Then the first of the maximums in Figure 1b will be resultant from the reaction of AgNO<sub>2</sub> reduction to silver:



In the electrolyte, containing  $7.5 \text{ g dm}^{-3} \text{Ag}$ , as well as the background additives:  $\text{NH}_4\text{NO}_3$  and  $\text{NaNO}_2$  (Figure 1c), the patterns of relationship that we found, for both background additives separately, become apparent. In this case the electrode surface is characterized by higher activity compared to the electrolyte which contains only sodium nitrite (Figure 1b), and therefore the observed current maximums are higher.

The application of diagnostic criteria of the method of cyclic chronovoltammetry [18] demonstrates that in the electrolyte, containing  $\text{NaNO}_2$  together with  $\text{NH}_4\text{NO}_3$ , there is a CE-mechanism observed, i.e. a reversible chemical reaction (Reaction 3) occurs, which precedes the reversible transition of a charge (Reaction 1). It was established that in the electrolyte the potential difference, corresponding with the cathode and the anode currents maxima  $\Delta E^{c-a}$ , increases with the speed of potential  $V$  evolution; the function of the current  $(I_c / \sqrt{v})$  decreases with  $v$ , and the ratio  $I_a/I_c$  increases with the  $v$  increase. The same criteria applied for an electrolyte, containing only  $\text{NH}_4\text{NO}_3$  as background, testifying for the occurrence of one single reversible electrode reaction, and namely that of the reduction/oxidation of the silver complexes to silver, and vice versa.

### 3.2. Voltammograms in Cu electrolyte

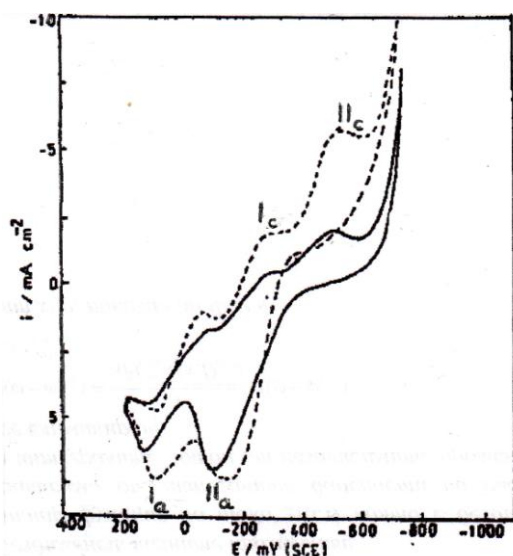


Fig. 2. Voltammograms on Cu electrode in (1):  $40 \text{ g dm}^{-3} \text{NH}_4\text{NO}_3$  and in (2):  $2.5 \text{ g dm}^{-3} \text{Cu}$  and  $40 \text{ g dm}^{-3} \text{NH}_4\text{NO}_3$ ,  $\text{pH}=9.0$  ( $v=30 \text{ mV s}^{-1}$ ).

We reported in our previous publication [17] on the results of the investigation of the processes of Cu reduction/oxidation in an amino-nitrate electrolyte. It is revealed that in the absence of copper, when the initial potential is much more

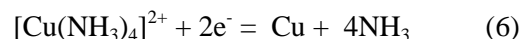
positive than the equilibrium, ( $E_{\text{eq}} = 0.273\text{V}$ ) two successive cathode peaks (peaks  $I_c$  and  $II_c$ ) are observed, along with the corresponding anode peaks, peak  $II_a$  and  $I_a$  (Figure 2, curve 1). This data correspond to those, obtained by other authors in ammonia electrolyte [12]. The first cathode peak ( $I_c$ ), as it follows from the course of the curves, is connected with the reduction of the copper cupri-ammonium ions  $[\text{Cu}(\text{NH}_3)_4]^{2+}$  to cupro-ammonium ions  $[\text{Cu}(\text{NH}_3)_2]^+$  in accordance with the reaction below (4):



On reaching the equilibrium concentration, the obtained cupro-ammonium ions  $[\text{Cu}(\text{NH}_3)_2]^+$  immediately enter in a disproportioning reaction (5):



This does not lead to the current peak but rather to its hold on certain level. The second cathode peak ( $II_c$ ) is connected with the direct reduction of the copper cupri-ammonium complexes to elementary copper according to the reaction:



The anode peaks  $II_a$  and  $I_a$  are connected with a run of reactions, opposite to reactions (6) and (4), respectively. The entire mechanism of copper deposition from amino-nitrate electrolyte is reduced to ECE, running of two successive reversible

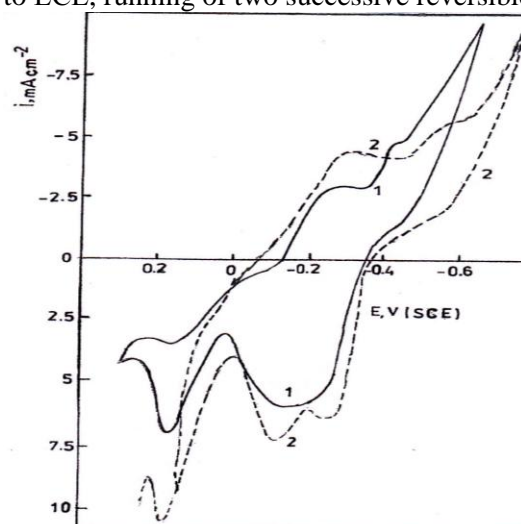
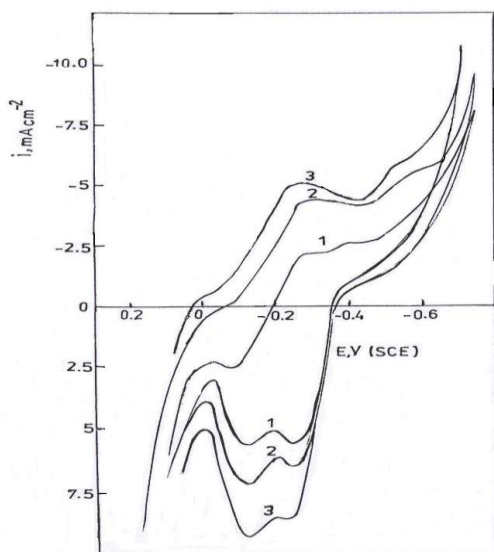


Fig. 3. Voltammograms on Cu electrode in (1):  $2.5 \text{ g dm}^{-3} \text{Cu}$  and  $40 \text{ g dm}^{-3} \text{NH}_4\text{NO}_3$  and in (2)  $2.5 \text{ g dm}^{-3} \text{Cu}$ ,  $40 \text{ g dm}^{-3} \text{NH}_4\text{NO}_3$  and  $15 \text{ g dm}^{-3} \text{NaNO}_2$ ,  $\text{pH}=9.0$  ( $v=30 \text{ mV s}^{-1}$ ).

electrochemical reactions (4) and (6), and of intermediate reversible chemical reaction of copper disproportioning (5) [12, 17].

Fig. 3 presents a comparison between the voltammograms, recorded on copper electrode in  $2.5 \text{ g dm}^{-3} \text{ Cu}$  and  $40 \text{ g dm}^{-3} \text{ NH}_4\text{NO}_3$  (Figure 3, curve 1) and in the solution, containing  $2.5 \text{ g dm}^{-3} \text{ Cu}$ ,  $40 \text{ g dm}^{-3} \text{ NH}_4\text{NO}_3$  and  $15 \text{ g dm}^{-3} \text{ NaNO}_2$  (Figure 3, curve 2). The comparison shows that the addition of  $\text{NaNO}_2$  in the solution results in current increase which corresponds to the incomplete reduction according to reaction (5). Besides, the rate of the useful reaction, that of the cupriammonium complexes reduction to copper (6), decreases. An approachment of potentials, corresponding to the two anode peaks, is observed in the anode area. A probable shift of potentials, corresponding to the origination and the respective oxidation of the two complex forms of copper on the anode area, takes place in the presence of  $\text{NaNO}_2$ . Figure 4 presents the voltammograms, recorded in the presence of both background additives and in the presence of copper ions as well, at three different rates of potential scanning. The rate increase of the potential scanning leads to the increase of the current peaks to a different degree, but for all of them the concentration polarization is obviously determinative.



**Fig. 4.** Voltammograms on Cu electrode in  $2.5 \text{ g dm}^{-3} \text{ Cu}$ ,  $40 \text{ g dm}^{-3} \text{ NH}_4\text{NO}_3$  and  $15 \text{ g dm}^{-3} \text{ NaNO}_2$ ,  $\text{pH}=9.0$  at scan rates „ $v$ ”: (1)  $20 \text{ mV s}^{-1}$ ; (2)  $30 \text{ mV s}^{-1}$ ; (3)  $50 \text{ mV s}^{-1}$ .

### 3.3. Voltammograms in an electrolyte for Cu and Ag co-deposition

The voltammograms, shown in Figure 5, are recorded in an electrolyte for the codeposition of copper and silver on copper electrodes (curve 1), and on silver ones (curve 2) in the presence of a

background just of  $40 \text{ g dm}^{-3} \text{ NH}_4\text{NO}_3$ . The change of the electrode type leads to current decrease, connected with difficulties in the deposition of metal on an electrode, different in nature. Current decrease is observed on the copper electrode which

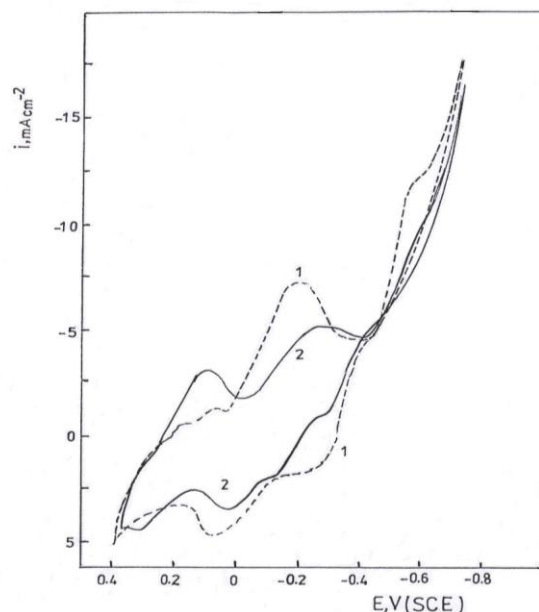


**Fig. 5.** Voltammograms on Cu electrode (1) and on Ag electrode (2) in  $2.5 \text{ g dm}^{-3} \text{ Cu}$ ;  $2.5 \text{ g dm}^{-3} \text{ Ag}$  and  $40 \text{ g dm}^{-3} \text{ NH}_4\text{NO}_3$ ,  $\text{pH}=9.0$  ( $v=30 \text{ mV s}^{-1}$ ).

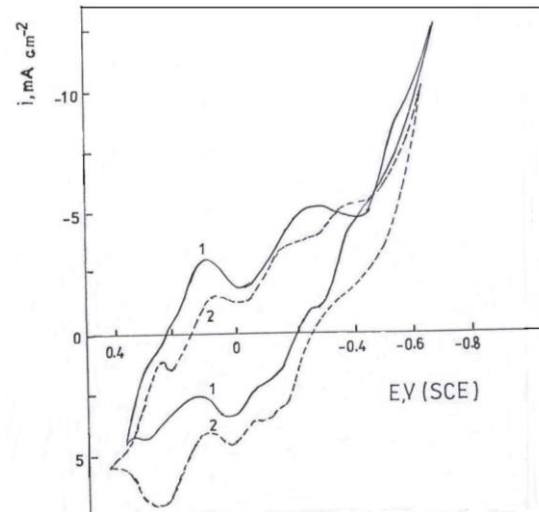
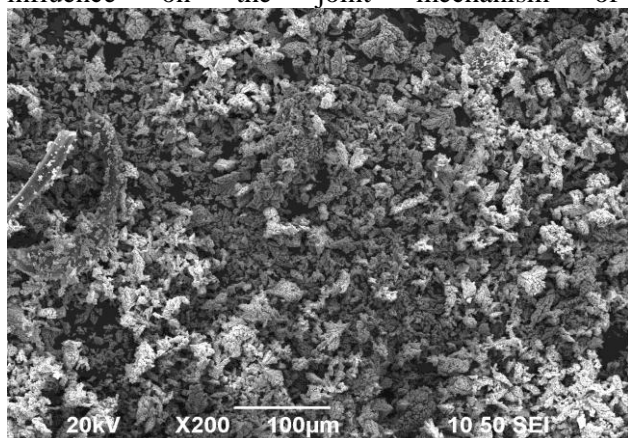


**Fig. 6.** Voltammograms on Ag electrode in  $2.5 \text{ g dm}^{-3} \text{ Cu}$ ,  $2.5 \text{ g dm}^{-3} \text{ Ag}$ ,  $40 \text{ g dm}^{-3} \text{ NH}_4\text{NO}_3$  (1) and in the same electrolyte with  $15 \text{ g dm}^{-3} \text{ NaNO}_2$  (2);  $\text{pH}=9.0$  ( $v=30 \text{ mV s}^{-1}$ ).

is connected with the reduction of the silver ammonium complexes to silver, and on the silver electrode, connected with the reduction of the copper complexes.

The  $\text{NaNO}_2$  effect on the kinetics of the Ag and Cu codeposition is shown in Figure 6. The

introduction of  $\text{NaNO}_2$  (Figure 6, curve 2) results in current decrease, connected with the silver and copper reduction – an effect that is established also in the separate deposition of the metals. In the same time, the two-stage mechanism of reduction/oxidation of the copper forms is more clearly visible in the curves, made in the presence of  $\text{NaNO}_2$  (Figure 6, curve 2) than the curves, made in the absence of  $\text{NaNO}_2$  (Figure 6, curve 1). Besides, a decrease of the cathode peak and a significant increase (and shift in potentials) of the anode peak, related to the forms of silver, are observed. Obviously,  $\text{NaNO}_2$  has a significant influence on the joint mechanism of

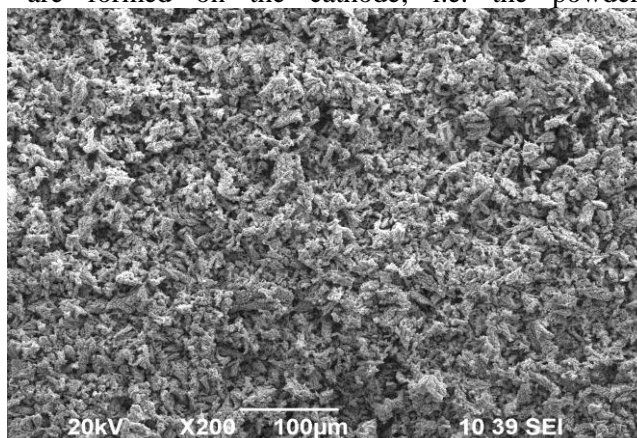


(a)

reduction/oxidation of copper and silver, which should reflect on the structure of the Ag–Cu plating, deposited from the electrolyte.

### 3.4. Morphology of the electrodeposited Ag-Cu powder

Figure 7 (a and b) shows the comparison between the electron micrographs (EM) of the Ag–Cu powder, prepared in the absence (Figure 7a) and in the presence of  $\text{NaNO}_2$  (Figure 7b) in the electrolyte at the same potential  $E = -0,850 \text{ V}$  (SCE). The electron micrographs show that in the absence of  $\text{NaNO}_2$ , powders of typically dendrite structure and average size of approximately  $50 \mu\text{m}$ , are formed on the cathode, i.e. the powder



(b)

**Fig. 7.** EM of Ag-Cu powder, deposited in  $5,0 \text{ g dm}^{-3} \text{ Cu}$ ;  $5,0 \text{ g dm}^{-3} \text{ Ag}$ ;  $40 \text{ g dm}^{-3} \text{ NH}_4\text{NO}_3$ ,  $\text{pH}=9,0$  (A) and in the same composition with  $15 \text{ g dm}^{-3} \text{ NaNO}_2$  (B),  $E = -0,850 \text{ V}$  on Ag-electrode.

dispersity is not sufficiently high (Figure 7a). On the contrary, in the presence of  $\text{NaNO}_2$ , the formed powders are much more finely dispersed (the average size of the particles is approximately  $20 \mu\text{m}$ , more homogeneous in morphological respect (Figure 7b).

## 4. CONCLUSIONS

It was found that the addition of  $\text{NaNO}_2$  to the aminonitrate electrolyte for Ag–Cu alloyed powder deposition through its participation in adsorption and chemical processes on the electrode surface changes significantly the mechanisms of both, the separate deposition and the codeposition of the two metals, which results in formation of more finely dispersed Ag–Cu powder.

## REFERENCES

- 1 Ch. Cheng, T. Arunagiri, O. Chyan, *American Journal of Undergraduate Research*, **2**, Nr 1, (2003).
- 2 D.Pilone and G.H.Kelsall, *Electrochimica Acta*, **51**, 3802, (2006).

- 3 D.L. Deborah and Chung at all, *Materials for Electronic Packaning*, London, UK, Butterworth-Heinemann, (1995).
- 4 K.I. Popov, M.G. Pavlovic, in „Electrodeposition of metal powders with controlled particles grains size and morphology, Modern Aspects of electrochemistry, vol.24, Eds.: B.E.Conway, J.O’M Bockris, R.E.White, Plenum Press, New York, pp. 299-391 (1993).
- 5 K.J. Popov, N.D. Nikolic, M.G. Pavlovic, *J. Serbian Chem. Soc.*, **74**, 397 (2006).
- 6 H.M.A.Solimen, H.H. Abdel-Rahman, *J.Braz. Chem.Soc.*, **17**, 705 (2006).
- 7 K.I. Popov, M.D.Maksimovic, S.K. Zecevic, M.R.Stojic, *Surf. Coat. Technol.*, **27**, 117 (1986).
- 8 M.G.Pavlovic, M.D.Maksimovic, K.I.Popov, M.B.Krsul, *J. Appl. Electrochem.*, **8**, 61 (1978).
- 9 A.T. Kuhn, P. Neufeld, K. Young, *J. Appl. Electrochem.*, **14**, 605 (1984).
- 10 A. Radisic, G.J. Lany, P.M. Hoffman, P.C. Searson, *J. Electrochem. Soc.*, **148**, 41 (2000).
- 11 P. Borthen, J.B. Hwang, H.H. Strechblow, D.M. Koev, *J. Phys. Chem.*, **104**, 5078 (2000).
- 12 D. Grycic, B. Pesic, *Electrochimica Acta*, **50**, 4426 (2005).

- 13 A. Rames, M.M. Hernandez, J. Gonzales, *J. Electrochem. Soc.*, **149**, 390 (2002).
- 14 D. Stoychev, I. Tomov, I. Vitanova, *J. Appl. Electrochem.*, **15**, 878 (1985); *ibid.*, **22**, 978 (1992).
- 15 V.Zh. Lazarov, D.S. Stoychev, *Bulg. Chem. Commun.*, **35**, No1, 65 (2003).
- 16 S. Rashkov, D. Stoychev, L. Mirkova, T. Vitanov, Chr. Naney, *Commun. Dept. Chem., Bulg. Acad. Sci.*, **18**, 152 (1985).
- 17 L.N. Petkov, K.N. Ignatova, *Bulg. Chem. Commun.*, **41**, 39 (2009).
- 18 E.R. Brown, R.F. Large, *Cyclic Voltammetry*, A. Weisberger (Ed.), Wiley Interscience, Part IIA, (1994)
- 19 F. Leicester Hamilton, *Calculations of Analytical Chemistry*, (2008).
- 20 <http://www.saltlakemetals.com/>, Company Information (2010).

## ИЗСЛЕДВАНЕ НА ВЛИЯНИЕТО НА НИТРИТНИ АНИОНИ В АМОНИЯЧЕН ЕЛЕКТРОЛИТ ЗА ОТЛАГАНЕ НА Ag-Cu

К. Игнатова, Д. Стойкова

<sup>1)</sup>Химико-технологичен и металургичен университет, бул. Св. Кл. Охридски, 8, 1756 София

<sup>2)</sup> Монетен двор, София

Постъпила на 16 юни 2010 г.; преработена на 29 октомври, 2010 г.

(Резюме)

С помощта на метода на цикличната хроноволтамперометрия (CV), е изследвано влиянието на нитритните аниони (под формата на  $\text{NaNO}_2$ ) върху кинетиката на самостоятелно и съвместно отлагане на Ag и Cu. Изследван е също и ефекта на природата на електрода (сребро и мед) и съотношението на основните компоненти в разтвора върху кинетиката на отлагане и на прахообразуване на Ag-Cu сплав.

Установено, че в отсъствие на  $\text{NO}_2^-$  йони, среброто се отлага едностадийно, като процесът е напълно обратим. В присъствие на  $\text{NaNO}_2$  в разтвора, етапът на редукция на сребърноамонячните комплекси се предшества от обратима химична реакция на образуване на  $\text{AgNO}_2$ , който се редуцира при по-отрицателни потенциали.

Медта в отсъствие и в присъствие на  $\text{NO}_2^-$  йони се отлага по двустадиен механизъм – непълна редукция на куприамонячните до купроамонячни йони и основният процес на електроотлагане на мед от куприамонячни йони. Като цяло присъствието на  $\text{NO}_2^-$  и намалението на съотношението  $\text{Ag}^+/\text{Cu}^{2+}$  в електролита подтиска електроотлагането на Ag и Cu и има за резултат формиране на по-финодисперсни Ag-Cu сплавни прахове.

## Phosphating of zinc surfaces in zinc-calcium solutions

D.I. Ivanova, L.B. Fachikov\*

University of Chemical Technology and Metallurgy, 8 Kl. Ohridski Blvd, 1756 Sofia, Bulgaria

Received: June 28, 2010; revised: September 21, 2010

This paper exhibits the results, obtained during the examination of the effect of calcium modified zinc phosphating compound on the processes of phosphate film formation on zinc surfaces. By means of gravimetric, chemical, electrochemical, and physical methods the characteristics of the compounds (density, pH, conductivity, total and free acidity) and of the produced coatings (thickness, phase and chemical composition, structure, protective capability) are determined.

It is found that with the increase of the working solution concentrations (5–15 % vol.), the thickness of the phosphate films increases, expressed stronger for the KAF-90 ZK compound; the medium temperature (20, 40, and 60°C) strongly affects the phosphate coating thickness for both phosphating compounds. The coatings, formed at 20°C, have the greatest thickness while the coatings, formed are at 60°C, the thinnest. The phosphate coatings consist of a single phase, the hopeite, and contain mainly the elements of Zn, P, O, a smaller quantity of Ni and traces of Ca for the coatings, produced in KAF-90 ZK solutions. The crystals nucleate from one center and grow spherulite-like. The phosphate coatings have high resistance in 3.5% NaCl. Those, produced in the calcium modified compound, exceed the ones produced in zinc-phosphate solutions.

**Key words:** zinc coatings, phosphating, carbon steels.

### 1. INTRODUCTION

During the past years, the production of zinc coated sheet steels with a lacquer-paint, laid on the surface, and polymer coatings, has considerably expanded. The most important indicator which determines the quality of such coatings is their adhesion to the metal surface. Because the adhesion of these coatings to metal has a physical and mechanical nature, the significance characteristics are the roughness and the surface tension. Therefore, the best preparation before laying organic coatings is to phosphate in such way that will increase 3–4 times the surface roughness and the surface tension. It provides good adhesion to zinc even for materials possessing high surface tension such as the polyethylene, polypropylene, and some others [1–4, 5].

The formation of a phosphate coating is a result of complex corrosion processes and of crystal nucleation and growth, running on the zinc surface. Their speed and interaction determine the crystallization kinetics, the structure and properties of the coating [3].

Compared to  $\text{Cr}^{6+}$ - passivation, phosphating improves the zinc resistance several times [1–3].

The phosphate films are considerably more resistant than the chromate at high temperatures. They ease the deep drawing, stamping, and rolling [4].

Optimum corrosion protection is achieved by phosphating and subsequent painting [3, 7].

The effect of phosphating Zn–Fe alloy coatings on the corrosion resistance is studied in [6]. It is found that the crystal phosphating shows much higher protection in comparison with the amorphous.

This paper presents the results, obtained during examination of the effect of calcium modified zinc phosphating compound on the processes of producing phosphate films on zinc surfaces. Determined are the density, pH, conductivity, and total and free acidity of the phosphating compound. The effect of the phosphating solution concentration and the temperature on the thickness of the formed coatings, their phase and chemical composition, is studied and their structure is characterized.

### 2. EXPERIMENTAL

#### *Materials and samples*

The specimens have the shape of disk (0.001 m<sup>2</sup>) and are made of mild steel sheet (0.17 % C) with thickness of 1.0 mm. The specimens are zinc-

\* To whom all correspondence should be sent:

E-mail: : [fachikov@uctm.edu](mailto:fachikov@uctm.edu)

coated in chloride electrolyte, and the zinc coating thickness is approximately of 12  $\mu\text{m}$ .

The preparation of the specimens prior to the tests covers in succession the following operations: alkaline cleaning, washing, etching, washing, and drying.

### Solutions

The working media are water solutions of the KAF-101 ZT zinc compound as well as of its modified alternative of KAF-90 ZK, where 10 % of the zinc phosphate is replaced by calcium phosphate, and for which the ratio of  $\text{P}_2\text{O}_5 : \text{NO}_3^- = 1:3$  is valid. The working conditions are as follows:

- concentrations: 5.0; 10.0; 15.0 % vol.
- temperatures: 20.0; 40.0; 60.0 °C.
- experiment duration: 5.0; 10.0; 15.0 min.

### Methods of investigation

*The gravimetric method.* This method is used for investigation of phosphate coating formation kinetics in dependence of the effects of various factors. Its essence, it consists of determination of the specimen mass prior to phosphating  $m_1$ , upon formation of the coating  $m_2$ , followed by its removal,  $m_3$ , measured in grams. By the values of  $m_1$ ,  $m_2$ , and  $m_3$ , the mass is calculated or to name it as it is accepted:  $M_1$  is the phosphate coating thickness,  $M_2$  is the dissolved substrate metal quantity, and  $M_3$  is the change of the specimen mass during phosphating [9, 10].

*The X-Ray structural method.* It is used for determination of the phosphate coating phase composition. The investigations are performed using the TUR-M-62 apparatus with source  $\text{CuK}\alpha$  600/1°C.

*EDX.* INCA Energy 350 System, Oxford Instruments made, is used.

*SEM.* The analyses are carried out using the JEOL JSM 6390 microscope.

*The electrochemical method.* Using PAR – 263A the change of the potential with time is measured by exposure of the phosphatized specimens in 3.5 % NaCl.

The preparation of the specimens, the equipment used the investigations, and the methods of work are described in details earlier [9, 10].

## 3. RESULTS AND DISCUSSION

### Characteristics of the phosphating solutions

Table 1 presents the values of the most important parameters such as the density,  $\rho$ ; pH;

conductivity,  $\sigma$ ; total ( $K_o$ ) and free ( $K_c$ ) acidity, which characterize the phosphating compounds. The data, given in the Table 1, exhibit that the densities of the both compounds are very close in value. However, the calcium modified phosphating compound has lower conductivity, higher pH, and possesses significantly lower total and free acidity.

**Table 1.** Characteristics of the phosphating compounds

Characteristic, compound	$\rho$ , $\text{g/cm}^3$	pH	$\sigma$ , $\text{mS/cm}$	$K_o$	$K_c$
KAF-90 ZK	1.330	1.08	163.7	280	32
KAF-101 ZT	1.335	1.00	168.7	320	40

### Gravimetric studies

These investigations determined the effect of the working solution concentration, the temperature, and the duration of the phosphating process on the thickness/mass of the produced coatings ( $M_1$ ), the quantity of the dissolved substrate metal ( $M_2$ ), and the change of the specimen masses ( $M_3$ ).

The parameters of concentrations (5, 10 and 15 % vol.) and temperatures (20, 40, 60 °C) are defined experimentally, criteria for their selection being the production of a uniform and dense phosphate film on the surface of the zinc coated specimens as well as the stability of the working solutions.

Figures 1 and 2 show the typical correlations of ‘thickness/mass of the coatings – time’, obtained at different concentrations and temperatures of the working solutions. It follows from the movement of the curves, in regards to the both examined phosphating solutions, that coating of greatest thickness is formed at the shortest time of specimen exposure to the working medium, i.e. 5 min. In case of a longer stay, the phosphate film mass/ thickness decreases or retains comparatively constant. All this shows that the phosphate coatings on the zinc surface form quickly (up to 5 min) after which their reorganization follows: interaction (exchange) with the components in the solution, resulting in compaction of the coatings and decrease in their mass. An exception of the observed regularity is the change of the specimens, obtained at 20°C, for all the examined concentrations of the KAF-90 ZK product. That is probably related to the known in the literature effect of the calcium ions on the crystal nucleation and growth during phosphating in zinc compounds, particularly at low solution temperatures [1, 4].

Fig. 1 and 2 show that with the increase of solution concentration, the phosphate film thickness

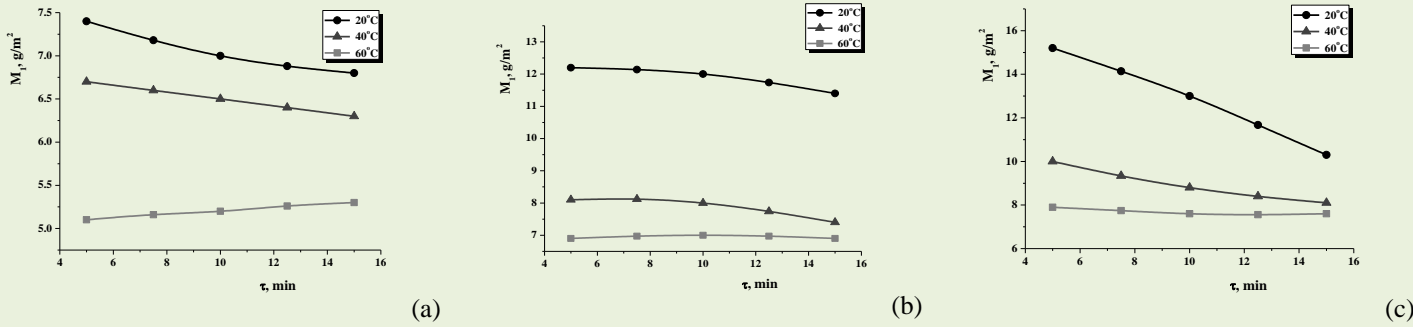


**Fig. 1.** Effect of the phosphating time,  $\tau$  on the thickness/ mass of the produced phosphate coating,  $M_1$ : a – 5 %; b – 10 %; c – 15 % (vol). (KAF-101 ZT)

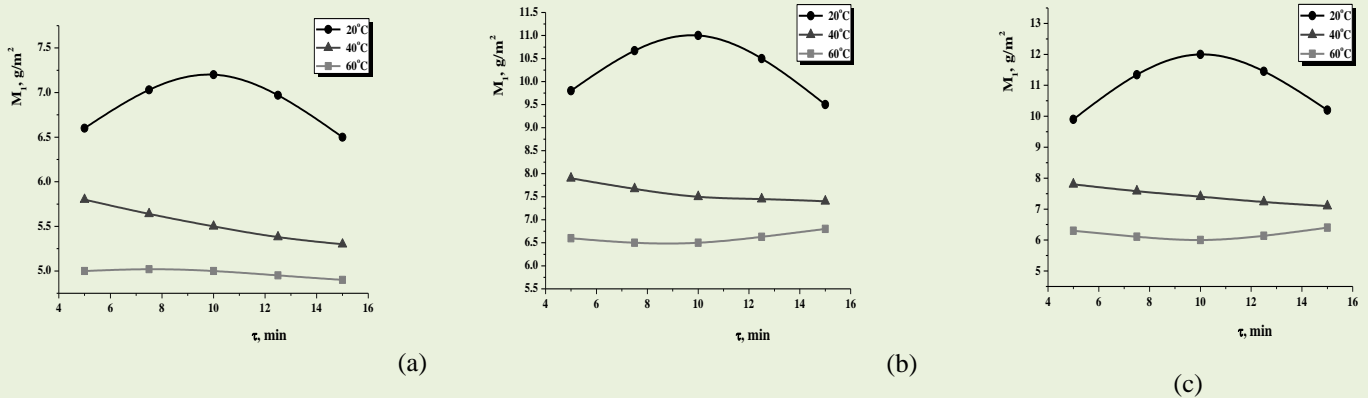


**Fig. 2.** Effect of the phosphating time,  $\tau$  on the thickness/ mass of the produced phosphate coating,  $M_1$ : a – 5 %; b – 10 %; c – 15 % vol. (KAF-90 ZK)

grows in both phosphating solutions, being the greatest at 20°C, and the smallest at 60°C. The presence of calcium ions (KAF-90 ZK) in the phosphating solution leads to the formation of thinner coatings, compared to those, formed in the pure zinc phosphating bath.

The visual observation (x 10) of the phosphatized zinc surfaces shows that with the temperature increase the uniformity and density of the coatings, formed in both phosphating solutions, increase.

The measurement of the mass ( $M_2$ ) of the dissolved substrate metal (Zn) in the process of phosphate coating production shows that this mass increases with the time and with increase in the working solution concentrations, which should be expected from the phosphating process mechanism. Besides the close values of  $M_2$ , obtained in zinc surface phosphating, it is also found that  $M_2$  decreases with the temperature increase in both phosphating baths under other similar conditions. The above observation is an indication for a faster and more economical formation of phosphate films by increasing the temperature of the working solutions.

#### X-ray phase analysis

The results of the X-ray phase analysis, unless KAF-90 ZK is calcium modified, show the presence only of *Hopeite*,  $(Zn_3(PO_4)_2 \cdot 4H_2O)$  and *zinc* in the formed phosphate coatings.

#### EDX – analysis

The EDX-analysis is performed on phosphatized specimens for both phosphating products at 60°C, in 15% vol. solutions, for 10 minutes (Fig. 3 and Fig. 4).

Determined by this analysis, the basic elements, contained in the coatings are Zn, P, O, and smaller quantity of Ni. The latter is contained in the solutions as an accelerator. The Ca contents in the phosphate coatings, formed in the solutions of KAF-90 ZK, are in the limit of error.

#### Electron microscope examinations

Fig. 5 shows photomicrography (SEM) of the phosphate coatings, formed on zinc coated specimens in the product solutions: (a) KAF - 101 ZT, and (b) KAF – 90 ZK, at a concentration of 15 % vol, for 10 minutes, and a temperature of 60°C.

It follows from the figure that the habitus of the coatings is permanent. The crystals form out from a

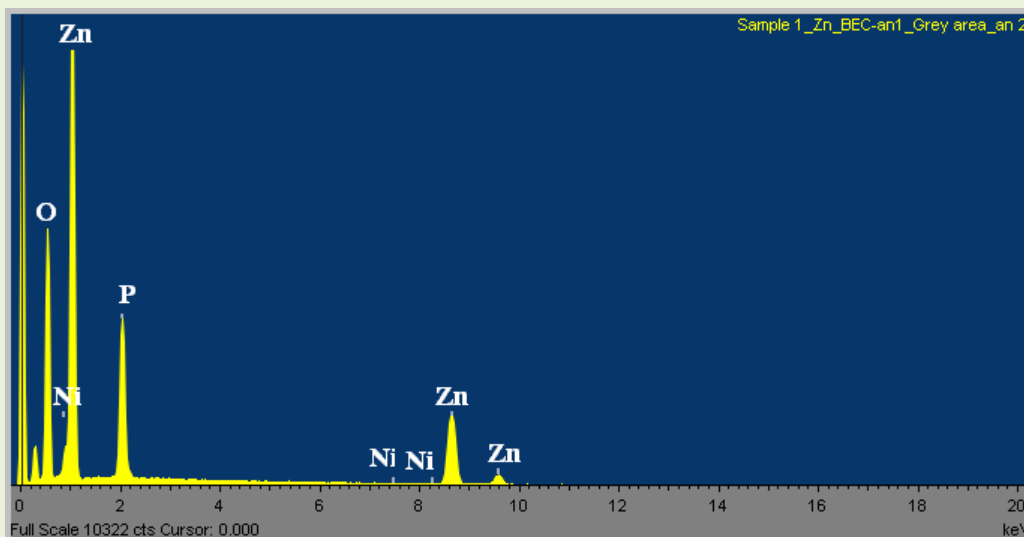


Fig.3. EDX – analysis of phosphate coatings formed in solutions of KAF-101 ZT.

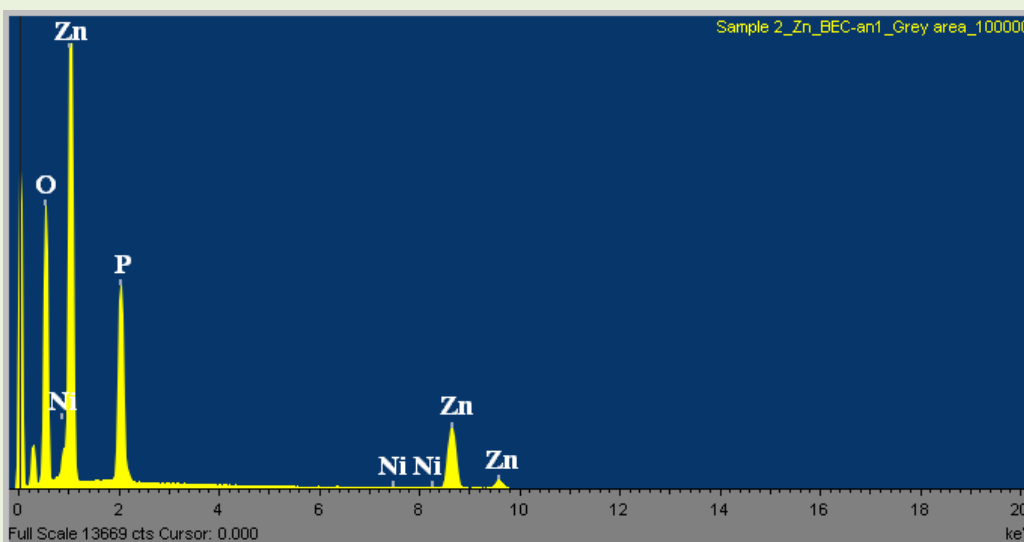


Fig.4. EDX – analysis of phosphate coatings formed in solutions of KAF-90 ZK.

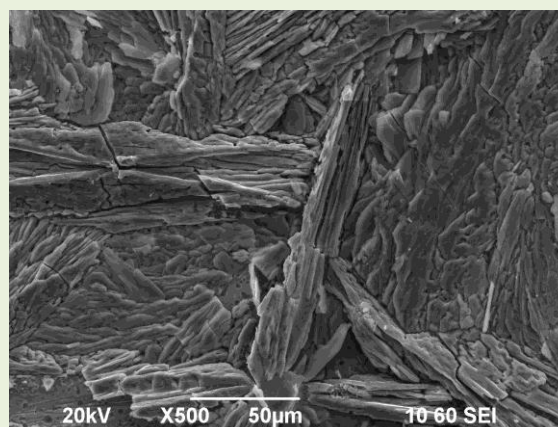
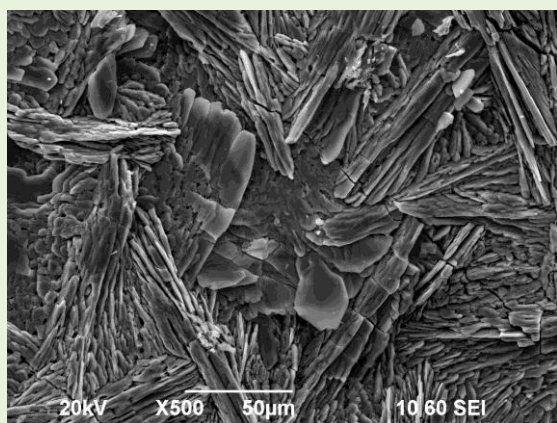


Fig. 5. Microphotography of phosphate coatings: a - KAF-101 ZT; b - KAF-90 ZK

single center and grow spherulite-like. Cracks are observed in the phosphate films of both

compounds. The crystal sizes are between 0.2 and 100 µm. The presence of more expressed and of

larger dimensions ‘leaf-like’ shapes of some of the crystallites, formed in the KAF-101ZT, could be pointed out as a more distinctive difference between the coatings.

#### Corrosion tests

The corrosion resistance, and the protective capability of the phosphate coatings, respectively (concentration of 15% vol., for 10 minutes at 60 °C), is determined in a 3.5% NaCl. The test is made by dipping the phosphatized specimens in NaCl. The coating is considered resistant and completely stable if there are no changes on the surface or coloring of the solution for two hours. This test also measures the corrosion potential of the specimens (Fig. 6) and the change of a non-phosphatized specimen potential is shown for a comparison.

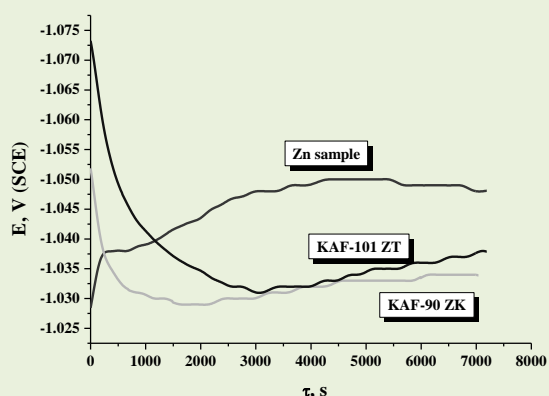


**Fig.6.** Dependence “potential, E – time,  $\tau$ ”, during exposure of phosphatized specimens in 3.5% NaCl, 20±2°C.

The figure shows that the non-phosphatized specimen potential shifts to a negative direction, and becomes stationary after 50 min in a value of about –1050 mV (SCE). This evidences that the zinc surface activates in the working medium in the very beginning of the process.

The potentials of the phosphatized surfaces, produced in both of the phosphating products (KAF-101 ZT and KAF-90 ZK), shift sharply to a positive direction immediately upon dipping into the corrosion medium (expressed stronger for KAF-90 ZK), and they become practically equal after approximately 50 min for KAF-101 ZT, and 20 min for KAF-90 ZK. The shift of the potentials to a positive direction, most probably, is due to filling of the pores in the coatings with corrosion compounds.

#### 4. CONCLUSIONS

The results, presented in this paper, suggest the following general conclusions:

- With increase of the concentration of the working solutions (5–15% vol.), the phosphate film thickness increases, expressed stronger for the KAF-90 ZK. Coatings of the greatest mass/thickness are formed within the shortest time of specimen exposure to the solutions, i.e. 5 min for all examined concentrations;

- The temperature of the medium (20, 40, and 60 °C) strongly affects the phosphate coating thickness for both phosphating products. The greatest thicknesses are formed at 20° C, and the thinnest at 60 °C.

- The mass of the phosphate coatings, produced in the both phosphating compounds, is greater in all specimen exposure times to the working solutions, than the mass of the dissolved zinc.

- The phosphate coatings consist of a hopeite single phase, and contain mainly the elements of Zn, P, O, smaller quantity of Ni, and traces of Ca, for the coatings formed in the solutions of KAF-90 ZK.

- The crystals nucleate from one center, and grow spherulite-like. The presence of more expressed and larger ‘leaf-like’ shapes of part of the crystallites, formed in the KAF-101 ZT, could be pointed out as a more important difference.

The phosphate coatings are of higher resistance to a 3.5% NaCl. Those, formed in the calcium modified product, have higher resistance than those produced in zinc-phosphate solutions.

#### REFERENCES

1. I.I. Khain, “Theory and Practice of Phosphating of Metals” (in Russian), Khimia, Leningrad, (1973).
2. G. Lorin, “Phosphating of Metals”, *Finishing Publications*, Teddington, UK, (1974).
3. D.B. Freeman., *Phosphating and Metal Pre-treatment*, Woodhead – Faulkner, Cambridge, (1986).
4. W. Rausch, “The Phosphating of Metals”, ASM International, Metals Park and Finishing Publications, Teddington, (1990).
5. E. Breval, M. Rachlity, *J. Mater.Sci.*, **28**, 1835 (1988).
6. M. Gladkovas, V. Burokas, A. Martušienė, D. Bučinskiene, *Chemija (Vilnius)*, **12**, 114 (2001).
7. T. Sugama, T. Takahashi, *J. Mater. Sci.*, **3**, 809 (1995).
8. H.A. Ponte, A.M. Maul, E.A. Alvarenga, *Materials Research*, **5**, 439 (2002).
9. D. Ivanova, L. Fachikov, *J. UCTM*, Sofia, **42**, 159 (2007).
10. L. Fachikov, D. Ivanova, D. Dimov, *J. UCTM*, **41**, 15 (2006).

## ФОСФАТИРАНЕ НА ЦИНКОВИ ПОВЪРХНОСТИ В ЦИНК-КАЛЦИЕВИ ПРЕПАРАТИ

Д. Иванова, Л. Фачиков

*Химикотехнологичен и металургичен университет, 1756 София, бул. "Кл. Охридски"8, България*

Постъпила на 28 юни, 2010 г.; преработена на 21 септември, 2010 г.

(Резюме)

В представената работа са показани резултатите, получени при изследване влиянието на модифициран с калций цинков фосфатиращ препарат, върху процесите на получаване на фосфатни филми върху цинкови повърхности. Посредством гравиметричен, химичен, електрохимични и физични методи са определени характеристиките на препаратите (плътност, рН, проводимост, обща и свободна киселинност) и на получаваните покрития (дебелина, фазов и химичен състав, структура, защитна способност).

Установено е, че с увеличаване на концентрацията (5-15%) на работните разтвори, дебелината на фосфатните филми нараства, по-силно изразено за препарата КАФ-90ЦК; температурата на средата (20, 40 и 60° С) оказва силно влияние върху дебелината на фосфатните покрития и за двата фосфатиращи препарата. С най-голяма дебелина са покритията получени при 20° С, а най-тънки - при 60° С; фосфатните покрития се състоят от една фаза: хопеит и съдържат главно елементите Zn, P, O, в по-малко количество Ni и следи от Ca, за покритията получени в разтвори на КАФ-90ЦК; кристалите се зараждат от един център и нарастват сферолитоподобно. Фосфатните покрития са с висока устойчивост в 3.5% NaCl като тези, получени в модифицирания с калций препарат, превъзхождат получените в цинково-фосфатните разтвори .

## Electrodeposition of molybdenum oxides from weakly alkaline ammonia-molybdate electrolytes

M.L. Petrova\*, M.S. Bojinov, I.H. Gadjov

University of Chemical Technology and Metallurgy 8 Kl. Ohridski Blvd., 1756 Sofia, Bulgaria

Received June 21, 2010; revised September 29, 2010

Electrochemical deposition is a promising method for the production of thin and dense MoO<sub>x</sub> coatings, employed as catalysts, selective solar absorbers and gas sensors. This work aims to investigate the processes of electrodeposition of molybdenum oxides from alkaline baths and to characterize their chemical composition, electrical and electrochemical properties. For the purpose, Mo oxides were deposited galvanostatically on Al substrates, coated by Zn to improve coating adhesion. The chemical composition of the molybdenum oxide surfaces was characterized by X-ray photoelectron spectroscopy (XPS). The stoichiometry of the oxide surfaces, their degree of hydroxylation, and the atomic O/Mo ratio were estimated. The electrical and electrochemical properties of the obtained oxides were characterized by voltammetry and electrochemical impedance spectra in a borate buffer solution. Tentative conclusions on the influence of the deposition current density and the pH of the electrolyte on the composition, electrical and electrochemical properties of the oxides are drawn on the basis of the obtained results.

**Keywords:** cathodic deposition, molybdenum oxides, alkaline electrolytes, electrochemical impedance spectroscopy

### INTRODUCTION

Electric, photoelectric, and electrochemical properties of molybdenum oxides are of primary significance for a number of important technical applications in such materials as catalysts, selective solar absorbers, and gas sensors [1 – 3]. One of the promising methods to produce molybdenum oxides with optimal properties is their cathodic deposition. Electrodeposition of Mo oxides from acidic electrolytes has been widely investigated [4 – 9], whereas data concerning such deposition from neutral and alkaline media remains relatively scarce [10 – 13]. Alkaline electrolytes are supposed to enable stabilization of molybdenum oxides of mixed valency. This work aims to investigate the processes of electrodeposition of mixed-valency molybdenum oxides from alkaline baths and to characterize their chemical composition, electrical and electrochemical properties.

### EXPERIMENTAL METHODS

Mo oxides were deposited on Al substrates (99.99%, working area of 8 cm<sup>2</sup>), chemically coated by Zn to improve the adhesion of the films. A conventional three-electrode cell was used with a platinum mesh as a counter electrode, located symmetrically around the working electrode, and a Ag/AgCl/3M KCl electrode as a reference ( $E =$

0.201 V vs. SHE). The pH of the electrolytes (8-10) was adjusted by using an NH<sub>3</sub>-CH<sub>3</sub>COONH<sub>4</sub> buffer, the electroactive salt being (NH<sub>4</sub>)<sub>6</sub>Mo<sub>7</sub>O<sub>24</sub>·4H<sub>2</sub>O (20 g l<sup>-1</sup>). Electrodeposition was conducted in a galvanostatic regime at a room temperature (22±2 °C). The range of current densities was between 0.05 and 0.4 A dm<sup>-2</sup>. The current efficiency of film formation was estimated by a gravimetric method. Steady-state current-potential curves and electrochemical impedance spectra (frequency range of 0.01 Hz – 10 kHz, a.c. amplitude of 10 mV rms) were measured by an Autolab PGSTAT 30/FRA2 apparatus, driven by GPES and FRA software (Eco Chemie, Netherlands). The chemical composition of the obtained molybdenum oxide surfaces was characterized by X-ray photoelectron spectroscopy (XPS). An Escalab II spectrometer with a monochromated Al K $\alpha$  radiation (1486.6 eV) was used. The analyser pass energy was 100 eV for the survey spectra and 20 eV for the high resolution spectra, the photoelectron take-off angle being 90°.

### RESULTS AND DISCUSSION

The dependence of the coating weight on the current density in electrolytes with pH 8-10 is presented in Fig.1. The deposition was conducted up to a constant charge of  $Q = 240 \text{ C dm}^2$ . The weight of the coating decreases about 2.5 times with the increase in the current density of the pH 10 electrolyte. On the other hand, the reduction of

\*To whom all correspondence should be sent:

E-mail: manon@abv.bg

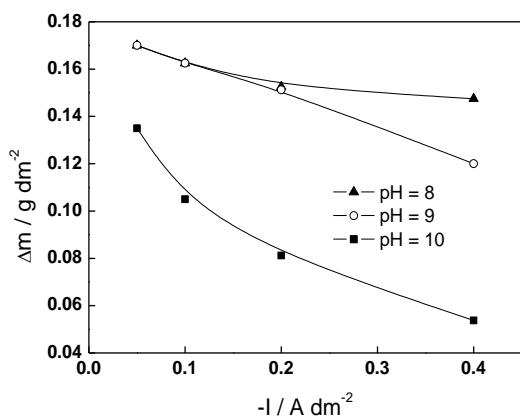


**Fig. 1** Dependence of the mass of the coating on current density in electrolytes with different pH.

weight in the pH 9 solution is from 0.17 to 0.12 g dm<sup>-2</sup>, being even smaller in the pH 8 electrolyte. The influence of the deposition current density on the weight of the coatings can be explained by the occurrence of two parallel reactions, the molybdenum oxide formation and the hydrogen evolution. It can be concluded that the highest current efficiency is achieved in the pH 8 electrolyte at current densities of 0.05 – 0.2 A dm<sup>-2</sup>.

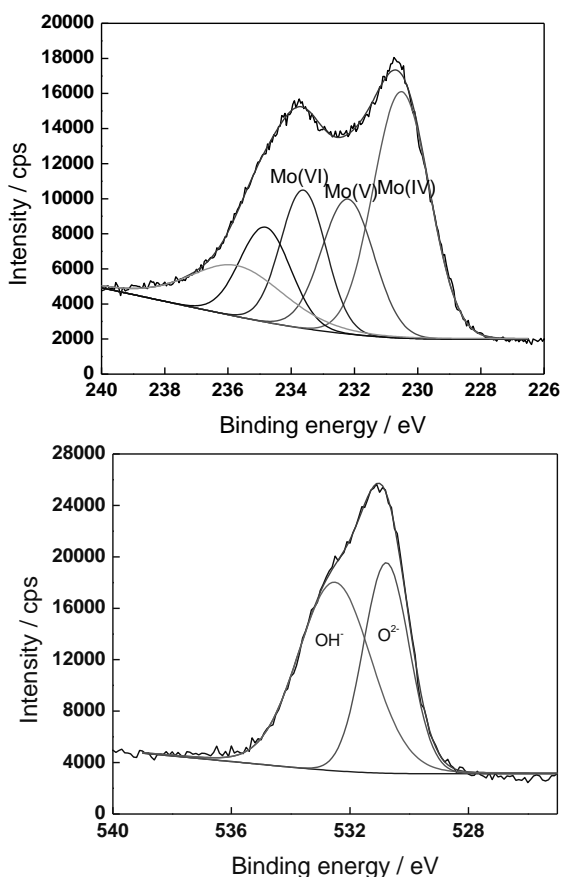


**Fig. 2** Detailed Mo3d and O1s XPS spectra at surface of the film formed by cathodic deposition in a pH 8 electrolyte.

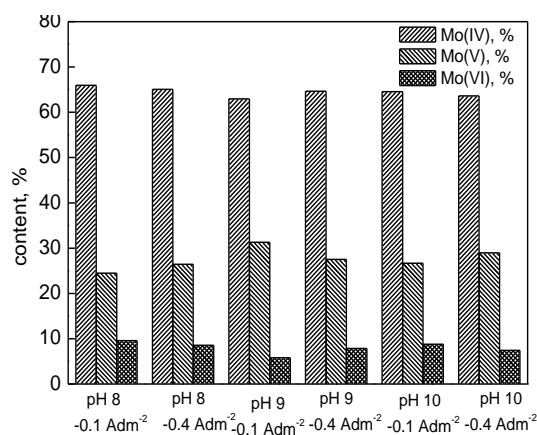


**Fig. 3** Distribution of the valence states of Mo as depending on electrolyte pH and current density.

The chemical composition of the obtained molybdenum oxide surfaces was characterized by X-ray photoelectron spectroscopy (XPS). As an example, the Mo3d and O1s spectra for oxides, formed in an electrolyte with pH 8 at current density of -0.1 A dm<sup>-2</sup>, are shown in Fig. 2. The results indicate the formation of mixed valency oxides, containing Mo (IV), Mo (V), and Mo (VI).

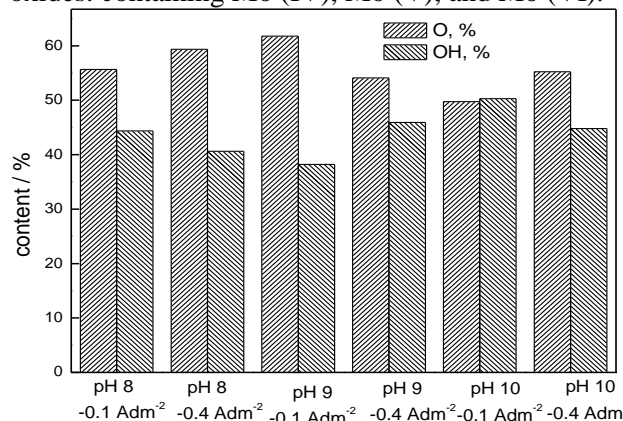


**Fig. 4** Percentages of oxygen bound as oxide and hydroxide as depending on pH and current density.

The surface fractions of Mo different valency states for films, obtained in all the studied electrolytes, are summarized in Fig. 3. The films consist mainly of Mo (IV) (65%) and Mo (V) (25–30%). The proportion of the valency states of Mo in the film was not found to depend neither on the pH nor on the current density within the experimental error.

The surface concentrations of oxygen, bound as oxide and hydroxide and calculated from the O1s spectra for the three electrolytes are presented in Fig. 4 as a function of the deposition current density. The presence of a significant amount of hydroxide (40%) for the films, formed in the three electrolytes, is an indication for a hydroxylated surface. The films, formed in the electrolyte of pH

8 at both current densities, and the film, formed in the solution of pH 9 at the lower current density, are less hydroxylated than those, formed in the pH 10 solution. The values of the O / Mo ratio vary between 2.5 and 3.2, which is another indication that the Mo in the surface film has a mixed valence. In general, the surface film can be denoted as  $\text{MoO}_x(\text{OH})_y$  in accordance with the hypotheses of other authors [14].

The electrochemical stability of the obtained oxides with respect to oxidation was characterized by measuring the steady-state current vs. the potential curves in an inert borate buffer solution (pH 7.3). The current vs. the potential curves of  $\text{MoO}_x(\text{OH})_y$ , deposited at a current density of  $0.2 \text{ A dm}^{-2}$ , are presented in Fig.5. The open circuit potential (OCP) of  $\text{MoO}_x(\text{OH})_y$  electrode depends slightly on the pH of the film formation and is located in the range of  $-0.87/-0.85 \text{ V}$ .

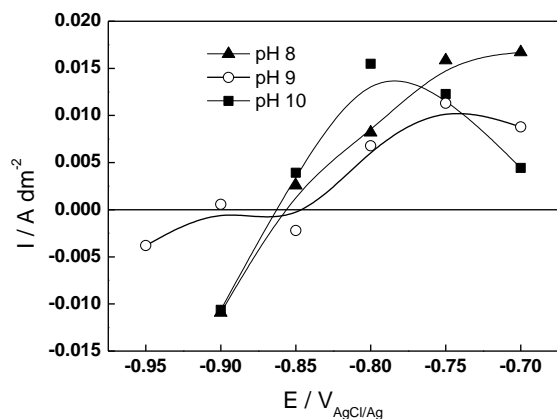


**Fig. 5** Current - potential curves of molybdenum oxides in a pH 7.3 borate buffer as dependence on the pH of the deposition electrolyte at a current density  $0.2 \text{ A dm}^{-2}$ .

At potentials less negative than the OCP, the current density reaches a maximum. This maximum is observed at the potential which is more negative. It is more negative at higher pH values of the forming electrolyte. The current-potential curves in this area are similar due to the oxidation of Mo(IV) in the film to a higher valency.

Fig. 6 shows the impedance spectra of  $\text{MoO}_x(\text{OH})_y$  films, obtained in the studied electrolytes at different current densities, measured at the rest potential in a pH 7.3 borate buffer. The values of the impedance magnitude at low frequencies are in the range of  $20-100 \text{ } \Omega\text{cm}^2$ , i.e. the films are fairly ionically conductive, and the impedance spectra are most likely dominated by the processes at the film/electrolyte interface. The impedance diagrams do not significantly depend on either the deposition current density or on the pH of the electrolyte, in

accordance with the fact that the films have almost identical chemical composition.

Two to three time constants are observed in the impedance spectra, the corresponding semicircles in the impedance plane being significantly depressed. This feature can be taken as an

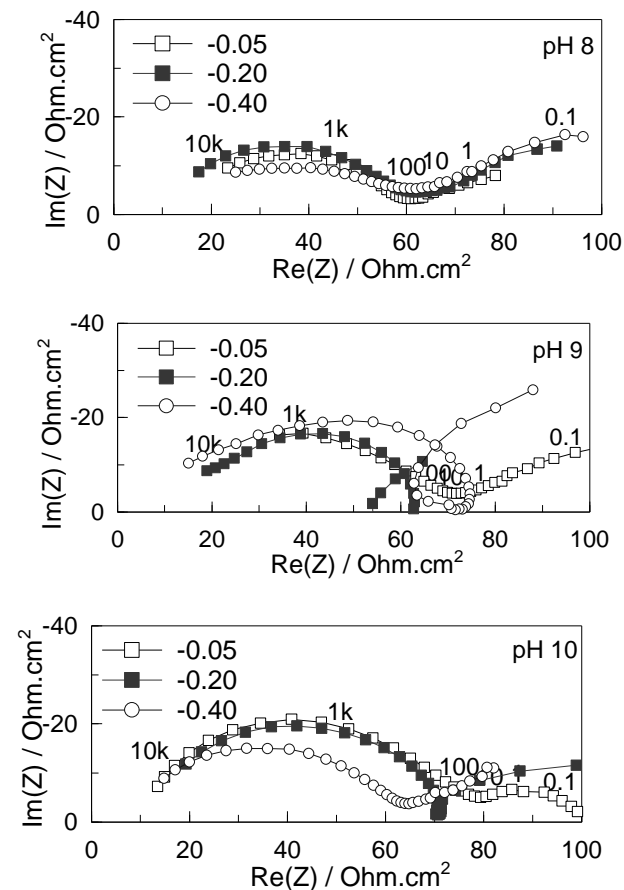


**Fig. 6** Impedance spectra of  $\text{MoO}_x(\text{OH})_y$  in a pH 7.3 borate buffer at open circuit as depending on the pH of the deposition electrolyte at different current densities ( $\text{A dm}^{-2}$ ).

indication for the geometric and/or energetic heterogeneity of the film/solution interface. The processes that take place in an open circuit in an inert electrolyte can be interpreted, due to the oxidation of Mo (IV), to higher valencies coupled with water reduction. Initial estimates of the capacitance of the film from the high-frequency semicircles indicate the presence of a thin layer with semiconductor properties [14, 15]. At lower frequencies, transport impedance is detected, most probably due to the transfer of protons and electrons through the mixed-conducting oxide.

## CONCLUSIONS

Cathodic electrodeposition of molybdenum oxides on Zn-coated Al from alkaline electrolytes with different pH and current densities was studied in this work. The electrochemical stability of the

obtained oxides was characterized by voltammetry and electrochemical impedance spectroscopy in a plain borate buffer solution. The chemical composition of the obtained molybdenum oxide surfaces was assessed by X-ray photoelectron spectroscopy (XPS). The following main conclusions can be drawn from the obtained results:

- The charge efficiency for cathodic deposition of molybdenum oxide from alkaline heptamolybdate baths is the highest at pH 8. The effect of the deposition current density on the charge efficiency is accordingly the smallest in electrolytes with this pH value.
- The cathodic deposit can be described as a layer with a good electronic and ionic conductivity and of typical composition of  $\text{MoO}_x(\text{OH})_y$ .
- The electrodeposition regime (pH of the electrolyte and current density) does not influence substantially neither the composition of the coating nor its electric properties.
- To clarify the mechanism of modification of oxides during anodic polarization, additional studies in a wider range of potentials, combined with the determination of the surface chemical composition, are needed.

**Acknowledgement:** *The funding of this work by the National Science Fund, Bulgarian Ministry of Education and Science, under contract VYX-307 / 2007 is gratefully acknowledged.*

## REFERENCES

1. T. He, J. Yao, *J. Photochem. Photobiol. C: Photochem. Rev.*, **4**, 125 (2003).
2. H. M. Pathan, S.-Ki Min, K.-D. Jung, O.-S. Joo, *Electrochem. Commun.*, **8**, 273 (2006).
3. L. Tian, L. Liu, L. Chen, N. Lu, H. Xu, *Sens. Act. B*, **105**, 484 (2005).
4. C. G. da Silva, I. C. P. Margarit-Mattos, O. R. Mattos, H. Perrot, B. Tribollet, V. Vivier, *Corros. Sci.*, **51**, 151 (2009).
5. E. Gómez, E. Pellicer, M. Duch, J. Esteve, E. Vallés, *Electrochim. Acta*, **51**, 3214 (2006).
6. R. Banica, P. Barvinschi, N. Vaszilcsin, T. Nyari, *J. Alloys Compd.*, **483** (2009) 402.
7. L. S. Sanches, C. B. Marino, L. H. Mascaro, *J. Alloys Compd.*, **439**, 342 (2007).
8. S. Dong, B. Wang, *J. Electroanal. Chem.*, **370**, 141 (1994).
9. E. Gómez, E. Pellicer, E. Vallés, *J. Electroanal. Chem.*, **580**, 222 (2005).
10. L. C. Sanches, C. B. Marino, L. H. Mascaro, *J. Alloys Compd.*, **439**, 342 (2007).
11. S. Liu, Q. Zhang, E. Wang, S. Dong, *Electrochem. Commun.*, **1**, 365 (1999).
12. V. V. Kuznetsov, M. R. Pavlov, D. I. Zimakov, S. A. Chepeleva, V. N. Kudryavtsev, *Russ. J. Electrochem.*, **40**, 711 (2004).
13. F. Wang, B. Lu, *Physica B*, **404**, 1901 (2009).
14. R. S. Patil, M.D. Uplane, P.S. Patil, *Appl. Surf. Sci.*, **252**, 8050 (2006).
15. F. Jahan, B. E. Smith, *Solar Energy Mater.*, **20.**, 215 (1990).

## ЕЛЕКТРОХИМИЧНО ОТЛАГАНЕ НА МОЛИБДЕНОВИ ОКСИДИ ИЗ СЛАБО АЛКАЛНИ ЕЛЕКТРОЛИТИ, СЪДЪРЖАЩИ АМОНИЕВ МОЛИБДАТ

М.Л. Петрова\*, М.С. Божинов, И.Х. Гаджов

*Химико-технологичен и металургичен университет, бул. Св. Климент Охридски, 1756 София*

Постъпила на 21 юни, 2010 г.; преработена на 29 септември, 2010 г.

(Резюме)

Електрохимичното отлагане е един от най-обещаващите методи за получаване на тънки и плътни  $\text{MoO}_x$  покрития, които намират приложение като катализатори, селективни слънчеви абсорбери и газови сензори. Настоящата работа има за цел да изследва процесите на електроотлагане на молибденови оксиди от алкални електролити, както и да характеризира техния химичен състав, електрични и електрохимични свойства. За целта, молибденови оксиди са отлагани галваностатично върху алуминиеви субстрати, покрити с контактно отложен Zn за подобряване на адхезията. Химичният състав на получените молибденово-оксидни повърхности е характеризирани чрез рентгенова фотоелектронна спектроскопия (XPS). Определени са стехиометрията на оксидните повърхности, тяхната степен на хидроксилиране и съотношението O/Mo. Електричните и електрохимични свойства на филмите са изследвани чрез волтамметрия и електрохимична импедансна спектроскопия в боратен буферен разтвор. На базата на получените резултати са направени предварителни заключения за влиянието на плътността на тока и pH на електролита върху химичния състав, електричните и електрохимични свойства на оксидите.

## Ni/Re-Co as electrocatalytic material for hydrogen evolution reaction in alkaline solution

V. P. Pashova<sup>1\*</sup>, L. G. Mirkova<sup>1</sup>, M. H. Monev<sup>1</sup>, P. Nowak<sup>2</sup>, G. Nawrat<sup>3</sup>

<sup>1</sup>Rostislav Kaischew Institute of Physical Chemistry, Bulgarian Academy of Sciences, Acad. G. Bonchev St., Building 11, Sofia 1113, Bulgaria

<sup>2</sup>Institute of Catalysis and Surface Chemistry, Polish Academy of Sciences, № 8 Niezapminajek St, Krakow 30239, Poland

<sup>3</sup>Silesian University of Technology, Department of Inorganic Chemistry, Technology and Fuels, Gliwice, Poland

Received July 6, 2010; Accepted August 7, 2010

The electrochemical behaviour of two modified electrodes, Ni/Re<sub>87</sub>-Co<sub>7</sub> and Ni/Re<sub>57</sub>-Co<sub>37</sub> (electrodeposited Ni, covered with a thin layer of electrodeposited Re-Co alloy), was studied with respect to the hydrogen evolution reaction (HER) in a 6 M KOH solution. The data are compared with those of the pure Ni electrode. Cyclic voltammetry, polarization measurements at various current densities, and the electrochemical permeation technique of Devanathan-Stachurski were used. Kinetics parameters of HER were determined on the basis of the Tafel plots. The diffusion coefficient of permeating hydrogen and the hydrogen concentration in the electrode subsurface were calculated on the basis of permeation transients. Both modified electrodes show significantly higher values of hydrogen evolution rate and exchanged current density than those of the pure Ni electrode. The values of HER overpotential on both modified electrodes are similar, and most important is that they are much lower than the HER overpotential value on the pure Ni electrode. The hydrogen permeation data are in accordance with the voltammetric measurements. Ni electrode, modified by alloy with a lower Re content (Ni/Re<sub>57</sub>-Co<sub>37</sub>), shows best electrocatalytic properties with regards to HER.

**Key words:** electrodeposition, rhenium alloy, hydrogen evolution reaction, alkaline water electrolysis

### INTRODUCTION

Hydrogen with a high purity is produced through water electrolysis, where Ni electrodes are usually employed. However, the high energy consumption is an essential disadvantage of this process. The problem can be solved by decreasing the overpotential of the cathodic and/or anodic reaction, either by an increase of the catalytic activity of the electrode or by an increase of its active surface.

The use of new materials on the base of Ni, for example alloys, is a possible way to decrease the HER overpotential. In this respect, the Ni-Co [1] and Ni-Re-Co [2] alloys are found to be effective.

The modification of Ni electrode surface with a thin layer of alloys of Co and Re could be another way for improvement of the properties of the Ni electrode. It has been found recently that HER on Ni/Re<sub>87</sub>-Co<sub>7</sub> electrode (electrodeposited Ni, covered with a thin layer of electrodeposited Re-Co alloy with a relatively high content of Re), runs at a considerably lower overpotential in 6 M KOH

solution, compared to the pure Ni electrode [3]. Due to the high price of Re, the decrease of the amount of Re in the alloy is of great importance.

The purpose of this study is directed towards obtaining and characterization of new Ni/Re-Co electrodes with a low content of Re with respect to HER.

### EXPERIMENTAL

Two types of working electrodes were obtained by electrodeposition of Re-Co alloy on one side of the electrodeposited Ni foil with a thickness of 90 μm, Ni/Re-Co with a high and with a low content of Re. For comparison, a pure Ni foil was also subjected to investigations.

The element composition of the electrodes, before and after electrochemical measurements, was determined by Energy Dispersive X-ray analysis (EDX) (JCSA 733 Jeol, Japan). The morphology of the samples was observed before and after the electrochemical measurements by Scanning Electron Microscopy (SEM) (JSM 5300, Jeol, Japan).

The electrochemical measurements were carried out in a three-electrode cell, equipped with Pt-counter electrode and Hg/HgO reference electrode.

\* To whom all correspondence should be sent:  
E-mail: : [vpashova@ipc.bas.bg](mailto:vpashova@ipc.bas.bg)

6 M KOH aqueous solution (analytical reagent grade) was used at a room temperature. Kinetic parameters of HER were evaluated on the basis of galvanostatic measurements at various current densities. The cyclic voltammetric dependences were obtained by scanning the potential beginning from the open circuit potential to the vertex potential in the cathodic direction, and to 800 mV in the anodic direction with a scan rate of 25 mV/s. All experiments were performed by using a potentiostat/galvanostat model of 263A (EG&G Princeton Applied Research, USA).

It was worth to investigate not only the hydrogen evolution but also the ability of the electrodes to absorb hydrogen, as well as the process of hydrogen diffusion. For this purpose, the Devanathan-Stachurski permeation technique was used [4]. The Ni/Re-Co electrode was mounted as a membrane in the cell. A thin Pd layer was electrodeposited in advance on the exit side of the membrane. Hydrogen was generated electrochemically on the entry (cathodic) side of the membrane under a galvanostatic control at  $I_1=10 \text{ mA/cm}^2$  in 6M KOH solution. 0.5 M NaOH solution was introduced into the ionization cell and 280 mV (Hg/HgO) potential was applied there. Both cells were equipped with a platinum grid as a counter electrode. At the constant positive potential, kept on the exit side of the membrane, all the hydrogen diffusing through the membrane and reaching the exit side of the membrane was oxidized. The ionization current, recorded under these conditions, was a direct measure of the hydrogen permeation rate ( $I_2$ ). The permeation current was recorded against time (transient) until reaching a steady state ( $I_2^{\text{st}}$ ). The  $I_2/I_1$  relation gives the value of the permeation efficiency ( $I_{pe}$ ). The values of the diffusion coefficient ( $D$ ) and the concentration ( $C_0$ ) of the hydrogen, absorbed into the first atomic layers of the electrode, were calculated by the equations, given in [5].

## RESULTS

According to the EDX analysis, the content of both electrode systems is nearly as follows: Ni/Re<sub>87</sub>-Co<sub>7</sub> and Ni/Re<sub>57</sub>-Co<sub>37</sub>. The remaining part to 100 % is oxygen.

The SEM images in Fig. 1 present the difference in the morphology of the pure Ni electrode and both Ni/Re-Co electrodes.

Pure Ni foil is characterized with a pyramidal structure, while both Ni/Re-Co electrodes show more grained structure than that of the pure Ni, which means more developed surface. The comparison between both Ni/Re-Co electrodes reveals that the Ni/Re<sub>57</sub>-Co<sub>37</sub> electrode has more developed surface than the Ni/Re<sub>87</sub>-Co<sub>7</sub> electrode. The CV curves of both modified Ni/Re-Co electrodes show a higher rate of HER, as well as a larger maximum of hydrogen desorption, compared to those of the pure Ni electrode, the effect being more evident at the electrode with a lower content of Re (Ni/Re<sub>57</sub>-Co<sub>37</sub>) (Fig. 2).

The positive effect of the modifying layer towards HER can be related with more developed surface of the double-layered electrodes, as well as with their higher catalytic activity.

Kinetics parameters of HER on the tested electrodes were evaluated on the basis of the Tafel plots (Fig.3).

Two different slopes are observed: first slope at a lower c.d. than 50 mA/cm<sup>2</sup> and second slope at a higher c.d. than 50 mA/cm<sup>2</sup>. The corresponding values of the main parameters, characterizing HER, are given in Table 1.

It could be concluded, based on the data, that the limiting stages of HER for the three electrodes are different in the first slope range. The Volmer mechanism is valid for the pure Ni electrode according to the values of  $b$  (118 mV/dec) and  $\alpha$  (0.5). In the case of Ni/Re<sub>87</sub>-Co<sub>7</sub>, the limiting stage

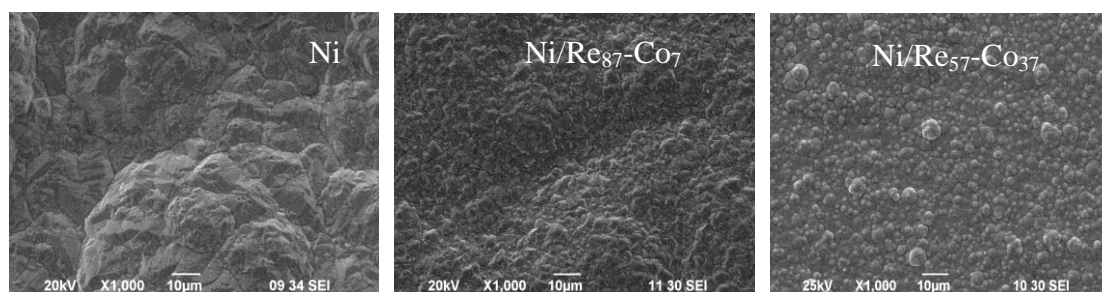
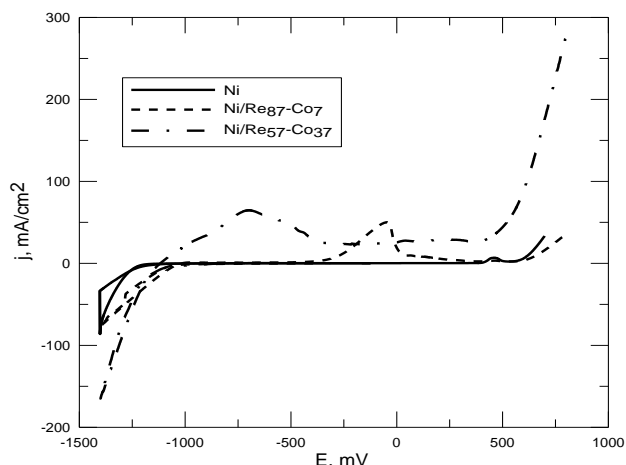
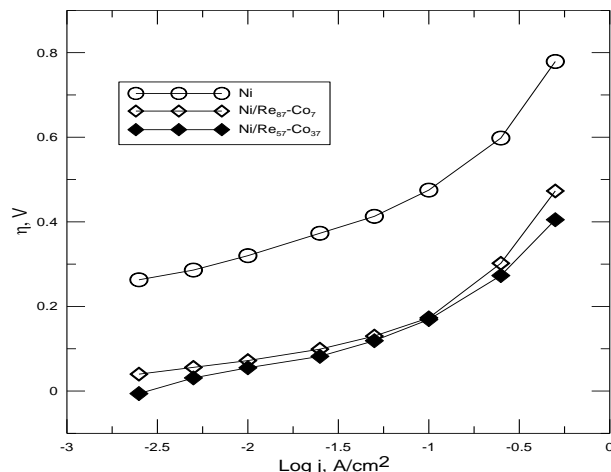


Fig. 1. SEM images of Ni, Ni/Re<sub>87</sub>-Co<sub>7</sub> and Ni/Re<sub>57</sub>-Co<sub>37</sub> electrodes.



**Fig. 2.** CV curves of Ni, Ni/Re<sub>87</sub>-Co<sub>7</sub> and Ni/Re<sub>57</sub>-Co<sub>37</sub> electrodes.



**Fig. 3.** Tafel plots of Ni, Ni/Re<sub>87</sub>-Co<sub>7</sub> and Ni/Re<sub>57</sub>-Co<sub>37</sub> electrodes.

**Table 1.** Kinetics parameters for HER on a pure Ni, Ni/Re<sub>87</sub>-Co<sub>7</sub> and Ni/Re<sub>57</sub>-Co<sub>37</sub> electrodes

Cathode material	Slope at lower cd than 50 mA/cm <sup>2</sup>			Slope at higher cd than 50 mA/cm <sup>2</sup>			η <sub>100</sub> , mV
	b, mV/dec	i <sub>0</sub> , A/cm <sup>2</sup>	α	b, mV/dec	i <sub>0</sub> , A/cm <sup>2</sup>	α	
Ni	118	1,67*10 <sup>-5</sup>	0,50	428	8,39*10 <sup>-3</sup>	0,14	475
Ni/Re <sub>87</sub> -Co <sub>7</sub>	68	7,36*10 <sup>-4</sup>	0,86	424	4,17*10 <sup>-2</sup>	0,14	173
Ni/Re <sub>57</sub> -Co <sub>37</sub>	91	2,63*10 <sup>-3</sup>	0,64	334	3,31*10 <sup>-2</sup>	0,18	169

**Note:** η<sub>100</sub> –overpotential of HER at 100 mA/cm<sup>2</sup>

of HER is the Heyrovsky electrochemical desorption according to the values of **b** which are near to 60 mV/dec, and the values of **α** which are higher than 0.5. These are typical values of the active electrodes, dissolving a large amount of hydrogen [6]. No single rate-determining step is observed in the case of Ni/Re<sub>57</sub>-Co<sub>37</sub>. The second slope of the Tafel plots is characterized with **α** value, much less than 0.5, and **b** value, much higher than 120 mV, for all electrodes, i.e. the mechanism of HER is probably one and the same. Such values of **α** and **b** are explained in the literature by impurity adsorption, blocking the charge transfer [7]. It could be suggested that the hydrogen bubbles play this role prior their evolution to the electrolyte.

Both modified Ni/Re<sub>87</sub>-Co<sub>7</sub> and Ni/Re<sub>57</sub>-Co<sub>37</sub> electrodes show higher values of **i**<sub>0</sub> (7.36\*10<sup>-4</sup> or 2.63\*10<sup>-3</sup>, respectively) than that of the pure Ni electrode (1.67\*10<sup>-5</sup>), the difference being between one and two orders of magnitude. The values of HER overpotential on both modified electrodes are similar, and most important, they are significantly lower than the overpotential value of HER on a pure Ni electrode (η<sub>100</sub> in Table 1). The values of the parameters **i**<sub>0</sub> and η reveal that the modification of the pure Ni electrode with a thin Re-Co layer leads to an increase of the catalytic activity towards

HER, the effect being more pronounced in the case of the Ni/Re<sub>57</sub>-Co<sub>37</sub> electrode.

According to the permeation measurements (Fig. 4 and Table 2), the values of the steady state permeation rate (I<sub>2</sub><sup>st</sup>) and of the permeation efficiency (I<sub>pe</sub>) of both Ni/Re-Co electrodes are higher than those of the pure Ni electrode, the effect being more pronounced at the electrode with a low content of Re in the alloy (about 3 times).

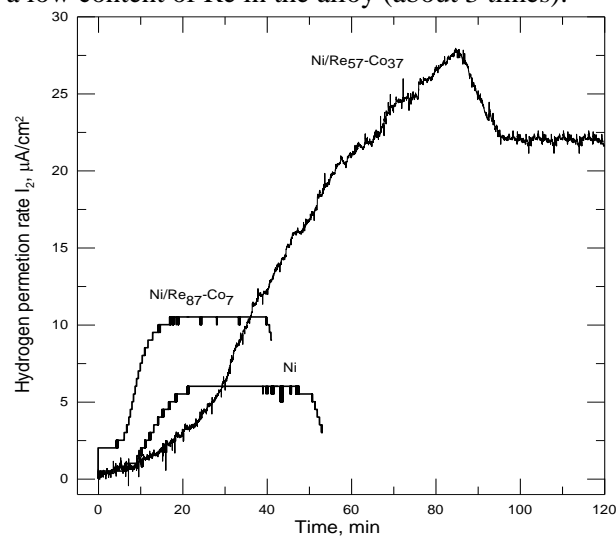


**Fig. 4.** Permeation transients of Ni, Ni/Re<sub>87</sub>-Co<sub>7</sub> and Ni/Re<sub>57</sub>-Co<sub>37</sub> electrodes, measured at a charging current I<sub>1</sub> = 10 mA/cm<sup>2</sup> and at E<sub>2</sub> = 280 mV (Hg/HgO).

The values of  $C_0$ , corresponding to the modified Ni/Re-Co electrodes, are also higher than that of the pure Ni, and in the case of Ni/Re<sub>57</sub>-Co<sub>37</sub>, the  $C_0$  value is one order of magnitude higher than that of the pure Ni electrode.

These results are in accordance with the larger maximum of hydrogen desorption in the anodic

**Table 2.** Steady state permeation rate ( $I_2^{st}$ ), permeation efficiency ( $I_{pe}$ ), diffusion coefficient ( $D$ ), and concentration ( $C_0$ ) of hydrogen in the subsurface layer of the Ni, Ni/Re<sub>87</sub>-Co<sub>7</sub>, and Ni/Re<sub>57</sub>-Co<sub>37</sub> electrodes

Cathode material	$I_2^{st}$ $\mu\text{A}/\text{cm}^2$	$I_{pe}$ %	$D$ $\text{cm}^2/\text{sec}$	$C_0$ $\text{Mol}/\text{cm}^3$
Ni	6.0	0.06	$1.5 \cdot 10^{-8}$	$3.7 \cdot 10^{-5}$
Ni/Re <sub>87</sub> -Co <sub>7</sub>	10.5	0.11	$2.0 \cdot 10^{-8}$	$4.9 \cdot 10^{-5}$
Ni/Re <sub>57</sub> -Co <sub>37</sub>	22	0.22	$0.5 \cdot 10^{-8}$	$4.1 \cdot 10^{-4}$

region of CV curves of the Ni/Re-Co electrodes (especially in the case of the Ni/Re<sub>57</sub>-Co<sub>37</sub> electrode), compared to the pure Ni electrode. However, the increase in the  $I_2^{st}$ ,  $I_{pe}$  and  $C_0$  in the case of modified Ni/Re-Co is not considerable, which means that it can not cause a considerable loss of hydrogen in the volume of the modified electrodes during water electrolysis.

## CONCLUSION

The comparison between both modified Ni/Re-Co electrodes (with high and low Re content) and the pure Ni electrode reveals the following features:

The electrochemical behaviour, with regards to HER, is characterized with a higher rate of hydrogen evolution, higher exchange current density, and lower hydrogen overpotential in the case of the modified electrodes, the effect being more pronounced at the electrode with a lower content of Re (Ni/Re<sub>57</sub>-Co<sub>37</sub>). These properties of the modified electrodes can be related to their more

developed surface, as well as to their higher catalytic activity. The more intensive hydrogen evolution at both modified electrodes is not accompanied with a considerable loss of hydrogen in the volume of the electrodes during the electrolysis.

The modified Ni/Co-Re electrodes could be, thereby, a promising electrocatalytic material for a negative electrode in alkaline water electrolysis. Further systematic investigations are needed in order to clarify the role of the Re in the Re-Co modifying layer, and to optimize the content of Re in the alloy with respect to the parameters of HER.

**Acknowledgements:** This study is supported by the Bulgarian Ministry of Education and Sciences in Bulgaria under the TK-X-1717/07 contract, and it is carried out in an academic collaboration with the group of Dr. P. Novak from the Institute of Catalysis and Surface Chemistry, Polish Academy of Sciences, Poland.

## REFERENCES

1. C. Lupi, A. Dell'Era, M. Pasquali, *Intern. J. Hydrogen Energy*, 34, 2101 (2009).
2. V. Pashova, L. Mirkova, M. Monev, *ECS Trans.*, 25, 395 (2010).
3. V. Pashova, L. Mirkova, M. Monev, P. Nowak, under preparation.
4. M. A.V. Devanathan, Z. Stachurski, *Proc. Roy. Soc. (London)*, A 270, 90 (1962).
5. E. Gileadi, M.A. Fullenwider, J.O'M Bockris, *J. Electrochem. Soc.*, 113, 926 (1966).
6. I. Paseka, *Electrochim. Acta*, 44, 4551 (1999).
7. M. Noel, K. Vasu, *Cyclic voltammetry and the frontiers of electrochemistry*, Oxford & IBH Publishing Co.PVT. Ltd., New Delhi, Bombay, Calcutta, 1990, p. 471.

## Ni/Re-Co КАТО ЕЛЕКТРОКАТАЛИТИЧЕН МАТЕРИАЛ ЗА ОТДЕЛЯНЕ НА ВОДОРОД В АЛКАЛЕН РАЗТВОР

В. Пашова<sup>1\*</sup>, Л. Миркова<sup>1</sup>, М. Монеv<sup>1</sup>, П. Новак<sup>2</sup>, Г. Наврат<sup>3</sup>

<sup>1</sup>Институт по физикохимия „Р. Каишев“, Българска академия на науките, ул. „Акад. Г. Бончев“, блок 11,1113  
София

<sup>2</sup>Институт по катализ и химия на повърхността, Полска академия на науките, ул. Незапминаек, 8, 30239  
Краков, Полша

<sup>3</sup>Силезийски технологичен университет, Департамент по неорганична химия, технология и горива, Гливица,  
Полша

Постъпила на 6 юли, 2010 г.; приета на 7 август, 2010 г.

(Резюме)

Изучено е електрохимичното поведение на два модифицирани електрода Ni/Re<sub>87</sub>-Co<sub>7</sub> и Ni/Re<sub>57</sub>-Co<sub>37</sub> (електроотложен никел, покрит с тънък слой електроотложена сплав Re-Co) по отношение на реакцията на отделяне на водород в разтвор на 6 М КОН. Данните са сравнени с тези на чист никелов електрод. Използвани са циклична волтаперометрия, поляризационни измервания при различни плътности на тока и електрохимичната пермиационна техника на Devanathan-Stachurski. На базата на Тафелови зависимости са определени кинетичните параметри на реакцията на отделяне на водород. На базата на пермиационните транзиенти са изчислени дифузионния коефициент на проникналия водород и концентрацията на абсорбирания водород в под-повърхностния слой на електрода. Двата модифицирани електрода показват значително по-високи стойности на скоростта на отделяне на водород и на обменния ток в сравнение с тези на чистия никелов електрод. Стойностите на свръхнапрежението на водородната реакция върху двата модифицирани електрода са подобни и най-важното, те са много по-ниски, отколкото съответната стойност върху чистия никелов електрод. Данните от пермиационните изследвания са в съгласие с волтаперометричните зависимости. Никеловият електрод, модифициран със сплав с по-ниско съдържание на Re (Ni/Re<sub>57</sub>-Co<sub>37</sub>), показва по-добри електрокаталитични свойства по отношение на реакцията на отделяне на водород.

## Corrosion characterization and protective ability of the LR -3 rust converter

G. M. Raichevski<sup>1</sup>, L. Lutov<sup>2</sup>, N. S. Boshkov<sup>1\*</sup>

<sup>1</sup> Institute of Physical Chemistry, Bulgarian Academy of Sciences, Acad. G. Bonchev St., building 11, Sofia 1113, Bulgaria

<sup>2</sup> University of Sofia, Department of Chemistry, No. 1 James Bourchier St, Sofia, Bulgaria

Received: July 8, 2010; accepted October 5, 2010

LR-3 rust converter is designed to convert the rust on iron and steel in a non-soluble and stable protecting dark-colored layer. The converter contains organic solvents, mineral acid, complex forming agents and inorganic salts the latter used as active additives for the converting process and distinguished with adsorption-oxidizing properties. The high concentration of organic compounds strongly increases the wetting ability of the converter ensuring better penetration in the finest pores and micro-cracks. This leads to a complete interaction with the rust as well as to a better converting process and excellent adhesion to the metal substrate.

In order to characterize the corrosion resistance of the LR-3 converted layer, it is tested in a model medium of free aerated 0.5M Na<sub>2</sub>SO<sub>4</sub>. The protective characteristics of the layer are investigated with electrochemical methods, polarization resistance measurements and anodic potentiodynamic curves. Using the optical microscopic method, the thickness and some special features of the appeared converted film are established. A certificate, confirming some physical and functional characteristics of the LR-3 rust converter, is also presented.

This composition stands out as a product of new generation among the other known rust converters, and fully adheres to the modern tendencies. It can find wide application in the agriculture, power-engineering, metallurgy, mining, and in the chemical, military, construction, and transport mine industries, etc. Technological regulations for the production of LR-3 and instructions for its application in real conditions are also prepared.

**Keywords:** rust converter, corrosion, polarization curves, polarization resistance

### INTRODUCTION

Iron and steel are the main materials for construction in almost all technical and technological branches. They are often subject of a corrosion attack in an aggressive media. As a result, their surface is covered with rust, the latter being mainly a mixture of iron oxides and hydroxides in different quantities. The newly appeared corrosion products distinguish in general with a loose structure, and do not fulfill the function of a protective barrier film, aimed to inhibit the corrosion processes in a sufficient degree. For these reasons, the additional treatment of corroding iron surfaces with rust converters is a promising alternative for a better protection.

In most cases this treatment leads to appearance of thin and dense film on the metal surface. This film is resistant against corrosion in liquid and gaseous phases even at wide regions of pH. Nevertheless, this converted layer is not impermeable barrier against metal ions transportation from the film/metal adhesion zone.

But yet, this film can inhibit the movement of aggressive ions (the latter provoking the beginning of dissolution or depassivation processes) from the surrounding medium to the metal surface [1–4].

### EXPERIMENTAL

The rust converter, used for these investigations, is a multi-component mixture in a liquid phase, the latter consisting of selected organic compounds and negligible water content. Active additives for the rust converting process are some specific inorganic salts with adsorption-oxidizing properties and complex forming agents. The obtained protective film can fulfill two main functions:

- barrier – locks the development of the destructive corrosion processes into the substrate;
- acts as a promising primer for the following polymeric and other organic coatings.

The created rust converted layers are tested with different methods, mainly electrochemical, for example [5–9]:

- Polarization resistance and electrode potential measurements in selected model corrosion media;
- Potentiodynamic polarization curves;
- SEM and optical microscope (cross-sections) studies;

\*To whom all correspondence should be sent:  
E-mail: nbojkov@ipchp.ipc.bas.bg

- Accelerated investigations at laboratory, model or natural conditions.

### 2.1. Sample preparation

The corroded samples (working area of 4 cm<sup>2</sup>) are initially carefully scraped with a brush to remove the loose part of the rusted layer. Thereafter, they are treated with the LR-3 converter and leaved for several hours. After this time, the rust on the iron surface is converted to high-valent iron oxides and phosphates, both compounds being non-soluble, stable, and forming a dark-colored protecting layer. The organic compounds, present in high concentration in the solution, strongly increase the wetting ability of the converter. This ensures the complete interaction with the rust and leads to excellent adhesion of the converted layer and to metal substrate.

### 2.2. Polarization resistance ( $R_p$ ) measurements

The protective ability of the 'iron/converted layer' systems is estimated by polarization resistance ( $R_p$ ) measurements in the range of  $\pm 25$  mV in relation to the corrosion potential. These investigations are carried out in a three-electrode experimental cell with Luggin-Haber capillary for minimizing the ohmic resistance of the model corrosion medium. Platinum plate is used as a counter electrode while the corrosion potentials are measured with respect to the saturated calomel electrode (SCE). Stern-Geary equation is applied to determine the value of the polarization resistance. As a rule, a higher  $R_p$  value corresponds to a higher corrosion resistance and to a lower corrosion rate [10].

### 2.3. Potentiodynamic polarization curves

Iron samples, covered with rust converted layers or not treated samples were investigated through potentiodynamic polarization (linear sweep polarization) using PAR Versa Stat equipment at a scan rate of 1 mV/s.

### 2.4. Microscopic investigations

These investigations are aimed to study the preliminary prepared cross-sections of selected samples, treated with LR-3. The thickness and some specific features, for example extend of the conversion process of the newly appeared protective films, are also established.

### 2.5. Corrosion medium

A model corrosion medium of free aerated 0.5M Na<sub>2</sub>SO<sub>4</sub> solution (pH 6) at ambient temperature of about 20 °C is used during the investigations.

## 3. RESULTS AND DISCUSSION

### 3.1. Polarization resistance

The results concerning the polarization resistance ( $R_p$ ,  $\Omega \cdot \text{cm}^2$ ) of the 'purely' rusty iron samples (non-treated with the LR-3 converter) and the additionally treated samples in a model corrosion medium are presented below:

-  $R_p$  value for the rusty iron sample - 185  $\Omega \cdot \text{cm}^2$ ;

-  $R_p$  value for the sample with an additionally converted film - 390  $\Omega \cdot \text{cm}^2$ .

This data contain average results for 5 samples, treated or not treated with the converter, respectively. Similar are the results upon a prolonged test for 6 days in the model medium. The obtained values clearly confirm the better protective characteristics of the converted rusty sample, compared to the non-treated one in the presence of sulfate ions as an aggressive component.

### 3.2. Potentiodynamic polarization curves

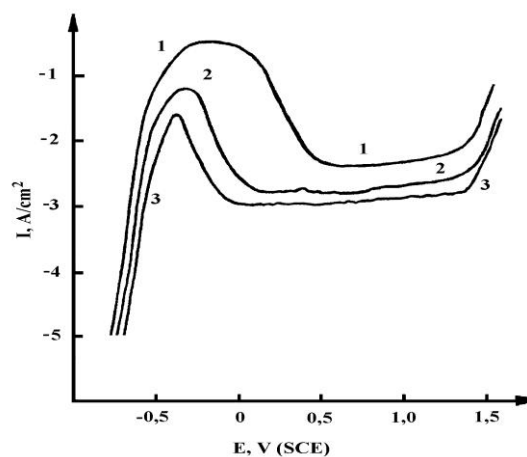


**Fig. 1.** Anodic potentiodynamic polarization curves of iron samples in 0.5 M Na<sub>2</sub>SO<sub>4</sub> solution (scan rate 1 mV/sec): 1 – "clean" iron; 2 – rusty iron; 3 – rusty iron additionally treated with LR-3.

Figure 1 presents the anodic potentiodynamic curves of 3 different sample types. Curve 1 demonstrates the anodic behavior of an iron plate, initially cleaned from rust using an emery cloth, degreased and thereafter anodically polarized.

Curve 2 shows that the presence of rust layer, as a result of the corrosion process, affects, to a certain degree, positively the anodic behavior. This is, for example, the rate hampering of the active dissolution in this medium (barrier effect) which leads to easier passivation. In this case the additional effects are: the shifting of the passivation potential ( $E_{\text{pass}}$ ) to a negative direction with about 350-400 mV, the wider passive zone, and the lower

anodic current density. These are very important signs that the rust, appearing on the surface, inhibits, to a certain degree, the penetration of the corrosive medium in depth in direction to the substrate.

In the case when the whole surface is uniformly covered with a compact rust converted layer, the positive effects are clearly expressed (see curve 3): slight shifting of  $E_{\text{pass}}$  to a negative direction (faster passivation process), wider passive area, compared to the other two samples, and lowest anodic current density value. Additionally, the obtained results demonstrate the increased susceptibility of the converted rusty layers to a passivation under anodic polarization.

### 3.3. Microscopic investigations

Figure 2 demonstrates a metallographic cross-section image, obtained using an optical microscope. It can be concluded that the rusty layer is of a loose structure, and its adhesion to the substrate is not strong enough.

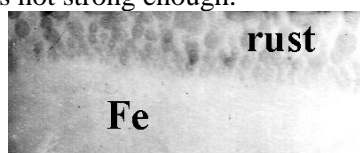


**Fig. 2.** Metallographic cross-section (magnification x1000) of rusted sample.

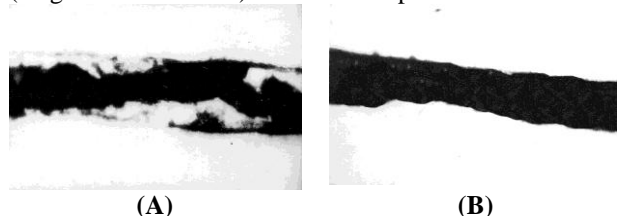


**Fig. 3.** Metallographic cross-sections (magnification x1000) of rusted samples with different extent of rust converting: A – low extent of converting; B – high extent of converting.

**Table 1**

No	Parameters	Requirements / Values	Results from the analyses
1	Appearance	Light movable solution	Corresponds
2.	Color	Green	Corresponds
3.	Sense of smell	Acetone	Corresponds
4.	pH value	About 1,5	1,3
5.	Specific weight	0,9 – 1,1	0,97
6.	Time for complete converting of the rust	6 hours	Corresponds
7.	Heat-proof	Up to 150 °C	Corresponds
8.	Frost-resistance	Up to -40 °C	Corresponds
9.	Corrosion resistance of the layer in 3% NaCl at 20 °C	Not less than 10 days without damages	Corresponds
10.	Transition resistance of the layer after converting ( $\Omega/\text{m}^2$ )	More than $1 \cdot 10^3$	$2 \cdot 10^3$

In general, this is the reason for the initial (preliminary) mechanical, and in some cases, the electrochemical treatment of the sample. In practical terms, this process is time consuming and needs automation. In all cases, the strong adhesion of the converted layer to the substrate is a very important factor for its protective ability.

Additionally, selected areas with different extent of rust converting are presented in Figure 3. Fig. 3A (left) demonstrates when the conversion process has been partially applied. The black zones are these places where almost the whole rust is converted, ensuring an improved corrosion resistance. White areas are the places where the process is not fully completed and where rusted and converted sections exist at the same time. Figure 3B shows a zone where the converting process is almost complete.



**Fig. 4.** Images of rusted stud (left) and iron plate (right) after treatment with LR-3.

Figure 4 demonstrates the decorative appearance of some details and their surfaces after the treatment with LR-3. It can be registered that the application of the rust converter leads to some changes in the color. The main result is the disappearing of the rusted areas and the presence of zones with dark color which are the places with the protecting converted layer.

### 3.4. Exemplary Certificate for LR-3

The exemplary Certificate for some physical and functional parameters of the investigated rust converter is presented in Table 1.

### 4. CONCLUSION

As already mentioned, the received protective film can perform two main functions: 1) to lock the destructive corrosion processes in depth; 2) to act as a promising ground coat for an additional treatment such as painting, coating, etc.

Possessing all these properties, this composition brings an improved corrosion resistance of the treated iron details, and refers to the modern tendencies in the preparation of new rust converter types. It can find wide practical application in different industrial branches. Consumption norm is approximately 50-100 ml/m<sup>2</sup> depending on the rust amount on the corroded metal surface.

The treatment can be done by applying the rust converter with a soft cloth over the surface or by pulverizing. LR-3 can be easily packed in plastic containers of 50 to 100L volume. The containers should be hermetically sealed in order to avoid evaporation of the organic solvents. Dissolution of the inorganic solid substances is done under electro-mechanical stirring. The production process is carried out at 20°C under stirring of the individual components. The addition of each single component is done upon complete dissolution of the previous one. The received solution must stay for 24 h before usage.

**Acknowledgements:** The authors express their gratitude to the Bulgarian National Fund for Scientific Researches; and the DTK-02-31/2009 project for the financial support of the presented investigations.

### REFERENCES

- 1 A. Swift, A.J. Paul, J.C. Vickermann, *Surf. and Interface analysis*, **20**, 27 (1993).
- 2 K. Barton, Protection against atmospheric corrosion, London. Wiley, 1976.
- 3 I. Matsushima, T. Ueno, *Corros. Sci.*, **11**, 129 (1971).
- 4 A. Collazo, X.R. Nóvoa, C. Pérez, B. Puga, *Electrochim. Acta*, **53**, 25, 7565 (2008).
- 5 C. A. Barrero, L. M. Ocampo, C. E. Arroyave, *Corros. Sci.*, **43**, 6, 1003 (2001).
- 6 L. M. Ocampo, I. C. P. Margarit, O. R. Mattos, S. I. Córdoba-de-Torresi, F. L. Fragata, *Corros. Sci.*, **46**, 6, 1515 (2004).
- 7 M. Favre, D. Landolt, *Corros. Sci.*, **34**, 9, 1481 (1993).
- 8 G. Cerisola, A. Barbucci, M. Caretta, *Progress in Organic Coatings*, **24**, 1-4, 21, (1994).
- 9 N. Boshkov, G. Raichevski, IV. Corrosion Symposium, Istanbul, 25-27 October 1994, 39.
- 10 M. Stern, A.L. Geary, *J. of the Electrochem. Soc.*, **104**, 56, (1957).

## ОХАРАКТЕРИЗИРАНЕ НА КОРОЗИЯТА И ЗАЩИТНИТЕ СВОЙСТВА НА ПРЕОБРАЗОВАТЕЛ НА РЪЖДА LR-3

Г.М. Райчевски<sup>1</sup>, Л. Лютов<sup>2</sup>, Н.С. Божков<sup>1</sup>

<sup>1</sup>) *Институт по физикохимия, Българска академия на науките, София 1113*

<sup>2</sup>) *Химически факултет, Софийски университет «Св. Климент Охридски», бул. Джеймс Баучер 1, София*

Постъпила на 8 юли, 2010 г.; приета на 5 октомври, 2010 г.

(Резюме)

Ръждопреобразувателят LR-3 е създаден с цел преобразуване на наличната ръжда върху желязо и стомана в неразтворим и стабилен слой с характерен тъмен цвят. Преобразувателят съдържа органични разтворители, минерална киселина, комплексообразуващи агенти и неорганични соли, които са активни добавки в процеса на преобразуване и се отличават с окислително-адсорбционни свойства. Високата концентрация на органични добавки силно повишава омокрящата способност и подобрява проникването и в най-фините пори и микропукнатини. Това води до едно комплексно взаимодействие с ръждата, както и до нейното по-пълно преобразуване и отлична адхезия към металната повърхност.

С цел характеризирание на корозионната устойчивост на обработения с LR-3 слой са проведени изпитания в моделна среда на свободно аериран разтвор на 0.5M Na<sub>2</sub>SO<sub>4</sub>. Защитните характеристики на ръждопреобразувания слой са оценени с електрохимични методи, измерване на поляризационното съпротивление и анодни потенциодинамични криви. Дебелината и някои особености на новообразувания филм са изследвани с оптичен микроскопичен метод. Представен е и сертификат за някои физични и функционални характеристики на самия ръждопреобразувател.

Новоразработеният състав е от нова генерация продукти и изцяло следва съвременните тенденции. Той може да намери приложение в земеделието, металургията, минното дело, както и в химическата, военната, строителната и транспортната промишлености. Подготвен е технологичен регламент за производството на LR-3, както и инструкции за неговото приложение в реални условия.

## Non-platinum electrode materials for hydrogen evolution: effect of catalyst support and metallic phase

P. Paunović<sup>1\*</sup>, D. Stoevska Gogovska<sup>1</sup>, O. Popovski<sup>2</sup>, I. Radev<sup>3</sup>, E. Lefterova<sup>3</sup>, E. Slavcheva<sup>3</sup>, A. T. Dimitrov<sup>1</sup> and S. Hadži Jordanov<sup>1</sup>

<sup>1</sup>Faculty of Technology and Metallurgy, University of Ss Cyril and Methodius, Skopje

<sup>1</sup>Faculty of Technology and Metallurgy, University of Ss Cyril and Methodius, 16 Ruger Bošković St, 1000 Skopje

<sup>2</sup>Military Academy, Mihajlo Apostolski Str., b.b., 1000 Skopje

<sup>3</sup>Institute of Electrochemistry and Energy Systems, Bulgarian Academy of Sciences, Acad.G.Bonchev St., Building 10, 1113 Sofia, Bulgaria

Received: June 17, 2010; accepted September 11, 2010

This work is concerned with the preparation and the characterization of nano-structured composite electrocatalytic material for hydrogen evolution based on Co as a hyper d-metallic phase and anatase (TiO<sub>2</sub>) as a hypo d-phase, both deposited on a carbon substrate. The main goal is to replace the Pt as an electrocatalytic material, partially or completely. Two types of support material were used: Vulcan XC-72 and multiwalled carbon nanotubes (MWCNTs). Also two non-platinum metals were used as a hyper d-metallic phase: Ni and Co. The best performances were shown by the Co electrocatalyst, deposited on activated MWCNTs. This one approaches and even slightly exceeds the catalytic activity of the traditional Pt electrocatalyst, deposited on Vulcan XC-72. To improve the disadvantages of this electrocatalyst (instability in acid media and passivation in alkaline media) a precious metal (Pt or Ru) was added into the metallic phase. Only 20 % of the precious metal in the metallic phase considerably improves the electrocatalytic activity for the hydrogen evolution.

Co was shown to promote decreasing platinum particle size. From 12 nm in the catalyst with pure platinum as the metallic phase, the size of Pt particles decreases to 3-4 nm in the catalyst with mixed metallic phase (80% Co + 20% Pt).

**Key words:** hydrogen evolution, hypo-hyper d-electrocatalysts, Vulcan XC-72, multiwalled carbon nanotubes MWCNTs, metallic phase: Co, Ni, Pt, and Ru.

### INTRODUCTION

The innovation of non-platinum electrode materials for water electrolyzers/fuel cells is a very important issue, within the hydrogen economy, related to the most promising energy system in the future. The commercial application of Pt, still the leading electrode material, is limited due to its high cost and limited reserves. It was estimated that current Pt resources can cover only part of the automotive needs [1]. Electricity demands are not included in this estimation.

Therefore, the main goal of the modern electrocatalysis and material science, employed in the hydrogen economy, is to reduce or even to replace platinum in the MEA, keeping the same level of efficiency. There are two main approaches to achieve this: i) exploration of synergetic mixture of non-platinum electrocatalytic materials (e.g.,

Jakšić hypo-hyper d-concept [2]) and ii) replacement of the traditional carbon support materials (e.g., Vulcan XC-72) with carbon nanotubes [1, 3].

According to Jakšić's interpretation [4-6] of Brewer valence-bond theory [7], significant synergetic effect of the catalytic activity can be achieved by alloying metal on the right side of transition series (good catalyst as an individual metal) with metal on the left side (bad catalyst as an individual metal). Bonding occurs between the metal with more electrons on the outer shell (the hyper d-component) and the metal with less valence electrons, i.e. more vacant orbitals – hypo d-component. Hypo and hyper d-components may be not only in the elemental state but also in higher oxidation states. Depending on the valence state of the hypo and the hyper d-components, we can divide these electrocatalysts into five main groups: i) intermetallic catalysts, ii) metal-sulfides/phosphides, iii) catalysts based on Raney Ni, mixed oxides, and v) hypo oxide – hyper metal [8]. These

\* To whom all correspondence should be sent.  
E-mail: pericap@tmf.ukim.edu.mk

catalysts can be used with the same effectiveness for both, the hydrogen evolution and the fuel cells.

The other approach to enhance the performance of the electrode materials is the improvement of the support materials. The support materials have to possess several very important characteristics such as the: *i*) highly developed surface area to provide better dispersion of the nano-scaled catalytic particles; *ii*) high electric conductivity to allow efficient electron transfer to ions, involved in the electrochemical reactions, *iii*) mechanical and chemical stability; and *iv*) strong metal-support interaction (SMSI) to improve intrinsic catalytic activity of the active catalytic phase. In this context, the carbon nanostructured materials, such as the carbon blacks, are commercially the most used support material [9, 10] due to their high surface area, conductivity and compositional homogeneity. Recently, the production of carbon nanotubes (CNTs) as catalyst support became a subject of intensive research [1, 3, 11]. CNTs show superior surface characteristics (high surface area and pore size distribution), electronic conductivity, mechanical and thermal properties, etc. These characteristics offer a great potential for electrocatalyst support materials aimed to serve both hydrogen electrolyzers/fuel cells. CNTs electronic conductivity is in the range between  $10^3$  and  $10^4$  S·cm<sup>-1</sup>. In comparison, the Vulcan XC-72 electronic conductivity is of 4 S·cm<sup>-1</sup>. Furthermore, the specific surface area of Vulcan XC-72 is 250 m<sup>2</sup>·g<sup>-1</sup>, while that of the CNT is 200-900 m<sup>2</sup>·g<sup>-1</sup>. Also, the pores in Vulcan XC-72 are smaller than 2 nm, while CNTs have not pores smaller than 2 nm. So, the metallic phase may sink into pores that reduce active reactive sites over the catalytic surface [3].

Pathways for obtaining of non-platinum electrocatalysts or electrocatalysts with reduced amount of Pt are shown in this work. In this context, TiO<sub>2</sub> (anatase) was added to the carbon support, Vulcan XC-72 was replaced with MWCNTs, and finally MWCNTs were activated before metallic phase deposition. Co, Ni, and metallic mixtures of Co-Pt and Co-Ru were used as catalytic metallic phase.

## EXPERIMENTAL

The studied catalysts contain 10 % hyper d-metallic phase, 18% TiO<sub>2</sub> as a hypo d-component, and the rest is carbon substrate. For comparison, Ni, Co, and Pt electrocatalysts were prepared only on the Vulcan XC-72 catalyst support (10 % Me and the rest is a carbon phase). Organometallics were

used as precursors to obtain a metallic phase, Me-2,4-pentaedionate (Alfa Aesar, Johnson Matthey, GmbH, Me = Co, Ni, Pt, Ru). TiO<sub>2</sub> was produced from Ti-isopropoxide (Aldrich, 97%). Vulcan XC-72 (Cabot Corp. Boston, Mass.) or multiwalled carbon nanotubes (MWCNTs, *Guangzhou Yorkpoint Energy Company, China*) were used as a carbon substrate. The catalysts were produced by sol-gel procedure, simplified in some steps by the authors of this work [12, 13]. Firstly, TiO<sub>2</sub> was deposited on carbon substrate, and further, the modified support was thermally treated at 480° for 1 h in the H<sub>2</sub> + N<sub>2</sub> atmosphere. In the next step, the metallic phase was grafted on the support and the obtained mixture was thermally treated at 250°C for 2 h.

Activation/purification of the so-prepared MWCNTs was performed in a 28% (mass.) HNO<sub>3</sub>. The process was carried out at a room temperature for 4 h. MWCNTs were stirred into the solution by magnetic stirrer. After filtering and washing, the activated MWCNTs were dried at 90°C for 24 h. Table 1 shows the composition of the studied electrocatalysts.

**Table 1.** Composition of the studied electrocatalysts

Sample No	Catalysts composition
0	10% Pt + Vulcan XC-72
1	10% Ni + Vulcan XC-72
2	10% Co + Vulcan XC-72
3	10% Co + 18% TiO <sub>2</sub> + Vulcan XC-72
4	10% Co + 18% TiO <sub>2</sub> + MWCNTs
5	10% Co + 18% TiO <sub>2</sub> + MWCNTs(a)
6	10% CoPt (4:1 wt.) + 18% TiO <sub>2</sub> + MWCNTs(a)
7	10% CoPt (1:1 wt.) + 18% TiO <sub>2</sub> + MWCNTs(a)
8	10% Pt + 18% TiO <sub>2</sub> + MWCNTs(a)
9	10% CoRu (4:1 wt.) + 18% TiO <sub>2</sub> + MWCNTs(a)
10	10% CoRu (1:1 wt.) + 18% TiO <sub>2</sub> + MWCNTs(a)
11	10% Ru + 18% TiO <sub>2</sub> + MWCNTs(a)
12	10% CoRuPt (4:0,5:0,5 wt.) + 18% TiO <sub>2</sub> + MWCNTs(a)

To identify the intrinsic changes, caused by the modifications, spectroscopic and structural techniques were employed. XRD and SEM techniques were used for structural characterization. XRD measurements were carried out by Philips APD 15 X-Ray diffractometer, with CuK<sub>α</sub> radiation, while SEM observations were carried out by JEOL Scanning Electron Microscope, model JEM 200 CX. Infrared spectroscopy was employed to determine the

strength of hypo-hyper *d*- interaction (TiO<sub>2</sub>/Ni) using FTIR spectrometer, model Bruker Vector 22.

Catalyst surface area was determined through double layer capacity, measured by cyclic voltammetry [14, 15]. The ratio of real versus geometric surface area of the electrodes was determined as a quotient of catalyst double layer capacity  $C_{dl}$  versus double layer capacity  $C_{dl0}$  of a pure oxide surface.

Further, the produced catalysts were electrochemically tested for hydrogen evolution reaction. Porous electrodes aimed for three phase operation (solid electrode, liquid electrolyte, and H<sub>2</sub> gas as a product) were prepared. They consist of two layers: *i*) catalytic layer facing the electrolyte, covered by catalyst with a low amount of PTFE, and *ii*) gas-diffusion layer facing the gas side, consisted of Vulcan XC-72 (or MWCNTs) bonded with PTFE. The procedure of electrode preparation is described elsewhere [16]. Electrochemical investigations were performed using AMEL equipment (AMEL 568 Function Generator, Potentiostat/Galvanostat 2053 and a SOFTASSIST 2.0 software package). The counter electrode was of platinum wire and the reference electrode of Hg/HgO. The electrolyte comprised an aqueous solution of 3.5 M KOH (p.a., Merck) at a room temperature.

## RESULTS AND DISCUSSION

The first step of the study was the preparation and testing of non-platinum electrocatalysts, deposited on the most used support material, the Vulcan XC-72. Ni and Co were used as metallic phase. Why Co and Ni? Ni is a non-noble metal of platinum group, while Co is near the Ni in the periodic table, having similar properties. It was expected that both catalysts will show close catalytic activity for the hydrogen evolution. But, the Ni-based catalysts (sample 1) showed very inferior activity related to that of the Co-based one (sample 2, see Table 2).

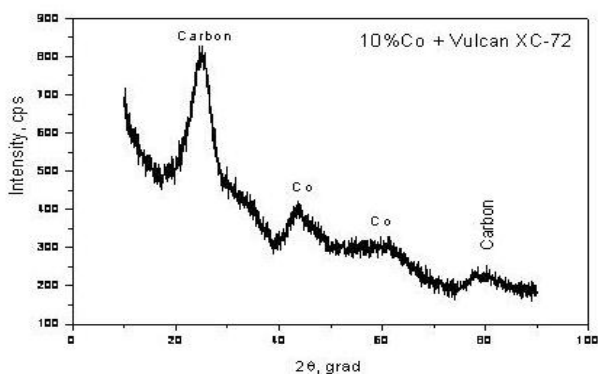


**Fig. 1.** XRD spectra of the a) Ni- and b) Co-based electrocatalysts deposited on Vulcan XC-72.

The difference in the overpotentials for hydrogen evolution at a reference current density of 60 mA·cm<sup>-2</sup>, was 150 mV. This is due to the much higher size of the Ni particles, compared to those of the Co. It was determined by the XRD analysis (see Fig. 1) that Ni is crystalline with particle size of 15-20 nm. There are no pronounced peaks in the Co XRD spectra, which is a characteristic for amorphous phases with particle size less than 2 nm. Thus, the real surface area of the active catalytic centers, dispersed over the catalyst surface, is considerably higher in the case of a Co-based electrocatalyst. Compared to the corresponding Pt-based catalysts (sample 0), the activity of both non-platinum samples is considerably lower. The improvement of the Co-based electrocatalyst is discussed further down.

**Table 2.**

Sample No	Catalysts composition	$\eta_{60}$ , mV
0	10% Pt + Vulcan XC-72	220
1	10% Ni + Vulcan XC-72	530
2	10% Co + Vulcan XC-72	380
3	10% Co + 18% TiO <sub>2</sub> + Vulcan XC-72	265
4	10% Co + 18% TiO <sub>2</sub> + MWCNTs	235
5	10% Co + 18% TiO <sub>2</sub> + MWCNTs(a)	215
6	10% CoPt (4:1 wt.) + 18% TiO <sub>2</sub> + MWCNTs(a)	135
7	10% CoPt (1:1 wt.) + 18% TiO <sub>2</sub> + MWCNTs(a)	115
8	10% Pt + 18% TiO <sub>2</sub> + MWCNTs(a)	125
9	10% CoRu (4:1 wt.) + 18% TiO <sub>2</sub> + MWCNTs(a)	145
10	10% CoRu (1:1 wt.) + 18% TiO <sub>2</sub> + MWCNTs(a)	135
11	10% Ru + 18% TiO <sub>2</sub> + MWCNTs(a)	90
12	10% CoRuPt (4:0,5:0,5 wt.) + 18% TiO <sub>2</sub> + MWCNTs(a)	125

### Addition of anatase

First modification step of the new Co-based electrocatalyst was the addition of hypo *d*-phase TiO<sub>2</sub> (anatase). Hypo *d*- component has a bifunctional role, as a catalyst support (with carbon phase) and it contributes to the catalyst overall synergetic effect by the so called Strong Metal-Support Interaction (SMSI). The unique role of the anatase form of titania in the improvement of the catalytic activity in both, the heterogeneous chemical catalysis and the electrocatalysis, has been noticed by other authors [17, 18]. The addition of anatase in the catalyst support, contributes to the reduction of the overpotential for the hydrogen

evolution even down to 115 mV (see Table 2). This considerable rise of the catalytic activity of the modified Co-based electrocatalyst (sample 3) is resulted by the strong hypo-hyper *d*-interaction between Co and TiO<sub>2</sub>. This consequently increases the intrinsic catalytic activity. The above is illustrated by the FTIR spectra, shown in Fig. 2.

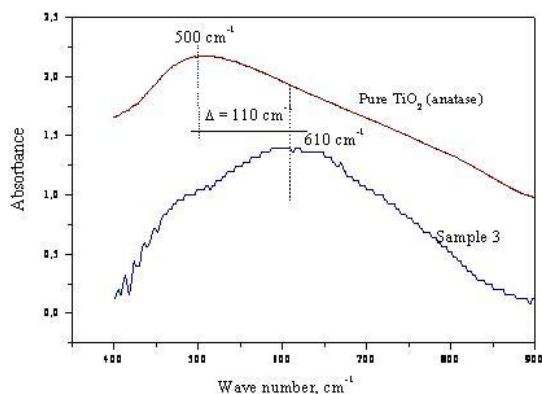


**Fig. 2.** FTIR spectra of the Co hypo-hyper *d*-electrocatalyst containing 10% Co + 18% TiO<sub>2</sub> + Vulcan XC-72 (sample 3) and pure TiO<sub>2</sub> (anatase).

The maximum of TiO<sub>2</sub> band, originated from the Co-based electrocatalyst, is shifted for a higher value of the wave number (110 cm<sup>-1</sup>) compared to the maximum of band which originated from the pure anatase. This shift is a result from the interaction between TiO<sub>2</sub> and Co atoms [19]. The higher the wave number shift is, the shorter is the bond between TiO<sub>2</sub> and hyper *d*-metallic phase, i.e. the higher the hypo-hyper *d*-interaction is.

#### *Replacement of Vulcan XC-72 with MWCNTs*

Instead of the conventional Vulcan XC-72 carbon substrate, multiwalled carbon nanotubes (MWCNTs) were involved in the next modification step. Fig. 3 shows the SEM images of Co-based electrocatalysts, deposited on both, the Vulcan XC-72 and the MWCNTs.

The catalyst particles, deposited on Vulcan X-72 are of a spherical shape (Fig. 3a.). There is a grouping of the particles in clusters (150 – 200 nm), whereat good adherence between particles is achieved. The particles are not uniformly distributed, and a number of holes appear between the aggregates. This contributes to the higher specific surface area, and consequently, to a higher electrocatalytic activity. Catalyst deposited on MWCNTs shows completely different morphology (Fig. 3b.). The particles of oxide and metallic phases, grafted on MWCNTs, are grouped in smaller clusters than those on Vulcan XC-72. Their inner structure, geometry, surface area, and conductive characteristics are favourable for use as

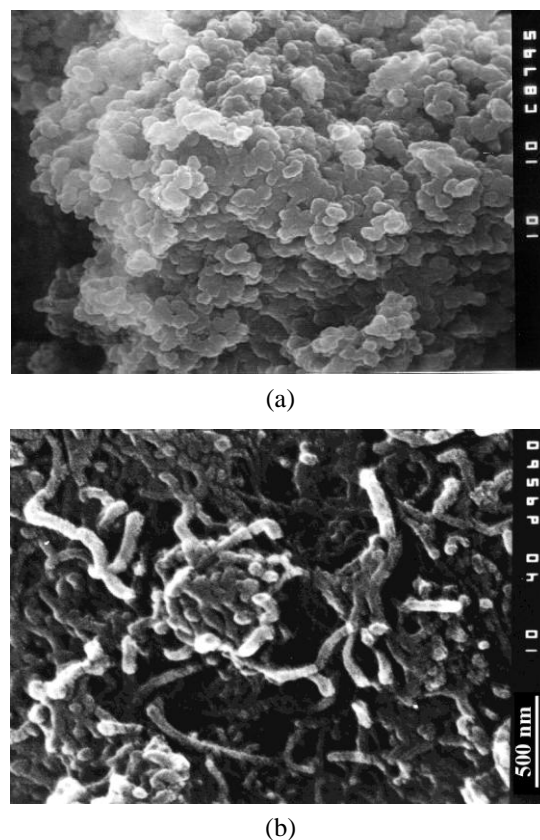


**Fig. 3.** SEM images of Co hypo-hyper *d*-electrocatalysts deposited on a) Vulcan XC-72 (sample 3) and b) MWCNTs (sample 4).

a carbon substrate of the nano-scaled electrocatalysts. Their high developed surface area enables better dispersion of active catalytic centres across the catalyst surface. On the other hand, MWCNT's high **inter- and trans-particle nano porosity** as well as its geometry (empty cylinders) do facilitate the escape of hydrogen molecules from catalyst surface [20]. Extra-conductive properties enable easier electron exchange with the hydrogen protons, which intensifies the formation of adsorbed hydrogen atoms and further hydrogen molecules. Estimation of real surface area by the value of double layer capacity ( $C_{dl}$ ), measured by cyclic voltammetry, showed that MWCNTs have twice higher developed surface area than Vulcan XC-72 [21]. The decrease of hydrogen overpotential in this modified catalyst (sample 4), compared with the previous modified one (sample 3), is of 30 mV.

#### *Activation of MWCNTs*

Further, purification/activation of MWCNTs was made. During this operation, three main processes occur: (i) removing of other carbonaceous phases such as the amorphous carbon, and (ii) rise of defect sites as a result of

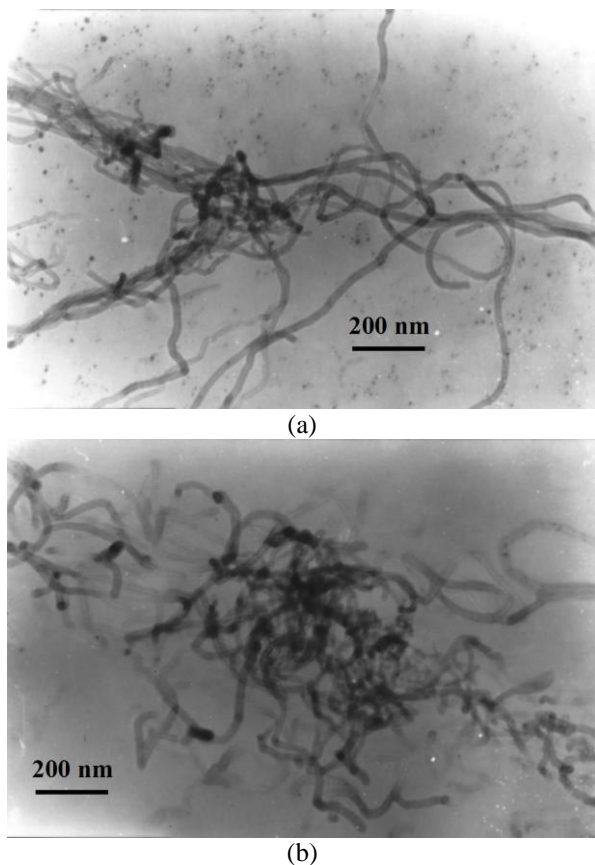


**Fig. 4.** TEM images of a) as-prepared and b) activated MWCNTs

shortening, thinning, and opening of the MWCNTs, and iii) functionalization of MWCNTs with oxide groups. The opening and shortening of the MWCNTs, and the increased number of the defective sites, results in the increase of their real surface area and reactivity, which are suitable for carbon substrates, used as electrocatalysts. This is illustrated by the TEM images of MWCNTs, before and after activation, in Fig. 4.

These changes in the support material contribute to a higher catalytic activity for the hydrogen evolution of the Co-based hypo-hyper d-electrocatalyst. In this case (sample 5) the hydrogen overpotential decreases to 20 mV in relation to the previous Co-catalyst (sample 4). This activity is very close to that of the traditional Pt electrocatalyst (Pt/Vulcan XC-72, sample 0). Thus, the maximal activity of the non-platinum Co-based catalyst approaches the Pt-based one, and slightly exceeds it. The performance of these electrocatalysts in the proton exchange membrane (PEM) electrolyte at lower cathodic overpotentials, however, was not so impressive, while at higher overpotentials, their activity approaches the performance of the traditional Pt catalyst [20].

#### Addition of Pt in the metallic phase

Therefore, catalysts with mixed metallic phase were prepared in the next phase of the investigations. They contained 10 % CoPt (Co:Pt = 4:1, wt., sample 6 and Co:Pt = 1:1, wt., sample 7), and a Pt-based catalyst (sample 8) with analogous composition, produced under the same conditions. These catalysts showed impressive catalytic activity which considerably exceeded the activity of the conventional platinum (sample 0). The catalysts with mixed metallic phase, Co:Pt = 1:1, wt., (sample 7), showed the best catalytic activity while

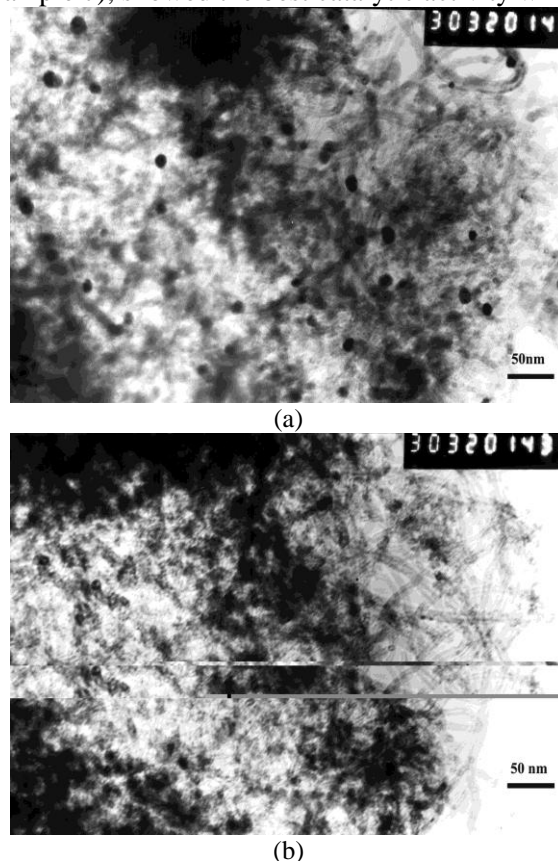


**Fig. 5.** TEM images of hypo-hyper d-electrocatalysts containing a) 10% Pt + 18% TiO<sub>2</sub> + MWCNTs(a) (sample 8) and b) 10% CoPt (1:1 wt.) + 18% TiO<sub>2</sub> + MWCNTs(a) (sample 7).

the catalysts with mixed metallic phase, Co:Pt = 4:1, wt. (sample 6), are less active but still very close to the activity of the pure Pt-based catalyst (sample 8). It sounds as a paradox, at first sight, when a catalyst with a double amount of Pt (sample 4) is less active. There is a logical explanation, however, for such order of the catalytic activity. Let's assume that the catalytic activity depends on the hypo-hyper d-interaction as well as on the surface area (particle size) of the metallic catalytic centres, dispersed over the catalyst surface. The intrinsic hypo-hyper d-interaction is the same in all

catalysts. They all have better porosity and dispersion of the metallic phase as a result of MWCNTs usage as catalyst support as well. Thus, the improved activity of the catalyst with less amount of platinum, is obviously related to the considerably lower size of the Pt crystallites in the mixed systems. As it was shown from the XRD analysis [22], the size of the Pt crystallites in sample 8 is near to 12 nm, while in the mixed systems (samples 6 and 7), Co promotes considerably lower (up to 3-4 times) size of the Pt particles. These results were confirmed by the TEM analysis (see Fig. 5). The lower amount of Pt is compensated by the highly developed surface of the Pt-phase in the mixed systems.

#### *Addition of Ru in the metallic phase*

The catalyst with pure Ru metallic phase (sample 11) has shown the best catalytic activity for hydrogen evolution. The overpotential is 35 mV (at reference current density of  $60 \text{ mA}\cdot\text{cm}^{-2}$ ) lower than that of the corresponding catalyst with pure Pt as a metallic phase (sample 8, see Table 2). Pt and Ru have very close intrinsic catalytic activity for hydrogen evolution. Also, the increase of intrinsic activity as a result of hypo-hyper *d*-interaction with  $\text{TiO}_2$  is the same. Thus, the higher activity of Ru in this case, is a result of smaller particles (near 6 times) than that of the Pt. This means more developed surface area of the metallic active catalytic centres on the catalyst surface. In the catalysts with mixed CoRu metallic phase (4:1 and 1:1 wt., sample 9 and 10), catalytic activity decrease to 55 and 45 mV respectively, compared to the catalyst with pure Ru (sample 11). In this case addition of Co (non-precious metal) with particles almost equal with that of Ru, results in corresponding decrease of catalytic activity. The last studied electrocatalyst (sample 12, containing 20% precious metal mixture of Ru and Pt, and Co in the metallic phase) shows better catalytic activity than the previous electrocatalysts, containing CoRu metallic phase (sample 9 and 19) for 20 and 10 mV, respectively. Due to the presence of Co, the Pt particles are very small (3-4 nm) and the catalytic activity increases.

It is obvious that hypo-hyper *d*-electrocatalysts (hypo-oxides + hyper-metals) are very promising in the reduction of platinum in the electrocatalysts, aimed for hydrogen evolution. In this context, MWCNTs have considerable contribution as an extraordinary carbon support.

## CONCLUSION

The investigations, presented in this paper, were motivated by the idea for reduction or even replacement of Pt in self-developed electrode material for hydrogen evolution. According to the presented results, the following conclusions could be done:

1) The catalytic activity for hydrogen evolution of a Co-based electrocatalyst is considerably higher than that of the Ni-based due to the smaller Co particles (2 nm) vs. the Ni particles (15 – 20 nm), and consequently the higher surface area of the active catalytic phase;

2) Catalytic activity of electrocatalysts, deposited on MWCNTs, is higher than that of the deposited on Vulcan XC-72 due to better surface characteristics (surface area > for twice, better inter-particle and trans-particle porosity). Further activation of the MWCNTs contributes to the improvement of the catalytic activity due to the shortening and opening of nanotubes, and consequently, the rise of real surface area [4];

3) Co electrocatalyst, deposited on activated MWCNTs, approaches, even exceeds the catalytic activity of the traditional Pt electrocatalyst, deposited on Vulcan XC-72;

4) Further addition of precious metals (Pt or Ru) in the metallic phase (only 20%) considerably improves the catalytic activity for hydrogen evolution, considerably exceeding the activity of the traditional Pt electrocatalyst, deposited on Vulcan XC-72;

5) In CoPt-based systems, the electrocatalyst with only 20% Pt in the metallic phase (sample 6) shows activity close to that of the corresponding catalyst with pure Pt metallic system (sample 8), while CoPt electrocatalyst with Co:Pt = 1:1 (sample 7) exceeds the activity of sample 8. This is due to the smaller particle size (higher surface area) of Pt in mixed metallic systems (3-4 nm) than that in the pure Pt system, where the size of the Pt particles is 12 nm [5];

6) The best performances for hydrogen evolution showed the Ru-based catalyst. Its better performances, related to the corresponding Pt-electrocatalyst, are due to the smaller particles of Ru (2 nm) than that of the Pt (12 nm). Further addition of Co in the Ru metallic phase linearly decreases the catalytic activity.

**Acknowledgement:** *This work has been supported by and carried out within the PROMETHEAS PL ICA2-2001-10037 EU Project, and the 13-1650/4-02 Project of the Ministry of Education and Science of the Republic of Macedonia.*

## REFERENCES

1. K. Lee, J. Zhang, H. Wang and D. P. Wilkinson, *J. Appl. Electrochem.*, **36**, 507 (2002).
2. M. M. Jakšić, *Electrochimica Acta*, **29**, 1539 (1984).
3. P. Serp, M. Corrias, P. Kalck, *Appl. Catal. A: General*, **253**, 337 (2003).
4. M. M. Jakšić, *Int. J. Hydr. Ener.*, **12**, 727 (1987).
5. M. M. Jakšić, *J. New Mater. Electrochem. Sys.*, **3**, 153 (2000).
6. M. M. Jakšić, *Solid State Ionics*, **136-137**, 733 (2000).
7. L. Brewer, *Science*, **161**, 115 (1968).
8. P. Paunović in *Nanostructured Materials for Advanced Technological Applications*, J.P. Reithmaier et al. (eds.), © Springer Science + Business Media B.V. (2009), p. 391.
9. K. Kinoshita, *Carbon, electrochemical and physicochemical properties*, John Wiley & Sons, New York, 1988).
10. E. Budevski, *J. Optoelec. Adv. Mater.*, **5**, 1319 (2003).
11. P. Paunović, A.T. Dimitrov, O. Popovski, E. Slavcheva, A. Grozdanov, E. Lefterova, Dj. Petruševski and S. Hadži Jordanov, *Mat. Res. Bull.*, **44**, 1816 (2009).
12. S. Hadži Jordanov, P. Paunović, O. Popovski, A. Dimitrov and D. Slavkov, *Bull. Chem Technol. Macedonia*, **23**, 101 (2004).
13. P. Paunović, O. Popovski, A.T. Dimitrov, D. Slavkov, E. Lefterova and S. Hadži Jordanov, *Electrochimica Acta*, **52**, 1610 (2006).
14. B. Marsan, N. Fradette, G. Beaudoin, *J. Electrochem. Soc.*, **139**, 1889 (1992).
15. L.M. Da Silva, L.A. De Faria, J.F.C. Boodts, *Electrochimica Acta*, **47**, 395 (2001).
16. BG patent Appl. N° 38581.
17. S. J. Tauster, S.C. Fung, *J. Catal.*, **55**, 29 (1978).
18. S.G. Neophytides, S. Zaferiatos, G. D. Papakonstantinou, J. M. Jakšić, F. E. Paloukis and M. M. Jakšić, *Int. J. Hydr. Energy*, **30**, 393 (2005).
19. P. Paunović, O. Popovski, A. T. Dimitrov, D. Slavkov, E. Lefterova and S. Hadži Jordanov, *Electrochimica Acta*, **52**, 4640 (2007).
20. P. Paunović, O. Popovski and I. Radev, *Bull. Chem. Technol. Macedonia*, **24**, 133 (2005).
21. P. Paunović, A. T. Dimitrov, O. Popovski, D. Slavkov and S. Hadži Jordanov, *Maced. J. Chem. Chem. Eng.*, **26**, 87 (2007).
22. P. Paunović, I. Radev, A.T. Dimitrov, O. Popovski, E. Lefterova, E. Slavcheva, S. Hadži Jordanov, *Int. J. Hydr. Energy*, **34**, 2866 (2009).

## Не-платиновни електродни материали за добиване на водород: ефект на подложката на катализатора и на металната фаза

П. Паунович<sup>1\*</sup>, Д. Стоевска-Гоговска<sup>1</sup>, О. Поповски<sup>2</sup>, И. Радев<sup>3</sup>, Е. Кефтерова<sup>3</sup>, Е. Славчева<sup>3</sup>, А.Т. Димитров<sup>1</sup>, С. ХаджиЙорданов<sup>1</sup>

<sup>1</sup> Факултет за технология и металургия, Университет "Св. Кирил и Методий", ул. Ругер Бошкович 16, Скопие, Република Македонија 16 Ruger Bošković St, 1000 Skopje

<sup>2</sup> Военна академия, ул. Михайло Апостолски, 1000 Скопие, Република Македонија

<sup>3</sup> Институт по електрохимия и енергийни системи, БАН, ул. Акад. Г. Бончев, бл. 10, 1113 София

Постъпила на 17 юни, 2010 г.; приета на 11 септември, 2010 г.

(Резюме)

Работата разглежда приготвянето и охарактеризирането на нано-структурирани композити като електро-каталитичен материал за добиването на водород, основан на кобалт като хипер d-метална фаза и анатаз (TiO<sub>2</sub>) като хипо d-фаза, и двете отложени върху въглероден носител. Главната цел е да се замени платината като електро-каталитичен материал, отчасти или напълно. Използвани са два типа носители: Vulcan XC-72 и многостенни въглеродни нано-тръби (MWCNT). Освен това като хипер d-метална фаза са използвани два не-платиновни метала: никел и кобалт. Най-добри показатели са показани от Co-електрокатализатор, отложен върху активирани MWCNT. Той се доближава и дори леко превъзхожда каталитичната активност на традиционния платинов катализатор, отложен върху Vulcan XC-72. За преодоляването на недостатъците на този електро-катализатор (нестабилност в кисела среда и пасивирание в алкална) в металната фаза се добавя благороден метал ((Pt или Ru). Само 20 % от благородния метал в металната фаза подобряват значително електро-каталитичната активност за отделянето на водород.

Оказва се, че кобалтът промотира намаляването на размера на платиновите частици – от 12 nm при катализатор от чиста платина, размерът им се намалява до 3-4 nm в катализатор със състав (80% Co + 20% Pt).

## Mediated enzyme electrodes

R. I. Boukoureshtlieva<sup>1\*</sup>, S. M. Hristov<sup>1</sup>, Y. D. Milusheva<sup>1</sup>, P. B. Atanassov<sup>2</sup>, and A. R. Kaisheva<sup>1</sup>

<sup>1</sup>*Institute of Electrochemistry and Energy Systems, BAS,*

<sup>2</sup>*Department of Chemical & Nuclear Engineering, University of New Mexico, Albuquerque, NM 87131*

Received: June 29, 2010; revised: October 21, 2010

This review summarizes the long time experience of the team at the Electrochemistry of Biocatalysts and Metal-Air Systems Department in the field of the mediated enzyme electrodes. Investigated is the redox behaviour of a mediated enzyme electrode depending on the kind of carbon materials, needed to produce the electrode (compact carbon material – pyrolytic graphite or dispersed carbon material - carbon black), the type of mediators (ferrocene derivatives, nickelocene and benzoquinone), and the type of enzyme (glucose oxidase and lactate oxidase).

**Key words:** mediator, enzyme electrode, pyrolytic graphite electrode, carbon black

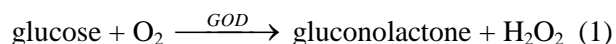
### INTRODUCTION

The research work in the field of the biosensors has expanded very rapidly since the development of glucose enzyme electrodes, which are of particular interest in the biomedical analysis field [1, 2]. The development of electrochemical biosensors which combine the specificity and the selectivity of the enzyme catalyst with the appropriate electrochemical techniques is of a great interest for the healthcare, the environmental control, the agriculture, the food and other industries [3, 4].

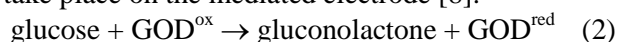
The electrochemical biosensor is a complicated device which converts a biological recognition process into an electrical signal, the amplitude of which is related to the concentration of the analyte. The coupling of the electron transfer of the enzyme with the electron transfer at the electrode poses a major problem to the biosensor development. In most cases the enzyme redox centres are essentially insulated within the enzyme molecule so that a direct electron transfer to the surface of the conventional electrode does practically not occur. The electrical communication between the redox centres of the enzyme and the electrode requires either the presence of oxygen and hydrogen peroxide and their diffusion to and from the enzyme redox centres, or the presence of a redox mediator [5].

Glucose oxidase (GOD) is one of the first enzymes used in the biocatalytic electrochemical sensing elements [6, 7]. The specific substrate for this enzyme, the  $\beta$ -D-glucose, undergoes oxidation

by oxygen producing of gluconolactone and hydrogen peroxide.



The detection principle is based on an electrochemical reaction in which the  $\text{H}_2\text{O}_2$  production or the  $\text{O}_2$  consumption is detected. The produced  $\text{H}_2\text{O}_2$  can be electrochemically oxidised on an electrode at a constant potential, and the generated anodic current is used to measure the glucose concentration. Together with the natural electron acceptor in reaction (1), oxygen, and other low-molecular-weight compounds are used as mediators between the enzyme and the electrode. The mediator is a low molecular weight redox couple, which shuttles electrons from the enzyme redox center to the surface of the electrode. The following scheme describes the reactions which take place on the mediated electrode [8]:



where  $\text{GOD}^{\text{ox}}$  and  $\text{GOD}^{\text{red}}$  are the enzyme in oxidized and reduced form of its active center, respectively,  $\text{M}^{\text{ox}}$  and  $\text{M}^{\text{red}}$  are the oxidized and the reduced form of the electrochemical mediator. The conjugation of the enzyme catalyzed steps (2) and (3) is accomplished through the electrochemical reaction (4).

The use of the electrochemical mediator in the amperometric enzyme electrodes is connected with two basic requirements to these electrodes: the amperometric signal of the electrode must be independent of the concentration of the dissolved oxygen in the electrolyte; and the working potential

---

\*To whom all correspondence should be sent:  
E-mail: renirib@abv.bg

of the enzyme electrode must be low enough so that no organic compound in the electrolyte could be oxidized simultaneously with the substrate [9].

Quinones, organic dyes such as methylene blue, phenazines, methyl violet, Alizarin yellow, prussian blue, thionin, azure A and C, toluidine blue, iron complexes such as hexacyanoferrate, ferrocene and their derivatives, act as mediators and have been widely used in a number of biosensors [8, 10–15]. Sometimes the oxidized form of the mediator is dissolved in a bulk solution, so that the concentration of the mediator on the electrode surface decreases. This results in a gradual degradation of the electrode performance. This process can be moderated by a covalent binding of the mediator on the electrode surface by some functional groups [16] or by including in a polymer film, deposited on the electrode surface [17]. This approach makes possible the stability improvement of the mediated enzyme electrode.

The reduced forms of the mediators can be electrochemically oxidized on an electrode at potentials lower than that of the  $H_2O_2$ . This gives a possibility to design biosensors, operating at potentials lower than those based on the natural enzymatic reaction (1). It must be noticed that a low working potential of the biosensor is preferable in order to decrease the rate of oxidation of some compounds, usually present in physiological fluids. The oxidation of this compound results in an electric signal, disturbing the signal, obtained by the glucose oxidation. In this way the possible interference with the amperometric signal of the biosensor is reduced [5].

## EXPERIMENTAL

A disk of pyrolytic graphite with a 5 mm diameter is press – fitted into a Teflon holder. Prior to use, the electrode was polished on fine emery paper. After washing with distilled water, the electrode is electrochemically activated in 0.1 M phosphate buffer by consecutive anodic polarization at + 0,2 V (vs. Ag/AgCl) for 2 minutes and cathodic polarization at – 0.5 V for 5 minutes. Under this procedure, the pyrolytic graphite surface is oxidized, and oxygen containing quinoidal groups are generated on it [18]. The presence of such groups promotes a strong adsorption of the enzyme and of the mediator on the pyrolytic graphite electrode surface.

The enzyme electrode is prepared by the application of mediator solution on the activated pyrolytic graphite surface, and after drying in the air, the electrode surface is covered with a GOD or

LOD solution of the enzyme in a phosphate buffer (pH 7). After drying at a room temperature, the electrode is washed in a buffer solution. Between measurements the enzyme electrode is kept at 4 °C.

The enzyme electrodes are prepared also by consecutive application of a mediator and an enzyme on the porous supporting layer of carbon black-PTFE (polytetrafluorethylene) material. In other cases, a porous matrix of carbon material, wet proofed with PTFE, is embedded in a plastic tube and covered by a thin layer of a mixture of the same wet proofed material and mediator (p-benzoquinone). This thin layer forms the face of the electrode onto which the enzyme is immobilized.

The electrochemical measurements are performed in a two- or three-electrode cell with an Ag/AgCl reference electrode and Pt counter electrode. The electrolytes comprise of a 0.1 M phosphate buffer solution and a 0.1 M phosphate buffer solution, containing 0.1M KCl.

## RESULTS AND DISCUSSION

### *Mediated enzyme electrodes, prepared from electrochemically activated pyrolytic graphite electrode*

The quasi-redox potentials of the investigated ferrocene derivatives are obtained from the cyclic voltammograms of an electrochemically activated pyrolytic graphite electrode, modified with the corresponding compound. The obtained experimental values of the quasi-redox potentials of the investigated ferrocene derivatives are in a good coincidence with the literature data, as well as with our data, previously obtained with the same ferrocene derivatives, adsorbed on another type of carbon electrode [19, 20, 21]. The ferrocene derivatives whose substituent displays a positive (electron donor) induction effect ( $-CH_3$ ,  $-CH_2OH$ ,  $-CH_2COOH$ ), possess a more negative quasi-redox potential than that of the ferrocene. Ferrocene derivatives, where the substituents have a negative induction effect, possess a more positive quasi-redox potential than that of the ferrocene. According to the electron structure of the substituents in the pentadienyl ring, the quasi-redox potential of the corresponding ferrocene derivative can be prognosticated, and its suitability to be used as a mediator in enzyme electrodes can be eventually estimated.

The methanol-ferrocene possesses a more negative quasi-redox potential than that of the ferrocene, so that it is suitable to be used as a mediator in glucose and lactate electrodes. The

cyclic voltammogram is measured in a 0.1M phosphate buffer (Fig. 1, full line) and in the same

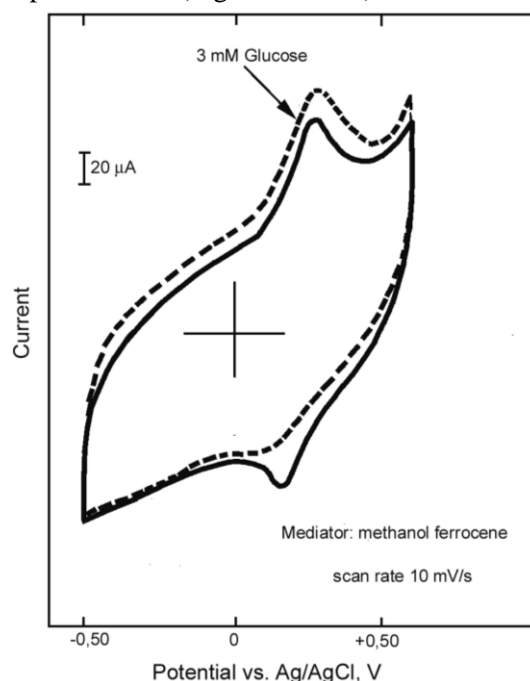


**Fig. 1.** Cyclic voltammograms of activated pyrographite electrodes with adsorbed GOD and methanolferrocene: in 0,1 M phosphate buffer (full line); in 0,1 M phosphate buffer containing 3 mM glucose (dotted line).

buffer which contains 3 mM of glucose (Fig. 1, dotted line). The observed increase of the anodic peak in the presence of glucose is due to the electrochemical oxidation of the reduced form of the mediator on the electrode surface. The decrease of the cathode peak is due to the consumption of part of the mediator through oxidation of the reduced form of the enzyme, obtained by the enzymatic oxidation of glucose. This effect, called the 'mediator effect', is observed also in the case of enzyme electrodes with another type of metallocene mediators [22].

The steady-state current of the investigated enzyme electrodes, as a function of the substrate concentration, is studied in both, the presence of oxygen dissolved in the electrolyte, and after the significant decrease of the dissolved oxygen concentration by blowing argon through the electrolyte. The behaviour of the lactate oxidase enzyme electrodes with mediator methanolferrocene or butylferrocene is also investigated. In order to check if the substrate (Li L-lactate) is directly oxidized on the electrode surface, electrode is prepared from electrochemically activated pyrolytic graphite, modified with a mediator and with a covering layer of Nafion. The steady-state current of these

electrodes at a constant potential of + 350 mV vs. Ag/AgCl is measured in the presence of Li L-lactate in the solution, and no amperometric signal is observed, i.e. the substrate is not directly oxidized on the electrode at this potential.

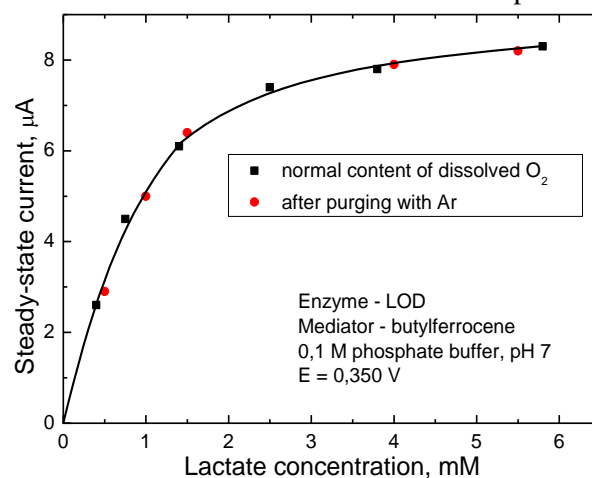


**Fig. 2.** Calibration curve of a lactate electrode with mediator butylferrocene: when electrolyte is with normal content of dissolved oxygen and after purging with Ar.

The calibration curve of a lactate electrode with butylferrocene is presented in Fig. 2. It is seen that the decrease in the oxygen concentration in the solution does not influence significantly the steady-state current of the electrode. This shows that the amperometric signal of the investigated electrode is generated mainly as a result of the action of the electrochemical mediator.

Application of the mediated enzyme electrode at a low working potential is preferable for the biosensing. The investigations are oriented at selecting those ferrocene derivatives which possess a redox potential lower than that of the ferrocene. Another way to achieve a mediated electrode with a low working potential is to use a structural analog of ferrocene which possesses a redox potential lower than that of the ferrocene. Investigations of the electrochemical behavior of the metallocenes in non-aqueous electrolyte have shown that the redox potential of a nickelocene/nichelocenium couple is ca. 0.4 V more negative than that of the ferrocene/ferrocenium couple [23, 24]. An investigation of nickelocene as an electrochemical mediator in GOD enzyme electrodes with low working potential is described for the first time in [25].

The stable cyclic voltammograms of the electrochemically activated pyrolytic graphite electrodes with adsorbed nickelocene and with adsorbed ferrocene are juxtaposed in Fig. 3. Two redox peaks, corresponding to the electrochemical reaction (3), are observed on each of the

voltammograms. The quasi redox potential of the nickelocene/nickelocenium couple is ca. 0,300 V more negative (cathodic) than that of the ferrocene/

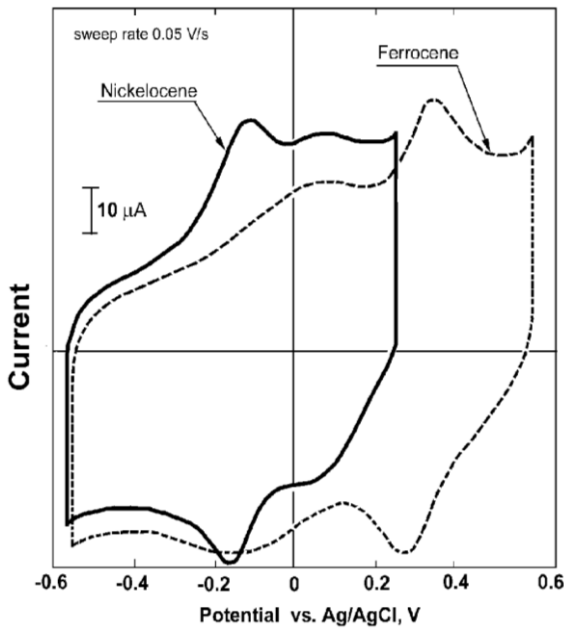


**Fig. 3.** Cyclic voltammograms of ferrocene and nickelocene adsorbed on activated pyrolytic electrode in 0,1 M phosphate buffer (pH 7.0).

ferrocenium couple (+ 0,230 V), obtained under the same conditions. This result is in agreement with the data for the redox potentials of the metallocenes in non-aqueous electrolytes [23, 24].

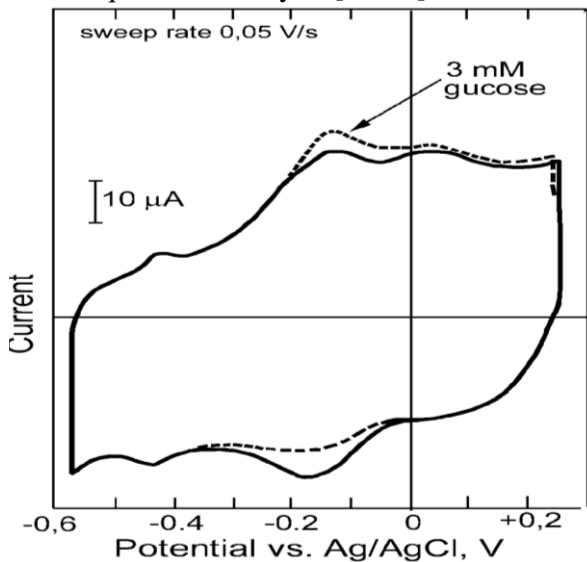


**Fig. 4.** Cyclic voltammograms of nickelocene GOD electrode in absence (full line) and in presence (dashed line) of 3 mM glucose in electrolyte (pH 7.0).

A nickelocene-mediated GOD electrode is prepared by adsorption of GOD on the electrochemically activated pyrolytic graphite with

adsorbed nickelocene. The cyclic voltammogram of such mediated electrode is presented in Fig. 4 (full line). In the presence of glucose (dotted line) the anodic peak of nickelocene ( $-0,105$  V) increases, whereas its cathode peak decreases. In the presence of the glucose, the oxidized form of the  $GOD^{ox}$  enzyme is reduced to  $GOD^{red}$  (2). The nickelocenium cations react with the  $GOD^{red}$  as a second substrate, which results in a decrease in their concentration (3), and correspondingly in a decrease of the cathode peak current of the electrochemical reduction of the nickelocenium to nickelocene. On the other hand, the nickelocene concentration increases due to reaction (3), which results in an increase in the anodic peak current of the electrochemical oxidation of nickelocene. The steady-state current of the nickelocene-mediated GOD electrode in 5 mM glucose solution vs. the controlled potential is presented in Fig. 5. At potentials more positive than the nickelocene redox potential ( $-0,105$  V), the steady-state current increases significantly and reaches a plateau in the potential range between 0.0 V and + 0.2 V. In the absence of glucose (background curve), the steady-state current is very low and is practically independent of the potential up to + 0.2 V.

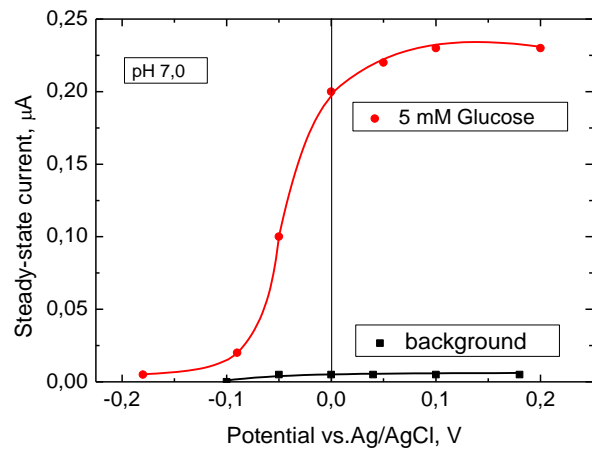


**Fig. 5.** Polarization curves of nickelocene-mediated GOD electrode in absence (background curve) and in presence of 5 mM glucose.

Fig. 6 presents the dependence of the steady-state amperometric response of the enzyme electrode with a nickelocene mediator at a potential of 0.0 V vs. Ag/AgCl as a function of the glucose concentration in the electrolyte. The removal of the dissolved oxygen in the cell by bubbling with Ar results in a small increase (less than 10 %) of the steady-state current in the whole investigated interval of glucose concentrations. The obtained calibration curve possesses a linear part of 0.05 mM

up to at least 1.00 mM of glucose. From the slope of the electrochemical Eadie-Hofstee plot the apparent Michaelis constant is obtained to be 1.10 mM.

The low value of the nickelocene/nickelocenium couple redox potential makes possible the use of adsorbed nickelocene as an electrochemical mediator in the amperometric glucose biosensors operation at potentials of ca. 0.00 V (vs. Ag/AgCl). This is important for the elimination of the

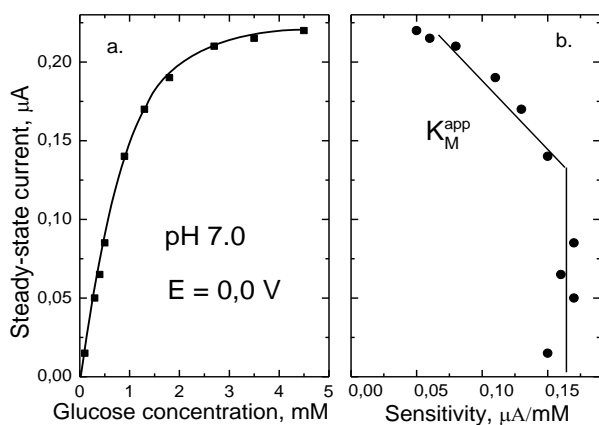


**Fig. 6.** (a) Calibration curve of nickelocene-mediated GOD electrode at  $E = 0,0 \text{ V}$  vs. Ag/AgCl, (b) the same data in electrochemical Eadie-Hofstee coordinates.

influence of interfering species in the real glucose assay.

#### *Mediated enzyme electrodes, prepared from PTFE modified carbon black*

PTFE modified carbon blacks are prepared as a powder material by a special technology [26], which allows the use of different carbon blacks, and at a controlled carbon black/PTFE ratio. This material possesses a very high porosity, combined with an electronic conductivity, and a high hydrophobicity. Enzymes can be immobilized easily on this surface by adsorption. Mediators are mixed with the PTFE modified carbon blacks to form a powdered composite material. Porous tablet with a significant mechanical strength are pressed from this composite material without the use of any additional binder. The electrode, of different shape and dimensions, can be cut out from the tablet. [10] describes the performance of the electrodes with GOD, immobilized on a porous matrix of carbon black wet proofed with PTFE, and p-benzoquinone (BQ) as a mediator.

Fig. 7 presents the steady-state current of the electrodes with constant amount of BQ (30 wt. % in the mixture) and with increasing amounts of GOD (from 0.05 to 0.35 mg per electrode) as a function

of glucose concentration. The current increases and tends to a saturation value with the increase in the glucose concentration. The saturation current and the slope of the linear part of the presented curves (at low glucose concentrations) increase with the amount of GOD in the electrolyte. The amperometric biosensor with mediated enzyme electrodes based on GOD, and mediators, adsorbed on carbon black surface, is described in [27]. The

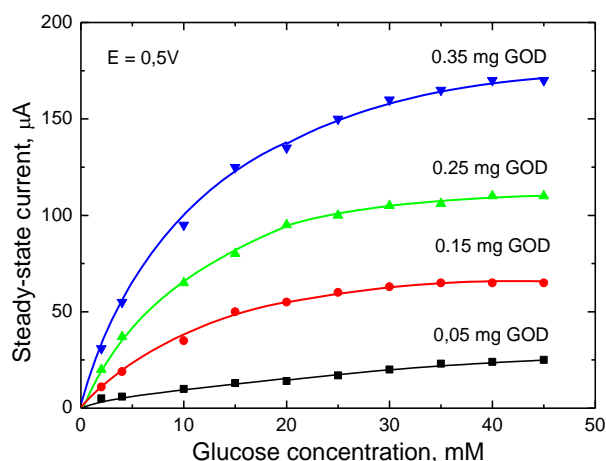


**Fig. 7.** Steady-state current of electrodes with 30 wt. % BQ and different amount of GOD as a function of the glucose concentration.

data, obtained with the mediator nickelocene, are juxtaposed with the results, obtained with ferrocene and its derivatives. The data show similar electrochemical behaviour of the investigated ferrocenes whether applied on the carbon black electrode or applied on the graphite electrode. The obtained difference between the anodic and cathodic peak potentials of the nickelocene, ferrocene and their derivatives on carbon black is bigger by 0.1V than that obtained under the same conditions on pyrolytic graphite. This can be explained by the multilayer coverage of the mediator on the carbon black surface. The adsorption of GOD on metallocene modified carbon black surface does not lead to a great change in the cyclic voltammograms of the electrodes. An insignificant decrease of the dynamic double-layer capacity of the electrode is observed, probably due to the partial blocking of the electrode surface by the adsorbed enzyme [27].

Fig. 8 presents the calibrations curves of a biosensor with ferrocene and nickelocene mediators. The figure shows that the nickelocene mediated glucose oxidase electrode exhibits a similar behaviour to that of the mediated with ferrocene. However, the quasi-redox potential of nickelocene/nickelocenium cation, which is by

0.3 V more negative than that of any of the investigated ferrocene derivatives, significantly lowers the operating potential of the biosensor to 0.00 V vs. Ag/AgCl electrode. This is important for direct glucose determination in the physiological fluids (blood, urine), where an increased selectivity of the assay is desirable. The close values of  $K_M^{\text{app}}$  for nickelocene and ferrocene-mediated electrodes are due to a similarity in the reaction mechanism.

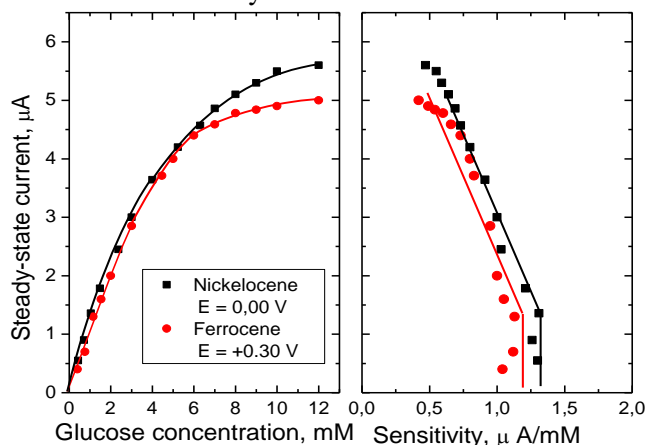


**Fig. 8.** (a) Dependence of the steady-state current of a mediated biosensor on glucose concentration; mediators ferrocene ( $E = +0,300$  V) and nickelocene ( $E = +0,0$  V). (b) Corresponding electrochemical Eadie-Hofstee plots.

## CONCLUSIONS

Enzyme electrodes of different range of linearly dependent signal from the substrate concentration and different sensitivity can be developed using various mediators.

The results, obtained with the electrochemically modified pyrolytic graphite or the PTFE modified carbon blacks, show that the future application of mediator enzyme electrodes (ferrocene, derivatives, nickelocene, other) is possible in the field of bioreactors and biofuel cell use.

## REFERENCES

1. A. Turner, I. Karube, G. Wilson, *Biosensors: Fundamentals and Application*, Oxford University Press, Oxford, 1987.
2. J. Czanan, *Anal Chem.*, **57**, 345A (1985).

3. *Biosensors: A Practical Approach*, edited by A. Cass, Oxford University Press, 1990.
4. J. Wang, *J. Pharmaceutical & Biomedical Analysis*, **19**, 47 (1999).
5. I. Iliev, A. Kaisheva, *Bulg. Chem. Commun.*, **27**, 558 (1994).
6. L. Clark and C. Lyons, *Ann. N.Y. Acad. Sci.*, **102**, 29 (1965).
7. J. Updike and G. Hicks, *Nature*, **214**, 986 (1967).
8. A. Cass, G. Davis, G. Francis, H. Hill, W. Aston, I. Higgins, E. Plotkin, L. Scott, A. Turner, *Anal. Chem.*, **56**, 667 (1984).
9. A. Chaubey, B. Malhotra, *Biosensors & Bioelectronics*, **17**, 441 (2002).
10. P. Atanasov, I. Iliev, *Commun. Dept. Chem.*, **22**, 295 (1989).
11. T. Ikeda, T. Shibata, M. Senda, *J. Electroanal. Chem.*, **261**, 351 (1989).
12. F. Ricci, G. Palleschi, *Biosensors & Bioelectronics*, **21**, 389 (2005).
13. J. Luong, C. Masson, R. Brown, K. Male, A. Nguyen, *Biosensors & Bioelectronics*, **9**, 577 (1994).
14. S. Hendry, M. Cardosi, E. Neuse, A. Turner, *Anal. Chim. Acta*, **281**, 453 (1995).
15. B. Brunetti, P. Ugo, L. Moretto, C. Martin, *J. Electroanal. Chem.*, **491**, 166 (2000).
16. B. Piro, V. Do, L. Le, M. Hedayatullah, M. Pham, *J. Electroanal. Chem.*, **486**, 133 (2000).
17. N. Foulds, C. Lowe, *Anal. Chem.*, **60**, 2473 (1988).
18. G. Jonsson, L. Gorton, L. Petterson, *Electroanalysis*, **49**, 49 (1991).
19. A. Kaisheva, S. Christov, I. Iliev, *Bulg. Chem. Commun.*, **27**, 598 (1994).
20. T. Ikeda, H. Hamada, K. Miki, M. Senda, *Agric. Biol. Chem.*, **49**, 541 (1985).
21. T. Ikeda, *Bull. Electrochem.*, **U8**, 145 (1992).
22. P. Atanasov, V. Bogdanovskaya, I. Iliev, M. Tarasevich, V. Vorobjev, *Elektrokhimiya* (in Russian), **25**, 1480 (1989).
23. J. Holloway, W. Geiger, *J. Am. Chem. Soc.*, **101**, 2038 (1979).
24. S. Kukharensko, *Dokl. Acad. Nauk SSSR* (in Russian), **303**, 112 (1988).
25. P. Atanasov, A. Kaisheva, S. Gamburzev, I. Iliev, *Electroanalysis*, **5**, 91 (1993).
26. I. Iliev, A. Kaisheva, *US Patent No 1392341*.
27. P. Atanasov, A. Kaisheva, S. Gamburzev, I. Iliev, *Sensors & Actuators B*, **8**, 59 (1992).

## МЕДИАТОРНИ ЕНЗИМНИ ЕЛЕКТРОДИ

Р. И. Букурещлиева<sup>1</sup>, С.М. Христов<sup>1</sup>, Й.Д. Милушева<sup>1</sup>, П.Б. Атанасов<sup>2</sup>,  
А.Р.Кайшева<sup>1</sup>

<sup>1</sup>*Институт по електрохимия и енергийни системи, БАН*

<sup>2</sup>*Университет на Ню Мексико, Албукърки, САЩ*

Постъпила на 29 юни, 2010 г. ; преработена на 21 октомври, 2010 г..

(Резюме)

В настоящата обзорна статия е обобщен дългогодишния опит на колектива от секция „Електрохимия на биокаталитичните и металовъздушни системи” в областта на медиаторните ензимни електроди. Изследвани са окислително-редукционните свойства на медиаторния ензимен електрод в зависимост от вида на въглеродните материали (компактен въглероден материал – пирографит, или дисперсен въглероден материал – въглеродни сажди); използваните медиатори (фероценови производни, никелоцен и бензохинон) и от вида на ензима (глюкозо-оксидаза и лактат-оксидаза).

## Electrodeposition of Silver-Cobalt Coatings. Electrolytes.

S. L. Nineva\*, Ts. V. Dobrovolska, I. N. Krastev

*Rostislav Kaischew Institute of Physical Chemistry, Bulgarian Academy of Sciences, Sofia 1113, Bulgaria*

Received: July 13, 2010; accepted: December 25, 2010

Literature data on silver, cobalt and silver-cobalt electrolytes are presented and discussed. The electrodeposition of the silver-cobalt coating is carried out from appropriate cyanide-pyrophosphate electrolytes at 50 °C. The studies show possibilities for deposition of compact silver-cobalt coatings with high cobalt content (up to 50%). The deposited coatings could be successfully used for further investigation of their physico-mechanical and electrical properties.

**Keywords:** electrodeposition, electrolyte, morphology, pyrophosphate, silver-cobalt coatings

### INTRODUCTION

The modern technology requires the development of new materials with designed properties. Often attempts were made to combine some properties of different metals and/or alloys in order to produce a new material with desired or sometimes unexpected properties. The interest in electrodeposition of silver-cobalt alloys is based on the possibility to synergize the unique electrical, thermal, catalytic and etc. properties of silver with the magnetic, mechanical, catalytic etc. properties of an element existing in two modifications and two valence states, like the cobalt. In principle, both metals are not miscible and dispersable in each other and acting through very high developed interface they could offer very attractive properties, like the observed giant magnetoresistance phenomena, typical for this system [1].

A literature research is presented in this paper, including the information about silver and cobalt electrolytes. Data on known electrolytes for silver-cobalt deposition, published previously [2] are introduced again in order to complete the information.

The electrochemical processes during electrodeposition of silver-cobalt alloys from cyanide-pyrophosphate electrolytes carried out at room temperature was presented in a previous paper [2]. The electrolyte composition and the electrolysis conditions allow the deposition of smooth and compact coatings in a small range of current densities.

In order to extend the working range of the current densities, investigations at higher temperature (50 °C) were performed. Preliminary

results of these investigations were briefly reported elsewhere [3].

More detailed investigations on the behavior of the electrolyte at higher temperature and on the composition and structure of the obtained coatings, are discussed in the following two papers, the one presented here is devoted to the morphological characteristic of the obtained silver, cobalt and silver-cobalt coatings, and the next, second one, reviews the electrode processes [4].

### REVIEW

#### *Electrodeposition of silver*

The excellent thermal and electrical conductivities of silver retain when this metal is deposited as a galvanic coating onto different substrates. As result, the silver electrodeposition is a widely applied and well researched process. One of the first patents on silver deposition appeared in 1840 [5]. The cyanide electrolyte, described in this patent, is one of the most used electrolytes up to now. It is composed on the basis of potassium dicyanoargentate with an excess of free cyanide ions. A lot of other electrolytes are suggested – onto nitrate, iodide, urea, thiocyanate, sulfamate, thiosulphate, and other bases [6–15]. A comprehensive review of the electrolytes for silver deposition is presented in the theses of I. Krastev [16, 17]. The electrochemical processes of silver deposition are just marked in this paper, due to the well presented and systematic literature data on this topic.

Literature data about sulfamate, ethylenediaminetetraacetate (EDTA), sulfosalicylate and etc. electrolytes for silver deposition are known [6, 11–17]. Some data on the most used non-cyanide silver electrolytes are presented in Table 1.

\* To whom all correspondence should be sent:  
E-mail: [snineva@ipc.bas.bg](mailto:snineva@ipc.bas.bg)

**Table 1.** Non-cyanide (or without free cyanide) electrolytes for silver deposition.

Type of electrolyte, [References]	Electrolyte composition	Concentration, g dm <sup>-3</sup>	J, A dm <sup>-2</sup>	T, °C	Note
Ferrocyanide [6]	AgCl	20–40	1–1.5	60–80	Soluble anodes can not be used because of the silver passivation in this solution
	K <sub>4</sub> [Fe(CN) <sub>6</sub> ]	160–200			
	K <sub>2</sub> CO <sub>3</sub> CO(NH <sub>2</sub> ) <sub>2</sub>	20			
Ferrocyanide – thiocyanate [6]	AgCl	15–40	0.5 – 1	20–60	One of the best substitutes for the hazardous cyanide electrolytes
	K <sub>4</sub> [Fe(CN) <sub>6</sub> ]	30–60			
	Na <sub>2</sub> CO <sub>3</sub>	20–35			
	KCNS	150			
Sulfite [6]	AgCl	40	0.2 – 0.5	15–25	Unstable electrolyte, fast decomposition
	K <sub>4</sub> [Fe(CN) <sub>6</sub> ]	60			
	Na <sub>2</sub> CO <sub>3</sub>	25			
	Na <sub>2</sub> SO <sub>3</sub>	100–150			
Thiocyanate [6]	Ag	25	0.5 – 1	15–25	Low throwing power
	NH <sub>4</sub> CNS	300			
	H <sub>3</sub> BO <sub>3</sub>	20			
Pyrophosphate [6]	Ag as AgNO <sub>3</sub>	15–90	0.5 – 3.5	room temper.	The throwing power is low, but the quality of the coating – very good
	K <sub>4</sub> P <sub>2</sub> O <sub>7</sub>	100–350			
	(NH <sub>4</sub> ) <sub>2</sub> CO <sub>3</sub>	20–145			
Iodide [6, 12, 14]	AgCl	30–60	0.1–0.25	20–40	Trend to electrolyte decomposition; the coatings absorb iodine
	KJ	400–450			
	Gelatine	1–2			
Bromide [12]	AgBr	40–50	1.3	18–20	Preliminary amalgam formation on the substrate is necessary
	NH <sub>4</sub> Br	600			
	HBr	8			
	Gelatine	2–4			
Succinimide [11, 14]	Ag	30	1	20–70	Low tarnish resistance
	Succinimide K <sub>2</sub> SO <sub>4</sub>	12–55 45			
Thiosulfate [6, 14]	Ag	30	0.4–1.0	15–30	Weak adhesion of the obtained coating, lower tarnish resistance, in comparison with coatings, from cyanide electrolytes
	Na <sub>2</sub> S <sub>2</sub> O <sub>3</sub>	300–500			
	NaOH	Up to pH 8–10			

### *Electrodeposition of cobalt*

The beginning of the industrial electroplating of the cobalt dates back to the early 20th century [18]. In the beginning, the interest arose from the decorative and corrosion-resistant properties of this metal [18, 19]. During the next 60 years of the 20<sup>th</sup> century the interest in the electrodeposition of cobalt and its alloys was renewed due to its magnetic properties [19, 20].

The electrodeposition of cobalt is described in details, including the applied aspects, in the review of F. R. Moral [19] which is related to the period before 1963, as well in some chapters in reference books, and in the scientific journals [20–24]. Later, Armanov [25] carried out some investigations on electrodeposited cobalt and cobalt alloy coatings, connected with the magnetic properties of these materials.

Cobalt is deposited from acid up to low alkaline electrolytes – sulphate, chloride, sulfamate, fluoride and fluoroborate, triethanolamine, gluconate, citrate, pyrophosphate, hydroxide, and etc. electrolytes.

The most cited and used electrolytes are summarized in Table 2. Some other specified electrolytes, like non-aqueous electrolytes and chloride electrolyte, used for the investigation of the oxygen evolution reaction [23, 26–28], are mentioned in the literature.

An appropriate complex electrolyte for cobalt electrodeposition is the pyrophosphate electrolyte. The nature of the pyrophosphate compound of the cobalt has been investigated in the first half of the 20<sup>th</sup> century [39, 40], and some years later, the information, concerning the usage of pyrophosphate electrolytes for deposition of cobalt alloys with tungsten and some ternary alloys [20, 37, 38], started to appear in the literature.

**Table 2.** Electrolytes for cobalt deposition.

Type of electrolyte, [References]	Electrolyte composition	Concentration, g dm <sup>-3</sup>	J, A dm <sup>-2</sup>	T, °C	Note
Sulfate, Ammonium sulfate [19-21, 23, 29]	CoSO <sub>4</sub> .7H <sub>2</sub> O	0 – 504	4 – 17	20 – 45	The specified composition is the most frequently used and cited in the literature. In some cases Na <sub>2</sub> SO <sub>4</sub> is used; pH 5–6.5 [4]
	Co(NH <sub>4</sub> ) <sub>2</sub> (SO <sub>4</sub> ) <sub>2</sub> x	0 – 175			
	6H <sub>2</sub> O				
	NaCl	0 – 17			
With Sulfuric acid [24]	H <sub>3</sub> BO <sub>3</sub>	0 – 45	Up to 20	30	pH down to 2 (with H <sub>2</sub> SO <sub>4</sub> )
	CoSO <sub>4</sub>	0.5 mol dm <sup>-3</sup>			
Chloride [19, 21, 23, 24, 30*, 31*]	H <sub>2</sub> SO <sub>4</sub>		1 – 12	25 – 71	pH down to 5 (with HCl) * Electrodeposition at potentiostatic conditions 1.18-1.28 V (SCE)
	CoCl <sub>2</sub> .6H <sub>2</sub> O	0 – 400			
	CoCl <sub>2</sub>	0 – 10 mM			
	H <sub>3</sub> BO <sub>3</sub>	0 – 25			
	NH <sub>4</sub> F.HF	0 – 86			
	NH <sub>4</sub> Cl	0 – 1 M			
Sulfamate [19, 21]	HCl		0.5 – 6	25 – 40	pH 5.2–5.5
	Co(SO <sub>3</sub> NH <sub>2</sub> ) <sub>2</sub>	250 – 450			
	Antipitting additive	0 – 375			
	Formaldehyde H <sub>3</sub> BO <sub>3</sub>	0 – 30			
Fluoride and fluoroborate [19, 21, 23]		0 – 30	4.1 – 6.5	25 – 50	pH 3.5
	Co(BF <sub>4</sub> ) <sub>2</sub>	0 – 160			
	CoF <sub>2</sub>	0 – 0.1216 ml dm <sup>-3</sup>			
	H <sub>3</sub> BO <sub>3</sub>	0 – 0.623			
Triethanolamine [20, 21]	HF		2	no data	pH 2.6–6.6 The coatings are bright; after prolonged electrolysis Co(OH) <sub>2</sub> precipitates.
	CoSO <sub>4</sub> .7H <sub>2</sub> O	75			
	N(C <sub>2</sub> H <sub>4</sub> OH) <sub>3</sub>	70 ml dm <sup>-3</sup>			
Citrate [32-35]		0 – 0.36	0.33-2	25 – 75	pH 2–7
	CoSO <sub>4</sub> .7H <sub>2</sub> O				
	CoCl <sub>2</sub>	0 – 0.50			
	Na <sub>3</sub> C <sub>6</sub> H <sub>5</sub> O <sub>7</sub> .2H <sub>2</sub> O	0.08 – 0.19			
Gluconate [36]	C <sub>6</sub> H <sub>8</sub> O <sub>7</sub>	0.05 – 0.10	2 - 3	25 – 50	*optimal amount of 50 g dm <sup>-3</sup> pH 2–5
	H <sub>3</sub> BO <sub>3</sub>	mol dm <sup>-3</sup>			
	CoSO <sub>4</sub> .7H <sub>2</sub> O	20 – 100			
	Na-gluconate	10 – 100*			
Pyrophosphate [21, 37*, 38*]	H <sub>3</sub> BO <sub>3</sub>	0 – 50	Up to 20	30 – 60	* Mainly used for codeposition of Co with W;
	CoCl <sub>2</sub> .6H <sub>2</sub> O	6 – 60			
	Na <sub>2</sub> WO <sub>4</sub> .2H <sub>2</sub> O	3.3 – 165			
	K <sub>4</sub> P <sub>2</sub> O <sub>7</sub>	15.2 – 152			
Hydroxide [21]	NH <sub>4</sub> C <sub>6</sub> H <sub>7</sub> O <sub>7</sub>	10 – 12	1.25 – 2.50	70 – 90	Electrolyte for flexible and well leveled coatings
	Co(OH) <sub>2</sub>	10			
	NaOH	140			
	EDTA	64			
Formaldehyde used as brightener [20, 21]	Bone glue	0 – 10	no data	no data	The addition of Cd increases the brightness of the coating and improves the leveling effect
	CoSO <sub>4</sub> .7H <sub>2</sub> O	200			
	NH <sub>4</sub> COOCH <sub>3</sub>	30			
	CH <sub>3</sub> COOH	1			
	HCHO	3			
	CdSO <sub>4</sub> .8H <sub>2</sub> O	0.2			

#### *Electrodeposition of silver-cobalt alloys*

The electrodeposition of silver-cobalt alloys is relatively rarely investigated. The existing literature data on the deposition of this alloy are insufficient and incomplete [41]. The reason for this is the big difference between the deposition potentials of both metals and the difficulties, connected with the preparation of stable electrolytes with high metal concentrations. Silver is a noble metal, more positive than cobalt, and this is the reason for the use of complex compounds to bring the deposition potentials of both metals close together. Table 3

shows the best known electrolytes for silver-cobalt alloy deposition [2].

Most of the investigations, described in the literature, are related to the silver-cobalt electrodeposition from cyanide-pyrophosphate electrolytes.

The electrodeposition of silver from cyanide complex electrolytes, as well as the influence of different anions onto the hydrogen evolution reaction from such electrolytes are well researched [5, 16, 48]. It is shown in the work of Halder [40]

**Table 3.** Electrolytes for silver-cobalt deposition

Type of electrolyte, [References]	Electrolyte composition	Concentration, g dm <sup>-3</sup>	J, A dm <sup>-2</sup>	T, °C	Note
Cyanide [41]	Ag as Ag <sub>2</sub> SO <sub>4</sub>	2.2	0.3 – 0.7	18	Cathodic current efficiency – 50%
	Co as Co(CN) <sub>2</sub>	0.6			
	NaCN	12			
Cyanide-pyrophosphate I [6, 42]	Ag as KAg(CN) <sub>2</sub>	1	0.1 – 1	20 – 60	Ag + Co ≤ 6 g dm <sup>-3</sup> Cathodic current efficiency - 40 - 50%, pH 7 – 10
	Co as CoSO <sub>4</sub> ·7H <sub>2</sub> O	5			
	K <sub>4</sub> P <sub>2</sub> O <sub>7</sub>	100			
Cyanide-pyrophosphate II [43, 44]	CoSO <sub>4</sub> ·7H <sub>2</sub> O	43	1 – 40 mA cm <sup>-2</sup>	40-45	pH 7 – 9.5
	K <sub>4</sub> P <sub>2</sub> O <sub>7</sub>	120			
	Ag as solution containing:	0.15 (2 ml)			
	KCN – 120 g dm <sup>-3</sup> ; AgCN – 40 g dm <sup>-3</sup> ; K <sub>2</sub> CO <sub>3</sub> – 20 g dm <sup>-3</sup>				
Thiocyanate [41]	Ag as AgNO <sub>3</sub>	11	0.8	50	The coating is hard, brittle, and can not be easily polished
	Co as Co(NO <sub>3</sub> ) <sub>2</sub> ·6H <sub>2</sub> O	6			
	NaSCN	98			
Nitrate [41]	Ag as AgNO <sub>3</sub>	10	0.4	47	-
	Co as Co(NO <sub>3</sub> ) <sub>2</sub> ·6H <sub>2</sub> O	18			
	Thiourea	215			
Citrate [45]	CoSO <sub>4</sub> ·7H <sub>2</sub> O	5 – 16	1 – 10 mA cm <sup>-2</sup>	85	pH 9.5
	Ag <sub>2</sub> SO <sub>4</sub> Na <sub>3</sub> C <sub>6</sub> H <sub>5</sub> O <sub>7</sub> ·2H <sub>2</sub> O	0.1 – 5.5			
	Na <sub>2</sub> SO <sub>4</sub> ·10H <sub>2</sub> O	76			
		4			
Perchlorate I [46]	CoSO <sub>4</sub> ·7H <sub>2</sub> O	10	3.75 mA cm <sup>-2</sup>	no data	pH ≤ 1
	60% HClO <sub>4</sub>	50			
	Thiourea	0.4			
	AgNO <sub>3</sub>	0.8			
Perchlorate II [47]	AgClO <sub>4</sub>	0.01	-	25	pH 3.7; Electrodeposition at potentiostatic conditions between -770 and -850 mV; The deposits are black and rough.
	Co(ClO <sub>4</sub> )	0.1			
	Thiourea	0.1			
	Gluconate	0.1			
	H <sub>3</sub> BO <sub>3</sub>	0.3			
	NaClO <sub>4</sub>	0.1			
Iodide [24]	AgI	0.01	100–700 A m <sup>-2</sup>	no data	pH 2.3
	CoSO <sub>4</sub> ·7H <sub>2</sub> O	0.1			
	KI	1			
	Cresol sulfonic acid	0.01			

that the pyrophosphate ions act as complexing agents for the cobalt ion. Literature data about silver-pyrophosphate complexes were found in the study of Orechova, cited in Gmelin [49]. More detailed investigations on the electrodeposition of silver from pyrophosphate electrolytes are presented by S. Pilauskene and V. Kajkaris [50].

### EXPERIMENTAL

The electrolyte has a very low metal concentration (sum of both metals – 6 g dm<sup>-3</sup>), without free cyanide and with an excess of free pyrophosphate ions (the concentration of potassium pyrophosphate is 100 g dm<sup>-3</sup>). The electrolyte is alkaline (pH 9–10), stable, with very well complexed ions of both metals, and it is appropriate for their co-deposition.

The composition of the electrolyte is:

Ag as KAg(CN)<sub>2</sub> – 1 and 10 g dm<sup>-3</sup> (0.009 and 0.09 mol dm<sup>-3</sup>); Co as CoSO<sub>4</sub>·7H<sub>2</sub>O varies – 5 and 10 g dm<sup>-3</sup> (0.085 and 0.17 mol dm<sup>-3</sup>); K<sub>4</sub>P<sub>2</sub>O<sub>7</sub> – 100 g dm<sup>-3</sup> (0.3 mol dm<sup>-3</sup>). The electrolytes were prepared using chemicals of *pro analysis* purity and distilled water by the following procedure:

Depending on the desired volume, each component was dissolved separately in distilled water as follows: KAg(CN)<sub>2</sub> and CoSO<sub>4</sub>·7H<sub>2</sub>O were dissolved each in water of about 1/5<sup>th</sup> of the end volume of the electrolyte. K<sub>4</sub>P<sub>2</sub>O<sub>7</sub> was dissolved in a water amount of 1/2 of the end volume of the electrolyte. After that, the obtained solutions were mixed together as follows: the dissolved cobalt salt was added under stirring into the pyrophosphate solution which obtains a dark violet color. After

that the silver salt was added therein. No changes in the appearance of the electrolyte were observed. It remains stable in time.

The experiments were performed in a 100 cm<sup>3</sup> glass cell at 50°C without stirring of the electrolyte, under galvanostatic conditions. Copper cathodes (2 × 1 × 0.03 cm) and platinum anodes were used. The preliminary preparation of the copper cathodes includes a standard procedure of electrochemical degreasing followed by pickling in a 20% solution of sulphuric acid. In order to avoid the contact deposition of silver, the cathode was immersed into the electrolyte under current.

The elemental composition on the coating surface was measured by Energy-dispersive X-ray spectroscopy (EDAX), and the surface morphology was studied by Scanning electron microscopy (SEM).

#### RESULTS AND DISCUSSION

The surface morphology of a silver coating, obtained at 0.2 A dm<sup>-2</sup> from the cyanide-

pyrophosphate electrolyte, containing 1 g dm<sup>-3</sup> Ag, is shown in Figure 1a. The coating is not compact due to the low metal concentration in the electrolyte. Generally (in the plating technologies), the silver is deposited from electrolytes with higher concentrations of the silver cyanide salt in order to increase the effectiveness of the deposition process. Such electrolytes are stable and do not precipitate. The surface morphology of a silver coating, obtained from cyanide-pyrophosphate electrolyte, containing 10 g dm<sup>-3</sup> Ag, is shown in Figure 1b. The well-formed silver crystallites are visible on the electrode surface.

The surface needle-like morphology of the cobalt coatings, deposited under galvanostatic conditions from the pyrophosphate electrolyte, is presented in Figure 2. The appearance of the coating could be related to the morphology of the cobalt coatings onto Cu- substrate, containing mixture of hcp Co and fcc Co [51].

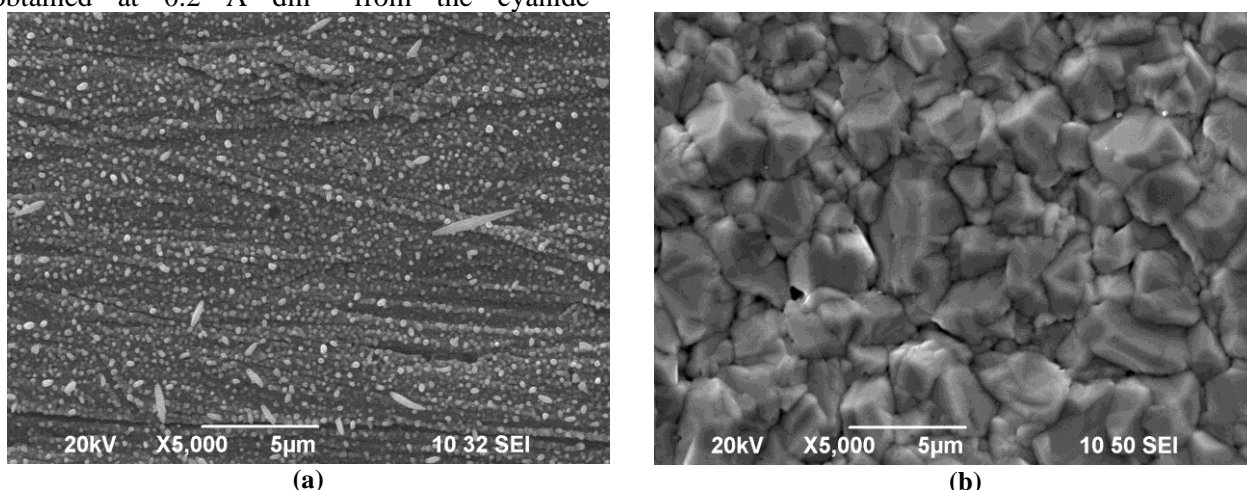


Fig. 1. SEM images of the surface morphology of galvanostatic deposited silver coating at 0.2 A dm<sup>-2</sup> from electrolytes containing 100 g dm<sup>-3</sup> K<sub>4</sub>P<sub>2</sub>O<sub>7</sub>; (a) - 1 g dm<sup>-3</sup> Ag; (b) - 10 g dm<sup>-3</sup> Ag.

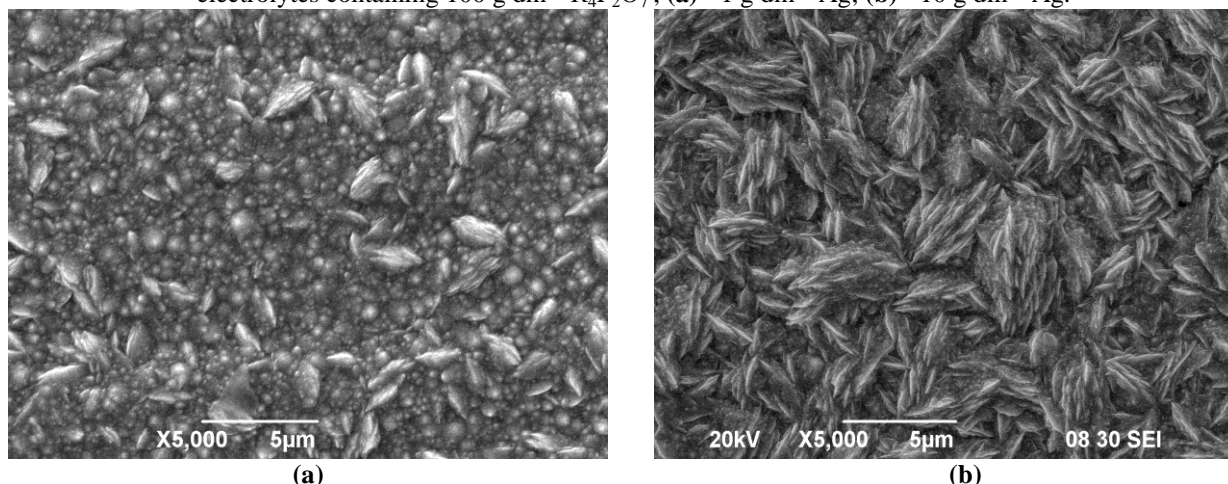
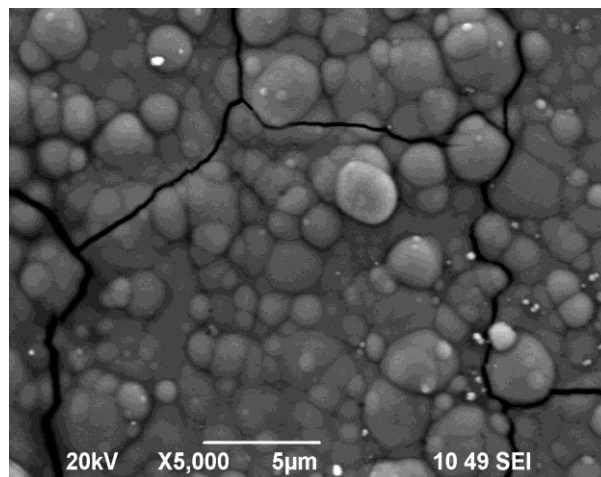


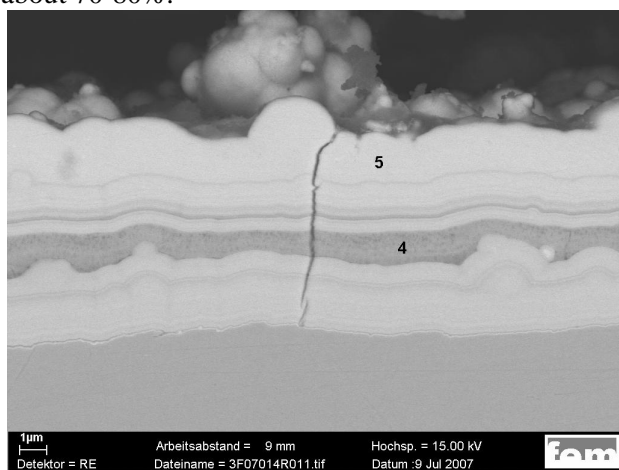
Fig. 2. SEM images of the surface morphology of galvanostatic deposited cobalt coating at 0.3 A dm<sup>-2</sup> from an electrolyte containing 100 g dm<sup>-3</sup> K<sub>4</sub>P<sub>2</sub>O<sub>7</sub> and: (a) - 5 g dm<sup>-3</sup> Co; (b) - 10 g dm<sup>-3</sup> Co.

The silver-cobalt coatings from the cyanide-pyrophosphate electrolyte, obtained at low current densities ( $0.1 \text{ A dm}^{-2}$ ), are white and contain practically only silver. With the increase of the current density to up to  $0.5 \text{ A dm}^{-2}$ , the coatings become grey and in the investigated range of current densities remain dark-grey, but compact.

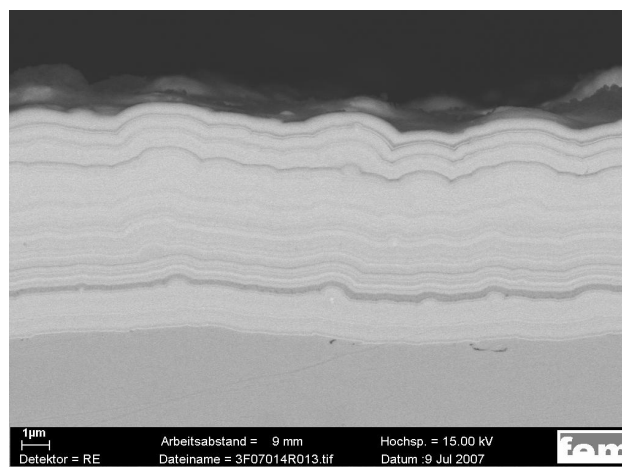
Figure 3 shows the morphology of an alloy coating with a cobalt content of about 40 wt.%. The coating has well-formed spheroids and the cobalt is distributed uniformly. At cobalt contents more than 25 wt. %, the coatings are stressed and some cracks appear. With the increase in the current density to up to  $0.4 \text{ A dm}^{-2}$ , the deposition of coatings with up to 50 wt. % cobalt is possible. They are heterogeneous, consisting of light and dark regions, but compact. The cathodic current efficiency is about 70-80%.



**Fig. 3.** SEM image of the alloy coating ( $1 \text{ g dm}^{-3} \text{ Ag}$ ,  $5 \text{ g dm}^{-3} \text{ Co}$ ,  $100 \text{ g dm}^{-3} \text{ K}_4\text{P}_2\text{O}_7$ ) deposited at  $0.3 \text{ A dm}^{-2}$ .



(a)



(b)

**Fig. 4.** SEM image of cross-sections of alloy coatings ( $1 \text{ g dm}^{-3} \text{ Ag}$ ,  $5 \text{ g dm}^{-3} \text{ Co}$ ,  $100 \text{ g dm}^{-3} \text{ K}_4\text{P}_2\text{O}_7$ ) deposited at:  
(a) -  $0.3 \text{ A dm}^{-2}$ : Spectrum 4-14.37 wt. % Ag, 80.99 wt. % Co, 4.64 wt. % O; Spectrum 5-90.25 wt. % Ag, 9.75 wt. % Co;  
(b) -  $0.4 \text{ A dm}^{-2}$ .

Figures 4a and 4b present cross-sections of alloy coatings, obtained at different current densities –  $0.3 \text{ A dm}^{-2}$  and  $0.4 \text{ A dm}^{-2}$ , respectively. Some layered structure of the coatings is observed. After exhaustion of the more positive element in the vicinity of the electrode during deposition of a sublayer of about  $2 - 3 \mu\text{m}$  thickness, the mechanism changes, and the formation of cobalt-rich sublayers starts (Figure 4a). With the increase of the current density, the influence of the natural convection also increases due to the faster exhaustion of the strong complexed metal ions, discharging on the cathodic surface which leads to a better defined multilayered structure (Figure 4b) with sublayers of about 100–150 nm thickness.

## CONCLUSIONS

On the basis of an extensive literature study the possible electrolytes for deposition of silver, cobalt and silver-cobalt alloy are reviewed. The possibilities for deposition of compact coatings with high cobalt content (of up to 50%), in a range of current densities of up to  $0.4 \text{ A dm}^{-2}$  at  $50 \text{ }^\circ\text{C}$ , are shown using a cyanide-pyrophosphate electrolyte. Cross-sections of the alloy deposits show spontaneous formation of structured multilayer coatings. The electrolyte could be successfully used for deposition of silver-cobalt compact coatings and further investigation of their physico-mechanical and electrical properties.

**Acknowledgement:** The authors express their gratitude to the Deutsche Forschungsgemeinschaft (DFG) (Project 436 BUL 113/97/0-4) for the support.

REFERENCES

1. J. Q. Xiao, J. S. Jiang, C. L. Chien, *Phys. Rev. Letters B*, **46**, 9266 (1992)
2. S. Nineva, Ts. Dobrovolska, I. Krastev, *Bulg. Chem. Com.*, **40**, 248 (2008)
3. S. Nineva, Ts. Dobrovolska, I. Krastev, in: *Nanoscale Phenomena and Structures*, D. Kashchiev (ed), Prof. M. Drinov Publishing House, Sofia, 2008, p. 277.
4. S. Nineva, Ts. Dobrovolska, I. Krastev, *Bulg. Chem. Commun.*, **43**, 96 (2011).
5. G. Elkington, H. Elkington, *GB Patent* 8447 (1840).
6. P. M. Viacheslavov, S. Ya. Grilihes, G. K. Burkat, E. G. Kruglova *Galvanotechnika blagorodnyh i redkih metallov*, 1st edn. Mashinostroenie, Leningrad, 1970.
7. A. Molchadskii, R. M. Vishomirskis, in: *Blestjashchie elektroliticheskie pokritija*, Yu. Matulis (ed), Mintis, Vilnius, 1969, p. 435.
8. P. M. Viacheslavov, *Elektricheskoe osajdenie splavov*, Mashinostroenie, Leningrad, 1986.
9. E. A. Nechaev, R. Yu Bek, N. T. Kudriavtsev, *Elektrokhimiya*, **1**, 1443 (1965).
10. E. A. Nechaev, R. Yu. Bek, *Elektrokhimiya*, **2**, 150 (1966).
11. S. Jayakrishnan, S. R. Natarajan, *Met. Finish.*, **94**, 12 (1996).
12. F. Fourcade, T. Tzedakis, *J. Electroanal. Chem.*, **493**, 20 (2000).
13. I. Krastev, A. Zielonka, S. Nakabayashi, K. Inokuma, *J. Appl. Electrochem.*, **31**, 1041 (2001).
14. A. Blair, *Met. Finish.*, **100**, 284 (2002).
15. G. M. De Oliveira, L. L. Barbosa, R. L. Broggi, J. A. Carlos, *J. Electroanal. Chem.*, 578, 151 (2005).
16. I. Krastev, PhD Thesis, IPC - BAS, Sofia, 1987.
17. I. Krastev, DSc Thesis, IPC - BAS, Sofia 2004.
18. L. Weisberg Inc, *GB Patent* 464814 (1937).
19. F. R. Moral, *Met. Finish.*, June, 82 (1964)
20. H. W. Dettner, L. Elze, *Handbuch der Galvanotechnik*, Band 2., Carl Hanser Verlag, München, 1966, p. 145.
21. Yu. Bubialis, in: *Blestiashtie elektroliticheskie pokritiia*, Yu. Matulis (ed), Mintis, Vilnius, 1969, p. 250.
22. N. Maki, N. Tanaka, in: *Encyclopedia of Electrochemistry of the Elements*, vol. III, Co Ni P, A. J. Bard (ed), Marcel Dekker Inc., New York, 1975.
23. G. A. Di Bari, in: *Schlesinger M, Modern Electroplating*, G. Paunovic (ed), Wiley & Sons Inc., New York, 2000, p. 572.
24. T. Watanabe, *Nano-Plating*, Elsevier, Amsterdam, 2004.
25. S. Armanov, *Electrochim. Acta*, **45**, 3323 (2000).
26. C. Q. Cui, S. P. Jiang, A. C. C. Tseung, *J. Electrochem. Soc.*, **138**, 1001 (1991).
27. C. Q. Cui, S. P. Jiang, A. C. C. Tseung, *J. Electrochem. Soc.*, **138**, 94 (1991).
28. L. Brossard, *Mater. Chem. Phys.*, **27**, 235 (1991).
29. M. Lafouresse, A. Medvedev, K. Kutuso, W. Schwarzacher, A. Masliy, *Russ J Electrochem.*, **43**, 856 (2007).
30. A. B. Soto, E. M. Arce, M. Palomar-Pardavé, I. González, *Electrochim. Acta*, **41**, 2647 (1996).
31. M. Palomar-Pardavé, I. González, A. B. Soto, E. M. Arce, *J. Electroanal. Chem.*, **44**, 125 (1998).
32. W. E. Clark, M. L. Holt, *Trans. Electrochem. Soc.*, **94**, 244 (1948).
33. S. S. Abd El Rehim, S. M. Abd El Wahaab, M. A. M. Ibrahim, M. M. Dankeria, *J. Chem. Technol. Biotechnol.*, **73**, 369 (1998).
34. T. Cohen-Hyams, W. D. Kaplan, J. Yahalom, *Electrochem Solid State Letters*, **5**, C75 (2002).
35. E. Gómez, E. Vallés, *J. Appl. Electrochem.*, **32**, 693 (2002).
36. S. S. Abd El Rehim, S. M. Abd El Wahaab, M. A. M. Ibrahim, M. M. Dankeria, *J. Appl. Electrochem.*, **32**, 1019 (2002).
37. K. Vasu, T.L. Rama Char, *Plating*, **49**, 60 (1962).
38. F. Campbell, J. A. von Fraunhofer, *Surface Technology*, **5**, 235 (1977).
39. H. Basset, W. L. Bedwell, J. B. Hutchinson, *J. Chem. Soc.*, Part II, 1412 (1936).
40. B. C. Haldar, *Nature*, **166**, 744 (1950).
41. A. Brenner, *Electrodeposition of Alloys*, vol. 1, Academic Press, New York, 1963.
42. G. K. Burkat, N. P. Fedotiev, P. M. Viacheslavov, K. M. Spiridonov, *Zh. Prikl. Chim.*, **2**, 291 (1968).
43. S. Valizadeh, G. Holmbom, P. Leisner, *Surf. and Coat. Techn.*, **105**, 213 (1998).
44. S. Valizadeh, J. M. George, P. Leisner, L. Hultman, *Thin Solid Films*, **402**, 262 (2002).
45. H. Zaman, A. Yamada, H. Fukuda, Y. Ueda, *J. Electrochem. Soc.*, **145**, 565 (1998).
46. V. M. Fedosyuk, O. I. Kasyutich, W. Schwarzacher, *J. Magn. Magn. Mat.*, **198**, 246 (1999).
47. J. Garcia-Torres, E. Gomez, X. Alcobe, E. Valles, *Cryst. Growth Des.*, **9**, 1671 (2009).
48. I. Krastev, N. Petkova, A. Zielonka, *Metall-oberflaeche*, **52**, 628 (1998).
49. *Gmelin Handbook of Inorganic and Organometallic Chemistry*, Silber 61, 18 (1974).
50. S. Pilauskene, V. Kaikaris, *Khimija I khimicheskaja tehnologija*, VII, 113 (1965).
51. M. S. Bhuiyan, B. J. Taylor, M. Paranthaman, J. R. Thompson, J. W. Sinclair, *J. Mater. Sci.*, **43**, 1644 (2008).

ЕЛЕКТРОЛИТНО ОТЛАГАНЕ НА СРЕБЪРНО-КОБАЛТОВИ ПОКРИТИЯ.  
ЕЛЕКТРОЛИТИ

С.Л. Нинева, Цв.В. Доброволска, Ив. Н. Кръстев

*Институт по физикохимия "Ростислав Каишев", Българска академия на науките, София 1113, България*

Постъпила на 13 юли, 2010 г.; приета на 25 декември 2010 г.

(Резюме)

Представени са и са дискутирани литературни данни за електролити за отлагане на сребърни, кобалтови и сребърно-кобалтови покрития. Проведено е електроотлагане на сребърно-кобалтови покрития от цианидно-пирофосфатни електролити при 50°C. Резултатите от изследванията показват възможности за отлагане на компактни сплавни слоеве с високо съдържание на кобалт (до 50%). Отложените покрития биха могли да бъдат успешно използвани за по-нататъшно изследване на физикомеханичните и електрични свойства на тази система.

## Electrodeposition of silver-cobalt coatings. The cyanide-pyrophosphate electrolyte

S. L. Nineva\*, Ts. V. Dobrovolska, I.N. Krastev

Rostislav Kaischew Institute of Physical Chemistry, Bulgarian Academy of Sciences, Sofia 1113, Bulgaria

Received July 16, 2010; revised December 25, 2010

The effect of the components in the cyanide-pyrophosphate electrolyte on the deposition of silver-cobalt alloy was investigated by means of cyclic voltammetry and other physico-chemical methods of analysis. Based on the results it could be assumed that the electrodeposition in the alloy electrolyte occurs from mixed cyanide-pyrophosphate complexes of silver and pyrophosphate-hydroxide complexes of cobalt.

**Keywords:** cyclic voltammetry, electrodeposition, pyrophosphate, silver-cobalt alloys, nuclear magnetic resonance (NMR)

### INTRODUCTION

An extensive literature study about electrolytes for electrodeposition of silver, cobalt and silver-cobalt alloys was reported in a previous paper [1]. On the base of the literature data an electrolyte for deposition of the alloy was selected. It was shown, that compact coatings with up to 50 wt. % cobalt could be deposited from the selected cyanide-pyrophosphate electrolyte. However, the mechanism of obtaining of these coatings was not clarified, and the influence of the components in the electrolyte was not extensively studied, as well.

The aim of this work is to investigate the effect of the components in the cyanide-pyrophosphate electrolyte on the deposition of silver-cobalt alloys by means of cyclic voltammetry and other physico-chemical methods of analysis.

### EXPERIMENTAL

The composition of the used electrolyte is:

Ag as  $\text{KAg}(\text{CN})_2 - 1 \text{ g dm}^{-3}$  ( $0.009 \text{ mol dm}^{-3}$ );  
Co as  $\text{CoSO}_4 \cdot 7\text{H}_2\text{O}$  varies – 3 and  $5 \text{ g dm}^{-3}$  ( $0.051$  and  $0.085 \text{ mol dm}^{-3}$ );  $\text{K}_4\text{P}_2\text{O}_7 - 100 \text{ g dm}^{-3}$  ( $0.3 \text{ mol dm}^{-3}$ ). The electrolytes were prepared using chemicals of *pro analysis* purity and distilled water by the procedure, described in the previous part of this study [1].

The electrode processes for the deposition and dissolution of cobalt, silver and the alloy were investigated by means of cyclic voltammetry. The experiments were performed in a  $100 \text{ cm}^3$  glass cell at  $50^\circ\text{C}$  without stirring of the electrolyte. The

working electrode with an area of  $1 \text{ cm}^2$  and two counter electrodes were made by platinum. Prior to each experiment, the platinum working electrode was etched in a 50%  $\text{HNO}_3$ . A reference electrode  $\text{Ag}|\text{AgCl}$  ( $E_{\text{Ag}|\text{AgCl}} = 0.197 \text{ V}$  vs. SHE) was used. At the time of the experiments, the reference electrode was placed in a separate cell, filled with 3 M KCl solution (Merck) and connected to the electrolyte cell by a Haber-Luggin capillary through an electrolyte bridge, containing also a 3 M KCl solution. The dissolution of silver coatings (30 sec,  $0.5 \text{ A dm}^{-2}$ ,  $10 \text{ g dm}^{-3}$  Ag,  $65 \text{ g dm}^{-3}$  KCN, galvanostatic conditions) in different electrolytes was investigated through linear polarization. The experiments were carried out by means of a computerized PAR 263A potentiostat/galvanostat, using the Soft Corr II software with a sweep rate of  $25 \text{ mV s}^{-1}$ .

Infrared spectra of precipitates were registered in the range of  $1200\text{--}400 \text{ cm}^{-1}$  on a Nicolet-320 FTIR spectrometer using the KBr pellet technique.

Nuclear Magnetic Resonance (NMR) measurements were carried out on Bruker Advance II+ 600 NMR spectrophotometer at 293 K (Ultrasield<sup>TM</sup> magnet D 262/54, 14.09 T; Software - Topspin 2.1, NMR Guide).

The thermodynamic ion-associative model (software – PHREEQCI v.2.14) was used to determine the existence form of the elements in the cyanide-pyrophosphate electrolyte. The method is based on the extended Debye-Hückel equation for the calculation of activity coefficients of complex and simple ions in the solution. The used thermodynamical constants are shown in Table 1.

Due to the absence of thermodynamic data about the formation of  $\text{Co}(\text{P}_2\text{O}_7)_n^{4n-2}$  complexes in the

\*To whom all correspondence should be sent:  
E-mail: snineva@ipc.bas.bg

**Table 1.** Thermodynamic constants.

	lg K	Ref.
$\text{H}^+ + \text{CN}^- = \text{HCN}$	9.21	[2]
$\text{Ag}^+ + 2\text{CN}^- = \text{Ag}(\text{CN})_2^-$	20.48	[2]
$\text{Ag}^+ + 3\text{CN}^- = \text{Ag}(\text{CN})_3^{2-}$	21.7	[2]
$\text{Ag}^+ + 4\text{CN}^- = \text{Ag}(\text{CN})_4^{3-}$	20.6	[2]
$\text{Ag}^+ + \text{H}_2\text{O} + \text{CN}^- = \text{Ag}(\text{CN})\text{OH} + \text{H}^+$	-0.777	[2]
$\text{Co}^{2+} + 3\text{CN}^- = \text{Co}(\text{CN})_3^-$	14.312	[2]
$\text{Co}^{2+} + 5\text{CN}^- = \text{Co}(\text{CN})_5^{3-}$	23	[2]
$\text{P}_2\text{O}_7^{4-} + \text{H}^+ = \text{HP}_2\text{O}_7^{3-}$	0.82	[3]
$\text{P}_2\text{O}_7^{4-} + 2\text{H}^+ = \text{H}_2\text{P}_2\text{O}_7^{2-}$	1.81	[3]
$\text{P}_2\text{O}_7^{4-} + 3\text{H}^+ = \text{H}_3\text{P}_2\text{O}_7^-$	6.13	[3]
$\text{P}_2\text{O}_7^{4-} + 4\text{H}^+ = \text{H}_4\text{P}_2\text{O}_7$	8.93	[3]
$\text{Ag}^+ + 2\text{P}_2\text{O}_7^{4-} = \text{Ag}(\text{P}_2\text{O}_7)_2^{7-}$	3.74	[4]
$\text{Cu}^{2+} + 2\text{P}_2\text{O}_7^{4-} = \text{Cu}(\text{P}_2\text{O}_7)_2^{6-}$	12.57	[5]
$\text{Cu}^{2+} + \text{P}_2\text{O}_7^{4-} = \text{CuP}_2\text{O}_7^{2-}$	8.80	[5]
$\text{Cu}^{2+} + 2\text{HP}_2\text{O}_7^{3-} = \text{Cu}(\text{HP}_2\text{O}_7)_2^{4-}$	16.40	[6]
$\text{Cu}^{2+} + \text{HP}_2\text{O}_7^{3-} = \text{Cu}(\text{HP}_2\text{O}_7)$	6.40	[6]

literature, the existing information about copper-pyrophosphate complexes was used because of some similarities in the behavior of cobalt and copper pyrophosphate solutions [7, 8].

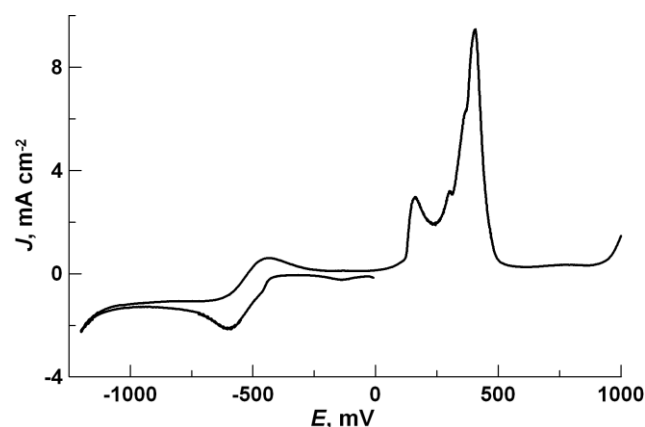
## RESULTS AND DISCUSSION

Figure 1 shows the cyclic voltammetric curve obtained in a water solution of potassium dicyanoargentate and potassium pyrophosphate.

The only cathodic peak at the potentials of around -600 mV results from the silver reduction from the silver cyanide complex, which confirms the previous results of silver deposition from water solutions of potassium dicyanoargentate onto different substrates [9]. This means that despite of the quantity, the pyrophosphate does not influence the polarization of the cathodic peak of the silver from potassium dicyanoargentate complex in the silver electrolyte. Two oxidation peaks are also registered: the first one at about -440 mV, and the second one, split in peaks at +160 mV and +405 mV. The dissolution of the coating occurs at the potentials of the split anodic maximum, while the first one is connected with the formation of passive film of silver insoluble compounds [10].

In order to elucidate the nature of the split peak in the anodic area, the experiment was carried out with changes of the scan direction at different cathodic potentials. Figure 2 shows the results. The splitting of the peak could be connected with the bonding of the dissolved silver by the different anions existing in the solution – the cyanide and the pyrophosphate ions. In the solution of potassium pyrophosphate the silver coating is dissolved at about +397 mV (Figure 3, curve 1). In the presence

of free cyanide ions in the pyrophosphate solution (curve 2) the silver dissolution peak is shifted with more than 250 mV in negative direction, which is a result of the strong complex-forming effect of the cyanide ions regarding to the silver. Curve 3 is obtained during dissolution of similar silver coatings in the solution of potassium dicyanoargentate and potassium pyrophosphate, in the absence of free cyanide.



**Fig. 1.** CV curves of an electrolyte containing 1 g dm<sup>-3</sup> Ag as KAg(CN)<sub>2</sub> and 100 g dm<sup>-3</sup> K<sub>4</sub>P<sub>2</sub>O<sub>7</sub>.

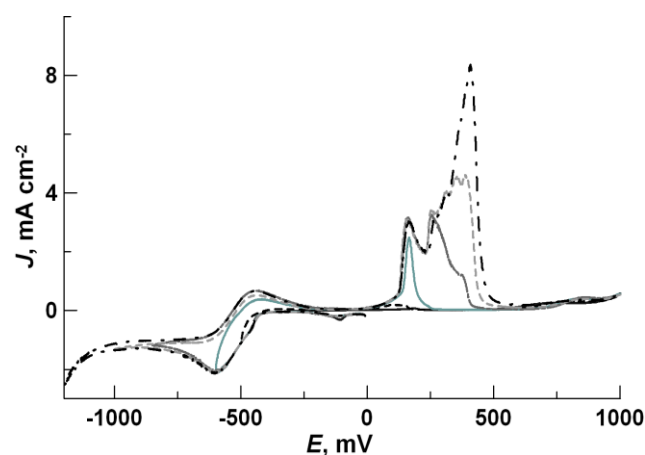


**Fig. 2.** CV curves of the electrolyte from Figure 1 with changes of scan direction at different cathodic potentials.

The curves, presented in Figures 2 and 3, allow for the conclusion that the dissolved silver, when in small amounts, combines together with the cyanide ions, released during its reduction in the cathodic period. This results in the appearance of the negative part of the split anodic peak. When higher amount of deposited silver in the case of more negative vertex potentials, is dissolved, the rest of the dissolved silver combines with the pyrophosphate anions, which results in the increase of the positive part of the split anodic peak (Figure 2).

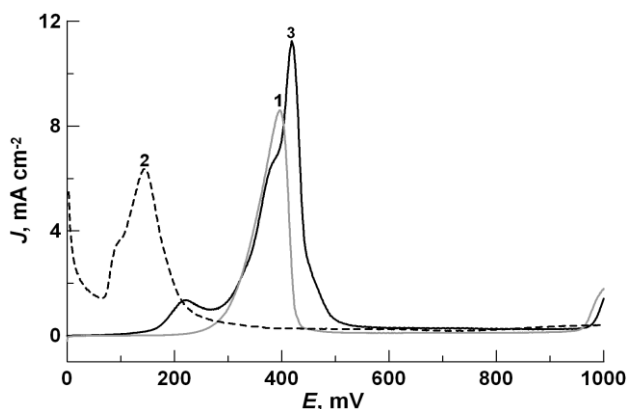


**Fig. 3.** Dissolution of silver coatings in different electrolytes. Curve 1 – pyrophosphate solution ( $K_4P_2O_7$ ,  $100 \text{ g}\cdot\text{dm}^{-3}$ ); Curve 2 – in the presence of free cyanide anions in the pyrophosphate solution ( $KCN$ ,  $1.207 \text{ g}\cdot\text{dm}^{-3}$  and  $K_4P_2O_7$ ,  $100 \text{ g}\cdot\text{dm}^{-3}$ ); Curve 3 – in the alloy electrolyte in absence of cobalt ( $Ag$  as  $KAg(CN)_2$  –  $1 \text{ g}\cdot\text{dm}^{-3}$  and  $K_4P_2O_7$  –  $100 \text{ g}\cdot\text{dm}^{-3}$ ).

The increased amount of deposited silver is connected with the longer deposition time when shifting the vertex potential in a more negative direction. Moreover, released cyanide ions during silver deposition contribute to the formation of silver complexes with more cyanide ligands [11]. The instability constant of the pyrophosphate complex of silver has a value of about  $K_{inst}=10^{-4}$  [4].

This is a weak complex of silver, compared with the silver-cyanide complex, which constant is of about  $K_{inst}=10^{-22}$ . In order to increase the polarization of the silver deposition from pyrophosphate electrolytes, the addition of a second complex-forming agent is recommended [12].

In order to determine the effect of the pyrophosphate ions on the strength of the bond between silver and cyanide ligands, measurements of the equilibrium potential of silver in dicyanoargentate-pyrophosphate solutions were performed. The data, as well as the obtained cyclic voltammetry curves in the presence of potassium dicyanoargentate and pyrophosphate separately and together, do not show any indications of a new complex formation. In order to clarify the nature of the possible chemical interactions of the silver metal ion with cyanide and pyrophosphate ligands, nuclear – magnetic resonance studies were performed. The NMR spectra of water solutions of potassium dicyanoargentate and potassium pyrophosphate have been registered separately and together. The techniques of the nuclear magnetic resonance require very high concentrations. By keeping the ratio of the investigated components constant (as in the electrolyte for alloy deposition –

$100 \text{ g}\cdot\text{dm}^{-3} K_4P_2O_7$  for each gram of silver), the concentrations have been increased up to their solubility limit.

Figure 4a shows the spectrum of potassium dicyanoargentate in water. One peak at about 562 ppm is observed.

Figure 4b shows the spectrum of potassium pyrophosphate in water. Besides the peak of pyrophosphate ions ( $-6.82 \text{ ppm}$ ) some other smaller peaks of unknown nature, most probably corresponding to another protonic compounds of a phosphorus, such as hydrogenphosphate, phosphate and etc., are observed.

In the solution, containing dicyanoargentate and potassium pyrophosphate, some shifting of the peak with about 20 ppm – up to 583 ppm is observed (Figure 4c).

In the literature, similar shifting of about 20 ppm is reported and attributed to the ligand changes in the complex. The confirmation needs additional experiments, and therefore, the carbon spectrum of the cyanide group in the water solution of potassium cyanide has been recorded. The comparison between both spectra confirms the idea that the addition of pyrophosphate to the dicyanoargentate ions do not result in the formation of some mixed cyanide-pyrophosphate complexes at a room temperature.

Figure 5 shows the cyclic voltammetric curve, obtained in the solution of cobalt sulphate and potassium pyrophosphate. Two maxima at about  $-923 \text{ mV}$  and  $-1107 \text{ mV}$  are registered in the cathodic region. The dissolution of the formed coatings is represented by the peak at about  $-400 \text{ mV}$ . The oxygen evolution reaction starts at very positive potentials. The existence of a pyrophosphate complex of cobalt has been mentioned in the literature [7], but data about its instability constant have not been found. In order to clarify the nature of the two peaks in the cathodic area, additional voltammetric investigations were performed.

An experiment, which was carried out with changes of the scan direction at different cathodic potentials, showed that the coatings deposited at potentials of both, the first and the second cathodic peaks, dissolve at the potentials of the mentioned above single anodic peak. The difference in the anodic behaviour is the deposit quantity which depends on the reached cathodic potential. According to Purin's studies [13] the cobalt electrodeposition from pyrophosphate electrolyte



1.09Ag  
 Sample: KAg(CN)<sub>2</sub> in H<sub>2</sub>O (cap. Ac-d6)  
 av600

561.55

```

NAME SA_120_bbo
EXPNO 2
PROCNO 1
Date_ 20080925
Time_ 8.23
INSTRUM spect
PROBHD 5 mm F4BBO BB-
PULPROG zg30
TD 4096
SOLVENT Shimming
NS 480
DS 0
SWH 30864.197 Hz
FIDRES 7.535204 Hz
AQ 0.0664052 sec
RG 64
DE 16.200 usec
TE 7.25 usec
D1 293.0 K
TD0 100.0000000 sec
===== CHANNEL f1 =====
NUC1 109Ag
P1 19.40 usec
PL1 0.00 dB
SF01 27.9393964 MHz
SI 16384
SF 27.9272480 MHz
WDW EM
SSB 0
LB 3.00 Hz
GB 0
PC 1.00
    
```

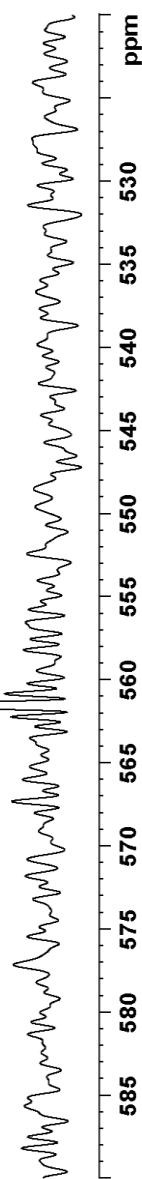


Fig. 4a. NMR spectrum of water solution of 0.1 mol dm<sup>-3</sup> KAg(CN)<sub>2</sub>.

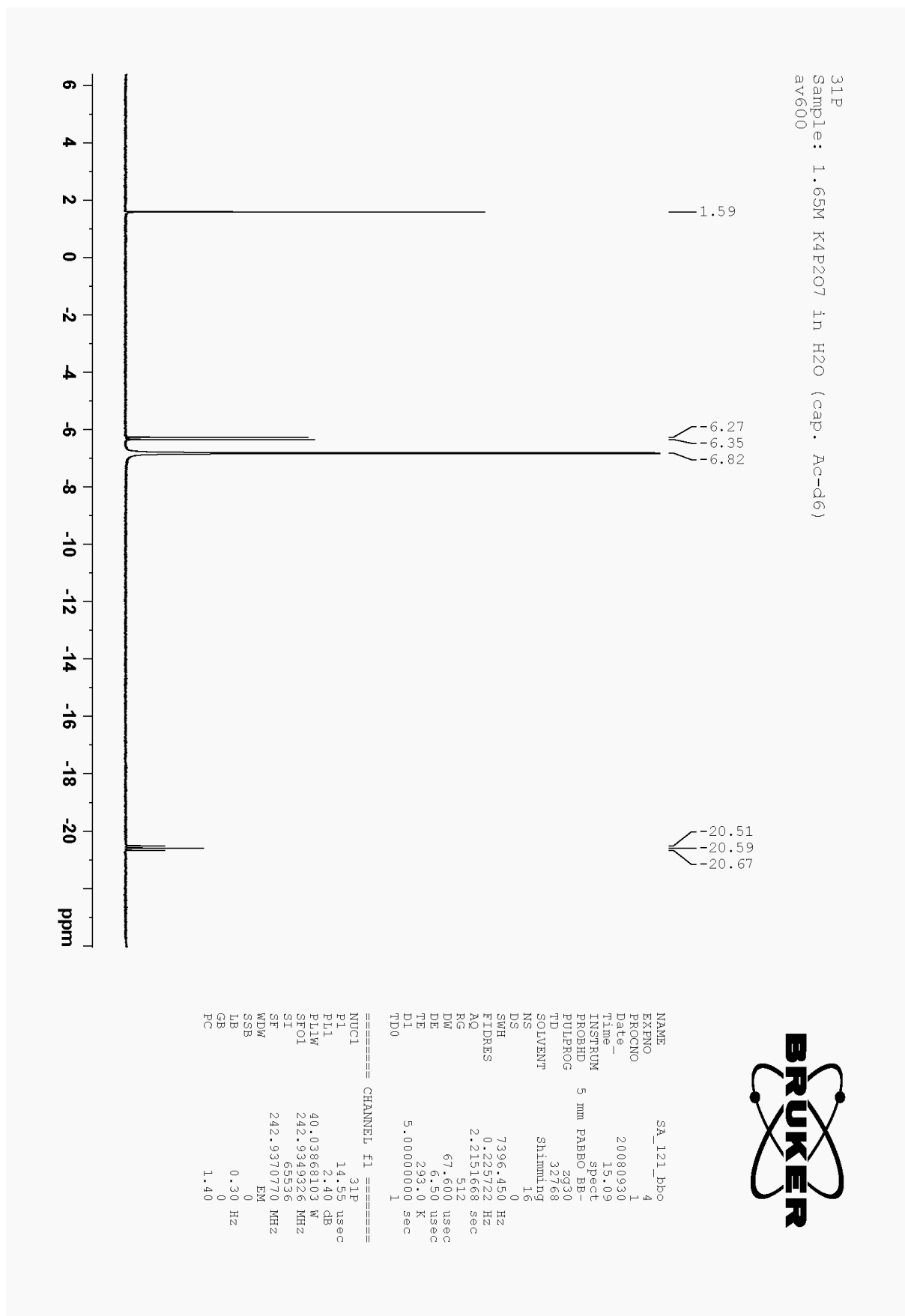


Fig. 4b. NMR spectrum of water solution of 1.65 mol dm<sup>-3</sup> K<sub>4</sub>P<sub>2</sub>O<sub>7</sub>.



109Ag  
 Sample: 0.05M KAg(CN)<sub>2</sub> + 1.65M K<sub>4</sub>P<sub>2</sub>O<sub>7</sub> in H<sub>2</sub>O (cap. Ac-d6)  
 av600

582.47

```

NAME SA_122_bbo
EXPNO 1
PROCNO 1
Date_ 20080930
Time_ 15.57
INSTRUM Spect
PROBHD 5 mm PABBO BB-
PULPROG zg
TD 65536
SOLVENT Shimming
NS 420
DS 0
SWH 30864.197 Hz
FIDRES 0.470950 Hz
AQ 1.0617332 sec
RG 362
DM 16.200 usec
DE 31.49 usec
TE 293.0 K
D1 20.00000000 sec
TD0 1

===== CHANNEL f1 =====
NUC1 109Ag
P1 6.50 usec
PL1 0.00 dB
SF01 27.9393964 MHz
SI 16384
SF 27.9272480 MHz
WDW EM
SSB 0
LB 3.00 Hz
GB 0
PC 1.00
    
```

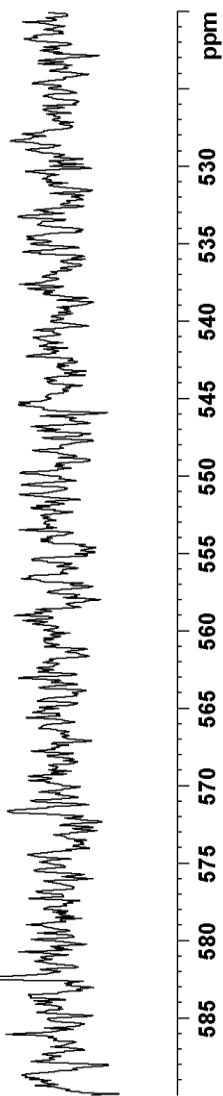
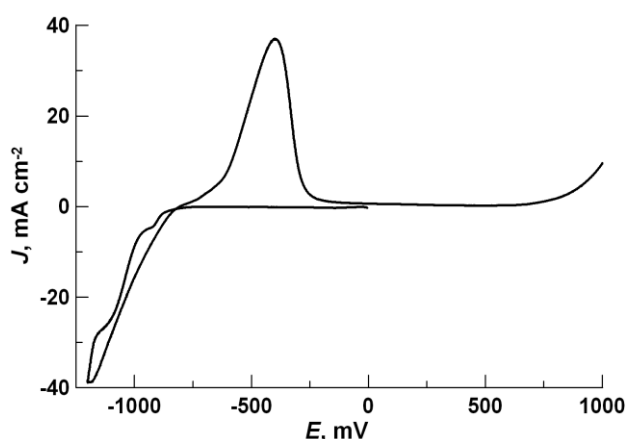


Fig. 4c. NMR spectra of water solution of 0.05 mol dm<sup>-3</sup> KAg(CN)<sub>2</sub> and 1.65 mol dm<sup>-3</sup> K<sub>4</sub>P<sub>2</sub>O<sub>7</sub>.



**Fig. 5.** CV curves of the electrolytes containing  $5 \text{ g dm}^{-3}$  Co as  $\text{CoSO}_4 \cdot 7\text{H}_2\text{O}$  and  $100 \text{ g dm}^{-3}$   $\text{K}_4\text{P}_2\text{O}_7$ .

shows strong pH dependence. He concludes that the main factors, determining the cathode processes are: destruction of cobalt-pyrophosphate complex, caused by alkalization in the vicinity of the electrode, and the following formation of passive layer which consists of hydroxide complexes and hydroxides of the cobalt.

In order to confirm Purin's conclusions, the experiments with changes in the pH value of the electrolyte were performed. The cobalt electrolyte was alkalized using  $2 \text{ g dm}^{-3}$  KOH which results in pH shifting up to 10.4 (initial pH value is 9.4). A change in the violet electrolyte colour was observed with intensification of the blue nuance. The CVA curve of the alkalized cobalt electrolyte shows the absence of the first cathodic peak, which refers to cobalt deposition from cobalt-pyrophosphate complex. This cathodic reaction is polarized probably due to the cobalt electrodeposition from mixed hydroxide-pyrophosphate complexes, formed easily in the preliminary alkalized cobalt electrolyte.

The obtained experimental results allow for the suggestion that the cobalt-pyrophosphate complex is destroyed by the alkalization and following accumulation of hydroxides in the vicinity of the electrode (as a result of simultaneous reduction reaction of both hydrogen and cobalt). This leads to formation of more complicated hydroxide-pyrophosphate complexes as well as to passivation effects on the cathode. As a result, the cobalt reduction from such complexes runs at higher polarization at the potential of the second cathodic maximum.

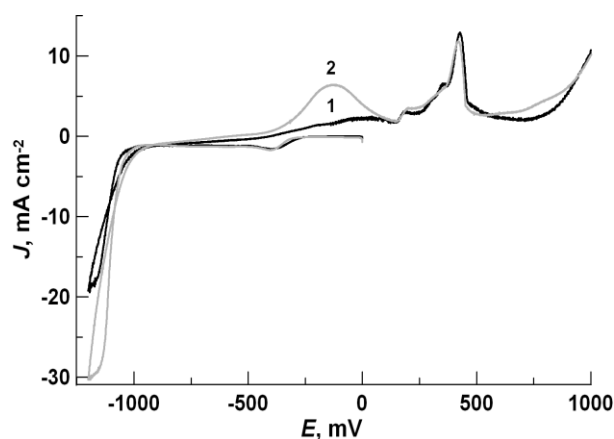


**Fig. 6.** CV curves in the alloy electrolyte ( $1 \text{ g dm}^{-3}$  Ag,  $3\text{--}5 \text{ g dm}^{-3}$  Co,  $100 \text{ g dm}^{-3}$   $\text{K}_4\text{P}_2\text{O}_7$ ). Curve 1 –  $3 \text{ g dm}^{-3}$  cobalt; Curve 2 –  $5 \text{ g dm}^{-3}$  cobalt.

The temperature has a strong influence on the destruction process of the cobalt-pyrophosphate complex. During the previous experiments, carried out at a room temperature [14], the existence of well defined cathodic peaks was not established. This study shows how the increase in temperature results in intensifying of the electrode processes in the cobalt electrolyte.

The cyclic voltammetric curves, obtained in the alloy electrolytes with different concentrations of cobalt –  $3 \text{ g dm}^{-3}$  (curve 1) and  $5 \text{ g dm}^{-3}$  (curve 2), are presented in Figure 6. The first cathodic peak, connected with the deposition of silver, is situated at potentials of about  $-400 \text{ mV}$ , i.e. at about  $200 \text{ mV}$  more positive potentials, compared to the electrolyte in the absence of cobalt (see Figure 1). Probably the depolarization effect is due to the changes in the silver complex type present in the electrolyte, i.e. from stronger cyanide to a weaker mixed cyanide-pyrophosphate. The depolarization effect is smaller at a room temperature [14].

The thermodynamic ion-associative modeling shows the possible existing ionic forms in the alloy electrolyte (Table 2).

The results of these theoretical calculations show the absence of a cobalt-cyanide complex and silver pyrophosphate complex in the solution and do not show any possibility of mixed complex formation.

However, the depolarization during electrodeposition of silver in the alloy electrolyte assumes the conclusion that a process of "recomplexation" of silver appears. The preparation

**Table 2.** The possible existing ionic forms in the alloy electrolyte, according to thermodynamical ion-associative modeling.

Ag species	%	Co species	%	K species	%	P species	%	S species	%	CN species	%
Ag(CN) <sup>2-</sup>	99.9	Co(P <sub>2</sub> O <sub>7</sub> ) <sub>2</sub> <sup>6-</sup>	73.87	K <sup>+</sup>	98.42	P <sub>2</sub> O <sub>7</sub> <sup>4-</sup>	51.27	SO <sub>4</sub> <sup>2-</sup>	77.26	Ag(CN) <sub>2</sub> <sup>-</sup>	99.95
Ag(CN)OH <sup>-</sup>	0.05	CoP <sub>2</sub> O <sub>7</sub> <sup>2-</sup>	26.13	KSO <sub>4</sub> <sup>-</sup>	1.58	Co(P <sub>2</sub> O <sub>7</sub> ) <sub>2</sub> <sup>6-</sup>	41.41	KSO <sub>4</sub> <sup>-</sup>	22.74	Ag(CN)OH <sup>-</sup>	0.05
AgSO <sub>4</sub> <sup>-</sup>	0.03	–	–	–	–	CoP <sub>2</sub> O <sub>7</sub> <sup>2-</sup>	7.32	–	–	–	–
Ag <sup>+</sup>	0.02	–	–	–	–	–	–	–	–	–	–

procedure of the alloy electrolyte includes a formation of cobalt pyrophosphate, and an already prepared cobalt electrolyte is added to the silver electrolyte. We can assume that the cobalt ions reduce the strength of the bonds between the silver and the cyanide ligands, and due to this fact, a new mixed cyanide-pyrophosphate complex of silver appears. The depolarization of the electrodeposition of silver in the alloy electrolyte at a room temperature is less than at a higher temperature. It could be assumed, that some destruction of the cyanide complex of silver and a following “re-complexation” could be the result of increase in the operation temperature. Moreover, the influence of the temperature onto the polarization of pyrophosphate electrolytes is mentioned by other authors [12].

The cobalt deposition peak is registered at about –1160 mV (3 g dm<sup>-3</sup> cobalt), or –1150 mV (5 g dm<sup>-3</sup> cobalt) (Figure 6), i.e., at potentials, similar to these in pure the pyrophosphate electrolytes (compare with Figure 5).

In the anodic part of the curve, the first dissolution peak is shifted to a positive direction in comparison with the peak, observed in the absence of silver (see Figure 5). This shift suggests for increased passivity of cobalt in the alloy electrolyte or its ennoblement due to the silver contribution to the cobalt phase. The increase of the cobalt concentration in the electrolyte leads to the increase of this dissolution peak, which is connected with a higher amount of deposited cobalt during the cathodic period.

The attempts to increase the metal concentrations lead to precipitation. The investigation of the precipitate with an IR-spectroscopy shows that it consists mainly of potassium sulphate. This allows for the conclusion that by removing of the precipitation, the metal concentration in the electrolyte could be successfully increased, leading to extended working conditions for electrodeposition.

## CONCLUSIONS

Different experimental studies were performed in order to establish the mechanism of the electrodeposition of silver cobalt alloys from

cyanide-pyrophosphate electrolytes. The obtained results showed that: the increase in the working temperature has a very strong influence on the investigated processes; the electrodeposition in the alloy electrolyte most probably occurs from mixed cyanide-pyrophosphate complexes of silver and pyrophosphate-hydroxide complexes of cobalt.

**Acknowledgement:** The authors express their gratitude to Dr. D. Rabadjieva from the Institute of General and Inorganic Chemistry, Bulgarian Academy of Sciences for the theoretical calculations of the possible ionic forms in the electrolyte; to Prof. S. Simova from the Institute of Organic Chemistry, Bulgarian Academy of Sciences for her helpful comments on the NMR-spectra; to Deutsche Forschungsgemeinschaft (DFG) (Project 436 BUL 113/97/0–4) for the support.

## REFERENCES

1. S. Nineva, Ts. Dobrovolska, I. Krastev, *Bulg. Chem. Commun.*, **43**, 88 (2011).
2. NIST Standard Reference Database 46 version 7.0, A. E. Martell, R. M. Smith (eds.), NIST, Gaithersburg, USA, 2003.
3. S. M. Lambert, J. I. Watters, *J. Am. Chem. Soc.*, **79**, 4262 (1957).
4. F. K. Andryushenko, V. V. Orehova, *Sb. Isledovaniya v oblasti galvanotekhniki*, Novocheerkask, 1965, p. 9.
5. J. J. Lingane, R. Karplus, *Ind. Eng. Chem., Anal. Ed.*, **18**, 191 (1946).
6. H. A. Laitinen, E. I. Osstott, *J. Am. Chem. Soc.*, **72**, 1729 (1950).
7. B. C. Haldar, *Nature*, **166**, 744 (1950).
8. B. C. Haldar, *Current Sci. (India)*, **19**, 244, 283 (1950).
9. Ts. Dobrovolska, PhD Thesis, IPC - BAS, Sofia, 2006.
10. I. Krastev, PhD Thesis, IPC - BAS, Sofia, 1987.
11. P. M. Viacheslavov, S. Ya. Griliches, G. K. Burkat, E. G. Kruglova, *Galvanotekhnika blagorodnyh i redkih metallov*, Mashinostroenie, Leningrad, 1 Ed., 1970, p.12.
12. B. A. Purin, V. A. Cera, E. A. Ozola, I. A. Vitinya, *Kompleksnie Elektroliti v galvanotekhnike*, Liesma, Riga, 1978, p. 100.
13. B. A. Purin, *Elektroosujdenie metallov iz pirofosfatnih elektrolitov*, Zinatne, Riga, 1975, p. 87.
14. S. Nineva, Ts. Dobrovolska, I. Krastev, *Bulg. Chem. Com.*, **40**, 248 (2008).

## ЕЛЕКТРО-ОТЛАГАНЕ НА СРЕБЪРНО-КОБАЛТОВИ ПОКРИТИЯ ИЗ ЦИАНИДНО-ПИРОФОСФАТЕН ЕЛЕКТРОЛИТ

Св.Л. Нинева, Цв.В. Доброволска, Ив.Н. Кръстев

*Институт по физикохимия "Ростислав Каишев", Българска академия на науките, София 1113, България*

Постъпила на 16 юли, 2010 г.; преработена на 25 декември 2010 г.

(Резюме)

Чрез циклична волтаперометрия и други физикохимични методи на анализ е изследвано влиянието на компонентите на цианидно-пирофосфатния електролит върху отлагането на сребърно-кобалтовата сплав. Съгласно получените резултати, може да се приеме, че електрохимичното отлагане в изследвания електролит се осъществява от смесен цианидно-пирофосфатен комплекс на среброто и пирофосфатно-хидроксиден комплекс на кобалта.

## Electrolytic cell for hydrogen and sulfuric acid production

K. Petrov\*, I. Nikolov, V. Nikolova, P. Iliev, D. Uzun, T. Vitanov

*Institute of Electrochemistry and Energy Systems, Bulgarian Academy of Sciences, G. Bonchev St., Building 10, 1113 Sofia, Bulgaria*

Received: May 15, 2010; revised: October 15, 2010

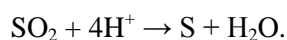
The anodic depolarization of sulfur dioxide reduces the thermodynamic potential of water splitting from 1.23 V to 0.29 V at 50 % H<sub>2</sub>SO<sub>4</sub> wt. and temperature of 25°C. This process leads to hydrogen and sulfuric acid production. The major problem of the electrolytic cell is the permeation of SO<sub>2</sub> into the cathode compartment where the ‘parasitic’ reaction of SO<sub>2</sub> + 4H<sup>+</sup> → S + H<sub>2</sub>O takes place, thus decreasing the hydrogen efficiency and poisoning the cathode catalyst. The original idea, supporting this study, is to use gas diffusion electrodes (GDEs) as anodes, designed to electrochemically oxidize SO<sub>2</sub>. Carbon GDEs have been developed and modified with cobalt phthalocyanine (CoPc). The GDEs serve as a membrane attenuating SO<sub>2</sub> permeation. An electrolytic cell with GDE has been designed and tested with: (i) different types of GDE; (ii) with and without membranes; and (iii) utilizing J/J<sub>2</sub> as a mediator. It has been found that when operating with gas mixtures which contain up to 20% vol. SO<sub>2</sub>, the main issue, namely its permeation into the electrolyte, can be solved. This beneficial approach can be used to treat waste gases with low SO<sub>2</sub> concentration which would have a favorable impact on the environment.

**Keywords:** hydrogen, sulfuric acid, electrolytic cell.

### INTRODUCTION

The water electrolysis is a pollution free technique for hydrogen production substituting the hydrocarbon use. In the conventional electrolyzers, the high operational voltage, caused by the kinetic hindrances of oxygen evolution, increases the production costs of the electrolyzed hydrogen multifold in comparison with the hydrogen, produced by the liquid fuel treatment. The anodic depolarization of sulfur dioxide reduces the water splitting thermodynamic potential from 1.23 V down to 0.29 V at 50 % H<sub>2</sub>SO<sub>4</sub> wt. and a temperature of 25°C [2]. This process results in both, hydrogen and sulfuric acid production.

The process has deserved the research efforts of many countries, and up to date number electrolyzer designs of this type have been developed [2–8]. Their construction employs immersed electrodes where the SO<sub>2</sub> enters the anodic space jointly with the electrolyte. However, this immediately creates one of the major problems, inherent to this type of electrolyzers, namely the permeation of SO<sub>2</sub> through the cation exchange membrane separating the anodic and the cathodic spaces and the SO<sub>2</sub> cathodic reduction according to the reaction:



Another disadvantage, even for the well working electrolyzers ( $E = 0,7 \text{ V}$  at  $i = 200 \text{ mA}\cdot\text{cm}^{-2}$ ), is that the electrodes are platinum catalyzed, which makes them quite sensitive to catalytic poisoning, particularly to the sulfur dioxide content (SO<sub>2</sub>), due to its penetration into the cathodic space. All efforts to solve these problems are directed to the electrolyzer design. An example of such design is to using two cation exchange membranes with an individual electrolyte circulation loop between the cathodic and the anodic space. [1]. In such cases, however, the problem with the intermediate electrolyte clean-up of the surfaces arises [9].

Our original idea is to use gas diffusion electrodes for electrolyzing cells which will operate with waste gases, produced by many industrial sources (thermoelectric power plants, enriching factories in the mining industry, etc.). Thus, the sulfur-acid electrolyzing method would be employed in its full capacity for the hydrogen production and SO<sub>2</sub> purification, and which is very important this would be beneficial economically and environmentally.

### THE CELL DESIGN

An novel electrolyzing cell was designed based on already developed immersed electrodes for sulfur dioxide oxidation, catalyzed with tungsten carbide.

Figure 1 illustrates the cell outline. The cell is designated to produce hydrogen from sulfur-acidic

\* To whom all correspondence should be sent:  
E-mail: kpetrov@bas.bg

solutions with SO<sub>2</sub> as anodic depolarizer. Other electrolyzing cell modifications have also been constructed with anodes, targeting at 95 – 100% SO<sub>2</sub> utilization. The cell allows for utilization of ion-exchange membranes which serve to separate the anolyte from the catholyte and enables the addition of KJ or HJ in the anolyte, aiming to support the homogeneous catalytic reaction between the SO<sub>2</sub> and the J.

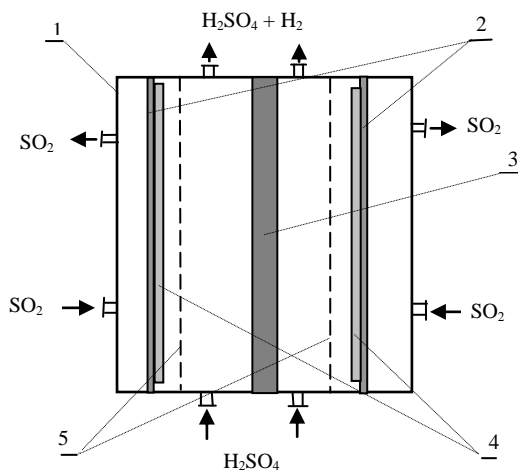


**Fig.1.** 1 - Cell housing, 2 – Gas diffusion anodes catalyzed with active carbon; 3 – Tungsten carbide cathode; 4 – Graphitized waddings soaked in potassium iodide; 5 – Cation exchange membranes.

This particular design has its fundamental advantages: 1) The GDEs serve as membranes, hence the SO<sub>2</sub> concentration in the electrolyte is considerably lower than the SO<sub>2</sub> concentrations when immersed types of anodes are employed. The membranes protect the cathodic space against sulfur dioxide penetration; 2) The activity of the cathode, manufactured with non-noble catalyst, is not influenced by the low SO<sub>2</sub> concentrations that may possibly penetrate into the cathodic space. The components of this electrolyzing cell are made of circularly shaped plexiglass. They are assembled as a filter-press-type stack. This facilitates the assembly of diverse modifications of the electrolyzing cell featuring various electrode positions, i.e, the distances between anode and cathode, as well as including cation-exchange membranes.

### EXPERIMENTAL CONDITIONS

The experiments employed a three-electrode cell with double layered working GD-electrodes [3], a tungsten carbide catalyst, and a (Hg/HgO) in 4.5 N H<sub>2</sub>SO<sub>4</sub> reference electrode. The controlling electronic potentiostat was of the Radelkis type. All measurements were taken at the range from 20 to

70°C. The active electrode surfaces varied between 10 cm<sup>2</sup> and 200 cm<sup>2</sup>. The electrolyte circulation was sustained by a peristaltic pump throughout the experiment. The studies, related to the experimental set-up operation with Air-SO<sub>2</sub> gas mixtures, were controlled by Brooks 5850 gas-mixing equipment which was used to mix precisely and maintain the desired proportion of the gas mixture components.

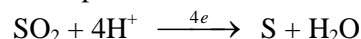
### EXPERIMENTAL RESULTS

The volt-amp characteristics have been taken at different temperatures and long term studies were also conducted. Throughout the measurements the SO<sub>2</sub> quantity, penetrated into the electrolyte, was controlled by iodometric analysis, and the produced hydrogen quantity was determined by volume exercising proper adjustments for the SO<sub>2</sub>

The oxidation efficiency for the SO<sub>2</sub> quantity, oxidized onto the GDE to the total SO<sub>2</sub> quantity within the anodic space, was calculated by the following basic equation:

$$X = (1 - C_{\text{out}} / C_{\text{in}}) \times 100 \%, \quad (1)$$

where  $C_{\text{out}}$  is the SO<sub>2</sub> concentration at the outlet of the gas chamber, and  $C_{\text{in}}$  at the inlet. The optimal electrolyte flow rate was selected in a way to prevent the penetration of sulfur dioxide from the anodic compartment into the cathodic space, and its reduction to sulfur. Figure 2 depicts the level of reduction of the SO<sub>2</sub> concentration. SO<sub>2</sub> penetrates into the catholyte and increases the hydrogen output as a function of the electrolyte flow rate. Figure 2 illustrates also the fact that at the selected flow rate of 5 – 6 L/h the "parasitic" reaction of



does not take place practically. Taking this into consideration, all measurements were conducted at this electrolyte flow rate.

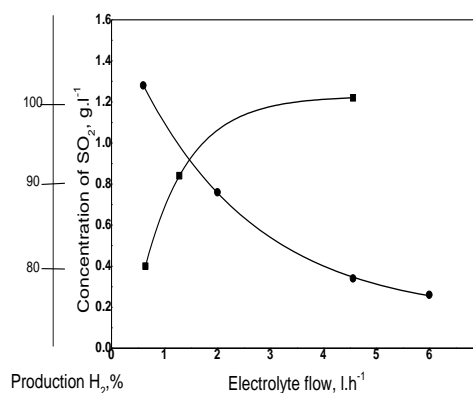


**Fig.2.** Influence of electrolyte flow rate on the yield of hydrogen (■) and oxidation of SO<sub>2</sub> (●).  $S_{\text{el-d}} = 10 \text{ cm}^2$ ; 20 % H<sub>2</sub>SO<sub>4</sub>,  $t = 20 \text{ }^\circ\text{C}$ .

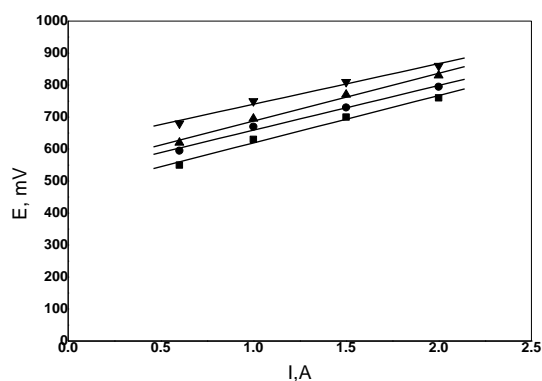


**Fig. 3.** Volt-ampere characteristics of electrolytic cell taken at different temperatures. For producing of Hydrogen from sulfuric-acid solution as anodic depolarized with sulfur dioxide.  $S_{el-d} = 10 \text{ cm}^2$ ; 20 %  $\text{H}_2\text{SO}_4$ ;  $d_{el-d} = 6 \text{ l/h}$ ; ( $\blacktriangledown$ ) - 20 °C; ( $\blacktriangle$ ) - 40 °C; ( $\blacklozenge$ ) - 60 °C; ( $\blacksquare$ ) - 70 °C.

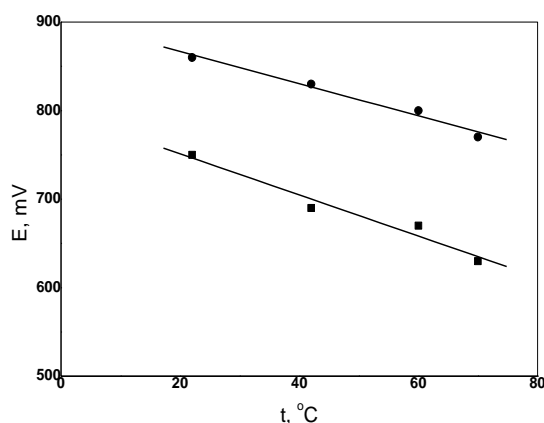


**Fig. 3a** Temperature dependence for the same cell; ( $\blacksquare$ ) –  $I = 1 \text{ A}$ ; ( $\bullet$ ) -  $I = 2 \text{ A}$ .

Figure 3 shows the electrolyzer cell volt-amp characteristics, taken at different temperatures. Shown in the subsequent Figure 3a, a single temperature rise of 10°C results to some 20 mV of voltage reduction. It was calculated, based on the individual electrode volt-amp characteristics, that the ohmic losses are 30 mV at  $I=1\text{A}$  and close to 60 mV at  $I = 2\text{A}$ , respectively.

The long term studies have demonstrated that the designed cell is functionally stable for 100 hours. The voltage necessary to support the operation of such type of electrolyzing cell is with some 0.5 Volts lower compared to the conventional water electrolyzers, even for the most unfavorable working conditions at 20°C [9]. The sulfur dioxide penetration through the GDEs, resulting in its reduction to sulfur on the cathode and in collector corrosion in sustainable operational mode, could be considered as disadvantage of this system,

particularly for electrolyzing cells with electrode surface area of  $S_{el} = 200 \text{ cm}^2$ . In this case, the sulfur dioxide practical utilization does not surpass 40%.

The experimental results have confirmed that semi-permeable cation-exchange membranes utilization does not lead to radical solution of the problem, in spite of some  $\text{SO}_2$  reduction within the cathodic space (1.24 g/L in the anolyte and 0.280 g/L in the catholyte), but is still sufficient to back up the  $\text{SO}_2$  reduction to sulfur at a perceptible rate.

In order to solve the issue for the proposed electrolyzing cell design, improved gas diffusion electrodes were developed to attain practically a 75% sulfur dioxide utilization [3]. This aim was achieved by means of variation of the active layer composition. These GDEs of enhanced sulfur dioxide utilization facilitate the cathodic space protection against  $\text{SO}_2$  penetration. Unfortunately the 75% utilization, achieved up to date, is not sufficient enough to solve the problem of  $\text{SO}_2$  permeation into the cathodic space.

Another approach was looked after, namely employing the addition of a redox couple iodine-iodine ion to the anolyte. It is well known [10] that in this cases the following anodic reaction takes place:



while the produced iodine oxidizes the penetrated into the solution  $\text{SO}_2$ :



which is a homogeneous catalytic reaction.

It is easily observed that the  $\text{I}_2/\text{I}^-$  couple serves as a mediator for the  $\text{SO}_2$  oxidation. These reactions lower the anodic reaction potential, acquiring the electrochemical potential of the redox couple.

To back-up the above reactions a new family of GDEs were developed as well as a novel cell design, where graphitized wadding, impregnated with potassium iodide, were inserted behind the anode. The iodide amount was experimentally optimized, taking into account the penetration of non-reacted sulfur dioxide through the GDE. The final optimal value is  $C_{KI} = 1.2 \cdot 10^{-1} \text{ moles/L}$ . Behind the anode, a cation exchange membrane has been positioned to separate the anodic and the cathodic spaces. Figure 4 is an illustration of the relationship, describing the sulfur dioxide utilization as a function of the current density. It is observed that at a current density of  $I > 70 \text{ mA/cm}^2$ , the  $\text{SO}_2$  utilization reaches the desired 100%. A cell of such design with electrode surface area of  $10 \text{ cm}^2$  was operational for 40 hours ( $I = 100 \text{ mA/cm}^2$ )

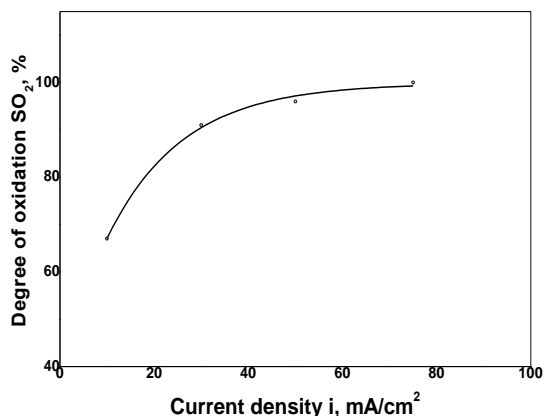


**Fig. 4.** Relationship between degree of oxidation of sulfur dioxide and current density.  $C_{KJ} = 1.2 \cdot 10^{-1} \text{M.l}^{-1}$ ;  $S_{el-d} = 10 \text{ cm}^2$ ;  $t^{\circ} = 25^{\circ}\text{C}$ ;  $4.5 \text{ N H}_2\text{SO}_4$ .

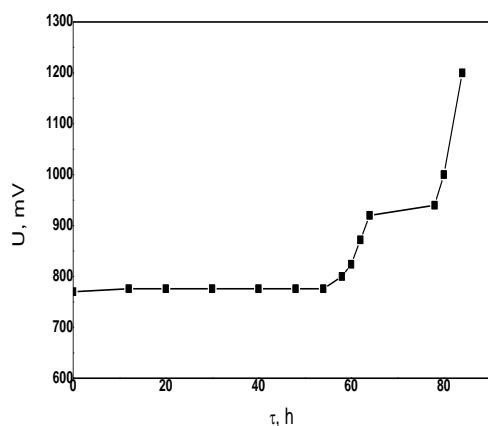


**Fig. 5.** Long- term test of electrolytic cell operating with homogenous catalyst potassium iodide.  $20 \text{ \% H}_2\text{SO}_4$ ;  $20^{\circ}\text{C}$ ;  $C_{KJ \text{ anolit}} = 2.5 \cdot 10^{-2} \text{M}$ ;  $S_{el-d} = 10 \text{ cm}^2$  usability  $\text{SO}_2 = 95 - 100 \text{ \%}$ ;  $i_a = 100 \text{ mA/cm}^2$ .

without any registered presence of  $\text{SO}_2$  in the catholyte, circulating with a flow rate of some  $0.3 \text{ L/h}$ . The cell voltage throughout this study varied from  $750$  to  $810 \text{ mV}$ , as seen on Figure 5. Unfortunately, other problems occur either related to the iodide separation from the produced sulfur dioxide or to the metallic iodine blockage of the gas diffusion anodes.

We searched an innovative solution to solve finally the problems, associated with the sulfur dioxide electrolysis, based on utilizing gas mixtures of sulfur dioxide and air. As mentioned above our original idea was to feed the GDE anode, employed as electrolyzer, with waste gases, containing  $\text{SO}_2$ . The waste gases utilization implies reduced  $\text{SO}_2$  partial pressure in the gas and the resultant decline. Figure 6 shows the correlation, describing the current density and the  $\text{SO}_2$  oxidation level on the

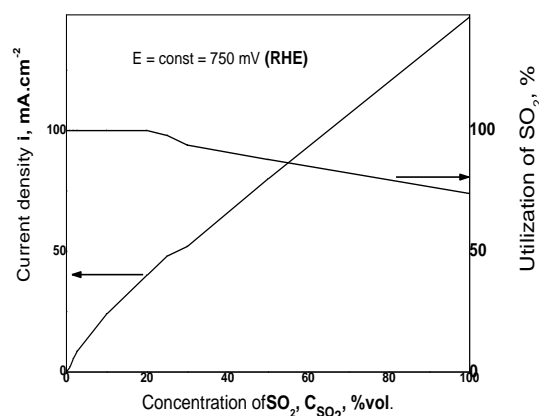


**Fig. 6** Relationship between current density and degree of oxidation on the  $\text{SO}_2$  concentration in the gas mixture (air +  $\text{SO}_2$ ) at constant potential;  $E = 750 \text{ mV vs RHE}$ ;  $t = 25^{\circ}\text{C}$ ;  $4.5 \text{ N H}_2\text{SO}_4$ ; catalyst: Norit – NK/CoPc.

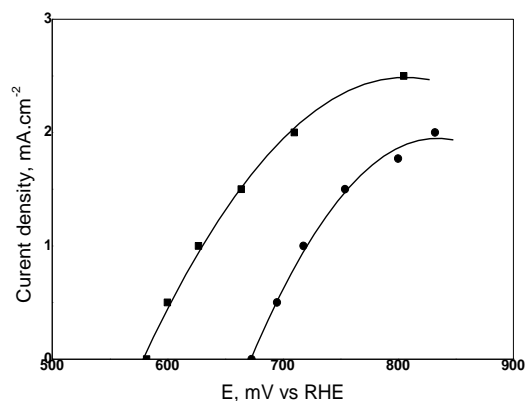


**Fig. 7.** Polarization curves of gas diffusion electrodes operating with  $\text{SO}_2 + \text{air}$  mixture;  $t = 25^{\circ}\text{C}$ ;  $4.5 \text{ N H}_2\text{SO}_4$ ; (●) Norit + CoPc,  $0.24 \text{ \% vol. SO}_2$ ; (■) Norit NK,  $1 \text{ \% vol. SO}_2$ .

$\text{SO}_2$  concentration in the gas mixture at constant potential of  $E = 750 \text{ mV (RHE)}$ , at which as shown in Figure 4, the electrodes maintain their stability. It is again easily observed that the electrodes attain current densities of  $I = 50 \text{ mA.cm}^{-2}$  at  $\text{SO}_2$  concentration of  $C_{\text{SO}_2} = 25 \text{ \% vol.}$  and  $I = 80 \text{ mA.cm}^{-2}$  at  $C_{\text{SO}_2} = 50 \text{ \% vol.}$  The other correlation shown in Figure 6 and displays the  $100\% \text{ SO}_2$  oxidation level at  $C_{\text{SO}_2} = 20 \text{ \% vol.}$  This result is extremely important since it provides for solving the major problem for sulfur-acidic electrolysis, namely the  $\text{SO}_2$  permeation into the cathodic space. The plot shows also that this is accompanied by reduction of the operational current density, too.

As mentioned above, the capability of the GDEs to operate at low partial  $\text{SO}_2$  pressures is of practical significance from the environmental point of view. Since the  $\text{SO}_2$  concentration in the waste gases of many chemical processes is below  $1\%$  by

volume, comprehensive measurements were carried out at these low concentrations. Figure 7 presents the polarization curves for the SO<sub>2</sub> oxidation at C<sub>SO<sub>2</sub></sub> = 0.24 vol. % on the catalyst with Norit + CoPc and with Norit only. The current densities at 750 mV vs. RHE are from 1.5 to 2.0 mA.cm<sup>-2</sup> for both catalysts. The Norit + CoPc exhibits high catalytic activity and the above cited current density had been attained at a fourfold lower SO<sub>2</sub> concentration than in the case of pure Norit catalyst. These polarization curves demonstrate the GDE capability to operate at low SO<sub>2</sub> concentrations, whereby the penetration of SO<sub>2</sub> into the electrolyte is avoided, cf. Figure 6.

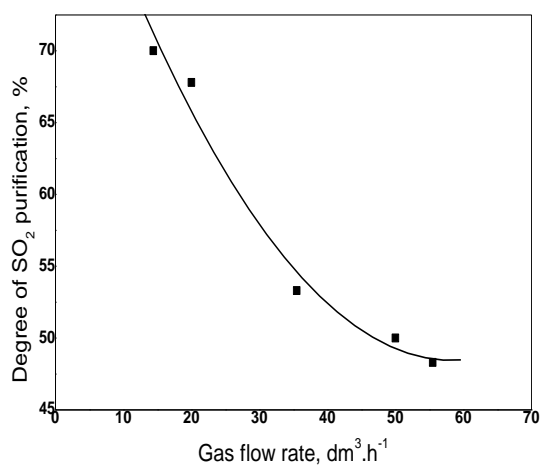


**Fig. 8.** Relationship between degree of SO<sub>2</sub> purification on the low rate of the gas mixture at constant potential: E = 750 mV vs. RHE; t = 25 °C; 4.5 N H<sub>2</sub>SO<sub>4</sub>; GDE: S = 200 cm<sup>2</sup>; 1 vol % SO<sub>2</sub> in air; i ≈ 2 mA.cm<sup>-2</sup>.

In this manner specific amounts of waste gases (at selected low gas flow rates in the gas chamber) can be purified. Figure 8 illustrates the correlation between the level of SO<sub>2</sub> removal by a GDE of 200 cm<sup>2</sup> surface area and the flow rate of the gas mixture (SO<sub>2</sub> + air), supplied to the electrode. The electrode potential was maintained at constant 750 mV vs. RHE. The attained current density of about 2 mA.cm<sup>-2</sup> varied insignificantly with the gas mixture flow rate. It is evident that under these conditions the electrode removes some 50 to 70 % of the SO<sub>2</sub> from the waste gas which initially contained a concentration of C<sub>SO<sub>2</sub></sub>=1.0 % vol. This

implies a considerable environmental effect, even with the less active Norit –NK catalyst.

## CONCLUSION

The major problem, inherent to the sulfur-acidic method for hydrogen production, namely SO<sub>2</sub> permeation into the cathodic space, was successfully resolved.

An innovative electrolyzing cell design was proposed. This design involves an advantageous GDE exploitation, providing for utilization of the SO<sub>2</sub> containing waste gases. The feasibility of the GDEs' operation at low SO<sub>2</sub> partial pressures was demonstrated.

This inventive technique provides for both, hydrogen production and harmful sulfur dioxide pollutant purification.

## REFERENCES:

1. P.W. Lu, R.L. Ammon, *J. Electrochem.Soc.*, **127**, 2610 (1980).
2. P.W. Lu, E.R. Garcia, R.L. Ammon, *J. Appl. Electrochem.*, **11**, 347 (1981).
3. B.D. Struck, R. Junginger, H. Neumeister, B. Dujka, *Int. J. Hydrogen Energy*, **7**, 43 (1982).
4. А. Горбачев, Ф. Андриющенко, Л. Ищенко, Л. Опарин, В. Купина, *Вопр. Атом. Науки и Техн. Атомн. Водород Энерг. Технол.* **2**, 18 (1981).
5. S. Charton, P. Rivalier, D. Ode, J. Morandini, J.P. Caire, Hydrogen production by the Westinghouse process: modelling and optimization of the two-phase electrolysis cell, 3rd International conference on the simulation of electrochemical processes, WIT, Bologna, pp. 11–22 (2009).
6. S. Chartona, J. Janviera, P. Rivaliera, E. Chaînet, J.-P. Caire, *Int. J. Hydrogen Energy*, **35**, 1537 (2010).
7. F. Jomard, J.P. Feraud, J. Morandini, Y. du Terrail Couvat, J.P. Caire, *J. Appl. Electrochem.*, **38**, 297 (2008).
8. B.D. Struck, H. Neumeister, B. Dujka, U. Siebert, D. Trienbach, Report EUR 8300 EN (1983).
9. R.L. Lehey, *Int. J. Hydrogen Energy*, **8**, 401 (1983).
10. B.N. Grgur, M.M. Gvozdenović, J.S. Stevanović, B.Z. Jugović, Lj.T. Trišović, *Chem. Eng. J.*, **124**, 47 (2006).

## ЕЛЕКТРОЛИЗНА КЛЕТКА ЗА ПОЛУЧАВАНЕ НА ВОДОРОД И СЯРНА КИСЕЛИНА

К. Петров, И. Николов, В. Николова, П. Илиев, Дж. Узун, Т. Витанов

*Институт по електрохимия и енергийни системи, Българска академия на науките, ул. Акад. Г. Бончев, бл. 10,  
1113 София*

Постъпила на 15 май, 2010 г.; преработена на 15 октомври, 2010 г.

(Резюме)

Анодната деполяризация на серния диоксид понижава термодинамичния потенциал за разлагането на водата от 1.23 V до 0.29 V в сярно-кисела среда от 50 % (тегл.) H<sub>2</sub>SO<sub>4</sub> при 25°C. Този процес води до получаването на водород и сярна киселина. Основният проблем на електролизната клетка в този случай е проникването на SO<sub>2</sub> в катодното пространство, където протича “паразитната” реакция  $SO_2 + 4H^+ \rightarrow S + H_2O$ , като при това се понижава ефективността по водород и се отравя катодния катализатор. Оригиналната идея, породила това изследване е в използването на газови дифузионни електроди (GDEs) като аноди, предназначени за окислението на SO<sub>2</sub>. Разработени са въглеродни GDE-електроди, като са модифицирани с кобалтовфталоцианин (CoPc). Газово-дифузионният електрод служи като мембрана, забавяща проникването на SO<sub>2</sub>. Разработена е електролизна клетка и е изпитана при: (а) различни типове GDE; (б) с и без мембрани и (в) използващи редокс-системата J/J<sub>2</sub> като медиатор. Намерено е, че при работа с газова смес, съдържаща до 20% (об.) SO<sub>2</sub>, се решава основния въпрос, т.е. проникването на серния диоксид в електролита. Този подход може да се използва за третирането на отпадъчни газове с благоприятен ефект върху околната среда.

## Experimental metal hydride-air fuel cell

S.M. Hristov\*, R.I. Boukoureshtlieva, Y.D. Milusheva

*Institute of Electrochemistry and Energy Systems, BAS, Acad. G. Bonchev St., Building 10, Sofia 1113, Bulgaria*

Received: July 22, 2010; revised: October 20, 2010

Commercially available metal hydride alloys of the AB<sub>5</sub>-type and air gas-diffusion electrodes were used as anode and cathode materials for the experimental fuel cell where NaBH<sub>4</sub> is used as hydrogen supply.

Air gas-diffusion electrodes with identical gas-supplying layer, and catalytic layer from pyrolysed CoTMPP were prepared, characterized, and selected as suitable for cathode material.

Experimental low-temperature borohydride fuel cell was constructed and optimized. The exploitation of the developed cell is safe, since the fuel is dissolved in the electrolyte and there is no need to work with compressed or condensed hydrogen.

The proposed fuel cell structure comprises an experimental plastic two-electrode electrochemical cell. The obtained operational characteristics indicated for its possible application as a real fuel cell.

**Key-words:** metal hydride alloys, air gas-diffusion electrodes, borohydride fuel cell

### INTRODUCTION

The fuel cell represents an electrochemical energy transformer. It directly transforms chemical energy into thermal and electric. There are different types of fuel cells, each one having an optimal application. They are classified mainly by the type of used electrolyte or in terms of their working temperature.

Methanol and sodium borohydride (NaBH<sub>4</sub>) are important fuel candidates for portable and mobile applications at an ambient temperature. Since the late 1990s, NaBH<sub>4</sub> is presented as a promising hydrogen storage material and an attractive fuel to use in the so-called Direct Borohydride Fuel Cell (DBFCs) [1–3]. The recent rapid progress in the development of DBFCs is reviewed in [4]. However, the discussion of DBFC was brief. This is not surprising since there is little literature published before the year of 2000.

A direct borohydride fuel cell uses the NaBH<sub>4</sub> solution as fuel, and electricity is produced via the following reaction:



The DBFC can be compared, thermodynamically and energetically, to the direct methanol fuel cell (DMFC) and to the polymer electrolyte membrane fuel cell (PEMFC). The comparison is favourable to the DBFC technology

[5]. The DBFC theoretical open circuit voltage of 1.64 V is higher than those of the DMFC (1.21 V) and the PEMFC (1.23 V).

In principle, the DBFC can only work in an alkaline environment because BH<sub>4</sub><sup>-</sup> is unstable in neutral or acidic medium. The electrocatalysts for both, the anode and the cathode in the DBFC with alkaline fuel, are not necessarily limited to noble metals [6]. Low cost catalysts can be expected to result in a good performance. The research of catalysts for the DBFC anode has been well documented [7, 8]. Non-platinum cathode catalysts such as MnO<sub>2</sub> [9], Co-porphyrins [10], perovskite oxides [11], etc. have been studied extensively. Ma and co-workers [12] demonstrated DBFC in which iron phthalocyanine is used as a cathodic catalyst, and hydrogen storage alloy can be used as an anodic catalyst.

In this work we present an experimental metal hydride air fuel cell which uses complex alkaline hydrides as a fuel. This fuel cell will demonstrate the possibility to use conventional metal hydride alloys as anodes, on one hand, and air gas diffusion electrodes as cathodes, on the other hand.

### EXPERIMENTAL

The proposed fuel cell structure comprises an experimental plastic two-electrode electrochemical cell. The anode and the cathode are placed in an electrolyte space, filled in with electrolyte. In most experiments 6 or 7 M KOH, containing 1M NaBH<sub>4</sub>, was used as working electrolyte.

\* To whom all correspondence should be sent:  
E-mail: SHristov@bas.bg

Three types of commercial AB<sub>5</sub> metal hydride alloys, AKL-86, AKL-1002, and AKL-1519 (Triebacher, Germany) were investigated as a potential anode material in the DBFC. The initial alloys were pre-treated in a NaBH<sub>4</sub> solution (12–24 h), filtered, mixed with PTFE (polytetrafluorethylene) paste, and coated upon Ni foam.

The air gas-diffusion electrodes with gas layers are prepared from a special hydrophobic material, carbon black P 1042 and PTFE by a special technology. Four types of catalysts are used for the catalytic layer: VS 50-CoTMPP 700, pyrolyzed CoTMPP, AC CoNi, and NORIT NK. The catalytic layers of all electrodes are made from 20 mg/cm<sup>2</sup> of catalyst. For the initial experiments, the air electrodes are mounted on the experimental electrochemical cell filled in with 7M KOH electrolyte. The cell is equipped with Zn reference electrode and counter electrode of stainless steel. The characteristics of the electrodes are measured when operating on air or on pure oxygen.

Round shared anode and cathode with geometric area of 7.5 cm<sup>2</sup> and effective working area of about 5 cm<sup>2</sup> were prepared. The electrodes were sintered at 280° C under pressure of 200 kg/cm<sup>2</sup> in the course of 2 min. The electric current collector (Ni-plated Fe grid) was pressed on each electrode.

The electrochemical measurements with the described fuel cell were performed using computerized potentiostat – galvanostat, GAMRY module, and various digital multimeters.

## RESULTS AND DISCUSSION

The polarization curves of the air gas-diffusion electrodes, operating on air and pure oxygen in alkaline electrolyte, are presented in Figure 1 (a. and b.). The air electrodes are prepared with identical gas-supplying layers. Four types of catalysts are used for the catalytic layer. It is well known that the performance of the air electrode is influenced not only by the activity of the catalyst, but also by all transport processes, taking place in its porous structure. Transport hindrances in the electrode are function not only of its overall structure, but also of the porous structure and the surface properties of the catalyst. Methods for diagnostic the activity and the transport properties of the air gas-diffusion electrode are proposed. It is theoretically and experimentally shown that the value  $\Delta E = E_{\text{oxygen}} - E_{\text{air}}$  can be used as a measure for the transport hindrances in the air electrode [13, 14].

The activities of the catalysts are compared based on the experimental Tafel plots (Fig.2). It is seen that the most active catalysts are the VS 50-CoTMPP 700 and the pyrolyzed CoTMPP.

The effect of the cell structure upon the electrochemical behaviour was studied in detail. The long-term experience in the development,

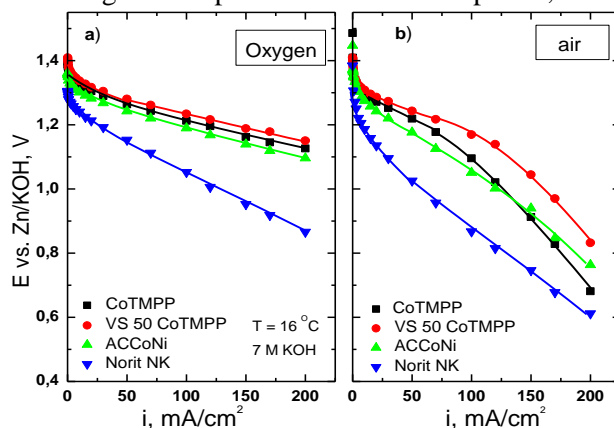


**Fig. 1.** Polarization curves of air electrodes with catalysts NORIT NK, VS 50-CoTMPP 700, pyrolyzed CoTMPP and AC CoNi, operating with pure oxygen (a) and with air (b).

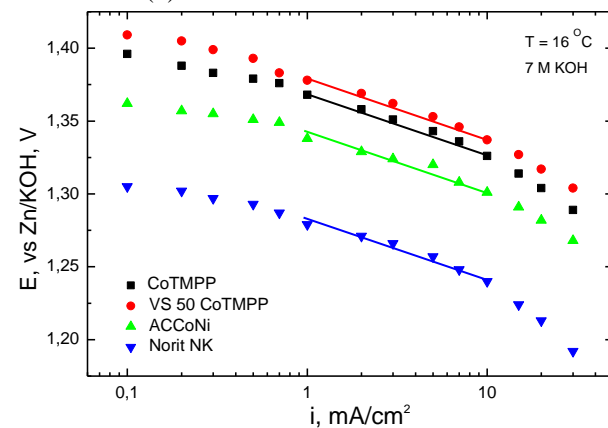


**Fig. 2.** Tafel plots of the air electrodes with the investigated catalysts.

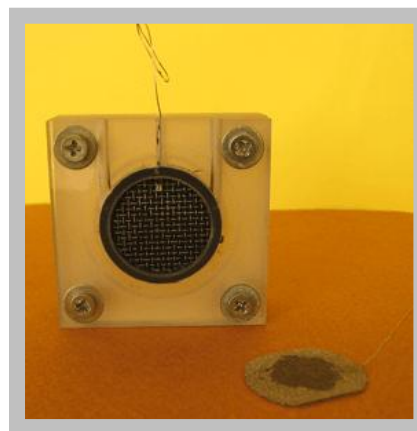


**Fig. 3.** Photograph of the described electrochemical cell.

testing, and construction of various types of power sources [15] will serve as a base for the successful construction of the experimental borohydride fuel cell, presented in this work (Fig. 3).

The current voltage and the corresponding power characteristics of the cell are given in Fig. 4. The power values are over 140 mW for the cell equipped with an AKL-86 anode.

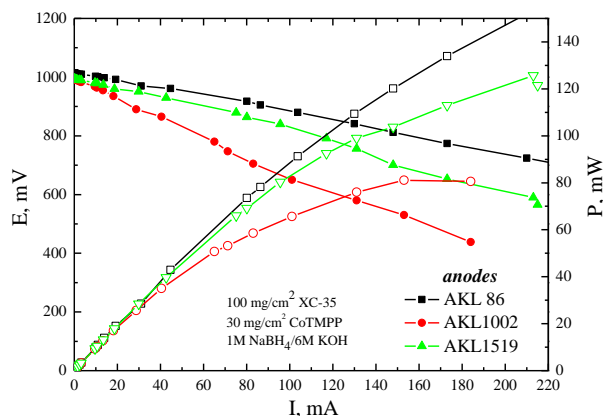


**Fig. 4.** Polarization and power characteristics of a borohydride fuel cell

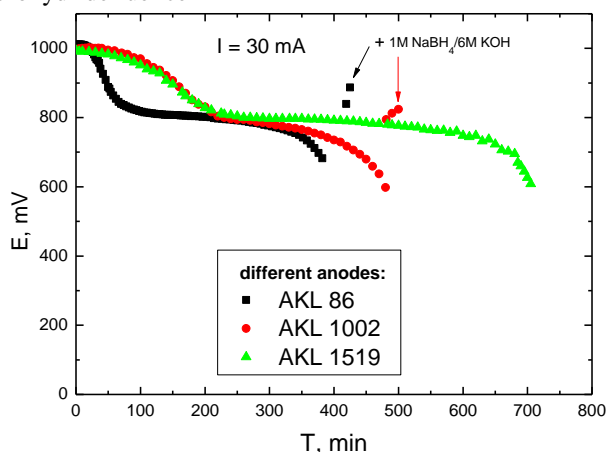


**Fig. 5.** Discharge curves of the experimental fuel cell.

Borohydride participation in the electrode reaction is clearly evident when we compare the discharge curves, obtained in the alkaline electrolytes which contain sodium borohydride (Fig.5). The immersion of different type of electrodes in sodium borohydride solution leads probably to a hydrogen absorption or hydride formation like the electrochemical charging does. This also explains the appearance of the second plateau on the curves as a result of the electro-oxidation of hydrogen, absorbed in the electrode.

For the application in practice, however, more detailed experiments and data analysis for optimization of the operation conditions such as the

borohydride concentration, temperature, etc., should be performed with electrodes of AKL-86, AKL-1002, and AKL-1519 alloys.

## CONCLUSIONS

An experimental metal hydride-air fuel cell was constructed, tested, and optimized.  $AB_5$  – type metal hydride alloys and air gas-diffusion electrodes were used as electrode materials. The current-voltage, power, and discharge characteristics of the described system render the characteristics suitable for use in low-temperature borohydride fuel cells.

**Acknowledgements:** The authors would like to thank the National Science Fund of Bulgaria, Ministry of Education and Science (New Technologies in the Energy Sector thematic program, Metal Hydride-Air Fuel Cell program, contract № D01-368/16.06.06) for the financial support of this work.

## REFERENCES

- 1 J. Larminie, A. Dicks, Fuel Cell Systems Explained, 2nd Edn., J. Wiley, New York, 2003
- 2 G. Hoogers, Fuel Cell technology Handbook, CRC Press LLS, 2003
- 3 L. Gu, N. Luo, G. Miley, *J. Power Sources*, **173**, 77 (2007).
- 4 C. Ponce de Leon, F. Walsh, D. Pletcher, D. Browning, J. Lakeman, *J. Power Sources*, **155**, 172 (2006).
- 5 U. Demirci, *J. Power Sources*, **172**, 676 (2007).
- 6 B. Liu, Z. Li, *J. Power Sources*, **187**, 291 (2009).
- 7 E. Guenge, M. Atwan, D. Northwood, *J. Electrochem. Soc.*, **153**, A150 (2006).
- 8 M. Atwan, D. Northwood, E. Gyenge, *J. New Mater. Electrochem. Syst.*, **8**, 243 (2005).
- 9 Y. Wang, Y. Xia, *Electrochem. Commun.*, **8**, 1775 (2006).
- 10 H. Cheng, K. Scott, *J. Electroanal. Chem.*, **596**, 117 (2006).
- 11 L. Jorissen, *J. Power Sources*, **155**, 23 (2006).
- 12 J. Ma, J. Wang, Y. Liu, *J. Power Sources*, **172**, 220 (2007).
- 13 A. Kaisheva, I. Iliev, S. Gamburgcev, *J. Power Sources*, **13**, 181 (1984).
- 14 R. Boukoureshlieva, S. Hristov, J. Milusheva, A. Kaisheva, Annual Proceedings of TU – Varna (2010) p. 16.
- 15 S. Hristov, Y. Petrov, A. Kaisheva, R. Boukoureshlieva, *Bulg. Chem. Commun.*, **38**, 208 (2006).

## ЕКСПЕРИМЕНТАЛЕН ГОРИВЕН ЕЛЕМЕНТ МЕТАЛЕН ХИДРИД-ВЪЗДУХ

С. М. Христов, Р. И. Букурещлиева, Й. Д. Милушева

ИЕЕС, БАН, 1113 София, ул. „Акад. Г. Бончев” №10

Постъпила на 22 юли, 2010 г.; преработена на 20 октомври, 2010 г.

(Резюме)

Метал хидридни сплави тип  $AB_5$  и въздушни газодифузионни електроди са съответно анодни и катодни материали в експериментален горивен елемент.  $NaBH_4$  е използван за доставяне на водород.

Изготвени, охарактеризирани и селектирани са подходящи за катодни материали въздушни газодифузионни електроди. Те са с идентичен газов слой и каталитичен слой от пиролизиран  $CoTMPP$ .

Конструиран и оптимизиран е експериментален нискотемпературен борхидриден горивен елемент. Получените работни характеристики показват възможности за бъдещо приложение като реален горивен елемент.

## Electrochemical deposition of alloys based on Ni-Fe-Co, containing W,P, and their characterization for hydrogen evolution reaction

V. D. Bachvarov<sup>1</sup>, M. H. Arnaudova<sup>1</sup>, R. St. Rashkov<sup>1\*</sup>, A. Zielonka<sup>2</sup>

<sup>1</sup>*Institute of Physical Chemistry, Bulgarian Academy of Sciences, Sofia, Bulgaria*

<sup>2</sup>*Forschungsinstitut für Edelmetalle und Metallchemie, Schwäbisch Gmünd, Germany*

Received: August 2, 2010; revised: October 14, 2010

Alloys with different composition were produced by electrodeposition dependence of electrolysis conditions. Alloys, rich in Fe and Co or rich in Ni, were obtained due to anomalous electrodeposition of Co and Fe. The morphology and component distribution were characterized by SEM and EDX analyses. The hydrogen evolution reaction (HER) on these materials was investigated by galvanostatic steady-state curves in 6 M KOH. The catalytic activity is improved when the alloys contain more Fe and Co than Ni and W, and especially in the presence of P, even in small amounts (3 to 3.5%). This significantly reduces polarization for HER. This fact may be directly connected to the increase of the real surface of the alloys.

**Keywords:** electrodeposition, Ni-Fe-Co alloys, hydrogen evolution reaction, polarization curves

### Introduction

One of the most common electrode materials is based on nickel and its alloys because of their good catalytic activity for hydrogen evolution reaction (HER). These electrodes play an important role in various electrochemical processes. In order to improve the properties of these materials and increase their electrocatalytic activity, various methods are applied such as alloying with other elements, incorporation of composite components and other changes aiming to obtain electrodes with well-developed, rough or porous surface. Codeposition of nickel with transition metals, binary [1–3] and ternary alloys [4–7], which have better catalytic activity, compared with the pure metal, is one of the most popular methods.

Lupi et al. [3] studied the electrocatalytic performance of Ni-Co alloy for HER, ranging the composition from 0 to 100%. The hydrogen overpotentials appear to be lower in the case of Co concentration, ranging between 41 and 64 wt. %, where the synergism between the catalytic properties of the Ni (low hydrogen over-potential) and Co (high hydrogen adsorption) is best pronounced and which allowed obtaining of a larger value of the exchange current density.

Electrodeposited iron is more active for the hydrogen than the pure nickel, but Ni-Fe [5] alloys show further high activity for the hydrogen evolution. The carbon addition to iron or nickel

through the complexing agent (for example lysine), into the electrolyte, remarkably enhances the activity for hydrogen evolution and changes the mechanism of hydrogen evolution. Ternary Ni-Fe-C alloys show the highest activity for hydrogen evolution compared with pure Ni and Ni-Fe alloy. The Ni-P alloys also possess good catalytic activity toward HER [8–9]. The activity of these electrodes depended on the method of preparation and P content [8]. The activity was higher for the materials, deposited at lower temperatures and for those, containing smaller amounts of P. It was found that the crystal size is correlated with the catalytic activity of the hydrogen evolution in alkaline media. The activity increased when crystal size decreased [9]. It is proposed that the increased catalytic activity is caused by an increased amount of amorphous phase surrounding the Ni crystals. This phase is able to absorb large amount of hydrogen.

The electrodeposition of the iron-group metals, their binary and ternary alloys were published [4, 10–14]. Also, the anomalous behavior of these alloys was studied [13]. The results revealed that Ni was inhibited by the presence of Fe<sup>2+</sup> and Co<sup>2+</sup> ions [14], while Fe deposition rate was enhanced by the presence of Co<sup>2+</sup> and Ni<sup>2+</sup> ions.

The aim of this work is to produce multiple component systems, based on the iron-group metals (including phosphorus) via electrodeposition, and to compare their electrocatalytic behavior for HER

\*To whom all correspondence should be sent:  
E-mail: rasho@ipc.bas.bg

## EXPERIMENTAL

The samples were prepared by electrodeposition under galvanostatic conditions in thermostatic glass cell with and without magnetic stirring. The electrolyte compositions are given in Table 1.

**Table 1**

Electrolyte compositions g dm <sup>-3</sup>	Electrolyte I	Electrolyte II
NiSO <sub>4</sub> ·7H <sub>2</sub> O	75	75
NiCl <sub>2</sub> ·6 H <sub>2</sub> O	12.5	12.5
Fe SO <sub>4</sub> ·7H <sub>2</sub> O	25	25
CoSO <sub>4</sub> ·7H <sub>2</sub> O	25	25
Na <sub>2</sub> WO <sub>4</sub> ·2H <sub>2</sub> O	30	30
Na <sub>3</sub> C <sub>6</sub> H <sub>5</sub> O <sub>7</sub> ·2H <sub>2</sub> O	125	125
NaH <sub>2</sub> PO <sub>2</sub> ·H <sub>2</sub> O	–	25

The electrolysis conditions for electrolyte I and II are – 3, 5, 7 and 10 A/dm<sup>2</sup>, t = 50°C, stirring - 0 min<sup>-1</sup> and 100 min<sup>-1</sup>, pH-5.5. Copper plates with geometric area of 2 cm<sup>2</sup> were used as substrates for cathodic deposits, and Pt-Ti mash for an anode. Electrochemical measurements for HER were made in a conventional three-electrode cell with platinum as a counter electrode and SCE as a reference in 6 M KOH.

The surface morphology of the alloys was analysed by scanning electron microscopy (SEM) using Leo 1455VP and Leo Supra 55VP, equipped with energy dispersion X-ray (EDX) detectors, Oxford Inca 200. The element content in the deposit bulk was determined by X-ray fluorescence analysis (Fischerscope X-RAY HDAL).

## RESULTS AND DISCUSSION

Alloys with different composition were produced by electrodeposition dependence of the electrolysis conditions. Alloys, rich in Fe and Co or rich in Ni, were obtained due to anomalous electrodeposition of Co and Fe. The alloys with different component composition of the electrolytes, given in Table 1, were electrodeposited. The component composition of the alloy was determined by X-ray fluorescence analysis (Fischerscope X-RAY HDAL). The results (Fig.1a) showed that in the absence of stirring and NaH<sub>2</sub>PO<sub>2</sub>, nickel and tungsten are predominant in the obtained alloys. The amount of W increases slightly (from 28 to 33 wt.%) with the current density increase. The content of nickel increases, while the amounts of the included Co and Fe decrease with the increasing current density (to 5A/dm<sup>2</sup>), and then remains almost unchanged for all three elements.

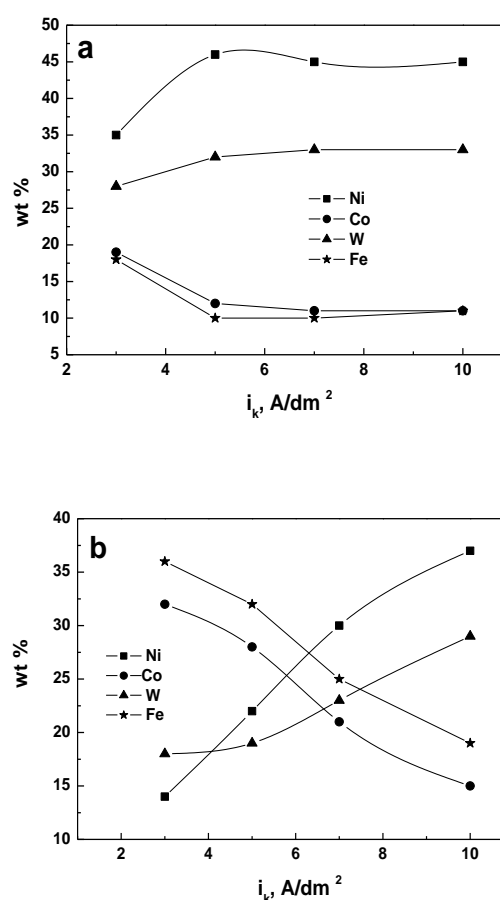


**Fig.1.** Dependence of the weight % of alloy components obtained from electrolyte I (Table 1) on the current density by X-ray fluorescence analysis: a) – without stirring; b)- stirring 100 min<sup>-1</sup>

The current density increase leads to growth of the nickel and tungsten content in the deposit (Fig.1b), while the amounts of Co and Fe decrease by stirring (100 min<sup>-1</sup>). Thus, different composition of layers is produced. For example, Fe-Co-W-Ni alloys are obtained at 3 A/ dm<sup>2</sup> while Ni-W-Fe-Co alloys at 10 A/dm<sup>2</sup>.

The content of W strongly reduces without stirring in the presence of phosphorus in the electrolyte (Fig.2a). The current density increase does not influence essentially the composition of the electrochemically obtained alloys. The nickel content increases up to 40%, while the content of Co and Fe decreases by stirring (fig.2b). The Fe-Co-Ni-W alloys are obtained at a low current density, while the Ni-Fe-Co-W alloys are prepared at high current densities. It is interesting that the amount of the main components (Ni-Fe-Co) is approximately the same (about 31–34 wt.%) in the alloy at 7 A/dm<sup>2</sup> (Fig.2b). The obtained results show that qualitatively different alloy composition

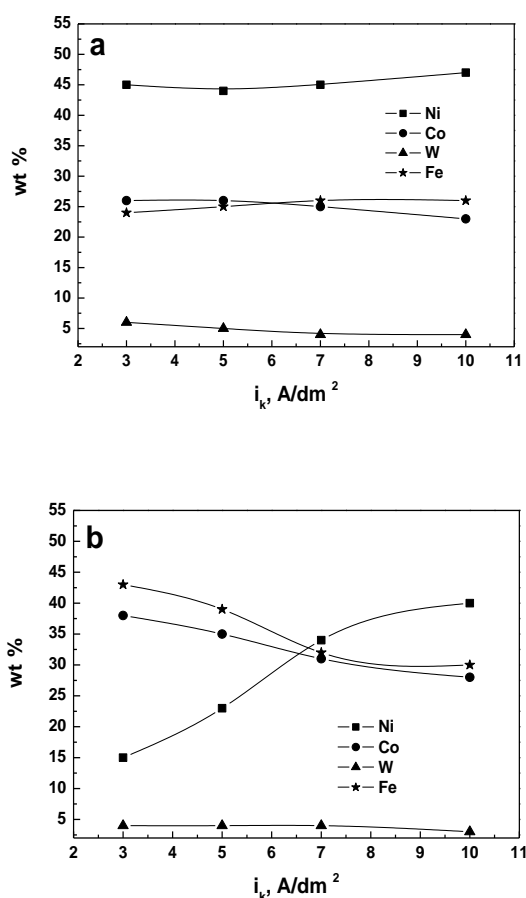


**Fig. 2.** Dependence of the weight % of alloy components obtained from electrolyte II (Table 1) on the current density in the presence of P by X-ray fluorescence analysis: a) – without stirring; b)- stirring 100 min<sup>-1</sup>

**Table 2**

Current density, A/dm <sup>2</sup>	Ni wt %	Co wt %	W wt %	Fe wt %	P wt %
3, stirring 100 min <sup>-1</sup>	15	37	5	40	3
7, stirring 100 min <sup>-1</sup>	32	30	4	31	3
10, stirring 100 min <sup>-1</sup>	37	26	5	29	3
3, without stirring	42,5	25	6	23	3,5
10, without stirring	44	23	5,5	24	3,5

deposits can be obtained under the varying conditions of the electrolysis process.

The X-ray fluorescence analysis does not allow the determination of P, included in the deposits are obtained from electrolyte II. Therefore, some of the samples were analyzed by the EDX method. The data from the analysis are presented in Table 2. The results show that independently of the electrolysis process conditions (with and without stirring and current density), the P content was approximately the same (about 3–3.5 wt %).

The method of polarization curves, as a criterion for the catalytic activity of the material, was used to study the HER. The deposited electrodes with a geometric surface of 2 cm<sup>2</sup> were tested for HER in 6 M KOH. The experiments were carried out under galvanostatic steady-state conditions. Before starting the measurements, the electrode surface was polarized for 30 min by applying a relatively high (100 mA/cm<sup>2</sup>) cathodic current. Then the current was lowered to 10 mA/cm<sup>2</sup>. The reproducible polarization curves are presented in Fig.3. The alloys, obtained from electrolytes I and II, with different content of basic components (Ni-Fe-Co-W), were selected. Polarization dependencies of the pure nickel and nickel-tungsten are also presented for a comparison. The Ni<sub>65</sub>W<sub>35</sub>

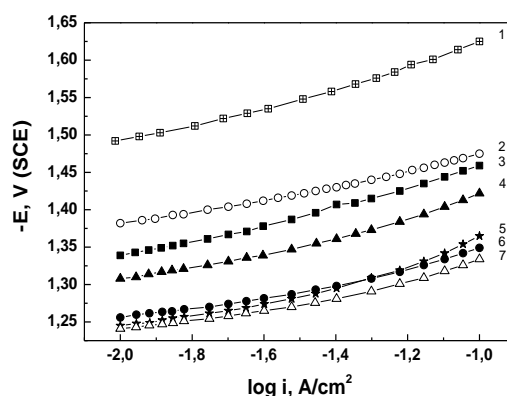


**Fig.3.** Polarization curves of some obtained alloys in 6 M KOH: 1-Ni; 2-Ni<sub>65</sub>W<sub>35</sub>; 3-Ni<sub>46</sub>W<sub>32</sub>Co<sub>12</sub>Fe<sub>10</sub>; 4-Fe<sub>32</sub>Co<sub>28</sub>Ni<sub>22</sub>W<sub>19</sub>; 5-Fe<sub>40</sub>Co<sub>37</sub>Ni<sub>15</sub>W<sub>5</sub>P<sub>3</sub>; 6-Ni<sub>42</sub>Co<sub>25</sub>Fe<sub>23</sub>W<sub>6</sub>P<sub>3.5</sub>; 7-Ni<sub>32</sub>Fe<sub>31</sub>Co<sub>30</sub>W<sub>4</sub>P<sub>3</sub> alloy (Fig.3, curve-2), obtained under the conditions given in [7], shows lower hydrogen over-potential than the pure nickel. The addition of Co and Fe to NiW alloys reduces the polarization for HER. A similar dependence on the nickel-iron and nickel-cobalt alloys was established by [3,5]. The catalytic activity is improved when the alloys contain more Fe and Co (curve 4) than Ni and W (curve 3). The presence of P, even in small amounts (see Table 2), significantly reduces the hydrogen overvoltage (curves 5, 6, and 7 in Fig.3). These curves show similar catalytic characteristics, although they have radically different composition. Comparing the P containing alloys, the alloy with approximately the same content of main components (Ni<sub>32</sub>Fe<sub>31</sub>Co<sub>30</sub>W<sub>4</sub>P<sub>3</sub>) shows the lowest polarization. It is known that the high catalytic activity of nickel alloys depends not only on the

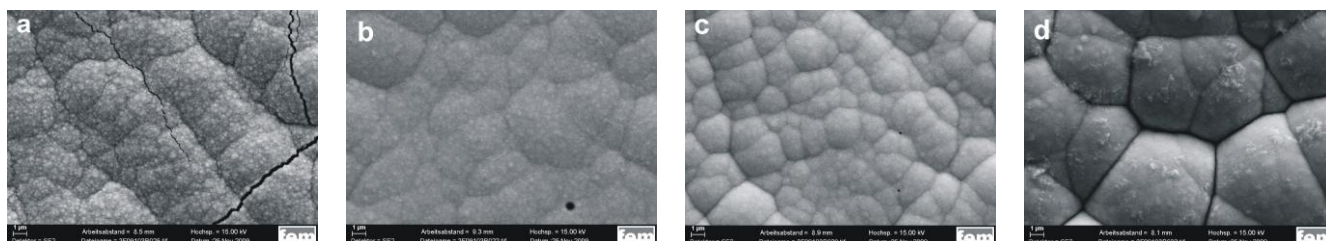


**Fig.4.** SEM images at 5 000x magnification: a)  $\text{Ni}_{46}\text{W}_{32}\text{Co}_{12}\text{Fe}_{10}$ ; b)- $\text{Fe}_{32}\text{Co}_{28}\text{Ni}_{22}\text{W}_{19}$ ; c)- $\text{Fe}_{40}\text{Co}_{37}\text{Ni}_{15}\text{W}_5\text{P}_3$ ; d)- $\text{Ni}_{32}\text{Fe}_{31}\text{Co}_{30}\text{W}_4\text{P}_3$ .

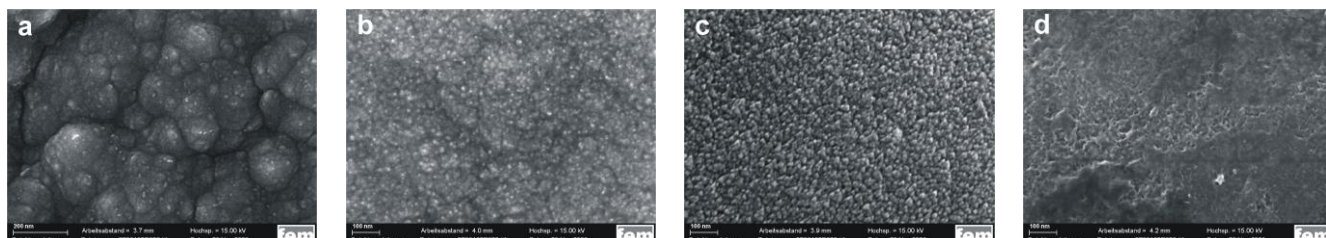


**Fig.5.** SEM images at 100 000x magnification: a)- $\text{Ni}_{46}\text{W}_{32}\text{Co}_{12}\text{Fe}_{10}$ ; b)- $\text{Fe}_{32}\text{Co}_{28}\text{Ni}_{22}\text{W}_{19}$ ; c)- $\text{Fe}_{40}\text{Co}_{37}\text{Ni}_{15}\text{W}_5\text{P}_3$ ; d)- $\text{Ni}_{32}\text{Fe}_{31}\text{Co}_{30}\text{W}_4\text{P}_3$ .

component composition but also on the component real surface.

The alloy morphology, corresponding to the polarization curves, is presented in Fig. 4 and 5. SEM investigations were carried out at various magnifications. A different size globular surface structure of the obtained deposits at 5 000x magnification for all alloys is observed (Fig.4). A better performance of the surface and the crystalline size is acquired at 100 000x magnification (Fig.5).

The availability of P in the alloys and probably lower content of W leads to a strong reduction in the size of crystals (Fig. 5c and d). This fact may be directly connected to the increase in the real surface of the alloys. Burchardt *et al.* [9] were found also that the differences in the electrode activities of Ni-P alloys are principally due to differences in the real surface area. Comparing figures 3 and 5, the results show that  $\text{Ni}_{32}\text{Fe}_{31}\text{Co}_{30}\text{W}_4\text{P}_3$  alloy presents the lowest polarization (Fig.3, curve 7), which owns the finest surface morphology (Fig.5d). In opposite,  $\text{Ni}_{46}\text{W}_{32}\text{Co}_{12}\text{Fe}_{10}$  alloy has the largest crystal grains (Fig.5a) and shows the highest polarization dependence (Fig.3, curve 3) for HER than the other multiple component alloys.

### CONCLUSIONS

Alloys, based on Ni-Fe-Co with the addition of W and P, were electrodeposited. It is shown that in dependence of the electrolysis process conditions rich of nickel and tungsten or iron and cobalt alloys can be obtained. The hydrogen overvoltage is reduced when the alloys contain more Fe and Co than Ni and W in the layers without phosphorus. The presence of phosphorus (3 to 3.5%) in the

alloys significantly reduces the content of tungsten in them. Polarization dependences of these alloys show better catalytic characteristics for HER than the deposits without phosphorus content. The reason for such result is probably the synergy between Ni and Co, from one hand, and the reduction of the crystal grain size, from the other hand, which determines a more developed surface.

**Acknowledgements:** The authors would like to thank the National Science Fund of Bulgaria, the Ministry of Education and Science (contract DTK 02–31/2009) for the financial support of this work. This work is partially supported by the Deutsche Forschungsgemeinschaft (DFG) within BUL-436 112/38/04, a joint research project of the Institute of Physical Chemistry of the BAS, Bulgaria and the Forschungsinstitut für Edelmetalle und Metallchemie, Germany.

### REFERENCES

1. Ch. Fan, D.L. Piron, A. Sleb, P. Paradis, *J. Electrochem. Soc.*, **141**, 382 (1994).
2. R. Rashkov, N. Atanassov, A. Jannakoudakis, P. Jannakoudakis, E. Theodoridou, *J. Electrochem. Soc.*, **153**, C152 (2006).
3. C. Lupi, A. Dell’Era, M. Pasquali, *Int. J. Hydrogen Energy*, **34**, 2101 (2009).
4. I. Arul Raj, K.I. Vasu, *J. of Appl. Electrochem.*, **22**, 471 (1992).
5. S. Meguro, T. Sasaki, H. Katagiri, H. Habazaki, A. Kawashima, T. Sakaki, K. Asami, K. Hashimoto, *J. Electrochem. Soc.*, **147**, 3003 (2000).
6. G. Lu, P. Evans, G. Zangari, *J. Electrochem. Soc.*, **150**, A551 (2003).
7. R. Rashkov, *Bul. Chem. Commun.*, **40**, 211 (2008).

8. R.K. Shervedani, A. Lasia, *J. Electrochem. Soc.*, **144**, 511 (1997).
9. T. Burchardt, V. Hansen, T. Våland, *Electrochim. Acta*, **46**, 2761 (2001).
10. N. Atanassov, M. Bratoeva, *Trans IMF*, **76**, 39 (1998).
11. K.Y. Sasaki, B. Talbot, *J. Electrochem. Soc.*, **145**, 981 (1998).
12. N.V. Myung, K. Nobe, *J. Electrochem. Soc.*, **148**, C136 (2001).
13. N. Zech, E.J. Podlaha, D. Landolt, *J. Electrochem. Soc.*, **146**, 2886 (1999).
14. Y. Zhuang, E.J. Podlaha, *J. Electrochem. Soc.*, **147**, 2231 (2000).

ЕЛЕКТРОХИМИЧНО ОТЛОЖЕНИ СПЛАВИ НА ОСНОВА Ni-Fe-Co,  
СЪДЪРЖАЩИ W, P И ТЯХНОТО ОХАРАКТЕРИЗИРАНЕ ЗА РЕАКЦИЯТА НА  
ОТДЕЛЯНЕ НА ВОДОРОД

В. Бъчваров<sup>1</sup>, М. Арнаудова<sup>1</sup>, Р. Рашков<sup>1</sup>, А. Цилонка<sup>2</sup>

<sup>1</sup>Институт по физикохимия „Акад. Р. Кашиев“, Българска академия на науките,  
ул. „Акад. Г. Бончев“ бл. 11, 1113 София

<sup>2</sup>Институт по благородни метали и химия на металите, Швебиш Гмюнд, Германия

Постъпила: 2 август, 2010 г.; преработена на 14 октомври, 2010 г.

(Резюме)

Синтезирани са електрохимично различни по състав сплави в зависимост от условията на електролиза. Сплави, богати на Fe и Co или богати на Ni са получени поради аномалното отлагане на Co и Fe. Морфологията и разпределението на компонентите са охарактеризирани чрез SEM и EDX анализи. Реакцията на отделяне на водород върху тези материали е изследвана посредством галваностатични криви в 6M KOH. Каталитичната активност се подобрява, когато сплавта съдържа повече Fe и Co, отколкото Ni и W и особено в присъствието на P в сплавта, дори в малки количества (3 до 3.5%). Тази концентрация на P значително понижава поляризацията на реакцията на отделяне на водород. Този факт вероятно се дължи на увеличението на реалната повърхност на сплавта.

## Differential impedance analysis of $\text{BaCe}_{0,85}\text{Y}_{0,15}\text{O}_{2,925}$

M. Z. Krapchanska\*, D. E. Vladikova, G. S. Raikova, M. P. Slavova, Z. B. Stoynov

*Institute of Electrochemistry and Energy Systems, Bulgarian Academy of Sciences,  
10 Acad. G. Bonchev St., 1113 Sofia, Bulgaria*

Received September 16, 2010; accepted September 20, 2010

In this study the technique of the Differential Impedance Analysis (DIA) is applied for characterization of the proton conducting material  $\text{BaCe}_{0,85}\text{Y}_{0,15}\text{O}_{2,925}$  (BCY15), which will be used in a new dual membrane fuel cell design. The BCY15 was investigated in symmetrical electrolyte supported half cell with Ag electrodes. The impedance measurements were performed in a temperature interval of 200 – 700°C. The combination of DIA and correction of the measurement rig parasitic inductance and resistance (L-correction) ensured a good separation of the bulk and grain boundaries contribution. The comparison of the results, obtained for the BCY15 proton conductivity, with the literature data demonstrates the good quality of the developed material.

**Keywords:** Impedance Spectroscopy, Differential Impedance Analysis, Yttrium Doped Barium Cerate ( $\text{BaCe}_{0,85}\text{Y}_{0,15}\text{O}_{2,925}$ )

### INTRODUCTION

The attempts for turning fuel cells into commercially successful alternative energy sources concern improvements towards lower cost, better stability of the performance, and higher fuel efficiency [1]. The main pathway for achievement of those objectives in solid oxide fuel cells (SOFCs) is the reduction of the operating temperature down to 600–700°C [2, 3], since those conditions will increase the cell stability, improve the compatibility of the materials, and ensure replacement of the ceramic interconnects with the cheaper metallic alloys. However, dilution of the fuel with water by-product is a principle construction disadvantage of the classical SOFCs, which is closely related to their lower efficiency. A new concept for overcoming this problem, known as the IDEAL-Cell after the acronym of the FP7 European project, is under development [4, 5]. It is based on a cell design with three independent chambers for hydrogen, oxygen, and water (Fig. 1a). In addition the efficiency of the system could be enhanced by an easy and independent application of pressure on the water-free hydrogen and oxygen electrodes. The proof of the proposed concept is the first stage in the development of the new design, for which a 3-chambered testing cell has to be produced with routine raw materials.

The aim of this study is the impedance

characterization of the proton conducting yttrium doped barium cerate ( $\text{BaCe}_{0,85}\text{Y}_{0,15}\text{O}_{2,925}$ ) for application in the new dual membrane fuel cell design as electrolyte in the hydrogen chamber and in the porous mixed conducting central membrane chamber (CM), where the water is produced and evacuated.

### EXPERIMENTAL

The BCY15 electrolyte material was investigated in symmetrical electrolyte supported half cell with Ag electrodes (Fig. 1b). Since the central membrane consists of three phases - BCY15, oxygen conducting electrolyte  $\text{Ce}_{0,85}\text{Y}_{0,15}\text{O}_{1,925}$  (YDC15), and pores, it is important to study the behaviour of the hydrogen conducting phase in the presence of both, the YDC15 and the pores. The investigations were performed on central membrane supported half cell  $\text{Ag}/\text{YDC15}_{\text{porous}}+\text{BCY15}_{\text{porous}}/\text{Ag}$  (Fig. 1c) which ensured direct measurement of the BCY resistivity in the central membrane.

The impedance measurements were performed with a Solartron 1260 Frequency Response Analyser in a temperature interval of 200 – 700°C, at scanning range from 10 MHz down to 0.1 Hz, and density of 5 points/decade. They were done in two modes: potentiostatic and galvanostatic. The change of mode and amplitude, which depends on the sample resistance, ensures higher quality of the measured data. Wet hydrogen (3%  $\text{H}_2\text{O}$ ), diluted

\* To whom all correspondence should be sent:  
E-mail: [milenazk@bas.bg](mailto:milenazk@bas.bg)

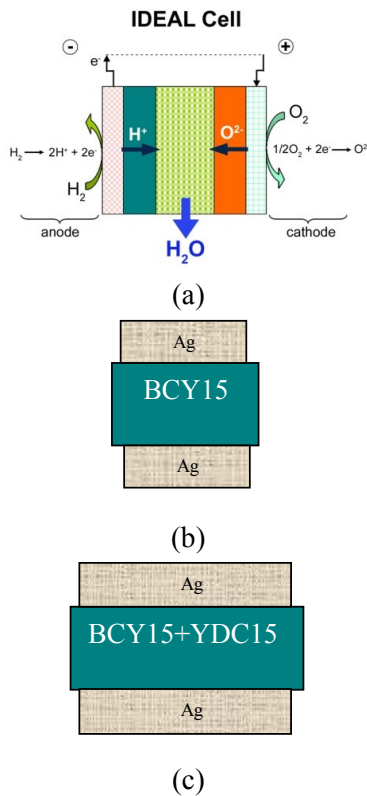


**Fig.1.** IDEAL Cell: a) concept; b) symmetrical electrolyte supported half cell Ag/BCY15/Ag; c) symmetrical CM supported half cell Ag/YDC15<sub>porous</sub>+BCY15<sub>porous</sub>/Ag

with nitrogen or argon and air/oxygen for evaluation of the CM oxygen conductivity, were applied. The experiments at lower temperatures ensure information about the electrolyte behaviour, including separation of the bulk from the grain boundaries contribution, while at higher temperatures the electrode reaction behaviour is well pronounced. For more precise determination of the BCY15 resistivity and activation energy, a correction of the measurement rig parasitic inductance and resistance was performed following a well developed specialized procedure (Fig. 2) [6, 7].

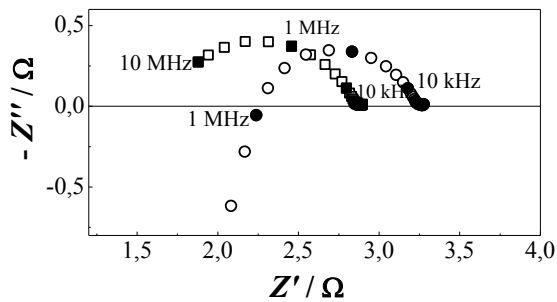


**Fig. 2.** Complex plane impedance diagrams of Ag/CM/Ag half cell before (●) and after (■) correction for parasitic resistance and inductance.

For a deeper insight into the investigated processes (recognition and separation of different steps and characterization of the rate-limiting one), the data were analysed by the technique of the Differential Impedance Analysis (DIA) [6–9]. DIA works with no preliminary working hypotheses, because the information about the model structure is extracted directly from the experimental data. After a specialized mathematical procedure, the initial data set (frequency  $\omega$ , real and imaginary components of the impedance) is presented in new coordinates, which give the frequency dependence ( $\nu = \lg \omega^{-1}$ ) of the effective parameters ( $\hat{P}$ ), additive effective resistance  $\hat{r}_{ad}$ , effective resistance  $\hat{R}$ , effective capacitance  $\hat{C}$ , and effective time-constant  $\hat{T} = \hat{R} \hat{C}$ . The approach is deterministic. The new form of presentation, called temporal analysis, recognizes well sub-models with lumped parameters. It also identifies frequency dependent behavior, which can be additionally analyzed by secondary analysis. More information about the secondary DIA can be found in [6–8]. In addition, the method has high selectivity and good noise immunity. The application of DIA is demonstrated in the example, shown in Fig. 3. It represents a two step reaction (i.e. a process described with 2 time-constants). The two plateaus, observed in the temporal plots, exhibit the presence of two time constants (Fig. 3b). They are separated by a region of frequency dispersion, which corresponds to the transition between the two reaction steps.

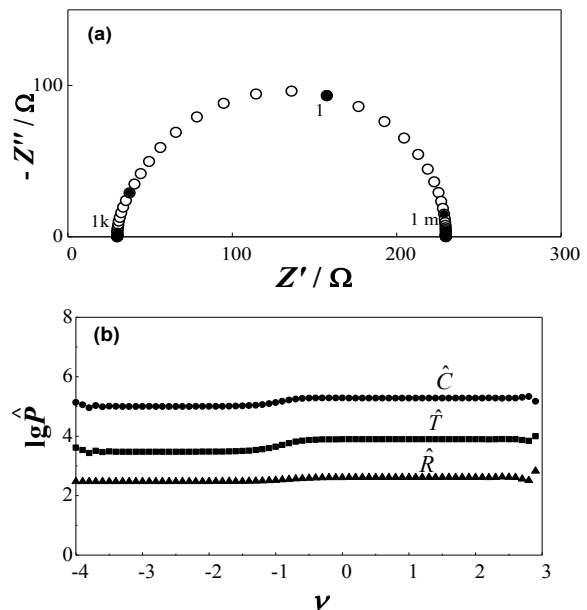


**Fig. 3.** DIA of simulated Faradaic reaction involving one adsorbed species: a) complex plane impedance diagram; b) temporal plots.

Thus the presence of plateaus ensures the recognition of the model, while their position enables the parametric identification. This example demonstrates also the good DIA selectivity, which can distinguish two time-constants with high degree of mixing.

## RESULTS AND DISCUSSION

The impedance measurements of testing cell with dense electrolyte, the Ag/BCY15/Ag (Fig. 4a), were performed in a single gas flow (wet hydrogen). The data were analyzed by DIA. The grain boundaries contribution can be estimated by the corresponding plateau in the  $\hat{R}$  - plot (Fig. 4b).

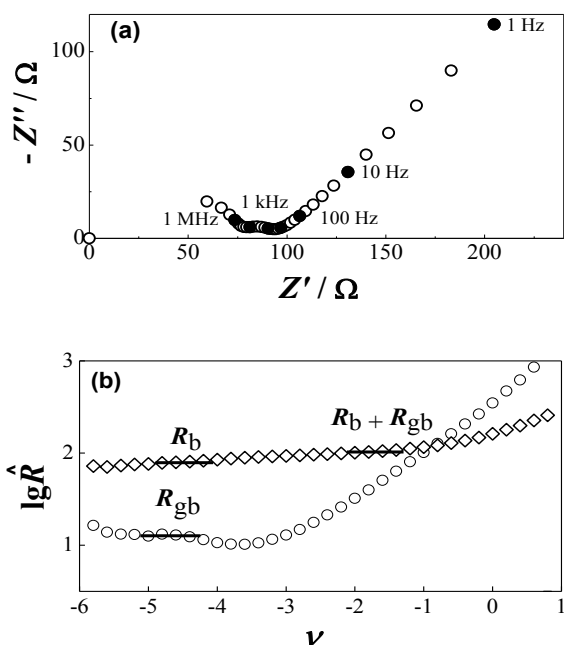


**Fig. 4.** Complex plane impedance diagram of symmetric half cell Ag/BCY15/Ag at 200 °C: a) Z-plot; b)  $\hat{r}_{ad}$  ( $\diamond$ ) and  $\hat{R}$  ( $\circ$ ) temporal plots.

The contribution of the bulk is insufficient for identification. However, the first plateau in the  $\hat{r}_{ad}$  - plot recognizes this parameter, which is an additive term in respect to the grain boundaries performance. The combination of L-correction and information, extracted from  $\hat{R}$  and  $\hat{r}_{ad}$  temporal plots, enables a good separation of the bulk and grain boundaries contribution for the hydrogen conducting electrolyte in a wide temperature range [10]. The Arrhenius plot of dense BCY15 is presented in Fig. 5. To be noticed here is the faster decrease of the grain boundaries resistivity with the temperature. Thus, at operating temperatures (600–700°C), the bulk contribution is dominating.

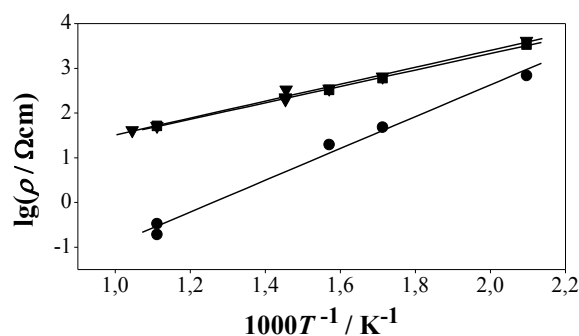


**Fig. 5.** Arrhenius plots for dense BCY15: (●) grain boundaries ( $E_a=0.71\text{eV}$ ); (■) bulk ( $E_a=0.36\text{eV}$ ) and (▼) total ( $E_a=0.37\text{eV}$ ).

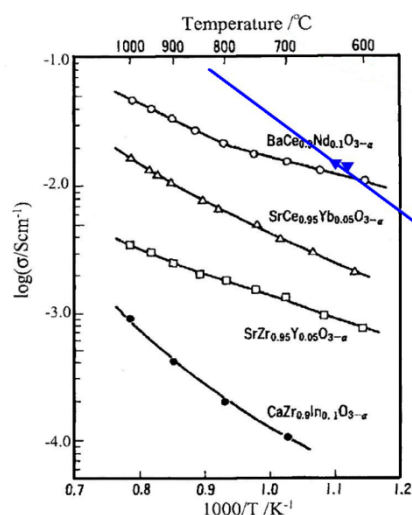


**Fig. 6.** Comparison of the BCY15 proton conductivity ( $\blacktriangledown$ ) with data from the literature.

The comparison of the results, obtained for the BCY15 proton conductivity using the literature data, demonstrates the good quality of the developed material [11–13] (Fig. 6).

The results obtained on CM half cells in a single gas atmosphere were used for quantitative estimation of the effect of the pores and the presence of the second phase on the resistivity of every electrolyte phase. This estimation does not take into account the influence of the water vapor formation and evacuation. The DIA procedure was successfully applied for estimation of both, the bulk and the grain boundary resistivity.

The grain boundary contribution was determined from the  $\hat{R}$ -temporal plot, although the contribution of the bulk is invisible in the Z-plot (Fig. 7 a). The first plateau in the  $\hat{r}_{ad}$ -plot, which gives the sum of  $R_b$  and  $R_{gb}$ , ensured its estimation (Fig. 7b).

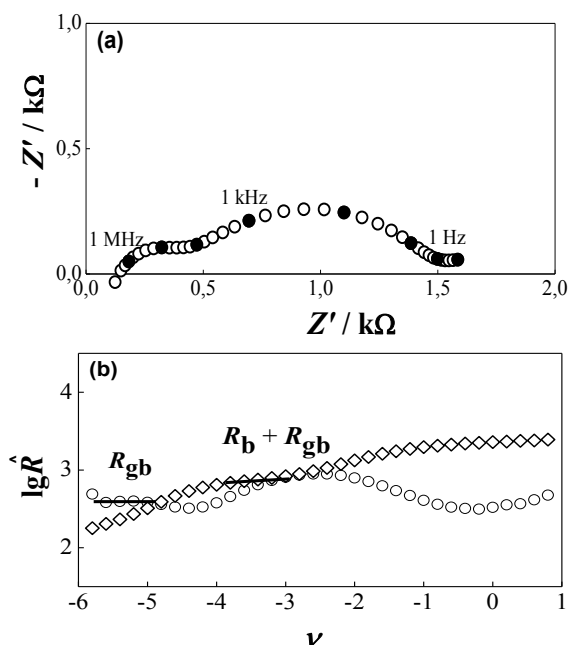


**Fig.7.** Complex plane impedance diagram and corresponding DIA plots for measurements of symmetric half cell Ag/CM/Ag at 300 °C in hydrogen: a) Z-plot; b)  $\hat{r}_{ad}$  ( $\diamond$ ) and  $\hat{R}$  ( $\circ$ ) temporal plots.

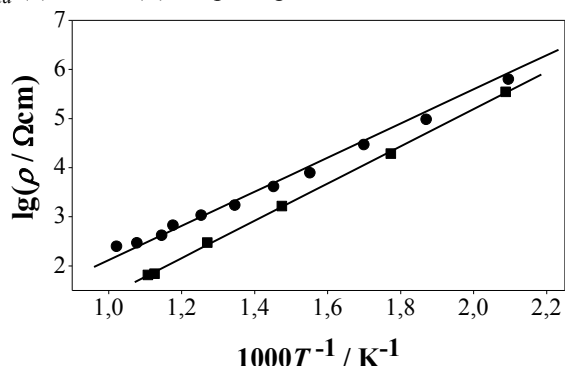


**Fig. 8.** Arrhenius plots for CM: (■) in  $H_2$ : total  $E_a=0.74$  eV; (●) in  $O_2$ : total  $E_a=0.70$  eV

The corresponding Arrhenius plots summarize the obtained results (Fig. 8). As it could be expected, the resistivity of the CM is lower in the hydrogen due to the higher proton conductivity of BCY15.

### CONCLUSIONS

The performed Differential Impedance Analysis of the proton conducting electrolyte BCY15 proved that it has stable performance in wet hydrogen atmosphere, which makes it desirable material for further application as a proton conductor in the hydrogen compartment and in the central membrane. The obtained results for the central membrane are very promising. They will be used for its further optimization by deeper insight into

the effect of composition and microstructure on the electrochemical performance.

**Acknowledgements:** The research, leading to these results, has received funding from the European Community Seventh Framework Programme (FP7/2007–2013) under grant agreement No 213389. Powders were fabricated by Marion Technologies. The samples were prepared by ARMINES.

### REFERENCES:

- 1.R. Calvo, *The Electrochemical Society Interphase* **13/3**, (2004) 7.
- 2.P. Larsen, C. Bagger, S. Linderoth, M. Mogensen, S. Primdahl, M. Jorgenson, P. Hendriksen, B. Kindl, N. Bonanos, F. Poulsen, K. Maegaard, in: H. Yokotawa, S. Singhal (Eds.), *Solid Oxide Fuel Cells (SOFCVII)*, The Electrochemical Society Proceedings Series, Pennington, NJ, 2001-16 (2001) 28.
- 3.D. Stover, R. Henne, P. Otschik, H. Schichl, in: H. Yokotawa, S. Singhal (Eds.), *Solid Oxide Fuel Cells (SOFCVII)*, *The Electrochemical Society Proceedings Series*, Pennington, NJ, 2001-16 (2001) 38.
4. www.ideal-cell.eu
- 5.A. Thorel, A. Chesnaud, M. Viviani, A. Barbucci, S. Presto, P. Piccardo, Z. Ilhan, D. Vladikova, Z. Stoynov “IDEAL-Cell, a high temperature Innovative DualMembrane fuel-Cell” in: *Solid Oxide Fuel Cells (SOFCXI)*, The Electrochemical Society Proceedings Series, Pennington, NJ, (2009) - to be published. K. Kreuer, *Electrochem. Soc. Proc.* **97-24** (1997) 17.
- 6.Z. Stoynov, D. Vladikova, *Impedance Spectroscopy of Electrochemical Power Sources* in: U. Garche (Ed.) *Encyclopedia of Electrochemical Power Sources*, Elsevier, 2009.
- 7.D. Vladikova, Z. Stoynov, *Differential Impedance Analysis*, Marin Drinov Academic Publishing House, Sofia, 2005.
- 8.D. Vladkova, Z. Stoynov, *J. Electroanal. Chem.* **572** (2004) 377.
- 9.D. Vladikova, Z. Stoynov, A. Barbucci, M. Viviani, P. Carpanese, J. Kilner, S. Skinner, R. Rudkin, *Electrochimica Acta* **53** (2008) 7491.
10. D. Vladkova, Z. Stoynov, G. Raikova - to be published
11. S. Singhal, K. Kendall, *Solid Oxide Fuel Cells: Fundamentals, Design and Applications*, Elsevier, 2003.
12. K. Liang, A. Nowick in: T. Ramanarayanan (Ed.), *Ionic and Mixed Conducting Ceramics III*, *The Electrochemical Society Proceedings Series*, Pennington, NJ, 97-24 (1997) 28.
13. Ph. Stevens, Y. Piffard, M. Caldes-Rouillon, Th. Delahaye, US Patent Application Publication, US2010/0015495 A1, Jan. 21 2010.

ДИФЕРЕНЦИАЛЕН ИМПЕДАНСЕН АНАЛИЗ НА BaCe<sub>0,85</sub>Y<sub>0,15</sub>O<sub>2,925</sub>

М. Кръпчанска, Д. Владикова, Г. Райкова, М. Славова, З. Стойнов

*Институт по електрохимия и енергийни системи, Българска академия на науките,  
ул. „Акад. Г. Бончев” бл. 10, 1113 София*

Постъпила на 16 септември, 2010 г.; приета на 20 септември, 2010 г.

(Резюме)

В това изследване е приложена техниката на диференциалния импедансен анализ (ДИА) за охарактеризиране на протонно проводимия материал BaCe<sub>0,85</sub>Y<sub>0,15</sub>O<sub>2,925</sub> (BCY15), с цел използването му в нова двойно мембранна горивна клетка. Експериментите са проведени в симетрична полу-клетка със Ag-електроди. Импедансните измервания са проведени в температурния интервал 200 - 700°C. Комбинацията от ДИА и корекцията за паразитна индуктивност и съпротивление (*L*-корекция) осигурява добро разделяне на проводимостта дължаща се на обема и границите на зърната. Сравняването на резултатите получени за протонната проводимост на BCY15 с данни от литературата показва доброто качество на разработения материал.

## Synthesis and electrochemical properties of the electrode materials for supercapacitors

M. Mladenov<sup>a\*</sup>, N. Petrov<sup>b</sup>, T. Budinova<sup>b</sup>, B. Tsyntsarski<sup>b</sup>, T. Petrov<sup>d</sup>, D. Kovacheva<sup>c</sup>, R. Raicheff<sup>a</sup>

<sup>a</sup>*Institute of Electrochemistry and Energy Systems, Bulgarian Academy of Sciences, Ac. G.Bonchev St., building 10, 1113 Sofia, Bulgaria*

<sup>b</sup>*Institute of Organic Chemistry, Bulgarian Academy of Sciences, Ac. G.Bonchev St., building 9, 1113 Sofia, Bulgaria,*

<sup>c</sup>*Institute of General and Inorganic Chemistry, Bulgarian Academy of Sciences, Ac. G.Bonchev St., building 11, 1113 Sofia, Bulgaria*

<sup>d</sup>*University of Chemical Technology and Metallurgy, 8 St. Kliment Ohridski Blvd., 1756 Sofia, Bulgaria*

Received: August 25, 2010; October 20, 2010

New electrode materials for supercapacitors - activated carbons, produced by carbonization of mixtures of coal tar pitch and furfural, with a subsequent hydrothermal treatment, were characterized and tested electrochemically. The microstructure, surface morphology and porous structure of the carbon materials were studied, and the main textural parameters and micropore size distribution were determined. Symmetric sandwich-type supercapacitor cells, with identical carbon electrodes and organic electrolyte, were assembled and subjected to charge-discharge cycling study at different current rates. Four types of carbons as electrodes with different specific surface area ( $1000 - 1600 \text{ m}^2 \text{ g}^{-1}$ ) and texture parameters, as well as three types of organic electrolytes ( $\text{Et}_4\text{NBF}_4 - \text{PC}$ ,  $\text{LiBF}_4 - \text{PC}$ ,  $\text{LiPF}_6 - \text{DMC/EC}$ ), were tested and compared with an asymmetric supercapacitor, composed by graphitized-activated carbon (carbon foam) as a negative electrode, and activated carbon/ $\text{Li}_4\text{Ti}_5\text{O}_{12}$  oxide composite as a positive electrode. The capacitance values of up to  $75 \text{ F.g}^{-1}$  were obtained for the symmetric supercapacitors, depending on the microstructure and the conductivity of the carbon material, and about two times higher capacitance was obtained for the asymmetric supercapacitor, with good cycleability of both supercapacitor systems.

**Keywords:** supercapacitors, electrode materials, organic electrolyte, nanostructured carbons, hybrid capacitor

### 1. INTRODUCTION

In the last years the electrochemical double-layer capacitors (supercapacitors) have attracted worldwide interest of the research groups and companies, working in the field of chemical power sources, due to their potential applications as energy storage devices. In the comparison of different energy storage devices, the batteries show the highest energy density (up to  $200 \text{ Wh kg}^{-1}$ ) but they have low power density (below  $500 \text{ W kg}^{-1}$ ) and a limited cycle life (usually less than 1000 cycles). The electrochemical capacitors tend to have lower energy density (up to  $10 \text{ Whkg}^{-1}$ ), compared to the batteries, but they can provide high power capability (above  $1000 \text{ Wkg}^{-1}$ ), high reversibility (90–95% or more) and excellent cycling characteristics (usually more than  $10^5$  cycles). Other advantages of the supercapacitors, compared with the rechargeable batteries, are their extremely low internal resistance, high output power, exceptionally low level of heat emission

while working, and an improved safety. Typically, they exhibit much larger (up to 200 times) capacitance than the conventional capacitors [1–5].

The integration of supercapacitors and batteries in the energy storage systems gives a possibility to combine the high transient performance of the supercapacitors with the high steady-state characteristics of the electrochemical power sources, and thus to attain effective control within the energy storage and consumption processes. The obtained hybrid power source effectively supplies energy for a long time, and in the same time, it is capable to cover high power peaks in both, the consumption and the charging.

Porous carbons are among the most attractive materials for preparation of electrodes for electrochemical capacitors. The main advantage of these materials is the possibility to produce highly porous structures with high specific surface area, and to regulate the porosity texture of the electrodes. On the other hand, the carbon materials give also possibilities to develop various composite electrode structures by adding electrochemically active materials to the carbon matrix [6, 7].

\* To whom all correspondence should be sent:  
E-mail: mladen47@bas.bg

The electrochemical cells in the carbon-based supercapacitors are usually symmetrical with identical carbon electrodes. In order to improve the energy density while keeping long cycle life, asymmetrical cells, consisting of different types of electrodes, were introduced. Thus, hybrid capacitor configurations, consisting of active carbon as a positive electrode and a negative electrode based on metal oxides (nickel, lead or manganese oxides) [8–10], conducting polymers [11], or Li intercalation oxides [12–13], were suggested, and promising results were obtained. An interesting approach in this respect is also the so called Li ion capacitor, using lithiated graphite and activated carbon for the negative and positive electrodes, respectively [14].

Our previous studies [15, 16] showed that nanoporous carbon materials can be synthesized from waste biomass (apricot stones and spent coffee grounds), and their pore texture could be readily regulated by appropriate thermal and hydrothermal treatment. The electrochemical tests showed promising characteristics (capacity values of up to 60 F.cm<sup>-2</sup>, cycling efficiency of 85–90%) of the symmetrical sandwich-type capacitor cells with tested carbon electrodes and organic electrolyte of Et<sub>4</sub>NBF<sub>4</sub> – PC.

The main objective of the this work is to study the electrochemical properties of the newly synthesized carbon electrode materials on the base of waste biomass for supercapacitors. Another aim of this work is to compare the capacitance behaviour of the symmetrical carbon-based supercapacitors with those of the asymmetrical supercapacitor, composed by carbon and carbon-Li<sub>4</sub>Ti<sub>5</sub>O<sub>12</sub> oxide composite electrodes.

## 2. EXPERIMENTAL

### 2.1. Synthesis of activated carbons

The mixtures of coal tar pitch and furfural in different proportions (ranging from 30 to 60 wt.%) were treated with concentrated H<sub>2</sub>SO<sub>4</sub> (drops of H<sub>2</sub>SO<sub>4</sub> were added to the mixtures with continuous stirring) at 120°C until solidification. The obtained solid product was heated at 600°C in a covered silica crucible with a heating rate of 10°C min<sup>-1</sup> under nitrogen atmosphere. The obtained solid product upon carbonization was further submitted to steam activation at 800°C for 1 hour for synthesizing the porous carbon. The samples were labelled with C (carbon) and F (furfural) followed by the content in furfural (CF–50 and CF–55). In order to explore the effect of the high temperatures on the electrochemical performance of the carbon materials, selected samples were submitted to an

additional heat treatment under nitrogen atmosphere. The CF–50 sample was treated at 1100°C and the CF–55 sample – at 1400°C. The samples, submitted to this additional heat treatment, were labelled with H (CF–50H and CF–55H).

### 2.2. Morphological and physicochemical characterization of the electrode materials

Powder X-ray diffraction spectra were collected within the range from 5 to 80° 2θ, with a constant step of 0.02° 2θ, on Bruker D8 Advance diffractometer with Cu Kα radiation and LynxEye detector. The spectra were evaluated with the *Diffractionplus* EVA and *Topas-4.2* packages. The morphology of the activated carbon was examined by means of a scanning electron microscope, the JEOL-Superprobe 733.

The synthesized carbons were characterized by N<sub>2</sub> adsorption at –196 °C, carried out in an automatic volumetric apparatus of ASAP 2020 – Micromeritics. The isotherms were used to calculate the specific surface area, pore volumes and pore size distributions; the latter - using the DFT method.

### 2.3. Electrochemical tests

The carbon electrodes were prepared from a mixture of 90wt.% activated carbon powder and 10wt.% polytetrafluoroethylene (PTFE binder – Aldrich, 60% suspension in water), and pressed on aluminum discs (surface area of 1.75 cm<sup>2</sup>). The active material mass was kept constant in all the experiments (15 mg cm<sup>-2</sup>). The electrodes were soaked in the electrolyte before the cell assembly. The sandwich-type symmetric capacitor cells were constituted of two identical carbon electrodes of comparable mass. The electrodes were electrically isolated by a ceramic-mat separator, soaked with an organic electrolyte, and the cell was assembled in a dry-box under argon. Three type of organic electrolytes: Et<sub>4</sub>NBF<sub>4</sub> – PC (propylene carbonate), LiBF<sub>4</sub> – PC and LiPF<sub>6</sub> – DMC/EC (dimethyl carbonate/ethylene carbonate in ratio 1:1) (Aldrich p.a.) were used.

The composite electrodes were prepared from electrochemically active nanostructured Li<sub>4</sub>Ti<sub>5</sub>O<sub>12</sub> oxide, carbon CF-50 and a conductive material (natural graphite NG–7 or acetylene black), in a 1:1:1 ratio. The asymmetric capacitor cell was composed by activated carbon as a negative electrode and activated carbon-Li<sub>4</sub>Ti<sub>5</sub>O<sub>12</sub> composite as a positive electrode with organic electrolyte LiPF<sub>6</sub>– DMC/EC.

The capacitor cells were subjected to galvanostatic charge-discharge cycling at different current rates using an Arbin Instrument System BU-2000 [16].

### 3. RESULTS AND DISCUSSIONS

#### 3.1. Physicochemical characterization

Powder X-Ray diffraction patterns of the CF-50 and CF-55 carbon materials are presented in Fig. 1. Patterns consist of two main amorphous “humps”, located at  $2\theta$  values of about  $24.5^\circ$  and  $43.5^\circ$ , corresponding to the (002) and (100)+(101) peaks of 2H-hexagonal crystalline graphite. Since carbon materials consist of small packs of graphene sheets, the positions of these two humps show the mean value of the interplanar distances in directions perpendicular to the sheets and within the sheets, correspondingly. The width of the peaks is related to the mean crystallite sizes within the corresponding directions, as presented in Table 1. The pattern of CF-50H sample, which is treated at higher temperature than the CF-50 sample, shows several stronger peaks imposed on the main amorphous-like powder pattern of activated carbon, indicating the formation of graphite domains with higher crystallite sizes.

**Table 1.** Main parameters obtained from XRD patterns of the carbon samples.

Sample	CF-50	CF-50H	CF-55	CF-55H
	carbon	carbon	graphite	carbon
(002)-position [Å]	3.719	3.732	3.379	3.711
Distance[nm] between graphene layers [nm]	0.56(6)	0.75(13)	3.23(44)	0.51(9)
(100)-position [Å]	2.081	2.079	2.132	2.083
Distance[nm] between C atoms in a graphene layer [nm]	0.86(10)	1.42(7)	14(1)	1.23(10)
	Degree of crystallinity $\approx 10\%$			

SEM-photographs of CF-55 sample, prior and upon high temperature thermal treatment, are

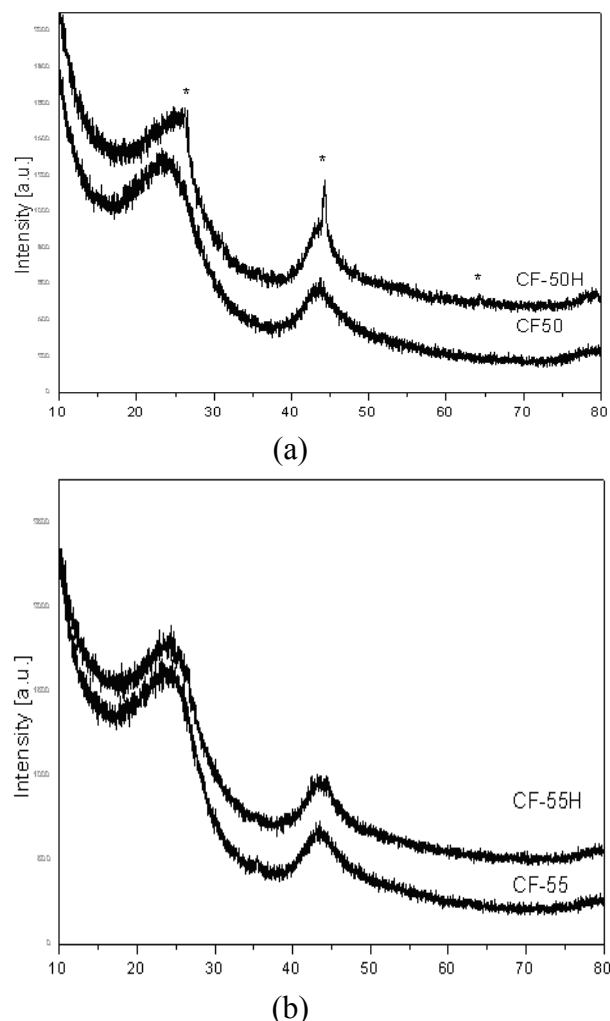


**Fig. 1.** X-ray diffraction patterns of the activated carbons: a - CF-50 and CF-50H, b - CF-55 and CF-55H.

presented in Fig. 2. No significant changes of the sample morphology are observed.

The pore structure of the carbons was investigated by gas adsorption [17]. The nitrogen adsorption isotherms at  $-196^\circ\text{C}$  of the samples were thus recorded (Fig. 3). The main textural parameters of the carbons, obtained from the analysis of the nitrogen adsorption isotherms, are compiled in Table 2. It can be seen from the data in the table that the furfural content has a strong effect on the porosity of the resulting carbons. The sample with the lower proportion of furfural (CF-50) exhibits a type I isotherm according to the BDDT classification, which is indicative for microporous materials. As the content of furfural rises, the isotherms gradually become of the I/IV type, with a clear opening of the knee at low relative pressures. This indicates for development of mesoporosity and widening of the microporosity in the CF-55sample.

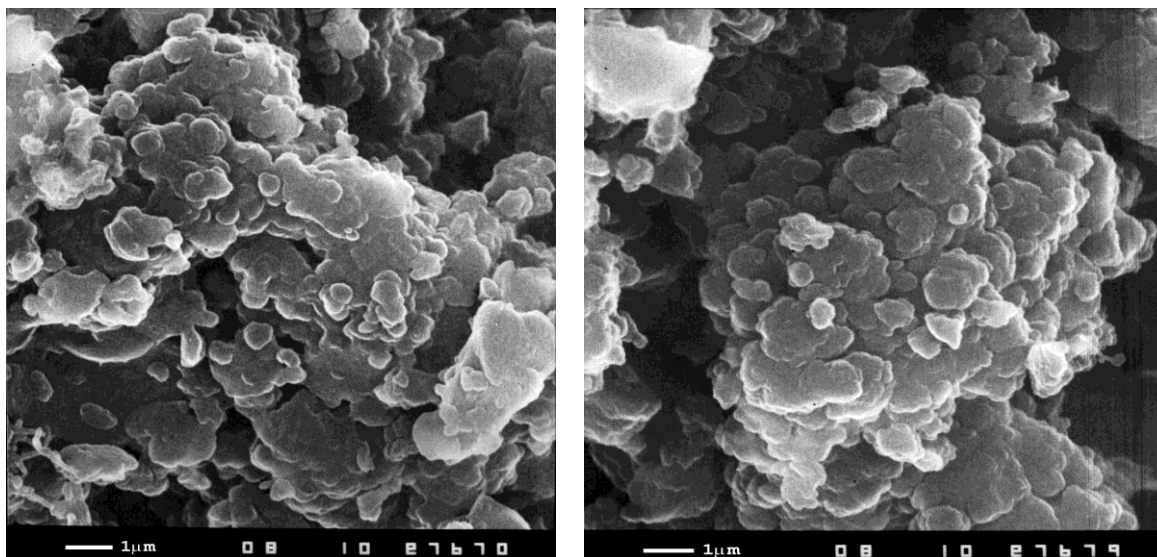
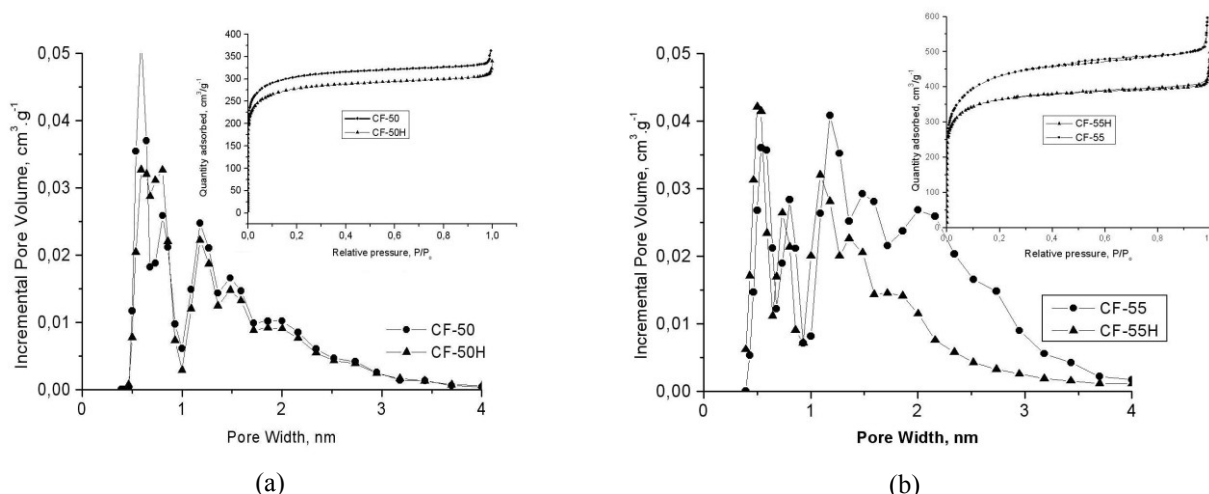


Fig.2. SEM-photograph of carbon samples CF-55 (left) and CF-55H (right).



(a)

(b)

Fig.3. Pore size distribution and N<sub>2</sub> adsorption isotherms of the activated carbons: a - CF-50 and CF-50H, b - CF-55 and CF-55H.

This observation was confirmed by the analysis of the PSD by the DFT method (Table 2 and Fig.3). Rising the furfural content in the initial mixture from 50% to 55% (CF-50 and CF-55) leads to increase of the micropore and mesopore volumes (cf. Table 2 and Fig. 3). It has been reported that the presence of oxygenated groups enhances the

**Table 2.** Main textural parameters of the carbons obtained from N<sub>2</sub> adsorption isotherms at -196°C.

Samples	S <sub>BET</sub> [m <sup>2</sup> g <sup>-1</sup> ]	V <sub>TOTAL</sub> <sup>a</sup> [cm <sup>3</sup> g <sup>-1</sup> ]	V <sub>MICRO</sub> <sup>b</sup> [cm <sup>3</sup> g <sup>-1</sup> ]	V <sub>MESO</sub> <sup>b</sup> [cm <sup>3</sup> g <sup>-1</sup> ]	W <sub>O</sub> N <sub>2</sub> <sup>c</sup> [cm <sup>3</sup> g <sup>-1</sup> ]
CF-50	1173	0.551	0.374	0.033	0.533
CF-50H	1071	0.486	0.338	0.033	0.473
CF-55	1613	0.761	0.492	0.177	0.604
CF-55H	1397	0.620	0.440	0.074	0.509

<sup>a</sup> evaluated at relative pressures of 0.99

<sup>c</sup> evaluated by DR approach

<sup>b</sup> evaluated by DFT method applied to N<sub>2</sub> adsorption data using slit-shaped pore model

inner resistance and the leakage current of carbon electrodes [18]. Taking into account the large amount of surface oxygen-containing functionalities in the CF-50 and CF-55 carbons, due to the incorporation of furfural in the synthesis [17], it is reasonable to expect a high resistance in these materials. Consequently, carbon samples were submitted to high thermal treatment in order to remove the surface functionalities (CF-50H and CF-55H). On the other hand, it is also known that heating at high temperature may favour internal rearrangements in the carbon structure, which (depending on the carbon precursor) can end up with an increase in the electrical conductivity, if graphite-like domains are formed during the rearrangements. The thermal treatment, however, may also cause some important modifications in the textural and structural properties of the carbon

skeleton (annealing effects). Thus it becomes necessary to investigate the porosity of the samples after such a treatment. The results show (Fig. 2) a decrease in the surface area and pore volumes of the treated carbons, which is more strongly expressed in the case of CF-55H (treated at a higher temperature), and more precisely for the mesopore volume.

### 3.2. Electrochemical performance

Two-electrode symmetric cells were used to evaluate the electrochemical characteristics of the carbon electrode material of CF-50 in different electrolytes:  $\text{Et}_4\text{NBF}_4$ -PC,  $\text{LiBF}_4$ -PC and  $\text{LiBF}_6$ -DMC/EC. The discharge capacities of the capacitors with different electrolytes are compared at different current rates (20 – 160  $\text{mA g}^{-1}$ ), in the potential range between 1.2 and 2.5 V, Fig. 4. As we can see, the capacity of CF-50 electrodes decreases gradually with the increase of the discharge current in all electrolytes, but this decrease is more pronounced for capacitors with electrolytes, containing  $\text{Li}^+$  ions. At low current rates (e.g. at about 20  $\text{mA g}^{-1}$ ) all three types of capacitors have very close capacity values. At high current rates, however, the capacitors with  $\text{Li}^+$  ions in the electrolyte demonstrate quite different behavior in comparison with the capacitor cell with  $\text{Et}_4\text{N}^+$  in the electrolyte, as the capacitance of the latter is much higher than those of the other two cells. Thus, the discharge capacity values of the carbon-based symmetric capacitors, depending on the employed organic electrolyte, can be ranked in the following order:  $\text{Et}_4\text{NBF}_4 > \text{LiBF}_4 > \text{LiPF}_6$ . The effect of the electrolyte on the discharge capacity may be related to the dimensions of the solvating 'guest' ions in the electrolyte. Additional investigation, however, is required in order to elucidate quantitatively the above effect. In the following electrochemical studies on the carbon electrode materials,  $\text{Et}_4\text{NBF}_4$ -PC was used as electrolyte in the capacitor cells.

The good cycleability of all three capacitors is illustrated in Fig.4. It shows the charge-discharge profiles of the capacitors after 50 cycles. The cell, using  $\text{Et}_4\text{NBF}_4$  electrolyte, demonstrates not only the highest capacity but the most stable cycleability as well. It should be noticed that the capacitor cells, using  $\text{Li}^+$ -base electrolyte, have not such high capacitance as expected, and moreover, their cycling performance is not so stable, especially at high current rates, as compared to this of the cell with  $\text{Et}_4\text{N}^+$ -based electrolyte. Two-electrode symmetric capacitor cells were assembled with

various active carbon materials (CF-50, CF-50H, CF-55 and CF-55H) as well as asymmetric capacitor cells, constituted by activated carbon (CF-50) and composite electrode (carbon CF-50/ $\text{Li}_4\text{Ti}_5\text{O}_{12}$  oxide with additive of natural graphite NG-7).

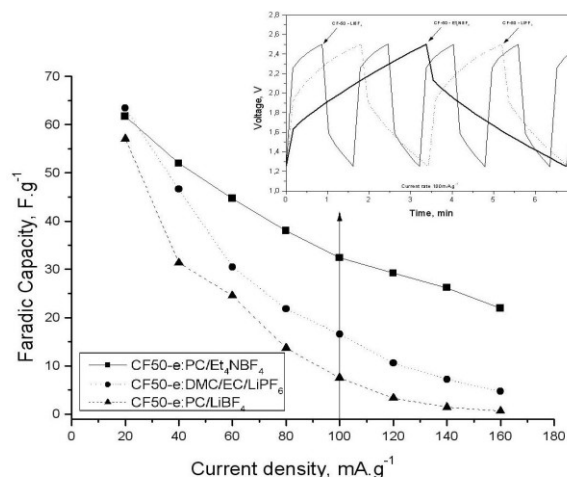


**Fig. 4.** Dependence of capacity on discharge current and cycling performance for symmetric cells carbon CF-50 and different electrolytes.

The PTFE content in the active material was kept constant (10 wt.%), and the organic electrolyte was of 1.5 M  $\text{Et}_4\text{NBF}_4$  in PC in all cases. The cells thus composed were subjected to galvanostatic cycling at different current rates (20 – 160  $\text{mA g}^{-1}$ ).

The capacitance of the capacitor cell was calculated from the slope of the potential – time (V-t) curves:

$$C = I / (dV/dt) \quad (1)$$

where  $C$  is the capacitance of the cell (F),  $I$  is the discharge current (A), and  $dV/dt$  is the slope of V-t curve ( $\text{V.s}^{-1}$ ).

In a symmetric cell, the specific capacitance  $C_{m_{AM}}$  (capacitance per unit mass activated carbon material,  $\text{F.g}^{-1}$ ) is related to the capacitance of the cell  $C$  and the carbon mass  $m_{AM}$  by the following equation:

$$C_{m_{AM}} = 2C / m_{AM} \quad (2)$$

Fig.5 presents typical capacity-current rate plots, obtained during galvanostatic charge/discharge cycling of different capacitor cells. We can see that all carbons show satisfactory capability of charge accumulation in the electric double layer up to current rates of about 150-160  $\text{mA.g}^{-1}$ . The capacitance values of the cell with carbon electrodes of CF-50 ( $S_{\text{BET}} = 1170 \text{ m}^2.\text{g}^{-1}$ ,  $V_M =$

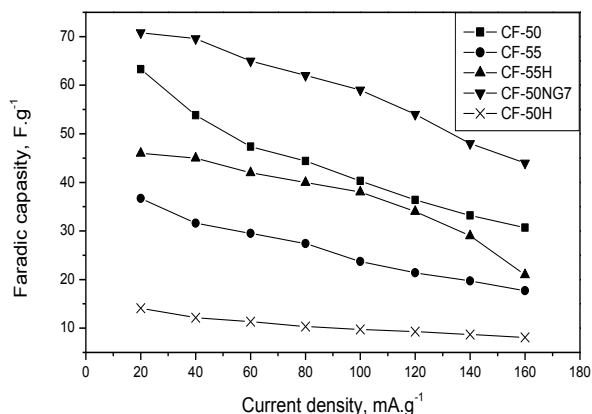


**Fig. 5.** Dependence of capacity on discharge current for symmetric cells with different carbons and  $\text{Et}_4\text{NBF}_4$  electrolyte (CF-50NG7 – carbon CF-50 with an addition of 10% natural graphite NG-7).

$0.374 \text{ cm}^3 \cdot \text{g}^{-1}$ ), however, are much higher than those of the cell with carbon electrodes of CF-55 ( $S_{\text{BET}} = 1600 \text{ m}^2 \cdot \text{g}^{-1}$ ,  $V_{\text{M}} = 0.492 \text{ cm}^3 \cdot \text{g}^{-1}$ ). It is usually anticipated that the capacitance of the porous carbon should be proportional to its available surface-area [19]. In practice, the major factors that contribute to this relationship, often with a complex non-linear character, are: the assumptions in the measurement of electrode surface-area, variations in the specific capacitance with differing morphology and pore-size distribution, variation in surface chemistry, conductivity of the carbon particles, etc. The activated carbons of CF-50 and CF-55 show quite different porous texture characteristics: pore volume, surface-area, and micropore size distribution (cf. Table 2 and Fig. 3).

There are contradictory reports in the literature on the effect of increasing surface area and porosity on the intrinsic electronic conductivity of compact carbon powders [19]. It seems logical to expect that the volumetric conductivity decreases as the microporosity ( $V_{\text{M}}$ ) and surface area ( $S_{\text{BET}}$ ) increase. In this respect, the results of some authors [17] show that the specific resistance of the cell, using activated carbon CF-50, is  $0.8 \Omega \text{ cm}^2$ , and  $1.2 \Omega \text{ cm}^2$  for the cell, using CF-55 carbon. In this comparison, the higher capacitance values of the cell with CF-50 carbon (30% more than the capacitance of the cell with CF-55 carbon, with the same electrolyte  $\text{Et}_4\text{NBF}_4 - \text{PC}$ ) is most probably due to its higher conductivity.

As mentioned above, the presence of oxygenated groups in the carbons of CF-50 and CF-55 enhances their inner electroresistance. Consequently, these carbons were submitted to

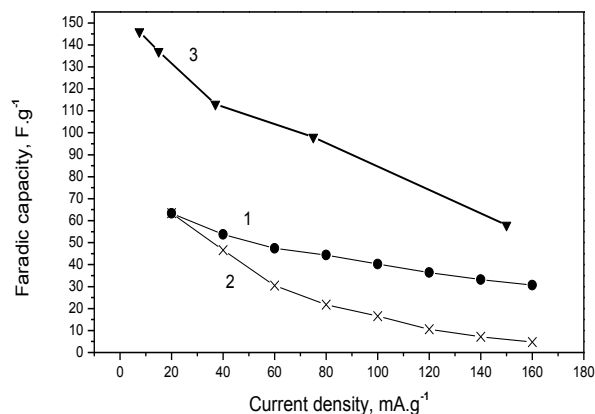


**Fig. 6.** Dependence of capacity on discharge current for symmetric cells (1- CF-50 –  $\text{Et}_4\text{NBF}_4$  and 2- CF-50 –  $\text{LiPF}_6$ ) and asymmetric cell (3- CF-50/composite CF-50 +  $\text{Li}_4\text{Ti}_5\text{O}_{12} - \text{LiPF}_6$ ).

thermal treatment at high temperature in order to remove the surface functionalities. Fig.1 and Table 1 show that this treatment leads to rearrangements in the carbon structure and graphitic-like domains are formed, proved by XRD analysis of the CF-50H (around 10% degree of crystallinity) and the CF-55H carbons. Depending on the carbon precursor this process can end up with an increase in the electrical conductivity and its Faradic capacity. The results in Fig. 5 show that the capacity of the CF-55 carbon increases after heat treatment (CF-55H), but the capacity of the CF-50 carbon at these conditions drastically decreases, and the cell using CF-50H carbon as electrodes demonstrates rather poor behaviour (capacity values  $10\text{--}15 \text{ F.g}^{-1}$  in the whole current range). It is possible to assume that during this treatment some rearrangements may occur in the CF-55 carbon, which results in important modifications in the textural and the structural properties of the carbon skeleton (annealing effects) – cf. Fig.1, Table 2, Fig.3

The addition of natural graphite, NG-7 (10 w%), to the CF-50 carbon decreases the specific resistance of the electrode from  $0.8$  down to  $0.5 \Omega \text{ cm}^2$ , thus increasing the electronic percolation [17]. As a result, the cell, using carbon material CF-50NG7 as electrodes, shows the best performance - capacitance value up to  $75 \text{ F.g}^{-1}$  at  $20 \text{ mA.g}^{-1}$  and satisfactory one (about  $50 \text{ F.g}^{-1}$ ) at  $160 \text{ mA.g}^{-1}$  (cf. Fig.5).

Fig.6 illustrates the dependence of the specific capacitance on the discharge current for symmetric carbon-based (CF-50) capacitors with  $\text{Et}_4\text{NBF}_4 - \text{PC}$  or  $\text{LiPF}_6 - \text{DMC/EC}$  electrolytes, and an asymmetric capacitor, composed by graphitized

carbon (CF-50H) as negative electrode and composite carbon CF-50 –  $\text{Li}_4\text{Ti}_5\text{O}_{12}$  oxide as positive electrode with  $\text{LiPF}_6$  – DMC/EC electrolyte. As expected, the capacity of the symmetric capacitor cell with  $\text{Li}^+$ -based electrolyte is lower than this of the capacitor with  $\text{Et}_4\text{NBF}_4$  electrolyte. The comparison of the capacity-discharge current plots shows also that the asymmetric capacitor demonstrates near twice as higher capacitance (up to  $150 \text{ F.g}^{-1}$ ) than those of the best symmetric one (up to  $70 \text{ F.g}^{-1}$ ) at all current rates. The higher capacitance values of the asymmetric capacitor could be explained with the occurrence of the process of intercalation of solvated  $\text{Li}^+$  ions into graphitized carbon and carbon –  $\text{Li}_4\text{Ti}_5\text{O}_{12}$  composite electrodes together with the ion adsorption.

#### 4. CONCLUSIONS

Based on the current study results, the following conclusions could be made:

a) New electrode materials for supercapacitors - activated nanostructured carbons are synthesized by carbonization of mixtures of coal tar pitch and furfural with subsequent hydrothermal treatment, and characterized physicochemically.

b) Composite electrodes for supercapacitors are produced from activated carbons, nanostructured electrochemically active  $\text{Li}_4\text{Ti}_5\text{O}_{12}$  oxide and a conductive additive (natural graphite NG-7 or acetylene black).

c) The organic electrolyte plays a very important role in the determination of the capacity performance of the symmetric carbon-based supercapacitors.

d) The conductivity, the pore size distribution and the chemical surface properties of the carbon materials contribute greatly to the charge storage behaviour of the electrodes in the symmetric supercapacitors.

e) The capacitance values of up to  $75 \text{ F.g}^{-1}$  are obtained for the symmetric carbon-based supercapacitors with  $\text{Et}_4\text{NBF}_4$  – PC electrolyte and about twice as higher capacitance for the asymmetric supercapacitor, composed by graphitized carbon as a negative electrode and carbon- $\text{Li}_4\text{Ti}_5\text{O}_{12}$  oxide composite as a positive electrode in  $\text{LiPF}_6$  – DMC/EC electrolyte, with good cycleability of both supercapacitor systems.

**Acknowledgment:** This work is supported by the Bulgarian NSF under the TK-X-1705 / 2007 Project.

#### REFERENCES

1. B.E. Conway, *Electrochemical Supercapacitors: Scientific Fundamentals and Technological Applications*, Kluwer Academic Publ., New York, 1999.
2. V. Khomenko, E. Raymundo-Pinero, F. Beguin, *J. Power Sources*, **177**, 643 (2008).
3. Y. Zhang, H. Feng, X. Wu, L. Wang, A. Zhang, T. Xia, H. Dong, V. Li, L. Zhang, *Intern. J. Hydrogen Energ.*, **34**, 4889 (2009).
4. J.Gamby, P. L.Taberna, P. Simon, J. F. Fanvarue, M. Chesneau, *J. Power Sources* **101**, 109 (2001).
5. A.Brucke, *J. Power Sources*, **91**, 37 (2000).
6. R. Kotz, M. Carlen, *Electrochim. Acta* **45**, 2483 (2000).
7. R.S. Brood, K.R Bulock, R.A.Leising, R.L.Middouh, J.R. Miller, E. Takeuchi, *J. Electrochem.Soc.* **151**, LOK1 (2002).
8. S. Razumov, A. Klementov, S. Letvinenko, A. Beliakov, *US Patent* 6,222,723 (2001)
9. W. G. Pell, B. E. Conway, *J. Power Sources*, **136**, 334 (2004).
- 10.V. Khomenko, E. Raymundo-Pinero, F. Beguin, *J. Power Sources*, **153**, 183 (2006).
11. C.A. Fabio, A. Giorgi, M. Mastragostino, F. Soavi, *J. Electrochem. Soc.*, **148**, A845 (2001).
12. G. G. Amatucci, F. Badway, A. Du Pasquier, T. Zheng, *J. Electrochem Soc.*, **148**, A930 (2001).
13. A. Du Pasquier, I. Blitz, J. Gural, S. Menocal, G.G. Amatucci, *J. Power Sources*, **143**, 62 (2003).
14. V. Khomenko, E. Raymundo-Pinero, F. Beguin, *J. Power Sources*, **177**, 643 (2008).
15. M. Mladenov, P. Zlatilova, R. Raicheff, S. Vassilev, N. Petrov, K. Belov, V. Trenev, *Bulg. Chem. Commun.*, **40**, 360 (2008).
16. M. Mladenov, R. Raicheff, N. Petrov, D. Kovacheva, R. Nickolov, V. Trenev, D. Bachvarov, K.Belov, *Proc. 4M/ICOMM 2009 Conference*, Karlsruhe, Germany (2009) 223
17. B. Petrova, B. Tsyntsarski, T. Budinova, N. Petrov, C.O. Ania, J.B. Parra, M. Mladenov, P. Tzvetkov, *Fuel Process. Technol.* (2010), doi: 10.1016/j.fuproc.2010.07.008
18. H. Wang, M.Yoshio, *Electrochem. Commun.* **10**, 382 (2008).
19. K.Naoi, A. Nishino, T. Morimoto (Eds), *Electrochemical Capacitors Compact Dictionary*, NTS, 2004, 89.

## СИНТЕЗ И ЕЛЕКТРОХИМИЧНИ СВОЙСТВА НА ЕЛЕКТРОДНИ МАТЕРИАЛИ ЗА СУПЕРКОНДЕНЗАТОРИ

М. Младенов<sup>а</sup>, Н. Петров<sup>в</sup>, Т. Будинова<sup>в</sup>, Б. Цинцарски<sup>в</sup>, Т. Петров<sup>д</sup>, Д. Ковачева<sup>с</sup>,  
Р. Райчев<sup>а</sup>

<sup>а</sup> *Институт по електрохимия и енергийни системи, Българска академия на науките, ул. Ак. Г. Бончев, бл. 10, 1113 София,*

<sup>в</sup> *Институт по органична химия, Българска академия на науките, ул. Ак. Г. Бончев, бл. 9, 1113 София*

<sup>с</sup> *Институт по обща и неорганична химия, Българска академия на науките, ул. Ак. Г. Бончев, бл. 11, 1113 София*

<sup>д</sup> *Химико-технологичен и металургичен университет, бул. Кл. Охридски, 1756 София*

Постъпила на 25 Август, 2010 г.; преработена на 20 Октомври, 2010 г.

(Резюме)

Синтезирани са нови електродни материали за суперкондензатори- активни въглини, получени чрез карбонизация на смеси от каменовъглен пек и фурфурал, с последваща хидротермална обработка. Изследвани са микроструктурата, повърхностната морфология и структурата на порите на получените въглеродни материали и са определени техните основни текстурни параметри и разпределението на порите по размери. Разработени са симетрични суперкондензаторни клетки (тип „сандвич“) с еднакви въгленови електроди и органичен електролит, които са подложени на зарядно-разрядно циклиране с различни плътности на тока. Като електроди са тествани четири вида въгленови материали с различна специфична повърхност ( $1000 - 1600 \text{ m}^2\text{g}^{-1}$ ), както и три вида органични електролити ( $\text{Et}_4\text{NBF}_4$ - PC,  $\text{LiBF}_4$ - PC и  $\text{LiPF}_6 - \text{DMC/EC}$ ). Работата на симетричните суперкондензатори е сравнена с тази на асиметричен тип суперкондензатор, съставен от активен въглен (въгленова пяна) като положителен електрод и композит – активен въглен /  $\text{Li}_4\text{Ti}_5\text{O}_{12}$  оксид, като отрицателен електрод. Получени са стойности на капацитета до  $75 \text{ Fg}^{-1}$  за симетричните суперкондензатори и 2 пъти по-високи стойности за асиметричния суперкондензатор, при много добра циклируемост и за двата типа електроди.

## Differential impedance analysis of the cathode compartment in dual membrane fuel cell

G. Raikova\*, D. Vladikova, Z. Stoynov

*Institute of Electrochemistry and Energy Sources, Bulgarian Academy of Sciences, Acad. G. Bonchev St, building.10, 1113 Sofia, Bulgaria*

Received: September 2, 2010; revised: October 27, 2010

The cathode/electrolyte LSCF48/YDC15 couple is a building block of a new innovative and competitive design of a high temperature fuel cell, operating in the range between 600 and 700°C. It is based on the idea for a junction between a proton conducting SOFC (PCFC) anode/electrolyte part and a SOFC cathode/electrolyte part through a mixed H<sup>+</sup> and O<sup>2-</sup> conducting porous ceramic membrane. Thus, in this concept, hydrogen, oxygen and water are located in three independent chambers, which allows for avoidance of gases dilution with water. The applicability of different technologies (tape casting and plasma spraying) for the cathode deposition is analyzed in this paper using the Differential Impedance Analysis (DIA). A two step reaction mechanism of oxygen reduction is recognized. The rate-limiting step is the transport of oxygen ions in the volume of the electrode towards the electrolyte. A higher degree of frequency dependence is registered for the plasma spraying deposition technology.

**Key words:** dual membrane fuel cell, symmetrical electrolyte supported half cell, Differential Impedance Analysis, tape casting, plasma spraying

### 1. INTRODUCTION

The electrochemical impedance spectroscopy (EIS) is an important tool for solid oxide fuel cell (SOFCs) studies since it is sensitive to sample configuration and fabrication quality, including adhesion between layers and mechanical stability. Therefore, it was chosen for testing of materials and components in an innovative and competitive design of high temperature fuel cell, named „IDEAL-Cell“ after the acronym of the FP7 European project „Innovative Dual mEmbrAne fuel-Cell“ [1,2]. The new concept is based on the idea for isolating the formation of the exhaust water in a separate chamber. For this purpose a junction of mixed conducting porous layer between a proton-conducting anode/electrolyte part (hydrogen compartment) and an oxygen-conducting electrolyte/cathode part (oxygen compartment) is introduced. Protons, created at the anode, progress towards the central membrane, where they meet the oxygen ions, created at the cathode. The produced water is evacuated through the pores of the central membrane and thus it does not dilute the two gases as it is in the conventional SOFC and PCFC [1, 2].

This work presents conductivity studies of the

oxygen compartment LSCF48/YDC15 couple, applying different technologies for deposition of the electrodes: tape casting and plasma spray. The measured impedance data are analyzed by the technique of the Differential Impedance Analysis (DIA) - an advanced method, which increases the information potential of the impedance data analysis, since it extracts the impedance model structure directly from the experimental data without a preliminary working hypothesis [3-5].

### 2. EXPERIMENTAL

The investigations were performed on symmetrical electrolyte supported half cells LSCF48/YDC15/LSCF48 [La<sub>0,6</sub>Sr<sub>0,4</sub>Co<sub>0,2</sub>Fe<sub>0,8</sub>O<sub>3-δ</sub>/Ce<sub>0,85</sub>Y<sub>0,15</sub>O<sub>2-δ</sub>/La<sub>0,6</sub>Sr<sub>0,4</sub>Co<sub>0,2</sub>Fe<sub>0,8</sub>O<sub>3-δ</sub>]. The electrolyte pellet was prepared by cold pressing and sintering. Electrodes with thickness of 15 to 50 μm were deposited by tape-casting (TC) and plasma spraying (PS).

The impedance measurements were performed on Solartron 1260 FRA over frequency range of 1MHz – 0.1Hz with density of 5 points per decade in a temperature interval of 100-800°C. The wide temperature range ensures impedance characterization of both, the electrolyte and the electrode. For improved data quality potentiostatic and galvanostatic regimes with different amplitudes were applied, depending on the cell impedance [6]. A procedure for correction of the parasitic errors

---

\* To whom all correspondence should be sent:  
E-mail: graikova@bas.bg

coming from the testing cell rig was used for more accurate estimations [3, 7].

### 3. RESULTS AND DISCUSSION

#### 3.1. Analysis of the electrolyte behavior

The performed DIA analysis of the electrolyte behavior recognizes Voigt's model structure with 2 time-constants, i.e. with 2 meshes with R and C in parallel connection which correspond to the bulk and grain boundary behavior (Fig.1).

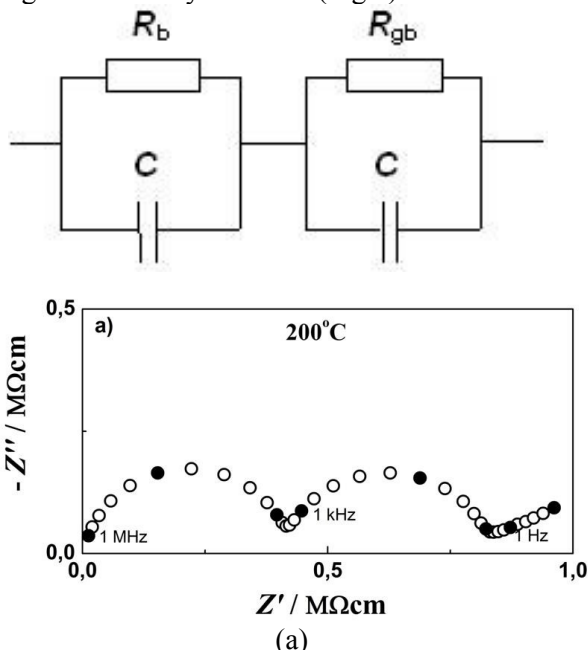


Fig.2. Complex plane impedance diagrams of symmetrical half cell with electrodes deposited by TC at different temperatures.

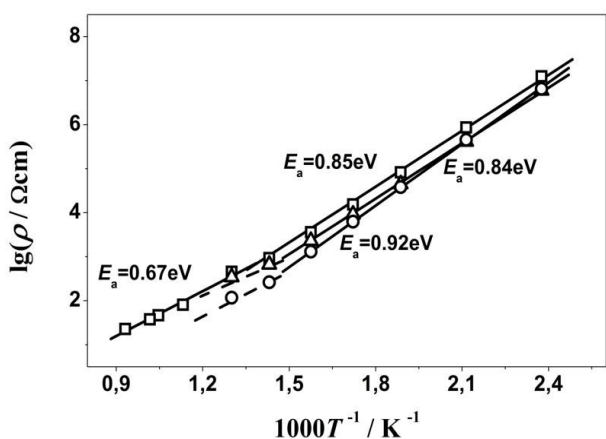


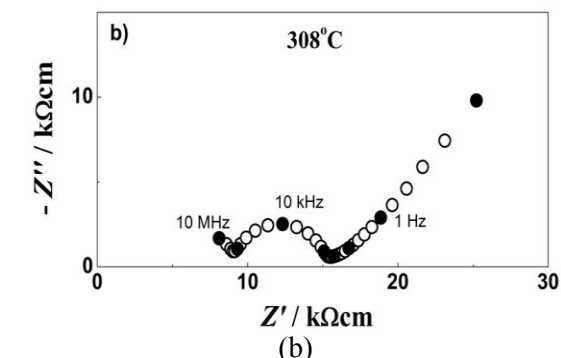
Fig. 3. Arrhenius plots for the bulk ( $\Delta$ ), grain boundary ( $\circ$ ) and total ( $\square$ ) resistivity of YDC15 electrolyte.

The TC samples show good performance, stability, reproducibility and easy fabrication. The impedance of the half cell with electrodes, deposited by TC, has been chosen as an internal standard for evaluation of the oxygen compartment.

Fig.1. Voigt's model description of the electrolyte behavior extracted from the experimental data by DIA.

The application of the procedure for correction of the measurement rig parasitic inductance and resistance in combination with DIA ensured their separation to up to 500°C, precise structural and parametric identification, and calculation of the corresponding activation energies (Figs. 2,3). It was found that YDC15 has resistivity similar to that of the electrolyte materials, developed for application at intermediate temperatures (Fig. 4).

Both bulk and grain boundary conductivities have similar activation energy, which confirms the formation of clean grain boundaries and good contacts. Their resistivity is also in the same range which is an evidence for the high quality of the shaping technology (Fig. 3). The TC procedure for LSCF deposition does not influence the electrolyte behavior



After PS deposition of the electrodes, DIA registered the appearance of strong frequency dependent behavior for the electrolyte grain

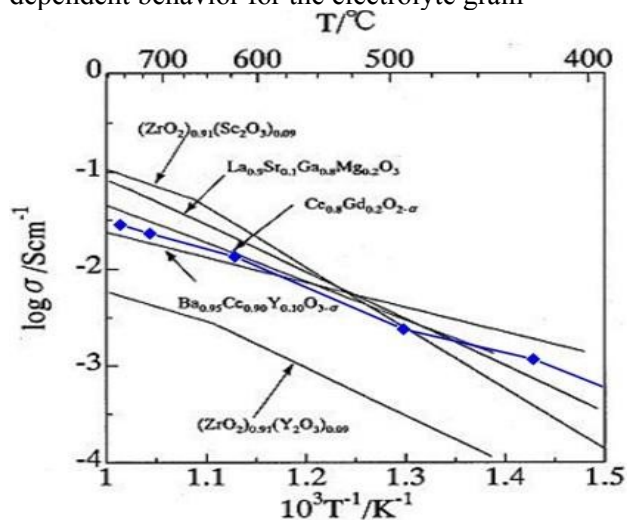
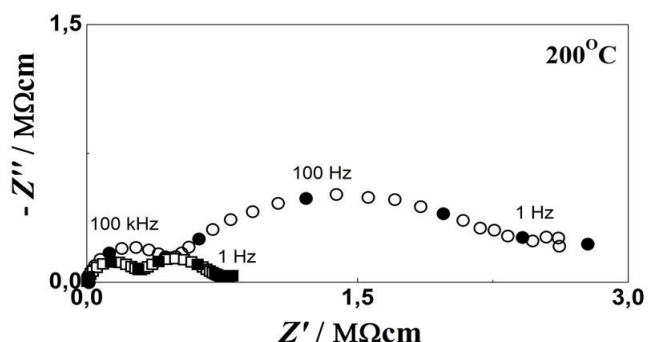


Fig. 4. Comparison of the YDC15 conductivity ( $\Delta$ ) with data from the literature [8].



**Fig. 5.** Complex plane impedance diagrams of symmetrical half cells with LSCF48 electrodes deposited by PS on sand blasted YDC substrate: (○) without cleaning after sandblasting and (□) with cleaning after sandblasting.

boundaries, i.e. grain boundaries resistance with CPE character (Fig. 5). This impedance behavior is an indicator for increased inhomogeneity, caused by the PS deposition. It could be related to the sandblasting pretreatment which produces additional surface roughness and could introduce some impurities at the interface. After a deep cleaning with acetone followed by ultrasonic treatment for removing the possible impurities, this phenomenon disappeared. As it can be noticed in Fig. 5 that the grain boundary resistance becomes comparable with that of the same substrate, measured in a cell with TC deposited electrodes (Fig. 2a).

### 3.2. Analysis of the cathode reaction mechanism

As to the cathode reaction, the following steps were identified for both, the TC and the PS deposition (Fig.6): charge transfer step at high frequencies, followed by a step corresponding to transport limitations. The charge transfer step is very fast for the TC sample, and its value is negligible. The contribution of the charge transfer is bigger for the PS deposited electrodes - about 30–40% of the total resistance.

The transport limitations, which are the rate-limiting step in both cases, are presented with bounded constant phase element (BCP). It describes the impedance of a bounded homogeneous layer with CPE behaviour of the conductivity in the elementary volume and a finite conductivity at d.c [3 – 4, 9]:

$$Z_{BCP}(i\omega) = A^{-1}(i\omega)^{-n} \text{th}R_0 A(i\omega)^n \quad (1)$$

where  $A$ ,  $n$  and  $R_0$  are the structural parameters of the element.

For the TC samples the coefficient  $n$  is close to 0.5, i.e. the transport is close to diffusion, while for the PS samples it decreases to 0.2. The physical

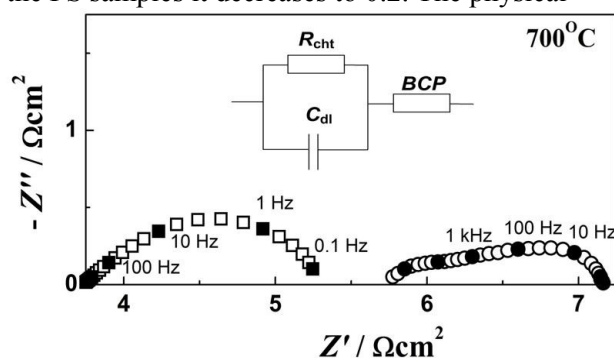


**Fig. 6.** Complex plane impedance diagrams of symmetric half cells LSCF48/YDC15/LSCF48 with electrodes deposited by TC (□) and PS (○) and corresponding equivalent circuit.

meaning of the low exponential coefficient corresponds to transport of species (oxygen ions) with restrictions in the host matrix. The bigger depression of the impedance arcs is usually connected with the bigger system inhomogeneity. This tendency is confirmed by the SEM images that show 2 types of structure in the PS deposited electrode layers (Fig. 7) - melted splats (Fig. 7a) and non-molten granulates (Fig. 7c).

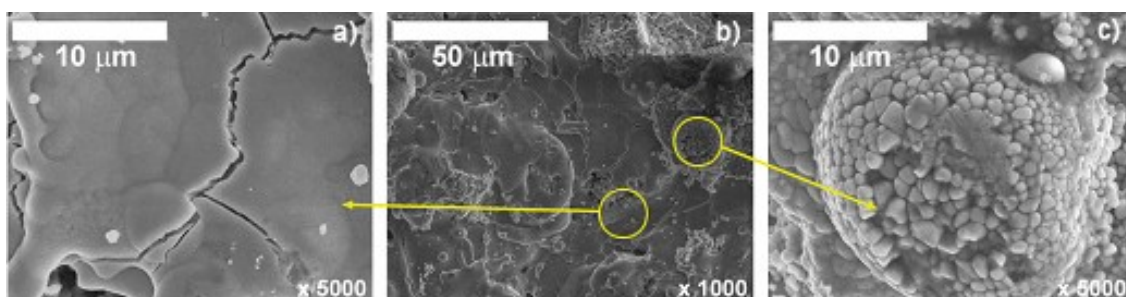


**Fig.7.** SEM images of plasma sprayed electrodes.

**Table 1.** ASR of LSCF48 electrodes deposited by tape casting and plasma spraying compared with data from the literature

Electrode Material	ASR at about 600	ASR at about 700
	°C $\Omega\text{cm}^2$	°C $\Omega\text{cm}^2$
LSCF48 (Tape casting)	3.80 (623 °C)	0.360- 0.400(725°C)
LSCF48 (Plasma spraying)	4.90 (615 °C)	0.800 (715 °C)
BSZF ( $\text{Ba}_{0.50}\text{Sr}_{0.50}\text{Zn}_{0.20}\text{Fe}_{0.80}\text{O}_{3-\delta}$ ) [9]	4.87	0.716
BSZF-GDC [9]	3.29	0.373
BSZF-GDC-Ag [9]	2.47	0.278
LSCN [10]	-	0.132 (750 °C)
( $\text{Sm}_{0.60}\text{Sr}_{0.20}$ ) $\text{CoO}_3$ -CYO-Ag [11]	7.10	0.900
( $\text{La}_{0.60}\text{Sr}_{0.20}$ ) $\text{CoO}_3$ -CGO-Ag [11]	0.830	0.190

The obtained results for the ASR of LSCF electrodes deposited by both techniques are competitive with the results from the literature (Table 1).

#### 4. CONCLUSIONS

The DIA analysis ensured deeper insight into the electrochemical behavior of the applied materials and deposition technologies for the oxygen compartment of the dual membrane fuel cell. The YDC15 electrolyte has good conductivity, stability and reproducibility, which makes it appropriate for further application. The applied LSCF electrode materials ensure cathode layers with good electrical properties.

The conductivity of the cathodes, deposited by the investigated techniques, shows that they are competitive, with slightly better performance and good reproducibility for the tape casting.

**Acknowledgements:** *The research, leading to these results, has received funding from the European Community's Seventh Framework Programme (FP7/2007-2013) under the grant agreement no 213389. The electrolyte supports and Tc deposition were performed in ARMINES, France. The PS electrodes were prepared by DLR, Germany. G. Raikova acknowledges also ALternative ENergy Sources (ALENES) BG051PO001/07/3.3-02/17.06, for its financial support that made possible her participation in the workshop.*

#### REFERENCES

1. www.ideal-cell.eu.
2. Thorel A.S., A. Chesnaud, M. Viviani, A. Barbucci, S. Presto, P. Piccardo, Z. Ilhan, D. Vladikova, Z. Stoynov, *Solid Oxide Fuel Cells 11 (SOFC-XI Part 1)*, 25 /2 (2009) 753.
3. Z. Stoynov, D. Vladikova, in: *Impedance Spectroscopy of Electrochemical Power Sources*, U. Garcke (Ed.) *Encyclopedia of Electrochemical Power Sources*, Vol. 3, Amsterdam, Elsevier, 2009, p.632.
4. Z. Stoynov, D. Vladkova, *Differential Impedance Analysis*, Marin Drinov Academic Publishing House, 2005, Sofia.
5. D. Vladikova, Z. Stoynov, *J. Electroanal. Chem.*, **572**, 377 (2002).
6. D. Vladikova, Z. Stoynov, G. Raikova A. Thorel, A. Chesnaud, J. Abreu, M. Viviani, A. Barbucci, S. Presto, P. Carpanese, *Electrochimica Acta*, to be published.
7. D. Vladikova, Z. Stoynov, G. Raikova, in: *Portable and Emergency Energy Sources*, Z. Stoynov, D. Vladikova (Eds.), Marin Drinov Academic Publishing House, Sofia, 2006, p.383.
8. S. C. Singhal, K. Kendall, *Solid Oxide Fuel Cells: Fundamentals, Design and Applications*, Elsevier, 2003.
9. L. Kong, Z. Lu, B. Wei, X. Huang, R. Su and W. Su, *Solid Oxide Fuel Cells 11 (SOFC-XI Part 3)*, 25/2, 2513, 2009.
10. Dutta, A., H. Gotz, S. Ghosh, R.N. Basu, *Solid Oxide Fuel Cells, 11 (SOFC-XI) part 3 (2009) 2657*.
11. M. Dokiya, *Solid State Ionics*, **152-153**, 383 2002.

## ДИФЕРЕНЦИАЛЕН ИМПЕДАНСЕН АНАЛИЗ НА КАТОДНИЯ ЕЛЕМЕНТ НА ДВОЙНО-МЕМБРАННА ГОРИВНА КЛЕТКА

Г. Райкова\*, Д. Владикова, З. Стойнов

*Институт по електрохимия и енергийни системи, Българска академия на науките,  
ул. „Акад. Г. Бончев” бл. 10, 1113 София*

Постъпила на 2 септември, 2010 г.; преработена на 27 октомври, 2010 г.

(Резюме)

Комбинацията катод/кислород проводящ електролит на базата LSCF48/YDC15 е използвана като градивен елемент на нов, иновативен и конкурентен дизайн на високо-температурна горивна клетка, работеща в интервала 600-700 °С. В основата на идеята е свързването на анод/електролитната част на протон проводяща твърдоокисна горивна клетка (PCFC) с катод/ електролитната част на класическа клетка (SOFC) чрез пореста керамична мембрана със смесена  $H^+$  и  $O^{2-}$  проводимост. По този начин водородът, кислородът и водата са разположени в три самостоятелни камери, което дава възможност да се избегне разреждането на двата газа с водата. В настоящата статия с помощта на диференциалния импедансен анализ (ДИА) са изследвани възможностите за отлагане на катода чрез различни технологии (лентово отливане и плазма-спрей). Установено е, че кислородната редукция протича като двустъпков процес. Скоростно-определящата стъпка е транспортирането на кислородни йони в обема на електрода. При плазма-спрей отлагането е регистрирана висока степен на честотна зависимост.

## Physical characterization of Pt-M binary electrocatalysts for water splitting

E.D. Lefterova\*, A.E. Stoyanova, G.R. Borisov, E.P. Slavcheva

*Institute of Electrochemistry and Energy Systems, Bulgarian Academy of Sciences, Acad. G. Bonchev Str. Building 10, 1113 Sofia, Bulgaria*

Received: September 7, 2010; revised: October 28, 2010

Combinations of mono- and bimetallic compounds, oxides and composite materials, in which Pt is partly or totally replaced by cheaper elements (Cr and Mn) were synthesised. Mechanically treated Ebonex was used as a support. The synthesized catalysts were characterized by several bulk and surface analysis, such as the XRD, XPS and SEM. XRD and XPS analysis showed that Cr- and Mn- components are in amorphous and oxidized state, while Pt is predominantly in metallic state. No alloying between Pt and Cr or Mn is registered. The catalysts are electrochemically tested toward oxygen evolution reaction (OER) for water splitting in a PEM electrolytic cell using a commercial Nafion 117 as a proton conducting electrolyte. It is seen that the best catalytic activity for the OER exhibits Pt-Cr/Ebonex. It has higher efficiency at lower Pt loading relative to all other compositions, including Pt/Ebonex. The results obtained are explained with electronic interactions between the metallic components and the support, providing a synergetic effect.

**Key words:** PEM water splitting, Pt/Cr/Mn-Ebonex electrocatalyst, XRD, XPS, SEM

### INTRODUCTION

Among the individual metals, Pt possesses the best catalytic activity toward the oxygen evolution reaction (OER) for PEM water splitting and is still the most frequently used catalyst [1, 2]. However, Pt being a noble metal is rather expensive. In addition, the world resources of this metal deplete fast, which imposes the need to search proper substitutes of Pt.

Generally, the efficiency of the electrocatalysts is determined by two major groups of factors, geometrics and electronics, and in this context there are two possibilities to enhance the activity of the pure Pt. The first one is to increase the surface area by dispersing it on a supporting the electro conductivity material with highly developed surface. The second one is to combine it with other pure metals under preliminary theoretical calculations and considerations, based on the Brewer interactive interionic bonding theory and corresponding predictions about the probability for hyper- hypo-d-electron interactions [3, 4].

The unique combination of the electrical conductivity, which approaches that of the metal, and the high corrosion resistance, which approaches that of the Ebonex ceramics (Magneli phase titanium oxides with general formula  $Ti_nO_{2n-1}$ ), gives a reason to consider it as a substitute

supportive material for the anodic catalyst [5-7].

The physical characteristics of the electrocatalysts (the phase and composition of the active components, the particle size and size distribution, the morphology and crystal planes, etc.) are very important not only for understanding of the catalyst performance but also for exploring the structure-activity relationship at the electron/molecular level, and ultimately for a rational design of new catalysts [8].

In this work combinations of mono- and bimetallic compounds, oxides and composite materials in which Pt is partly or totally replaced by cheaper elements (Cr and Mn) on Ebonex as a support, were synthesised using the sol-gel method. The prepared materials were characterized by several bulk and surface analysis, such as XRD, XPS and SEM, and their structure was discussed in relation to their electrocatalytic action toward OER in PEM water splitting.

### EXPERIMENTAL

#### *Catalyst synthesis*

The synthesis of the chosen composite materials consisted in direct selective grafting of platinum and other metals from acetylacetonate precursors ( $M[(C_5H_7O_2)_n]_m$  or M-acac (M = Pt, Cr, Mn). Commercial Ebonex powder was used as a substrate and it was subjected to mechanical treatment in a planetary ball mill for 40 h prior to the synthesis. The metallic part in each of the catalyst was 20 wt. %, while the metal ratio was

\* To whom all correspondence should be sent:  
E-mail: edlefterova@gmail.com

1:1. The preparation procedure was described in details elsewhere [3].

### Physical Characterization

The phase composition, the morphology and the surface structure of the catalysts under studying were investigated by the methods of X-Ray diffraction (XRD), X-ray photoelectron spectroscopy (XPS), and scanning electron microscopy (SEM). XRD spectra were recorded by Philips APD15 X-ray diffractometer. The diffraction data were collected at a constant rate of  $0.02^\circ \cdot \text{s}^{-1}$  over an angle range of  $2\theta = 10 - 90$  degrees. The size of Pt crystallites was determined by Scherrer equation [8, 9]

$$D = k\lambda / \beta \cos \Theta, \quad (1)$$

where  $D$  is the average dimension of crystallites,  $k$  is the Scherrer constant in the range of 0.85–1.0 in dependence of the crystal type (usually assumed to be  $k \approx 1$ );  $\lambda$  is the X-ray wavelength,  $\Theta$  is the Bragg angle, and  $\beta = \sqrt{\beta_s^2 + \beta_r^2}$  is the peak broadening in radians ( $\beta_s$  and  $\beta_r$  are peak widths of the sample and standard in radians). The XPS of the samples were recorded with ESCALAB MK II (VG Scenific, England) electron spectrometer. The photoelectrons were excited with a twin anode X-ray source using Al  $K\alpha$  ( $h\nu = 1486.6$  eV) radiation. C 1s photoelectron line at 284.6 eV was used as a reference for calibration. The morphology of the electrocatalysts was investigated through scanning (SEM) electron microscopy. JEOL JEM – 200 CX microscope was used in scanning regime.

### Laboratory PEM cell and test procedure

The electrochemical tests were performed on membrane electrode assemblies (MEAs), using a Nafion 117 membrane as an electrolyte. The catalysts under study were investigated as electrodes for the oxygen evolution reaction (OER), while a commercial E-TEK catalyst, containing 20 % Pt on a carbon support, was used to prepare both, the hydrogen (HE) and the reference electrodes (RE). The electrodes have a complex multilayered structure, consisting of gas diffusion, backing, and catalytic layers. The preparation procedure is described in details elsewhere [10].

The performance characteristics of the prepared MEA were investigated in a self made laboratory PEM electrolytic cell [6]. It consists of two gas compartments where hydrogen and oxygen evolution take place, separated by the membrane electrode assembly under study. A reference electrode is situated in the hydrogen evolution

compartment. The catalytic activity of the prepared catalysts was studied using the techniques of cyclovoltammetry and steady state polarization at operating temperature of  $20^\circ\text{C}$  and  $80^\circ\text{C}$ . All electrochemical measurements were carried out with a commercial Galvanostat/ Potentiosat POS 2 Bank Elektronik, Germany.

## RESULTS AND DISCUSSION

### Physical characteristics XRD analysis

Fig. 1 and Fig. 2 present the XRD spectra of the Ebonex and the synthesized composite catalysts. The Magneli phase titanium oxide characteristics for Ebonex are registered. Only the support peaks can be seen for the Mn-Ebonex and Cr-Ebonex (Fig. 1). The absence of peaks for the Cr and Mn metallic phase means that the M-components are amorphous and most probably are in an oxidized state.

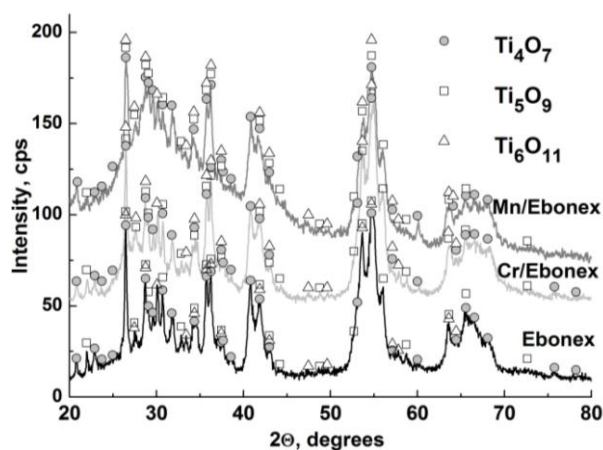


Fig. 1. XRD spectra of the Ebonex and the synthesized composite M/Ebonex (M=Mn, Cr) catalysts.

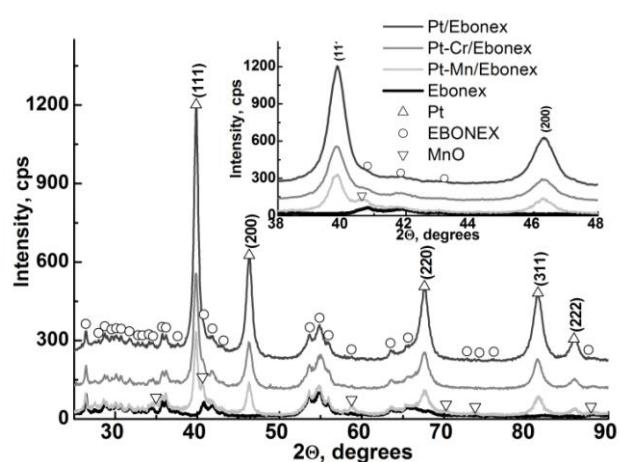


Fig. 2. XRD spectra of the composite Pt-M/Ebonex catalysts.

The appearance of MnO in the Pt-Mn/Ebonex spectrum (Fig. 2) supports this assumption. For all Pt-containing catalysts the fcc Pt peaks appear as well. There is no shift of the Pt peaks with the addition of the Cr or Mn (Fig. 2 inset), and hence there is no change in the Pt cell parameter (the deviation of the calculated values in Table 1 is within the error range). It implies that Mn and Cr are not incorporated in the Pt crystal cell. The intensity of the Pt XRD peaks of the different catalysts decreases in the order of Pt/Ebonex > Pt-Cr/Ebonex  $\approx$  Pt-Mn/Ebonex, which corresponds to the reduced Pt content in the Pt-M/Ebonex catalysts. The crystallite size is in the range between 13 and 16 nm.

**Table 1.** Calculated Pt cell parameters and crystallite size

Sample	Pt cell Å	Crystallite size nm	
		$D_{(111)}$	$D_{(200)}$
Pt/Ebonex	$3.9195 \pm 0.0004$	14	11
Pt-Cr/Ebonex	$3.9204 \pm 0.0005$	12	10
Pt-Mn/Ebonex	$3.9186 \pm 0.0008$	16	13

#### SEM analysis

The SEM images of Pt/Ebonex and Pt-Cr/Ebonex are shown in Fig. 3. The Pt particles of both catalysts are uniformly distributed on the Ebonex support. In the case of Pt/Ebonex the distribution density is higher which correlates with the XRD analysis. The average particle size is of 50–60 nm, meaning that one particle is composed of 4–5 crystallites.

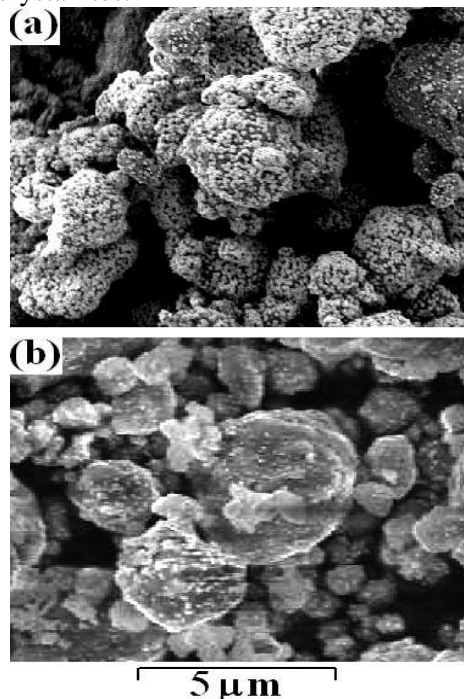


**Fig. 3.** SEM of the: (a) Pt/Ebonex catalyst; (b) Pt-Cr/Ebonex catalyst.

#### Electrochemical characteristics

The efficiency of the catalyst containing Pt, Cr and Mn is tested using the method of steady state polarisation. The anodic E/j- curves of the catalyst under study are presented in Fig. 4. The curves are recorded at the typical PEMWE operation temperature of 80°C.

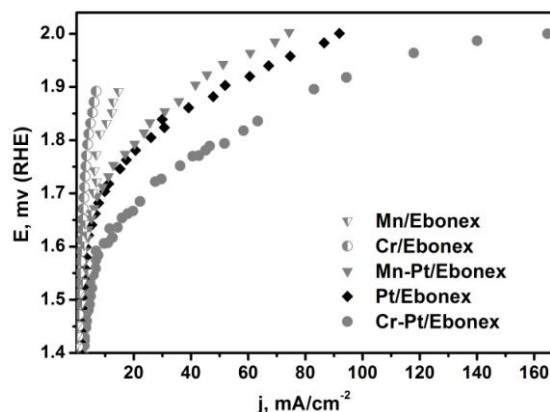


**Fig. 4.** Anodic E/j- curves of the catalysts recorded at 80°C.

It can be seen that the Pt free Cr/Ebonex and Mn/Ebonex do not demonstrate catalytic activity. The partial replacement of platinum with Mn does not facilitate the OER but results in improved mass activity, compared to pure Pt, while in the case of Cr substitution, the OER efficiency improves at reduced Pt loading.

Similar results, showing a positive effect of Cr and Mn inclusion on the Pt activity, have been reported by other authors for the carbon supported electrocatalysts [11–14]. The observed increase in the catalytic activity can be explained with the occurrence of hypo-hyper-d-electron interactions between both metals and the substrate. In order to verify this assumption the surface state of the prepared catalyst was studied further using XPS analysis.

The investigated catalysts show stability at high anodic potentials, which give reasons to consider Ebonex as an alternative support.

#### XPS analysis

XPS investigations were performed to identify the valence state of the components on the catalyst surface. Fig. 5 shows the 2p XPS spectra of Mn and Cr. These spectra confirm the supposition for the oxidized state of Mn and Cr based on the XRD data. The position of the Cr 2p<sub>3/2</sub> peak at 577.0 eV as well as the spin orbital splitting of 9.7 eV correspond to Cr<sup>3+</sup> (Cr<sub>2</sub>O<sub>3</sub>, CrOOH) [15, 16].

The Mn 2p peak is broad and covers different valence states of Mn (Fig. 5b). The peak around

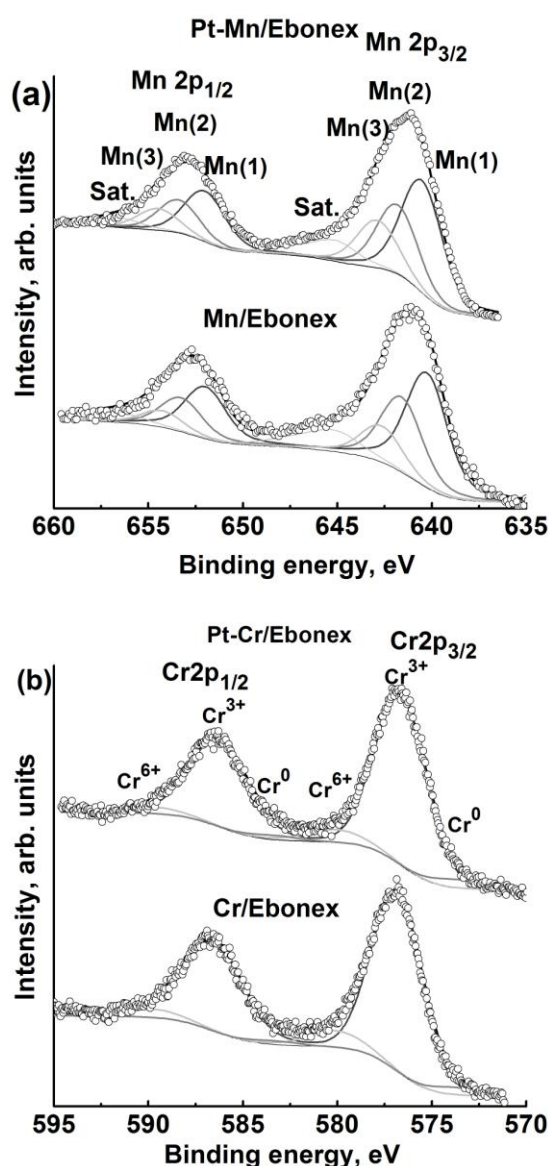


Fig. 5. 2p XPS spectra of: (a) Mn; (b) Cr.

640.0 – 640.7 eV (marked Mn(1)) in the Mn 2p<sub>3/2</sub> region is attributed to Mn<sup>2+</sup> cations, whereas the peaks around 641.6 eV (Mn(2)) and 642.6 eV (Mn(3)) are assigned to Mn<sup>3+</sup> and Mn<sup>4+</sup> cations respectively [17]. The formal deconvolution of the Mn 2p XPS peak into three components - Mn(1), Mn(2), and Mn(3), positioned around these values, generally implies availability of three Mn valence states. However, such a conclusion can be misleading due to the multiplet splitting nature of Mn 2p XPS spectrum for each of those three valence states with overlapping components [18], which complicates the peak interpretation. In our case, the fitting picture is close to the multiplet splitting spectrum of MnO, i.e. to Mn<sup>2+</sup>. The exchange splitting of the Mn 3s spectrum is more informative.

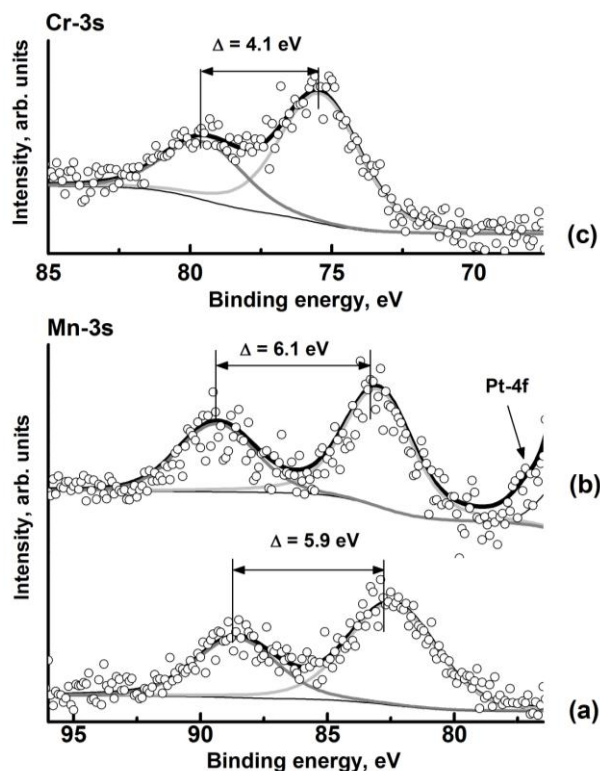


Fig. 6. 3s XPS spectra of: (a) Mn 3s of Mn/Ebonex catalyst; (b) Mn 3s of Pt-Mn/Ebonex catalyst; (c) Cr 3s of Cr/Ebonex catalyst

Fig. 6 presents the Mn 3s and Cr 3s XPS spectra which are used to establish the Mn and Cr valence states. The observed values of the exchange splitting of the 3s levels for the Mn and Cr ions are close to those found in [13] for some 3d metal oxides MO<sub>x</sub> (M = Cr, Mn). The splitting of the 3s level is 6.2-6.5 eV for Mn<sup>2+</sup>, 5.5 eV for Mn<sup>3+</sup>, and 4.5 eV for Mn<sup>4+</sup> [17,19], meaning that the Mn/Ebonex and Pt-Mn catalysts consist mainly of Mn<sup>2+</sup> species (splitting is 5.9–6.1 eV).

The magnitudes of the Cr 3s multiplet splittings are 3.8-4.2, and 3.5 eV for Cr<sup>2+</sup> (Cr<sub>2</sub>O<sub>3</sub>, CrOOH) and CrO<sub>2</sub> respectively [20]. From the value of the Cr 3s exchange splitting (4.1 eV) can be concluded that in Cr/Ebonex catalyst the Cr ions are trivalent.

The Cr 3s split spectrum of Pt-Cr /Ebonex catalyst overlaps with the Pt 4f line and for that reason it is presented together with the others Pt 4f spectra in Fig. 7.

The Pt 4f XPS spectra can be deconvoluted into 3 doublets corresponding to Pt<sup>0</sup> (~71.2 eV), Pt<sup>2+</sup> (~72.5 eV), and Pt<sup>4+</sup> (~75.0 eV). For Pt-Cr/Ebonex catalyst Cr 3s exchange splitting line is introduced in addition (Fig. 7b). As it can be seen, platinum presents mainly in metallic form. The second component indicates a surface oxidation of Pt which is higher in the case of Pt-Cr/Ebonex

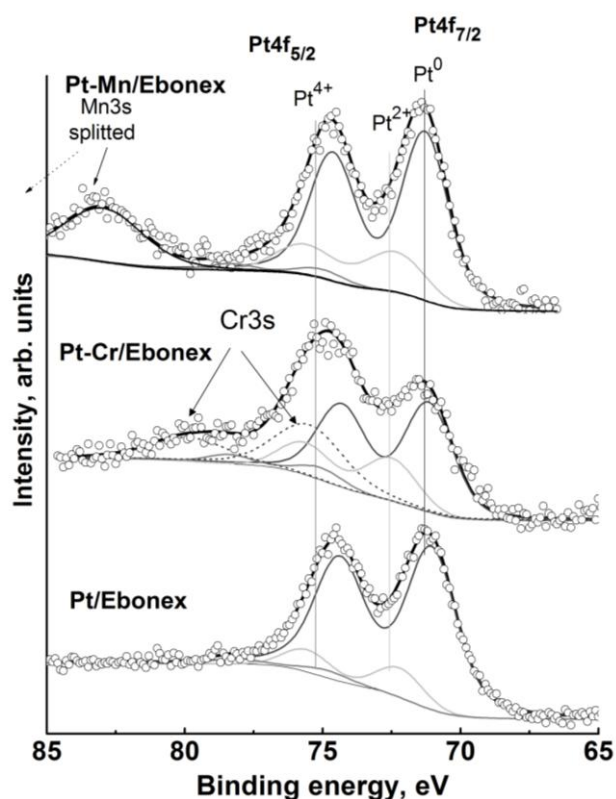


Fig. 7. Pt4f XPS spectra of Pt-M/Ebonex catalysts.

catalyst. We assume that besides  $\text{Pt}(\text{OH})_2$  formation [21], mixed Pt-O-Me (Me = Ti, Mn, Cr) bonds appear. These two oxide types are responsible for the hypo-hyper interaction, and it can explain the higher electrochemical activity of the Pt-Cr/Ebonex catalyst.

### CONCLUSIONS

The synthesized composite Pt-M (M = Cr, Mn) nanomaterials on Ebonex support were investigated as OER catalysts for PEM water splitting. Physical analysis showed that Cr- and Mn- components are in amorphous and oxidized state, while Pt is predominantly in a metallic state. No alloying between Pt and Cr/Mn is registered. The results from the electrochemical experiments demonstrate superior catalytic activity of the Pt-Cr/Ebonex compared with the Pt-Mn/Ebonex and the Pt/Ebonex catalysts.

This effect is explained with the occurrence of hypo-hyper-d-electron effects between both, the metals and the substrate, proven by XPS analysis.

**Acknowledgments:** This research has been carried out under the PemHydroGen project (contr. No. DTK 02/68, NSF, Bulgaria)

### REFERENCES

1. J. Shim, Chang-Rae, Hong-Ki Lee, Ju-Seong Lee, E. Cairns, *J. Power. Sources*, **102**, 172 (2001).
2. A. Pozio, M. De Francesco, A. Cemmi, F. Gardellini, L. Giorgi, *J. Power. Sources*, **105**, 13 (2002).
3. E. Slavcheva, T. Petkova, V. Nikolova, P. Iliev, S. Bliznakov, E. Lefterova, Y. Stoyanova, T. Vitanov, in: *Nanoscience & Nanotechnology*, Vol. 4, I. Dragieva, E. Balabanova (Eds.), Heron Press, Sofia, 2004, p. 263.
4. M. Jaksic, *Int. J. Hydrogen Energy*, **26**, 559 (2001).
5. Lj. Vračar, S. Gojkovic, N. Elezovic, V. Radmirović, M. Jakšić, N. Krastajić, *J. New Materials for Electrochem. Systems*, **9**, 99 (2006).
6. A. Stoyanova, E. Lefterova, V. Nikolova, P. Iliev, I. Dragieva, E. Slavcheva, *Bulg. Chem. Comm.*, **42**, 167 (2010)
7. E. Antolini, E. Gonzalez, *Solid State Ionics*, **180**, 746 (2009)
8. *PEM Fuel Cell Electrocatalysts and Catalyst Layers*, JiuJun Zhang (Eds.), Springer, 2008.
9. J. Lanford, A. Wilson, *J. Appl. Cryst.*, **11**, 102 (1978).
10. G. Topalov, E. Lefterova, E. Slavcheva, Proc. International Hydrogen Energy Congress and Exhibition IHEC 2007, Istanbul, Turkey, 13-15 July (2007) 1.
11. E. Antolini, J. Salgado, E. Gonzalez, *J. Power. Sources*, **160**, 957 (2006).
12. Jae-Sik Choi, W. Chung, H. Yong Ha, Tae-Hoon Lim, In-Hwan Oh, Seong-Ahn Hong, Ho-In Lee, *J. Power. Sources*, **156**, 466 (2006)
13. F. Lima, M. Calegari, E. Ticianelli, *Electrochim. Acta*, **52**, 3732 (2007).
14. J. Shim, Duck-Young Yoo, Ju-Seong Lee, *Electrochim. Acta*, **45**, 1943 (2000).
15. I. Ikemoto, K. Ishii, S. Kinoshita, H. Kuroda, M. Alario Franco, J. Thomas, *J. Solid State Chem.*, **17**, 425 (1976)
16. S. Sützer, F. Kadirgan, H.M. Söhmen, *Solar Energy Materials and Solar Cells*, **56**, 183 (1999).
17. S. Ardizzone, C. Bianchi, D. Tirelli, *Colloids and Surfaces A: Physicochemical and Engineering Aspects*, **134**, 305 (1998).
18. H. Nesbitt, D. Nanerjee, *Amer. Mineralogist*, **83**, 305 (1998).
19. V. Galakhov, M. Demeter, S. Bartkowski, M. Neumann, N. Ovechkina, E. Kurmaev, N. Lobachevskaya, Ya. Mukovskii, J. Mitchell, D. Ederer, *Phys. Rev. B*, **65**, 113102 (2002)
20. V. Tsurkan, M. Demeter, B. Schneider, D. Hartmann, M. Neumann, *Solid State Commun.*, **114**, 149 (2000).
21. S. Neophytides, S. Zafeiratos, G. Papakonstantinou, J. Jaksic, F.E. Paloukis, M. Jaksic, *Int. J. Hydrogen Energy*, **30**, 393 (2005).

**ФИЗИЧНО ОХАРАКТЕРИЗИРАНЕ НА Pt-M ДВУКОМПОНЕНТНИ  
ЕЛЕКТРОКАТАЛИЗАТОРИ ЗА РАЗЛАГАНЕ НА ВОДА**

**Е. Д. Лефтерова, А. Е. Стоянова, Г. Р. Борисов, Е. П. Славчева**

*Институт по електрохимия и енергийни системи – БАН  
ул. Акад. Г. Бончев бл. 10, 1113 София, България*

Постъпила на 7 септември, 2010 г.; преработена на 28 октомври, 2010 г.

(Резюме)

Синтезирани са комбинации от моно- и биметални смеси, оксиди и композитни материали, в които Pt е частично или изцяло заменена с по-евтини елементи (Cr и Mn). Като носител е използван механохимично третиран Ebonex. Синтезираните катализатори са охарактеризирани с обемни и повърхностни методи, като XRD, XPS и SEM. XRD и XPS анализите показват, че Cr- и Mn-компоненти са в аморфно и окислено състояние, докато Pt е предимно в метално състояние. Не е регистрирано сплавяване между Pt и Cr или Mn. Катализаторите са електрохимически изпитани по отношение на реакцията на отделяне на кислород при разлагане на водата в ПЕМ електролизна клетка. Като протонпроводящ електролит е използван търговският продукт Nafion 117. Установено е, че най-добра каталитична активност показва Pt-Cr/Ebonex, който проявява по-висока ефективност при по-ниски натоварвания на Pt в сравнение с всички други композиции, включително Pt/Ebonex. Получените резултати могат да се обяснят с електронни взаимодействия между металните частици и носителя, осигуряващи синергичен ефект.

## Growth and dissolution of anodic antimony oxide in oxalic acid electrolytes

I. G. Angelov, Chr. A. Girginov, E. Klein \*

University of Chemical Technology and Metallurgy, Department of Physical Chemistry, 8, Kl. Okhridsky Blvd., 1756 Sofia, Bulgaria

Submitted: July 27, 2010; accepted: October 8, 2010

The kinetics of anodic oxide growth on antimony in oxalic acid electrolytes was studied. The shapes of the voltage/time curves proved strongly to depend on the concentration of the electrolyte. Based on the different shapes, three electrolytes were chosen for investigations of the oxide film dissolution by means of impedance and open-circuit potential measurements. The rate of dissolution increases with increasing oxalic acid concentration. A relation is found between the shapes of the voltage/time curves and the proposed competitive process of film growth and dissolution, which includes the formation of an outer adherent layer of dissolution products. The proposed mechanism agrees well with some characteristics of the induction periods and explains adequately their appearance. The impedance studies indicate that the final thickness of the anodic oxide decreases with increasing concentration of the oxalic acid electrolyte. It is concluded that concentrations equal to or lower than 0.01 M (COOH)<sub>2</sub> have to be used in order to produce thick barrier-type anodic films.

**Key words:** anodic antimony oxide, oxide growth, oxalic acid anodizing, chemical dissolution, impedance measurements

### INTRODUCTION

The anodic passivation of antimony in acid and alkaline electrolytes has been described by El Wakkad and Hickling [1] in the early fifties of the last century. Since then, the anodic behavior of antimony has been extensively investigated in view of its use as constituent of alloys for lead-acid batteries [2, 3] or of materials for lithium-ion batteries [4]. Anodizing has been carried out in sulfuric acid electrolytes [2, 3, 5–8] or sulphuric acid with additives [9, 10], in phosphoric acid [11, 12], buffered phosphate solutions [13, 14] or phosphate esters [15], in a boric acid electrolyte [16], as well as in different neutral and alkaline media [17,18].

During constant current anodization, broad or restricted regions of linear potential rise with time are reported, depending on the nature of the electrolyte [16, 17], the current density [12], and the potential attained [5, 13]. Deviations from the linearity are ascribed to a duplex anodic film structure, composed of antimony oxides at different oxidation stages [1], the formation of an outer porous layer [12, 19], the structural or mechanical defects [7], the crystallization [5], the formation of outer layers of hydroxo sulfates [20] or phosphates.

Retarded potential rise with time has been observed in a number of cases [15, 21, 22]. The related induction periods have been ascribed [12] to the initial formation of a semi conducting layer with its consequent conversion into a barrier sub layer. The main disadvantage of anodic antimony oxides is their instability in most of the forming electrolytes. The oxide films are easily dissolved in acid, neutral and alkaline media, as ascertained by open-circuit potential and impedance measurements [1, 5, 7, 17, 19], and by ellipsometric studies [14].

Preliminary data on the oxidation of antimony in oxalic acid pointed at the possible occurrence of relatively thick oxide films with bright interference colors after anodization up to high voltages. This work reports on the growth and dissolution kinetics of anodic antimony oxide in oxalic acid solutions.

### EXPERIMENTAL

The specimens were cut from an antimony rod of 99.9995 % purity by means of a diamond disc. The cylindrical bodies were 1 cm thick; the working area of the antimony electrode was limited to one of the bases of the cylinder, having a surface of ca. 2.5 cm<sup>2</sup>. A silver lead-out was welded to the opposite base of each cylinder and the non-working area was isolated by thermoplastic epoxy resin. The electrodes were polished with fine-grained emery papers and electro polished for 60 s in 1:9 volume parts of 70 % HClO<sub>4</sub> to (CH<sub>3</sub>CO)<sub>2</sub>O at 20 °C and

\* To whom all correspondence should be sent.

E-mail: klnrdwr@yahoo.com

$0.3 \text{ A cm}^{-2}$ . After rinsing with methanol and water, the electrodes were brightened at  $20 \text{ }^\circ\text{C}$  for 10 min in 1: 1 volume parts of concentrated hydrochloric acid to water and thoroughly washed in deionized water.

Anodic growth and dissolution were studied in oxalic acid solutions with concentrations varying from 0.001 M to 0.1 M. In order to avoid some slowing down of the dissolution rate, due to saturation with ionic antimony species, large volumes of the most used solutions were prepared.

An especially designed galvanostat ( $0.5 \text{ A}$ ,  $600 \text{ V}$ ) was used for the anodization at the constant current density of  $2 \text{ mA cm}^{-2}$  under controlled temperature conditions. In order to improve reproducibility of results, anodizing was carried out in unstirred electrolytes. The variation of the open-circuit potential with time was measured against a saturated calomel electrode (SCE); measurements started immediately after switching off the polarization.

The dissolution rate was evaluated by means of ac impedance measurements at a frequency of  $1000 \text{ Hz}$ . An EG&G Instruments PAR model 273 potentiostat and 5208 two phase lock-in analyzer connected to an IBM personal computer via GPIB-II interface, and a M378 and M342 software were used to run the tests, to collect and evaluate the experimental data. The impedance measurements started about 30 s after switching off the polarization in order to avoid overloading of the potentiostat, due to non-dissipated space charge in anodic antimony oxide. The initial reciprocal specific capacitance,  $1/c_{s,0}$ , assumed to be proportional to the final thickness of the growing oxide film, was determined by extrapolation to zero time of the corresponding  $1/c_s(t)$ -curves.

## RESULTS AND DISCUSSION

Anodic oxide films on antimony were grown in a series of oxalic acid solutions with concentrations varying from 0.001 M to 0.1 M  $(\text{COOH})_2$ . The voltage/time dependence of the film growth under constant temperature ( $293 \text{ K}$ ) and current density ( $2 \text{ mA cm}^{-2}$ ) conditions without stirring is shown in Fig. 1 for six  $(\text{COOH})_2$  concentrations. No induction periods are observed in most of the solutions used. In the solutions with concentrations from 0.01 M to 0.03 M, the initial linear potential rise is followed by slowing down, arrest or passage through maximum values of the forming voltage. Except for the 0.01 M solution, a second potential rise up to high voltages always takes place. This second potential rise is only partially shown in the

figure. It can be concluded that the shape of the voltage/time curves gradually changes with the

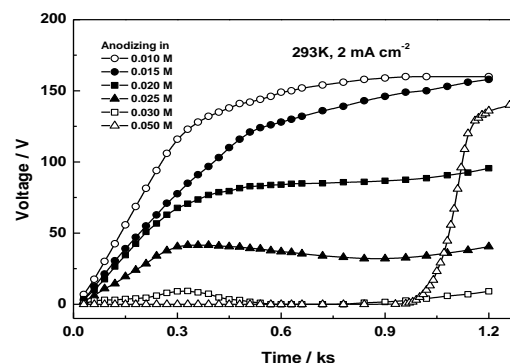


**Fig. 1.** Time variation of the forming voltage during anodization of antimony at  $293 \text{ K}$  and  $2 \text{ mA/cm}^2$  in unstirred aqueous solutions of oxalic acid with different concentrations.

increasing concentration of oxalic acid. Moreover, the ‘induction period’, observed in 0.05 M solutions, appears to be a reasonable sequence of the changes in shape. In this case, the assumed initial formation of a semi conducting layer can hardly account for the retarded potential rise [12].

Previous investigations, mentioned in the Introduction, have furnished unambiguous evidence both for the formation of duplex films on antimony and for their dissolution in the forming electrolytes. These facts could be useful in the attempt to explain the anodic behavior of antimony. For the purpose, three oxalic acid solutions with concentrations of 0.01 M, 0.03 M and 0.05 M were chosen as representative of forming electrolytes with different shapes of the voltage/time curves. The dissolution rate of films, grown up to 5 V, 40 V and 140 V, was studied in the above solutions by means of ac impedance measurements at  $1000 \text{ Hz}$ . The results are shown in Fig. 2. It can be seen that the anodic oxide dissolves at a high rate.

Only about 7 minutes are needed for the film, formed up to 140 V in 0.01 M  $(\text{COOH})_2$ , to dissolve almost completely (Fig. 2a); the essential decay in film thickness takes less than 2 minutes in the other two solutions (Figs. 2b and 2c). The graphs in the latter figures are presented in a large scale; the thickness changes after the second minute of dissolution numerically correspond to the range of  $1/c_s$ -values in Fig. 2a for the almost dissolved films.

After the initial decay in the film thickness during dissolution in 0.03 M and 0.05 M  $(\text{COOH})_2$ , the reciprocal specific capacitance consecutively passed through a minimum, gradually increased to a maximum, and afterwards, slowly decreased with

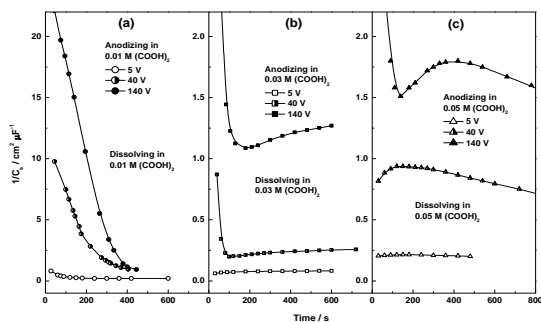


**Fig. 2.** Time variation of the reciprocal specific capacitance,  $1/c_s$ , of anodic antimony oxides grown without stirring in 0.01 M (a); 0.03 M (b) and 0.05 M (c) at 293 K and  $2 \text{ mA cm}^{-2}$  up to 5 V, 40 V and 140 V.

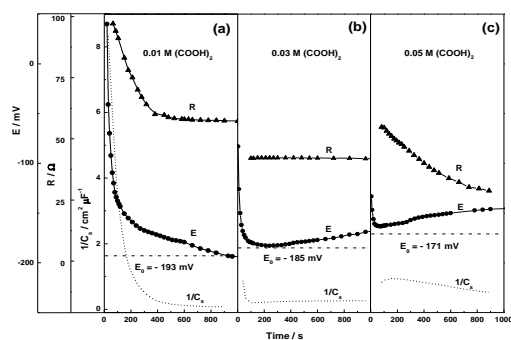


**Fig. 3.** Time variation of the resistance  $R$  and the open-circuit potential  $E$  of antimony oxide electrodes during dissolution in 0.01 M (a), 0.03 M (b) and 0.05 M (c) oxalic acid solutions after anodization up to 40 V at 293 K and  $2 \text{ mA cm}^{-2}$ . The dashed lines show the variation of the reciprocal specific capacitance,  $1/c_s$ , from Fig. 2. The dash-dotted lines mark the steady-state potential of non-anodized antimony in the electrolytes used. All potentials are measured versus saturated calomel electrode.

time, as illustrated in Fig. 2c, and partially in Fig. 2b. Such course of the curves could be attributed to the formation of an outer layer of dissolution products. The rapid dissolution of the oxide film in the oxalic acid electrolytes suggests the appearance of the outer layer since the very beginning of anodization as a result of the concurrence between film growth and dissolution. The layer grows further, parallel to the oxide film dissolution, and also dissolves in the electrolyte. Without deliberating about the nature of the dissolution products, a few suggestions can be made for the layer properties. First, a good adhesion to the oxide film is expected; second, the layer should dissolve in the contact electrolyte at a lower rate than that of the oxide, and finally, the layer should have a

porous structure which entangles but does not eliminate the migration of the electrolyte ions.

The above assumptions are in conformity with the experimental results. In addition, the time variation of the resistance and of the open-circuit potential was studied in order to gather more information about the dissolution process. The results in the three oxalic acid electrolytes are shown in Fig. 3.

The time variations of the open-circuit potential, the resistance and the reciprocal specific capacitance of the antimony oxide electrode in 0.01 M  $(\text{COOH})_2$  correlate well, as seen in Fig. 3a. After the abrupt initial decay, all three quantities slow down; the potential reaches its steady-state value in the electrolyte.

In 0.03 M  $(\text{COOH})_2$ , the potential passes through a flat minimum near to the steady-state value, and shifts to less negative values in apparent correlation with the variation of  $1/c_s$  (Fig. 3b). The reciprocal capacitance passes through a flat maximum after ca. 2.0 ks (not shown in the figure). This behavior was attributed to the final dissolution of the oxide film, the residual thickening of the layer formed from dissolution products and the ongoing dissolution of the outer layer. The resistance passes through a flat maximum and decreases slowly with time, most probably due to the concurrence between the growth and the dissolution of the outer layer.

In 0.05 M  $(\text{COOH})_2$ , both, the resistance and the reciprocal specific resistance, pass through a maximum and decrease afterwards, as illustrated in Fig. 3c. Here, again, final dissolution of the oxide film, residual thickening of the outer layer and its dissolution in the electrolyte can account for the observed behavior. The relatively fast resistance drop appears to be connected to a stronger dissolving action towards the outer layer of the 0.05 M solution compared with the other two electrolytes.

The open-circuit potentials in 0.03 M and 0.05 M solutions vary in time in a quite similar way. The potential shift in 0.05 M  $(\text{COOH})_2$  to less negative values, however, continues even after the decays in resistance and reciprocal capacitance have begun. Due to the various dissolution processes and the impeded diffusion in the unstirred electrolyte, its composition in the pores of the outer layer will be different from that in the bulk of the solution. Hence, the observed potential shift could be attributed to the electrolyte changes in the vicinity of the electrode rather than to the thickening of the outer layer.

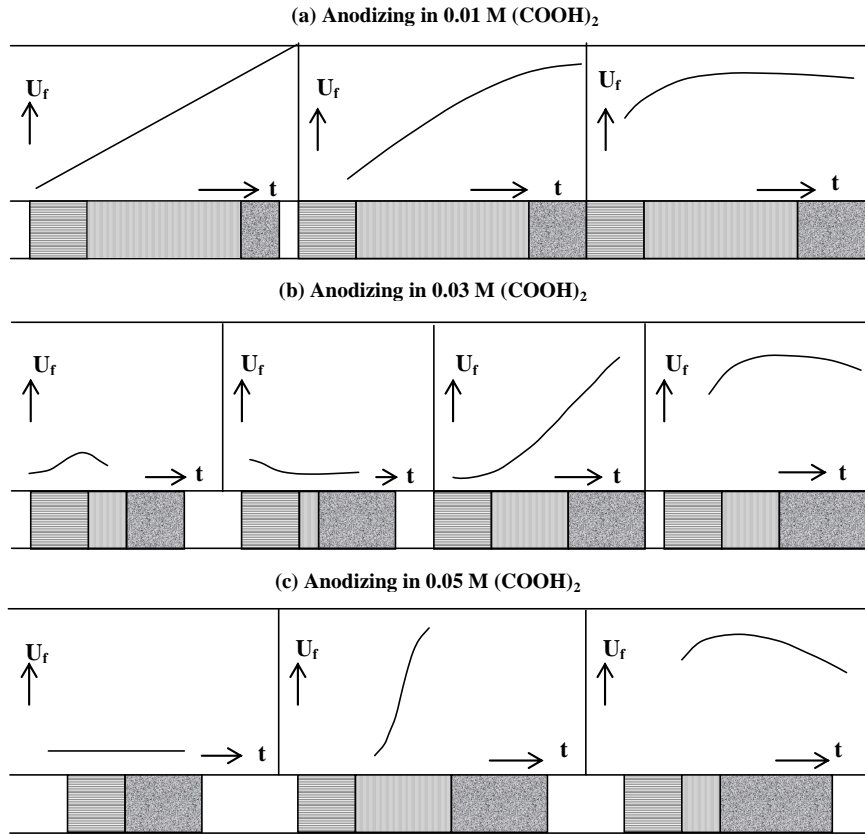


**Fig. 4.** Schematic presentation of the anodic behavior of antimony (■) in 0.01 M, 0.03 M and 0.05 M (COOH)<sub>2</sub>. The stages in growth and dissolution of the oxide film (▨) and of the layer formed from dissolution products (▩) are matched to the corresponding parts of the voltage/time curves. The width of the sectors is purely speculative and does not correspond to the real film or layer thicknesses.

Summarizing, the processes of film growth and dissolution of anodic antimony oxide in oxalic acid electrolytes are schematically depicted in Fig. 4. The relatively low dissolving effect of the 0.01 M solution permits the formation of a thick barrier-type anodic film up to voltages as high as 100 V. The continuous thinning of the oxide film and/or a field-assisted dissolution causes the consequent slowing down and the arrest of the voltage rise; the dissolution products adhere to the film surface, forming a porous outer layer which permits the migration of ions.

The stronger dissolving action of the 0.03 M electrolyte leads to the formation of a thin oxide film which gradually dissolves. For a given period of time, the rate of film growth equals to the dissolution rate, resulting in the thickening of the outer layer only. A larger coverage of the surface with dissolution products and/or an increased density of the outer layer provoke the increase of the real current density. The film growth starts then to prevail again over the dissolution. An almost linear voltage rise up to ca. 100 volts is observed, followed by a slowing down, and eventually by a

decrease, resulting in the reduction of the oxide thickness.

During almost 1 ks, no film growth is observed in the 0.05 M oxalic acid. This is the period of time, for which balancing of film growth and dissolution is assumed. Like in the 0.03 M solution, the accumulation of dissolution products in the outer layer leads to higher values of the real current density and an abrupt voltage rise is observed. The slow down and voltage decrease, as mentioned, resulted in lowering of the anodic film thickness.

Studies of the current density dependence of the induction periods of antimony in concentrated phosphoric acid [11] or in 0.05 M oxalic acid [22] showed a decrease of the induction period with increasing current density. The induction period appearance explanation, proposed in this work, agrees well with the above finding. A simple calculation indicates that the induction period disappears at a current density of ca. 5 mA cm<sup>-2</sup>, so this value is expected to correspond to the real current density, needed to overcome the dissolution and to restart anodizing of the electrode, covered with dissolution products. Furthermore, the

reported poor reproducibility of induction periods in stirred media [15, 21, 22] is now better understood in view of the complex influence of the hydrodynamics on the oxide film dissolution and the formation and dissolution of the porous outer layer.

The concentration of anions was found to play an important role in the film growth. Thus, the antimony oxide dissolution has proven to be promoted by phosphate ions [13]. A voltage/time dependence, similar to that of the antimony in 0.03 M (COOH)<sub>2</sub>, has been obtained for the same metal in KOH and Na<sub>2</sub>CO<sub>3</sub> solutions [23]. The shape of the curves was attributed to the presence of carbonate ions. Our studies showed an increasing dissolution rate with increasing concentration of the oxalic acid. As discussed before (Fig. 2), dissolution in 0.03 M and 0.05 M (COOH)<sub>2</sub> started at lower initial film thicknesses compared to the 0.01 M solution. This observation was considered when composing Fig. 4. Moreover, an additional check was undertaken. For the purpose, the initial parts of the capacitance/time or reciprocal capacitance/time curves for films, formed up to different voltages in the three studied electrolytes, were extrapolated to zero time, and the calculated values for the initial reciprocal specific capacitance  $1/c_{s,o}$  were plotted against the forming voltage. The curves for the films, formed in the 0.01 M and 0.05 M solutions, are shown in Fig. 5.

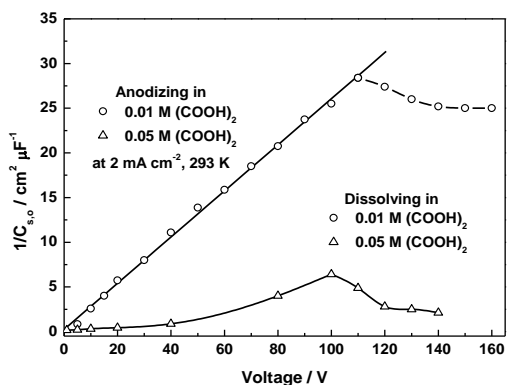


**Fig. 5.** Dependence of the initial reciprocal specific capacitance  $1/c_{s,o}$  of anodic antimony oxide on the final voltage attained during anodization in 0.01 M and 0.05 M (COOH)<sub>2</sub> at 293 K and 2 mA cm<sup>-2</sup>.

A linear increase of  $1/c_{s,o}$  with increasing voltage of up to about 100 V is observed for the films, grown in 0.01 M oxalic acid. Quite surprisingly, the attendant chemical film dissolution proved not to affect linearity, and relatively high film thicknesses were attained. Above 100 V, the

lowering of the film thickness is possibly related to additional field-assisted dissolution. The anodization in both 0.03 M (not shown) and 0.05 M solutions proved to be severely affected by chemical dissolution of the oxide films. The restricted non-linear increase of  $1/c_{s,o}$  with increasing voltage to up to 100 V would mean that the main contribution to the overall thickness is due to the outer porous layer. Above 100 V, the final film thickness decreased like that in the 0.01 M solution but films formed up to 120 V had almost the same residual thickness as those formed in 0.01 M solutions up to 10 V. The above results indicate that relatively thick barrier-type films on antimony can be obtained only in diluted oxalic acid solutions with concentrations equal to or lower than 0.01 M.

### CONCLUDING REMARKS

The studies of the growth and dissolution of anodic antimony oxide in oxalic acid electrolytes permitted to limit the concentration range for effective barrier anodizing of the antimony. A scheme of film dissolution was proposed, relating adequately the shapes of the voltage/time curves to the thickness changes, ascertained by impedance measurements. Additional analytical methods have to be used, however, to confirm the assumptions made.

### REFERENCES

1. S.E.S. El Wakkad, A. Hickling, *J. Phys. Chem.*, **57**, 203 (1953).
2. S. Laihonen, T. Laitinen, G. Sundholm, A. Yli-Penti, *Electrochim. Acta*, **35**, 229 (1990).
3. M. Metikoš-Huković, R. Babić, S. Brinić, *J. Power Sources*, **157**, 563 (2006).
4. D. Larcher, A.S. Prakash, L. Laffont, M. Womes, J. C. Jumas, J. Olivier-Fourcade, M. S. Hedge, J.-M. Tarascon, *J. Electrochem. Soc.*, **153**, A1778 (2006).
5. I.A. Ammar, A. Saad, *J. Electroanal. Chem.*, **30**, 395 (1971).
6. M. Metikoš-Huković, B. Lovreček, *Electrochim. Acta*, **25**, 717 (1980).
7. M.S. El-Basiouny, M.M. Hefny, A.S. Mogoda, *Annali di Chimica*, **74**, 729 (1984).
8. D. Pavlov, M. Bojinov, T. Laitinen, G. Sundholm, *Electrochim. Acta*, **36**, 2087 (1991).
9. A.S. Mogoda, T.M. Abd El-Haleem, *Thin Solid Films*, **441**, 6 (2003).
10. A.S. Mogoda, *Thin Solid Films*, **394**, 173 (2001).
11. A.A. Girginov, I.A. Kanazirski, E.H. Klein, *Compt. rend. Acad. bulg. Sci.*, **44**, 49 (1991).
12. M. Bojinov, I. Kanazirski, A. Girginov, *Electrochim. Acta*, **40**, 873 (1995).
13. O.E. Linares Pérez, M.D. Sanchez, M. López Teijelo, *J. Electroanal. Chem.*, **632**, 64 (2009).

14. O.E. Linarez Pérez, M.D. Sanchez, M. López Teijelo, *J. Electroanal. Chem.*, **645**, 143 (2010).
15. A. Girginov, E. Klein, V. Kalfova, S. Ikonopisov, *B. Electrochem.*, **4**, 631 (1988).
16. S.M. Ikonopisov, V.M. Kalfova, A.A. Girginov, *Compt. rend. Acad. bulg. Sci.*, **41**, 89 (1988).
17. I.A. Ammar, A. Saad, *J. Electroanal. Chem.*, **34**, 159 (1972).
18. L.L. Wickstrom, K. Nobe, *Corrosion – NACE*, **31**, 364 (1975).
19. M.M. Hefny, W.A. Badawy, A.S. Mogoda, M.S. El-Basiouny, *Electrochim. Acta*, **30**, 1017 (1985),
20. M. Bojinov, D. Pavlov, *J. Electroanal. Chem.*, **315**, 201 (1991).
21. S.M. Ikonopisov, A.A. Girginov, V.K. Tsochev, *Compt. rend. Acad. bulg. Sci.*, **25**, 653 (1971).
22. I.G. Angelov, E.H. Klein, A.A. Girginov, S.M. Ikonopisov, *Compt. rend. Acad. bulg. Sci.*, **43**, 61 (1990).
23. A.A. Girginov, S.M. Ikonopisov, *Soviet Electrochemistry*, **10**, 638 (1974) (in Russian).

## ОБРАЗУВАНЕ И РАЗТВАРЯНЕ НА АНОДЕН АНТИМОНОВ ОКСИД В РАЗТВОРИ НА ОКСАЛОВА КИСЕЛИНА

И. Г. Ангелов, Кр. А. Гиргинов, Е. Клайн\*

*Катедра „Физикохимия”, Химикотехнологичен и металургичен университет, бул. „Климент Охридски” № 8,  
1756 София*

Постъпила на 27 юли, 2010 г.; приета на 8 октомври, 2010 г.

(Резюме)

Изследвана е кинетиката на образуване на анодни оксидни филми върху антимон в разтвори на оксалова киселина. Установено е, че формата на кривите напрежение-време силно зависи от концентрацията на оксаловите електролити. Три електролита, в които се получават кинетични криви с различна форма, са избрани за изследвания на химичното разтваряне на филмите с помощта на импедансни измервания. Предложен е механизъм на основата на конкурентно нарастване и разтваряне на анодния филм, предполагащ образуването на външен порест слой от продуктите на разтварянето. Намерено е добро съответствие между експерименталните резултати и предложената схема за образуване и разтваряне на филмите. Установено е, че сравнително дебели анодни филми от бариерен тип се получават само в 0.01 моларна оксалова киселина.

## Corrosion stability of stainless steel, modified electrochemically with Ce<sub>2</sub>O<sub>3</sub>–CeO<sub>2</sub> films, in 3.5% NaCl media

D. Guergova<sup>1</sup>, E. Stoyanova<sup>1</sup>, D. Stoychev<sup>1\*</sup>, I. Avramova<sup>2</sup>, G. Atanasova<sup>2</sup>, P. Stefanov<sup>2</sup>

<sup>1</sup>Rostislav Kaischew Institute of Physical Chemistry, Bulgarian Academy of Sciences, 1113 Sofia, Bulgaria

<sup>2</sup>Institute of General and Inorganic Chemistry, Bulgarian Academy of Sciences, 1113 Sofia, Bulgaria

Received August 12, 2010; accepted October 25, 2010

This work is focused on the study of corrosion-protection ability of the thin ceria film, formed electrochemically on OC404 stainless steel (SS) in non-aqueous electrolytes. The influence of changes in the surface concentration of Ce<sub>2</sub>O<sub>3</sub>–CeO<sub>2</sub> on the corrosion behaviour of OC404 stainless steel in 3.5% NaCl was investigated prior to the thermal treatment as well as after it. A shift of corrosion potential in positive direction was found via polarization curve recording, as well as via decrease in the corrosion current, respectively decrease in the corrosion rate (enhancement of the corrosion protection) in the presence of ceria oxide films.

The data, acquired by AFM and XPS, are in a good agreement with these results. On the basis of the obtained results we can conclude that the presence of Ce<sub>2</sub>O<sub>3</sub>–CeO<sub>2</sub> film results in passivation and re-passivation of the steel surface and a slowdown in the pitting corrosion in an aggressive media. These conclusions are explained by the strong polarization influence of the Ce<sub>2</sub>O<sub>3</sub>–CeO<sub>2</sub> layers on the conjugated depolarization cathodic reaction of reduction of the dissolved oxygen.

**Key words:** corrosion protection, polarization, electrodeposited Ce<sub>2</sub>O<sub>3</sub>–CeO<sub>2</sub> thin films.

### INTRODUCTION

The option to use representatives of the rare-earth element group (Ce, La, Sm, Y) for the protection of Al, Fe and Zn articles against corrosion in aqueous solutions was studied for the first time by Hinton and coauthors at the beginning of the eighties of the 20th century [1–5]. According to the literature sources, the surface modification of stainless steels in particular [6–15], and the other metal alloys using rare-earth elements, leads to improvement of their resistance to corrosion in aqueous media, containing chloride ions, [16–19]. The increased corrosion stability is due to the formation of thin oxide films (whose protective action is associated with formation of soluble Ce<sub>2</sub>O<sub>3</sub>, Ce(OH)<sub>3</sub> and/or insoluble CeO<sub>2</sub> and Ce(OH)<sub>2</sub><sup>2+</sup> oxides/hydroxides) thus hindering the free diffusion of oxygen and adsorption of the aggressive Cl<sup>-</sup> ion on the metal surface, leading to acceleration of the pitting formation [19–22].

Our previous works showed that the electrochemical formation of Ce<sub>2</sub>O<sub>3</sub>–CeO<sub>2</sub> and Al<sub>2</sub>O<sub>3</sub> thin oxide films on OC404 stainless steel results in improvement of the passivation processes in media with an oxidizing action (0.1 N HNO<sub>3</sub>),

and in prevention of pitting corrosion appearance [23, 24]. The behavior of the above systems was studied in non-oxidizing media (0.1 N H<sub>2</sub>SO<sub>4</sub>) [25, 26]. Thereupon, it was established that the deposition of Ce<sub>2</sub>O<sub>3</sub>–CeO<sub>2</sub> oxides has a strongly expressed stabilizing effect on the passive state of SS. This effect is connected with the occurrence of effective reduction cathodic process of the CeO<sub>2</sub>, leading to a stable passive state. The oxide presence determines the restoration of the disrupted passive state of the thermally treated steel in an acidic media.

The aim of this investigation was to study the corrosion behavior, respectively the protective effect, of the electrochemically formed (in non-aqueous electrolytes) Ce<sub>2</sub>O<sub>3</sub>–CeO<sub>2</sub> films on the stainless steel (prior to and after the thermal treatment of the “oxide layer/stainless steel” system) in a 3.5% NaCl solution.

### EXPERIMENTAL

The test specimens, used in this study, were prepared from a sheet of OC404 type SS, with a thickness of 50 μm. The composition of the steel in wt. % was 20.0% Cr, 5.0% Al, 0.02% C, the rest being Fe.

The Ce<sub>2</sub>O<sub>3</sub>–CeO<sub>2</sub> layers were deposited electrochemically on SS from non-aqueous

\* To whom all correspondence should be sent:  
E-mail: [stoychev@ipc.bas.bg](mailto:stoychev@ipc.bas.bg)

electrolytes – their compositions and regimes are described in [27, 28].

The thickness of the deposited layers was ~1 μm. The layers were investigated upon deposition and upon thermal treatment (t.t.) at 450 C for 2 h in air.

The electrochemical behaviour of the samples (10 mm x 10 mm) was studied in a naturally aerated 3.5% NaCl aggressive media (pH = 6.5) at a room temperature in a standard three-electrode thermostatted cell (100 ml volume). A counter electrode, comprising a platinum plate (10 × 10 × 0.6 mm), and a calomel reference electrode (SCE), ( $E_{\text{Hg}/\text{Hg}_2\text{Cl}_2} = +0.240 \text{ V vs. SHE}$ ), were used. All potentials in the text are related to SCE. The anodic and cathodic potentiodynamic polarization curves were obtained using a 273 EG&G potentiostat/galvanostat (Germany), with a potential sweeping rate of 10 mV/s within the potential range from -1.500 to +1.000 V.

The corrosion potential ( $E_{\text{corr}}$ ), the breakdown potential ( $E_{\text{pitt}}$ ), and the corrosion current density ( $i_{\text{corr}}$ ) of the samples under investigation were determined based on potentiodynamic polarization curves, obtained in 3.5% NaCl solution.

The chemical composition and the oxidation state of the elements on the surface formed after immersion (for different time intervals) in an aggressive media – for the specimens “upon deposition” and upon thermal treatment, were studied using X-ray photoelectron spectroscopy (XPS). The XPS studies were performed in an Escalab II system (England) with Al  $K_{\alpha}$  radiation ( $h\nu = 1486.6 \text{ eV}$ ) and total instrumental resolution of ~ 1 eV. The vacuum in the chamber was  $10^{-7} \text{ Pa}$ . The binding energy (BE) was referred to the C1s line (of adventitious carbon) at 285.0 eV. The element concentrations were evaluated based on the integrated peak areas after Shirley-type of linear background subtraction using theoretical Scofield’s photoionization cross-sections [29].

The atomic force microscope (AFM) used for the surface imaging was a Q-scope 250 (Quesant, USA) with a head, designed for a scan area from 200 nm × 200 nm up to 80 μm × 80 μm. The lateral resolution was approximately 1 nm, and the resolution of the z-axis of approximately the same range. The measurements were performed in the non-contact mode with the following typical scan parameters: a scan rate of 0.5 to 3 Hz, integral and proportional gain in the range between 250 and 400, and image resolution of 300 to 600 dpi.

## RESULTS AND DISCUSSION

On the basis of the plotted complete potentiodynamic polarization curves in the range of the potentials from -1.500 to +1.000 V (these are not represented in this work), the basic electrochemical parameters of the corrosion process were determined for the studied systems (Tables 1 and 2). It follows from these results that:

- the cerium oxide films, deposited electrochemically on the stainless steel, create considerable shifts in the SS corrosion potential in a positive direction;
- this shifting grows up with the increase in the concentration of the oxides on the surface of the steel;
- the presence of cerium oxides leads to lowering of the corrosion current;
- the presence of cerium oxides determines a potentials shift of the pitting formation in a positive direction.

**Table 1.** Electrochemical parameters characterizing the corrosion behaviour of studied systems determined from potentiodynamic polarization curves.

Samples	$E_{\text{corr}}$ , V	$i_{\text{corr}}$ , A.cm <sup>-2</sup>	$E_{\text{pitt}}$ , V
SS	-0.172	$6.0 \times 10^{-7}$	-0.065
Ce <sub>2</sub> O <sub>3</sub> -CeO <sub>2</sub> (3.6 at.%)/SS	-0.168	$5.1 \times 10^{-7}$	-0.054
Ce <sub>2</sub> O <sub>3</sub> -CeO <sub>2</sub> (13.1 at.%)/SS	-0.163	$3.0 \times 10^{-7}$	0.052
Ce <sub>2</sub> O <sub>3</sub> -CeO <sub>2</sub> (25.7 at.%)/SS	-0.056	$6.9 \times 10^{-8}$	0.091

**Table 2.** Electrochemical parameters characterizing the corrosion behaviour of studied systems, after thermal treatment determined from potentiodynamic polarization curves.

Samples	$E_{\text{corr}}$ , V	$i_{\text{corr}}$ , A.cm <sup>-2</sup>	$E_{\text{pitt}}$ , V
SSt.t.	-1.083	$4.6 \times 10^{-6}$	-0.003
CeO <sub>2</sub> -Ce <sub>2</sub> O <sub>3</sub> (4.2 at.%)/SSt.t.	-0.300	$5.1 \times 10^{-7}$	-0.069
CeO <sub>2</sub> -Ce <sub>2</sub> O <sub>3</sub> (11.2 at.%)/SSt.t.	-0.284	$1.2 \times 10^{-7}$	0.091
CeO <sub>2</sub> -Ce <sub>2</sub> O <sub>3</sub> (29.6 at.%)/SSt.t.	-0.168	$1.3 \times 10^{-8}$	0.119

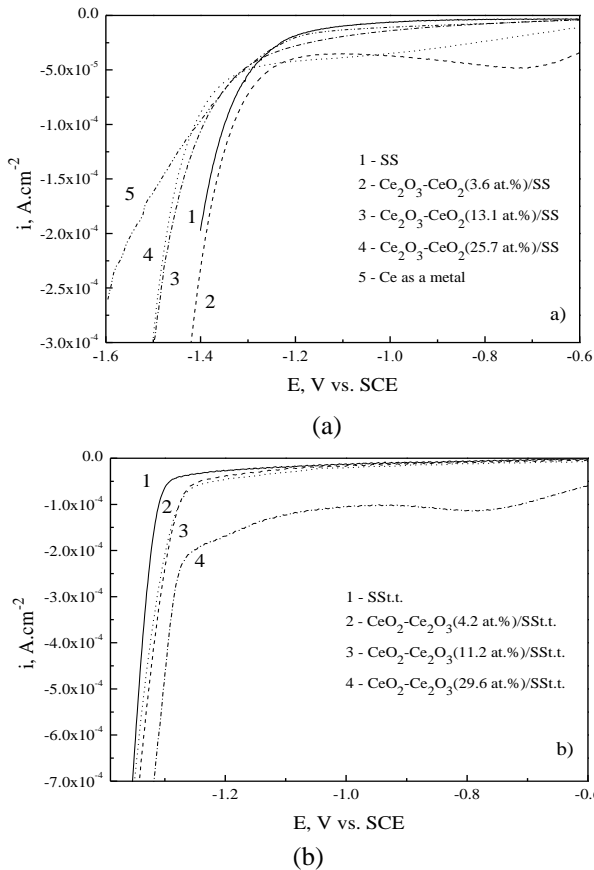
The obtained results show also that the thermal treatment of the studied samples causes a substantial change in the corrosion parameters, both, in the case of steel non-covered with cerium oxides, and in the case of the system cerium oxides/steel. As a consequence of the sample thermal treatment, the following is observed:

- $E_{\text{corr}}$  of the steel is shifted with more than 0.900 V in the negative direction;
- $i_{\text{corr}}$  of the steel is increased with an order of magnitude;
- $E_{\text{pitt}}$  of the steel is shifted in the positive direction with more than 60mV, while for the system of CeO<sub>2</sub>-Ce<sub>2</sub>O<sub>3</sub>/SS – with ~ 120 mV.

Thereupon, however, the respective corrosion potentials, which are characteristic for non-treated thermally systems, are not achieved, while the

corrosion currents and potentials of pitting formation are characterized by more favorable values, in terms of corrosion, compared to those, obtained for the non-treated thermally SS, respectively for the  $Ce_2O_3-CeO_2/SS$ .

Aiming to evaluate the protective effect of the electrodeposited cerium oxide films, we shall consider in details the anodic and the cathodic polarization curves for the studied systems in some specific zones of potentials, which characterize the occurring anodic and cathodic processes on the steel surface.



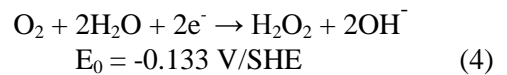
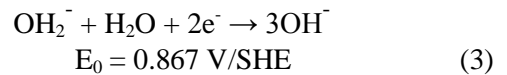
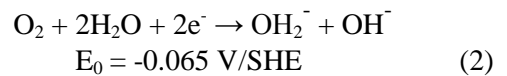
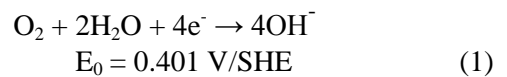
**Fig. 1.** Characteristic part of cathodic potentiodynamic polarization curves for the SS OC404 with Ce oxides surface modification, before (a) and after thermal treatment (b), obtained in 3.5% NaCl.

Fig. 1 illustrates the cathodic polarization curves, obtained in 3.5% NaCl solution, for stainless steel SS OC404 and for the systems of  $Ce_2O_3-CeO_2/SS$  before (a) and after thermal treatment (b). Fig. 1a represents the potentiodynamic curves for SS (curve 1) and for SS with various concentrations of the cerium oxide films, deposited on it electrochemically (curves 2-4). For comparison curve 5 was also plotted, characterizing the rate of the cathodic reduction process on metallic cerium.

It was necessary to carry out the investigation of the possible changes in the surface composition and the electrochemical (corrosion) behavior of the studied systems as a function of the duration of the thermal treatment in view of their application as supports of the catalytically active systems. These systems are calcinated (treated at high temperature) to undergo the respective transformations of the active phase or of the support, as well as in a number of other cases, in which it is possible to use SS, modified superficially with cerium oxide at high temperatures, and in the presence of chloride ions in the working environment [30, 31].

Fig. 1a clearly shows that the increase in the surface concentration of the cerium oxides in the case of non-treated thermally steel samples determines the increase in the reduction overpotential of the oxygen, dissolved in the corrosion medium. Such increase is inherent to this reaction in a native passive film on stainless steel, growing to values, close to those inherent to the metallic cerium. (In this case it is important to notice that the surface of the metallic Ce is always covered with a relatively thick layer of cerium oxides due to the extremely high affinity of Ce to oxygen [32]).

As reported in a study of Klaper et al. [33 and references therein] on the electrochemical reduction of oxygen in neutral and alkaline solutions, this process gives rise to formation of  $OH^-$  groups, following a four-electron pathway (Eq. (1)), or it can yield  $OH^-$  via hydrogen peroxide following a two-electron pathway (Eqs. (2) and (3)), or it can produce  $H_2O_2$  as a final reduction product (Eq. (4)).



Based on own data and on other authors data, we can make the important conclusion that for stainless steels and iron-chromium alloys, the mechanism and kinetics of oxygen reduction strongly depend on the material (chemical composition, surface state), the electrolyte (pH, chemical composition), and the conditions under

which the reaction is taking its course (hydrodynamics, temperature, polarization). These

authors, as well as the authors of the paper [34] pay special attention to the specific type of the stainless

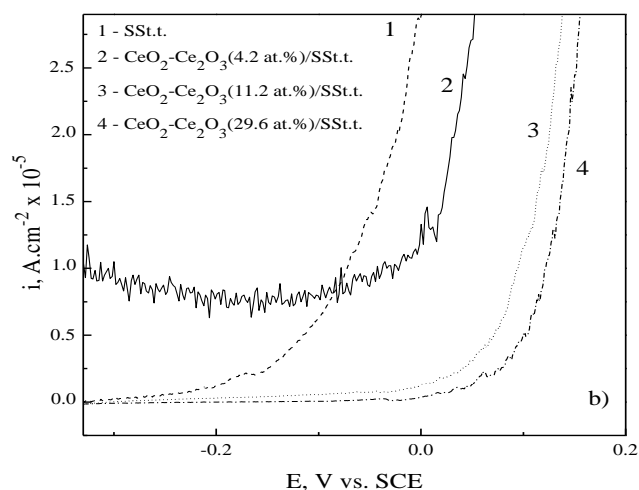
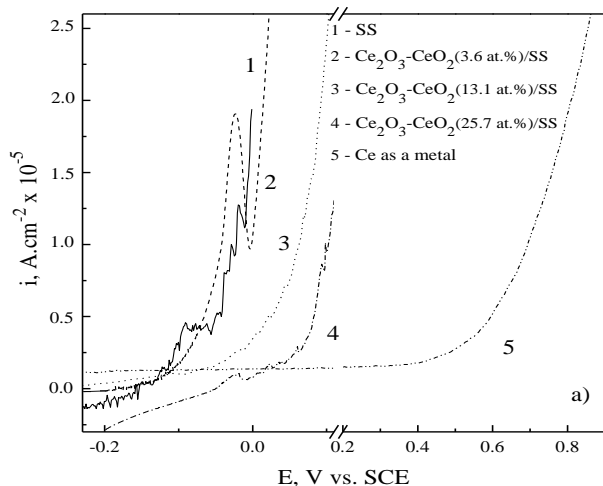


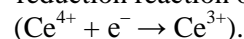
**Fig. 2.** Characteristic part of anodic potentiodynamic polarization curves for the SS OC404 with Ce oxides surface modification, before (a) and after thermal treatment (b), obtained in 3.5% NaCl.

steel. The presence of passive layers is also a very important factor, affecting the oxygen reduction reaction. Also, as far as localized corrosion of stainless steels is concerned, it preferably occurs within these layers rather than on the metallic surface, and therefore its catalytic activity should be related to the concentration of Fe (II) ions.

In the light of these considerations, the observed differences in the course of the curves 2-4, compared to curve 1 (for the SS non-coated with cerium oxides) in Fig. 1a are obviously due to the different nature of the support, on which the reduction process is occurring. Thereupon, we can clearly outline two zones of potentials (up to and above  $\sim -1.25$  V), in which the nature of the reduction process is changing. Up to  $-1.25$  V the steel surface, modified with cerium ions, determines a depolarizing effect, which (in our opinion) is due to reorganization of the mixed oxide films on the steel surface - see the corresponding peaks of oxidation in curve 2 (at  $E = \sim -0.090$  V and at  $-0.020$  V) in Fig. 2a. In the more negative range of potentials ( $E < -1.25$  V), which corresponds to the proper zone of cathodic reduction of oxygen, the increase in the concentration of cerium oxides leads to a substantial growth of the overpotential of this reaction, respectively to decrease in its rate. Such impedance of the oxygen reaction, which is a conjugated cathodic reaction during the occurrence of steel corrosion in the  $\text{Ce}_2\text{O}_3\text{-CeO}_2/\text{SS}$  system, obviously will lower the rate of the conjugated oxidation reaction, and thus, the total rate of the corrosion process. Besides this, such an inhibition of the cathodic reaction, under the conditions of passivity, is a guarantee for preservation of the

stable passive state of the stainless steel, respectively - for corrosion under conditions of passivity.

In the cases of thermally treated  $\text{SS}_{t.t.}$  and  $\text{CeO}_2\text{-Ce}_2\text{O}_3/\text{SS}_{t.t.}$  samples (Fig. 1b), which are known to have a disrupted surface passive film [26,35], we can observe an increase in the cathode current with about one order of magnitude, for both, the  $\text{SS}_{t.t.}$  and the  $\text{CeO}_2\text{-Ce}_2\text{O}_3/\text{SS}_{t.t.}$  system. At the same time, in the case of  $\text{CeO}_2\text{-Ce}_2\text{O}_3/\text{SS}_{t.t.}$  sample a considerable depolarizing effect is registered (with  $\sim 0.2$  V, in comparison with the  $\text{Ce}_2\text{O}_3\text{-CeO}_2/\text{SS}$  system) in regards to the cathodic reaction in the zone of the potentials ( $E < -1.25$  V), where the reaction of oxygen reduction is occurring. These results give us the reason to suppose that the occurrence of a second reduction process is also very probable in the thermally treated systems of  $\text{Ce}_2\text{O}_3\text{-CeO}_2/\text{SS}_{t.t.}$  within the zone of potentials  $< -1.25$  V, determining a mixed potential. Taking into account the fact that during the thermal treatment practically the whole amount of cerium oxides is converted into  $\text{CeO}_2$  state, i.e. in the form of  $\text{Ce}^{4+}$  ions (prior to the thermal treatment, for the films "upon deposition", the cerium oxides in the form of  $\text{Ce}_2\text{O}_3$  are dominating) [27, 28], it is logical to assume the  $\text{Ce}^{4+}$  reduction reaction occurrence



If such a reaction is really occurring, it could cause two effects. On one side it will compete with the first reaction, i.e. it will decrease the rate of the occurring cathodic oxygen reaction, while on the other side it will lead to the formation of  $\text{Ce}^{3+}$  ions in the aggressive medium, which possess a much more positive potential of oxidation (in view of the

reaction  $\text{Ce}^{3+} - e^- \rightarrow \text{Ce}^{4+}$  [36]) than the oxidative potentials of the steel components, respectively those of the natural passive film on it (Fe, Cr, Al), which are being oxidized in the course of its corrosion. Therefore, the presence of cerium oxides on the steel surface will lower the rate of corrosion, since it will lead to restoration of its passive state, disrupted as a result of the thermal treatment, due to the occurrence of an effective cathodic reaction of  $\text{Ce}^{4+}$  ions reduction ( $\text{Ce}^{4+} + e^- \rightarrow \text{Ce}^{3+}$ ).

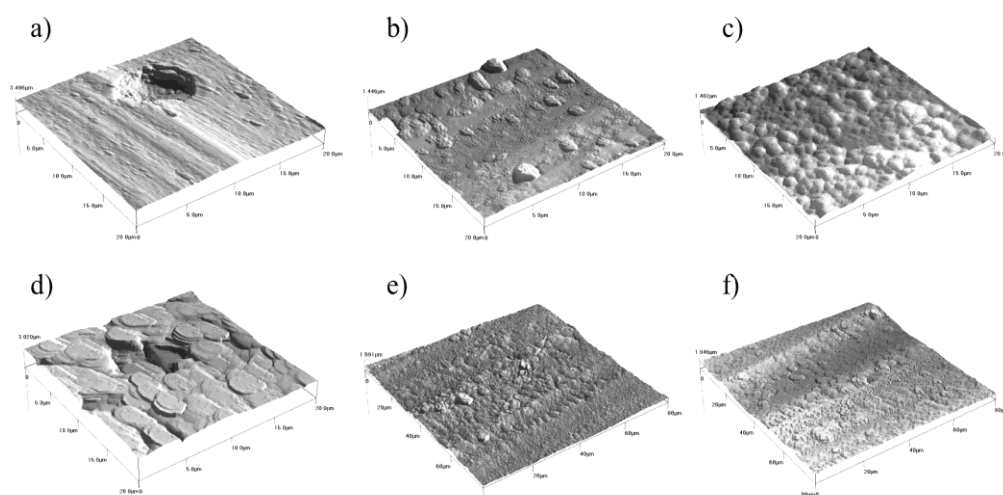
The reason for putting forward such a hypothesis is the dependence, established by K. Vetter, of the total reaction cathodic overpotential on the  $\text{Ce}^{3+}/\text{Ce}^{4+}$  electrode:  $\text{Ce}^{3+} \leftrightarrow \text{Ce}^{4+} + e^-$  [37]. Vetter unambiguously proves that the anodic diffusion-limited current density of this reaction is proportional to the concentration of  $\text{Ce}^{3+}$ , while that of the cathode is proportional to the concentration of  $\text{Ce}^{4+}$ . Thereupon, these quantities do not depend on the concentrations of other substances, possibly present in the electrolyte. However, at higher potentials and especially in the case of low current densities (i.e. values close to the equilibrium potential) complications occur. Such complications are connected with the parallel occurrence of another electrode reaction (formation of mixed potential, respectively). In these cases oxygen evolution reaction occurs [37]. The author explicitly proves in the same study that the rate of the reaction of the electron transfer in a direction to the cathode is proportional to the concentration of the  $\text{Ce}^{4+}$  and it does not depend on the  $\text{Ce}^{3+}$  concentration. This is the reason why in the case of non-treated thermally system of  $\text{Ce}_2\text{O}_3$ - $\text{CeO}_2/\text{SS}$ , when only  $\text{Ce}^{3+}$  ions have passed over to the aggressive medium, there is only one reaction occurring, i.e. the reduction of oxygen, while in the case of non-treated thermally system, simultaneous reduction of  $\text{Ce}^{4+}$  ( $\text{CeO}_2$ ) and of oxygen can occur. If this reduction occurs at more positive potentials, then it will dominate over the total rate of the cathodic reduction process. Evidence for this statement is supplied by the value of the cathodic current. It is higher with one order of magnitude for the thermally treated systems (Fig. 1b).

Fig. 2 illustrates sections of the anodic polarization curves, obtained in 3.5% NaCl, for stainless steel SS OC404 (curve 1) and for the  $\text{Ce}_2\text{O}_3$ - $\text{CeO}_2/\text{SS}$  systems with a different surface content of cerium oxides (from 3.6 up to 29.6 at. %), depending on the time interval of their deposition (from 50 sec up to 80 min) - curves 2, 3, 4, prior to the thermal treatment (Fig. 2a), and after it (Fig. 2b).

It is seen, in view of the obtained results, that in the case of non-treated thermally steel (Fig. 2a, curve 1) two peaks are observable (at  $E = \sim -0.090$  V and at  $E = -0.020$  V), characterizing the oxidation reactions occurrence, and what follows thereafter (at  $E \sim -0.008$  V) is a steep course of the curve, corresponding to the anodic evolution of oxygen via the reaction of  $4\text{OH}^- = 2\text{H}_2\text{O} + \text{O}_2 + 4e^-$ . At the lowest studied concentration of cerium oxide, deposited on steel (curve 2) up to potentials  $\sim -0.015$  V, a weak depolarizing effect is observed, whereupon the first peak is practically disappearing, while the second one (at  $E \sim -0.020$  V) grows stronger. Within the zone of potentials  $> -0.015$  V the presence of cerium oxide film gives rise to the overpotential of the anodic reaction of oxygen evolution. At the next concentration of cerium oxide on the steel (curve 3) a considerably stronger polarizing effect is observed in the zone of the potentials  $> -0.130$  V, while at the maximal studied concentration of cerium oxides (curve 4) the polarizing effect is present even to a greater extent within the entire interval of potentials. Respectively, the current of the reaction of oxygen evolution at each next value of the cerium oxides concentration is decreased substantially.

The action of the cerium oxide layers, deposited on the steel, is analogous also in the case of thermally treated samples (Fig. 2b). Some difference was established only in the case of the lowest concentration of cerium oxides (Fig. 2, curve 2), at which the depolarizing effect is preserved also at potentials  $> -0.015$  V. This is obviously associated with both, the strong cracking of the native passive film on the steel substrate, and the cerium oxide film deposited on it, which leads to a considerable decrease in the corrosion current of the steel, occurring as a result of depassivation ( $\sim 7 \cdot 10^{-6}$  A.cm<sup>-2</sup>), before reaching the zone of the anodic oxygen evolution. In the light of this result, it became especially important to find out how the surface modification with cerium oxide film influences the localization of the corrosion process, preceding the evolution of oxygen.

It is important, in this respect, that the corrosion resistance of stainless steels, under the conditions of anodic polarization (in solutions of  $\text{Cl}^-$  ions) is connected not only with the processes of passivation, but also with the processes, leading to disruption of the integrity of the passive film, and therefore, to the development of local corrosion. From the passive state theory prospective this



**Fig. 3.** AFM images for the samples after 5 min at the  $E_{pitt}$  in 3.5% NaCl: a) SS; b)  $CeO_2-Ce_2O_3(13.1 \text{ at.}\%)/SS$ ; c)  $CeO_2-Ce_2O_3(25.7 \text{ at.}\%)/SS$ ; d) SSt.t.; e)  $CeO_2-Ce_2O_3(4.2 \text{ at.}\%)/SSt.t.$ ; f)  $CeO_2-Ce_2O_3(29.6 \text{ at.}\%)/SSt.t.$

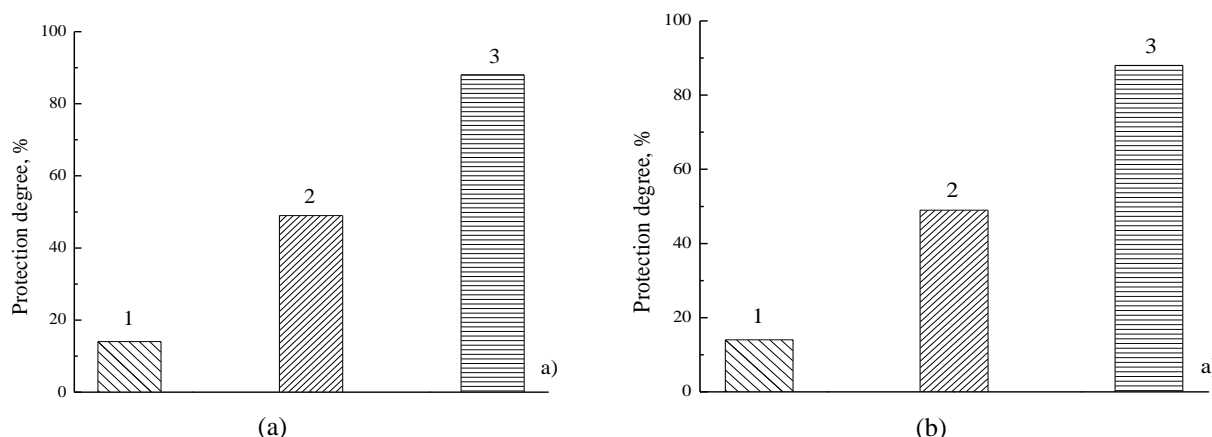


**Fig. 4.** Protection degree in 3.5% NaCl for different concentrations of  $Ce_2O_3-CeO_2$  oxides on SS before (a – 1-3.6 at.%; 2-13.1 at.%; 3-25.7 at.%) and after thermal treatment (b – 1-4.2 at.%; 2-11.2 at.%; 3-29.6 at.%).

phenomenon is associated with the gradual substitution of the oxygen in the passive film with chloride ions or in accordance with the adsorption theory – with substitution of the adsorbed oxygen on the surface with chlorine ions. This process begins upon reaching a definite value of the potential, known as the potential of pitting formation. As a result of its occurrence, the oxide film, protecting the steel surface, can be converted into a soluble metal chloride, resulting in appearance and development of pitting corrosion on separate sections of the surface.

Aiming at investigation of the propensity of the studied steel to pitting corrosion we used the anodic

potentiodynamic curves to estimate the values (Fig. 2a, 2b) of the potentials of pitting formation ( $E_{pitt}$ ) (Tables 1 and 2). The values of the potentials of pitting formation of samples, having ~5 at. % cerium oxides on the surface (before and after the thermal treatment), are close to that value for the steel itself (Fig. 2a, 2b) ( $E_{pitt}$ , Tables 1,2). The further increase in the surface concentration of ceria for the  $Ce_2O_3-CeO_2/SS$  system (above ~11.0 at. %) leads to a shift of  $E_{pitt}$  with more than ~100 mV in the positive direction. This effect is observed in both, the non-treated thermally steels, and the thermally treated samples. The shifting of  $E_{pitt}$  in

**Table 3.** Distribution of the elements (in at. %) in the surface layers of samples as deposited, thermally treated and after immersion in 3.5% NaCl for the samples corresponding to the curves 3.

Samples	Time of immersion, h	O, at. %		Fe, at. %		Cr, at. %		Al, at. %		Ce, at. %	
		~25°C	2 h 450°C	~25°C	2 h 450°C	~25°C	2 h 450°C	~25°C	2 h 450°C	~25°C	2 h 450°C
Ce	as deposited	67.6	64.2	0	10.6	1.6	2.4	17.7	11.6	13.1	11.2
oxides/S	after 1 h	74.7	73.9	0	8.4	1.8	2.9	13.4	10.4	10.4	4.4
S	after 2 h	73.6	79.6	0	6.7	3.3	3.4	14.4	7.4	8.7	2.9

the positive direction improves substantially the corrosion stability of the studied systems in regards to the pitting corrosion. The change in  $E_{\text{pitt}}$  determines the suppressed development not only of the pitting corrosion but also of the total corrosion, especially strongly expressed in the case of the thermally treated systems (Fig. 3). The basic reason for it (in our opinion) is the action of the cerium oxides which block the active sections (Fe sections) on the steel surface.

A support to this statement are the AFM observations on the appearance and the development of local corrosion on samples of non-treated and thermally treated steel (Fig. 3a, 3d), polarized anodically for 5 min, at the potential of pitting formation. Pitting spots are seen on the surface of the non-treated thermally samples. Besides that, damages are caused by the local and total corrosion in the thermally treated samples. After the electrodeposition of cerium oxides with different surface concentration at the same potential no appearance of pitting is observed (Fig. 3b, c, e, f). We attribute this to the effect of cerium oxides which modify the surface film and enrich it to chromium oxides (Table 3), blocking effectively the active sites on the steel surface.

The quantitative evaluation of the steel protection by cerium oxide films, based on the data in Tables 1 and 2, is shown in Fig. 4. It presents the dependence of the steel degree of protection on the  $\text{Ce}_2\text{O}_3$ - $\text{CeO}_2$  surface concentration, calculated using the formula:

$$\text{IP} = \frac{i_{\text{corr}}^0 - i}{i_{\text{corr}}^0} \times 100,$$

where:  $i_{\text{corr}}^0$  and  $i_{\text{corr}}$  are the corrosion current, taken from the polarization curves, with and without  $\text{Ce}_2\text{O}_3$ - $\text{CeO}_2$  on the surface of the working samples. The presence of Ce oxides enables high degree of protection reaching ~ 90%.

### CONCLUSIONS

It was found that the cerium oxide films, formed on OC404 steel, inhibit the oxygen depolarization reaction of the corrosion process. Thereupon, this effect stabilizes the stable passive state of the steel,

under investigation, in 3.5% NaCl solutions, which gives a guarantee for the proceeding of the corrosion under the conditions of a passive state.

It was shown that upon disturbing the steel passive state, as a result of the thermal treatment, the cerium oxide films act as efficient cathodic coating, restoring the passive state of the studied steel. In this case the zone of the potentials, inherent to the passive state, grows wider, being shifted to a positive direction to the potential of the pitting formation. Thus, the corrosion resistance of the studied steel to pitting corrosion is increased.

**Acknowledgements:** *This paper has been completed with the support of the National Fund for Scientific Investigation under Contract TK 01-185.*

### REFERENCES

1. B.R.W. Hinton, D.R. Arnott, N.E. Ryan, *Metals Forum*, **7**, 211 (1984).
2. B.R.W. Hinton, D.R. Arnott, N.E. Ryan, Asia Pacif. Interfinish 86 Conf., Hobart (1986).
3. D.R. Arnott, B.R.W. Hinton, N.E. Ryan, *Mat. Perf.*, August, 42 (1987).
4. B.R.W. Hinton, D.R. Arnott, 21st Annual Technical Meeting of the Int. Metallographie Soc., eds. P.J. Kenny, G.S. Cole, D.O. Norwood, J. Wylie, G.F. Vander Voort (Materials Park, OH: ASM International) 311 (1989).
5. B.R.W. Hinton, *J. Alloys Compd.*, **180**, 15 (1992).
6. F. Mansfeld, S. Lin and H. Shin, *Corrosion*, **45**, 615 (1989).
7. A.J. Devenport, H.S. Isaacs and M.W. Kendig, *Corr. Sci.* **32**, 653 (1989).
8. Y.C. Lu and M.B. Ives, *Corr. Sci.* **34**, 1773 (1993).
9. F. Mansfeld, Y. Wang, *Mat. Sci. & Engineering A* **198**, 51 (1995).
10. A.J. Aldykewicz Jr., H.S. Isaacs and A.J. Davenport, *J. Electrochem. Soc.*, **142**, 3342 (1995).
11. Y.C. Lu and M.B. Ives, *Corr. Sci.*, **37**, 145 (1995).
12. A.J. Aldykewicz Jr., H.S. Isaacs and A.J. Davenport, *J. Electrochem. Soc.*, **143**, 147 (1996).
13. I. Zhitomirsky, A. Petric, *Materials Letters*, **40** (6), 263 (1999).
14. I. Zhitomirsky, A. Petric, *Ceramics International*, **27**, 149 (2001).
15. A. Pardo, M.C. Merino, R. Arrabal, S. Merino, F. Viejo, M. Carboneras, *Surf. Coat. Technol.*, **200**, 2938 (2006).

16. Y.C. Lu and M.B. Ives, *Corr. Sci.*, **34**, 1773 (1993).
17. S. Virtanen, M.B. Ives, G.I. Sproule, P. Schmuki, M.J. Graham, *Corr. Sci.*, **39**, 1897 (1997).
19. C.B. Breslin, C. Chem, F. Mansfeld, E. Otero and F.J. Perez, Extended Abstracts of the 189th Meeting of the Electrochemical Society, Paper No.113, Los Angeles, CA (1996).
20. C. Wang, F. Jiang, F. Wang, *Corr. Sci.*, **46**, 75 (2004).
21. M.A. Arenas, J.J. de Damborenea, *Electrochim. Acta* **48**, 3693 (2003).
22. A. Pardo, M.C. Merino, R. Arrabal, F. Viejo, M. Carboneras, J.A. Munoz, *Corr. Sci.*, **48**, 3035 (2006).
23. M.F. Montemor, M.G.S. Ferreira, *Electrochim. Acta*, **52**, 6976 (2007).
24. D. Nikolova, E. Stoyanova, D. Stoychev, P. Stefanov, T. Marinova, *Surf. Coat. Technol.*, **201**, 1559 (2006).
25. D. Guergova, E. Stoyanova, D. Stoychev, G. Atanasova, I. Avramova, P. Stefanov, *Bulg. Chem. Commun.*, **40**, 227 (2008).
26. D. Nickolova, E. Stoyanova, D. Stoychev, I. Avramova, P. Stefanov, *Surf. Coat. Technol.*, **202**, 1876 (2008).
27. E. Stoyanova, D. Guergova, D. Stoychev, I. Avramova, P. Stefanov, *Electrochim. Acta*, **55**, 1725 (2010).
28. P. Stefanov, G. Atanasova, D. Stoychev, I. Valov, Ts. Marinova, Proc. 6th International Conference on Fundamental and Applied Aspects of Physical Chemistry "Physical Chemistry 2002", September 26-28, Belgrad, Yugoslavia, Vol. I, C-16-P, 198 (2002).
29. P. Stefanov, G. Atanasova, D. Stoychev, I. Valov, Ts. Marinova, *Surf. Coat. Technol.* **180**, 446 (2004).
30. J.H. Scofield, *J. Electron Spectrosc. Rel. Phenom.* **8**, 129 (1976).
31. Peter Kritzer, *J. of Supercritical Fluids*, 29,1 (2004).
32. J. Kašpar, P. Fornasiero, M. Graziani, *Catalysis Today*, **50**, 285 (1999).
33. Ya. A. Ugai, Inorganic chemistry, Publ. House "High School", Moscow (1989).
34. H.S. Klapper, J. Goellner, *Corr. Sci.*, **51**, 144 (2009).
35. R. Babic, M. Metikos-Hukovic, Oxygen reduction on stainless steel, *J. Appl. Electrochem.* **23**, 352 (1993).
36. D. Nicolova, E. Stoyanova, D. Stoychev, I. Avramova, P. Stefanov, Nanostructured Materials in Electroplating, Editors: D. Stoychev, E. Valova, I. Krastev, N. Atanassov, St. Kliment Ohridski University Press (2006).
37. N.D. Tomashov, G.P. Chernova, Passivity and Corrosion Protection, (in Russian) Publ. House "Nauka", Moscow (1963).
38. K. Vetter, Elektrochemische kinetik, Springer Verlag (1961), Translated Russian edition, Khimia Publ.H., "Electrode Ce<sup>3+</sup>/Ce<sup>4+</sup>", 493&115 (1967).

## Корозионна устойчивост на неръждаема стомана, модифицирана електрохимично с Ce<sub>2</sub>O<sub>3</sub>-CeO<sub>2</sub> филми, в среда от 3,5 % NaCl

Д.Гергова<sup>1</sup>, Е.Стойанова<sup>1</sup> Д.Стойчев<sup>1\*</sup>, И.Аврамова<sup>2</sup>, Г.Атанасова<sup>2</sup>, П.Стефанов<sup>2</sup>

<sup>1</sup>Институт по физикохимия "Акад.Р. Каишев", Българска академия на науките, София 1113, България

<sup>2</sup>Институт по обща и неорганична химия, Българска академия на науките, София 1113, България

Постъпила на 12 август 2010 г; приета на 25 октомври 2010 г

Работата е посветена на изследването на корозионно-защитната способност на цериево-оксидни филми, които са отложени електрохимично върху неръждаема стомана OC 404 (SS) от неводни електролити. Изследвано е влиянието на промяната на повърхностната концентрация на Ce<sub>2</sub>O<sub>3</sub>-CeO<sub>2</sub> върху корозионното поведение на SS в корозионно активна среда от 3.5% NaCl преди и след термична обработка на образците. Въз основа на построените поляризационни криви е установено отместване на корозионния потенциал на системата в положителна посока, както и понижаване на корозионните токове, респ. скоростта на корозия, когато върху повърхността на стоманата присъстват цериево-оксидни филми. Данните, получени от AFM и XPS анализите, са в добро съответствие с тези резултати.

Въз основа на получените резултати е направен извода, че наличието на Ce<sub>2</sub>O<sub>3</sub>-CeO<sub>2</sub> слоеве обуславя пасивиране и ре-пасивиране на стоманената повърхност, както и понижаване на питинговата корозия на стоманата. Тези ефекти са обяснени със силното поляризиращо влияние на Ce<sub>2</sub>O<sub>3</sub>-CeO<sub>2</sub> слоевете върху спрегнатата деполяризираща катодна реакция на редукция на разтворения в корозионната среда кислород.

## Kinetics of the hydrogen evolution reaction on Ni electrode in synthetic seawater – an alkaline solution

Y. Petrov<sup>1\*</sup>, J.-P. Schosger<sup>2</sup>, F. de Bruijn<sup>3</sup>

<sup>1</sup> Institute of Electrochemistry and Energy Systems, Bulgarian Academy of Science, 10 Acad. G. Bonchev Blvd., 1113 Sofia, Bulgaria

<sup>2</sup> Institute for Energy, Joint Research Center, Westerduinweg 3, 1755 LE Petten, the Netherlands

<sup>3</sup> Energy and Sustainability Research Institute Groningen, University of Groningen, Nijenborgh 4, 9747 AE Groningen, the Netherlands

Received: November 12, 2010; Revised: November 16, 2010

The electrolysis is a technology for production of hydrogen from renewable sources. Modern commercial electrolyzers focus on hydrogen as a chemical, and not as an energy carrier. For the future large-scale production for automotive applications, electrolyzer energy efficiency and the resulting hydrogen quality and cost are important factors that need more attention. The need of ultrapure water in the novel generation of electrolyzers also increases the cost, and therefore hinders their widespread introduction. The use of seawater could prove to be an economically viable solution. The current research investigates the influence of the contaminants in seawater on the hydrogen evolution reaction on Ni electrode in the temperature range of 25–80°C. The electrochemical kinetic parameters of the reaction – Tafel slope, charge transfer coefficient and exchange current density were evaluated by galvanostatic polarization and electrochemical impedance spectroscopy. Long-term stability test results are also described. All results were compared with the results, obtained in KOH prepared with ultrapure water.

**Keywords:** seawater electrolysis, hydrogen evolution reaction, kinetic parameters, rate constants, electrochemical impedance spectroscopy

### INTRODUCTION

The present energy system, based on the conversion of fossil fuels, is not sustainable and poses environmental hazards. Based on its unique characteristics (highest heat of combustion from all fuels –  $120,9 \times 10^6$  J/kg) [1], hydrogen is accredited as an energy carrier with major role in the future energy system [2–4]. In fact, it can be produced in renewable manner either directly – using sunlight or biomass, or indirectly – using electrolysis and power, supplied from wind, solar, geothermal, and hydropower sources. It can be stored or used as a fuel in fuel cells or internal combustion engines to produce electricity when needed. Contrary to the currently used methods for hydrogen production from fossil fuels, which have carbon dioxide (CO<sub>2</sub>) and other greenhouse gas (GHGs) emissions, the combination of electrolyzers and renewable energy sources would lead to sustainable hydrogen production.

Currently there are three different technologies for water electrolysis (WE) with hydrogen (H<sub>2</sub>) and

oxygen (O<sub>2</sub>) as end products. Based on the type of utilized electrolyte there are: 1- the most developed and commercially available alkaline water electrolyzers (AWE) [4]; 2 – polymer electrolyte membrane electrolyzers (PEMWE) which are still under development but small-scale units are also available on the market [5]; and 3 – solid oxide electrolyzers (SOWE), being under intensive development. The main advantages of the three systems are the comparatively high purity of the obtained end products and the absence of environmentally harmful emissions. Their disadvantages could be summarized as the high energy need for the process itself and the fact that there are strict standards for the quality of the used water - ASTM D1141 type water [6]. The latter prerequisite often calls for preliminary purification of the water, requiring additional energy consumption together with additional investments for constructing purification installations. The need for ultrapure water in the novel electrolyzer generation hinders their widespread application, and contributes to the high cost of the hydrogen.

Other technologies that are based on electrolysis and have H<sub>2</sub> as by-product are industrially available. The chlor-alkali electrolysis [7] uses

\* To whom all correspondence should be sent:  
E-mail: E-mail: yanko.petrov@gmail.com

sodium chloride (NaCl) solution as electrolyte and via various cell configuration, membrane, diaphragm and mercury cell technology, sodium hydroxide (NaOH) and chlorine (Cl<sub>2</sub>) are obtained. In all three cases, H<sub>2</sub> evolves at the cathode.

As the most abundant form of water on the planet, seawater would be an attractive feed for the production of hydrogen on a large scale by water electrolysis, based on renewable energy. However, there are several problems that need to be solved if hydrogen is to be produced by seawater electrolysis. Basically they are: the development of active cathodes for hydrogen evolution reaction (HER)[8, 9]; the exploring anodes that selectively evolve O<sub>2</sub> instead of Cl<sub>2</sub> [10]; or finding an environmentally safe way to dispose back the produced chlorine.

The aim of this study is to investigate the kinetics of HER on a nickel (Ni) electrode during electrolysis of synthetic seawater – an alkaline solution. Ni was chosen as a cathode material because it is known as metal with good electrocatalytic activity and stability towards HER in alkaline and neutral media even in the seawater.

## EXPERIMENTAL

The working electrode (WE) was cut from 99.9% purity Ni rod (Goodfellow Cambridge Ltd.), and had an exposed geometric area of 1 cm<sup>2</sup>. Specimens were polished successively with 800 and 1200-grade emery paper, washed with carbon tetrachloride, cleaned in an ultrasonic bath for 15 minutes, and then washed thoroughly with distilled water. To remove any spontaneously formed oxides before each measurement, WEs were polarized with a cathodic current of 0.3 A.cm<sup>-2</sup> for 30 minutes. The counter electrode (CE) was a platinum basket with high surface area. Saturated Calomel Electrode (Radiometer Analytical XR110) was employed as a reference electrode (RE), whose potential versus the Reversible Hydrogen Electrode (RHE) at 298.15 K is 0.244 V.

One compartment, 3.5L cylindrical Pyrex glass cell, equipped with water jacket for controlling the temperature by thermostat was used for the electrochemical measurements. The WE was positioned in the center while the CE was placed around it. The RE was connected to the cell through an electrolytic bridge which had a Luggin capillary, positioned close to the WE.

The artificial seawater was prepared using chemically pure reagents and 18 MΩ.cm distilled water. The composition of the artificial seawater,

containing no heavy metals and complying with ASTM D1141, is listed in Table 1.

**Table 1.** Artificial seawater composition according to ASTM D1141

Chemical compounds	Concentration, g/L	Chemical compounds	Concentration, g/L
NaCl	24.53	NaHCO <sub>3</sub>	0.201
MgCl <sub>2</sub> ·6H <sub>2</sub> O	11.103	KBr	0.101
Na <sub>2</sub> SO <sub>4</sub> ·10H <sub>2</sub> O	9.278	H <sub>3</sub> BO <sub>3</sub>	0.027
CaCl <sub>2</sub> ·2H <sub>2</sub> O	1.539	SrCl <sub>2</sub> ·6H <sub>2</sub> O	0.042
KCl	0.695	NaF	0.003

The electrochemical measurements were performed using SI 1287 Electrochemical Interface (Solartron), coupled with SI 1255 HF Frequency Response Analyzer (Solartron). The galvanostatic polarization curves ranging from 0.3 A.cm<sup>-2</sup> to 5 × 10<sup>-5</sup> A.cm<sup>-2</sup> (2 minutes per point) were recorded until reproducible results were obtained. The electrode potentials were corrected for iR<sub>s</sub> drop (ohmic drop), determined by Electrochemical Impedance Spectroscopy (EIS). In the EIS measurements the amplitude of the ac signal was 10 mV. A frequency range from 50 kHz to 0.1 Hz was covered with 10 points per decade. The real and imaginary components of the complex plane plots were analyzed using a complex nonlinear least-squares fitting (CNLS) program Zview 3.1 (Scribner Associates, Inc.) by which the experimental parameters of an electrical equivalent circuit were determined.

## RESULTS AND DISCUSSION

Fig.1 shows the experimental iR<sub>s</sub> corrected Tafel polarization plots of Ni electrode in artificial seawater at four temperatures under study. By extrapolation of Tafel lines to the HER equilibrium

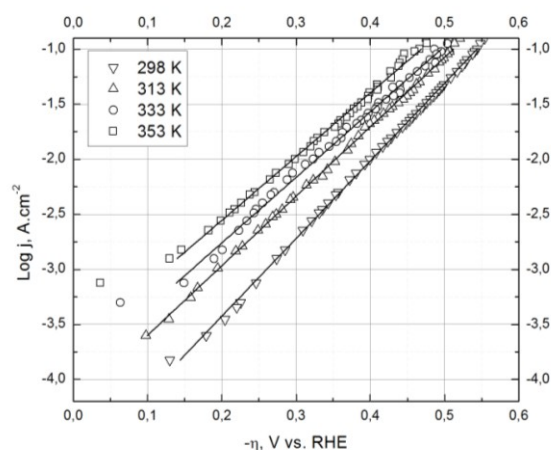


**Fig. 1.** iR corrected galvanostatic Tafel curves of seawater at four temperatures.

potential, the exchange current density  $-j_0$ , is calculated, and from Tafel slope  $-b$ , the value of the charge transfer coefficient  $-\alpha$  is obtained.

The values of the Tafel slope are higher than the theoretically calculated according to the relation  $-b = 2.3RT/\alpha F$ , assuming  $\alpha = 0.5$ . The charge transfer coefficient is ca.  $\sim 0.40 \pm 0.02$  while for KOH prepared with pure water it is about  $0.47 \pm 0.02$ , depending on the temperature. The results are summarized in Table 2. Large deviation from the theoretically calculated values of the Tafel slope are also reported in the literature for HER on various electrode materials in alkaline solution [11, 12].

**Table 2.** Apparent (per unit geometric area) kinetic parameters for HER in artificial seawater + 1 mol.dm<sup>-3</sup> KOH at four temperatures (\* - values obtained in the case of pure water + 1 mol.dm<sup>-3</sup> KOH)

T, K	$b$ , V.dec <sup>-1</sup>	$j_0$ , A.cm <sup>-2</sup>	$\alpha$	$-\eta_{100}$	$b_{theor.}$ , V.dec <sup>-1</sup>
298	0,142	$1,44 \times 10^{-5}$	0,42	0,544	0,118
313	0,158	$5,84 \times 10^{-5}$	0,38	0,512	0,124
333	0,167	$11,11 \times 10^{-5}$	0,39	0,495	0,132
353	0,172	$18,70 \times 10^{-5}$	0,41	0,486	0,140
298*	0,119	$0,92 \times 10^{-5}$	0,49	0,484	0,118
313*	0,132	$4,17 \times 10^{-5}$	0,47	0,452	0,124
333*	0,143	$8,05 \times 10^{-5}$	0,46	0,441	0,132
353*	0,154	$31,92 \times 10^{-5}$	0,46	0,382	0,140

A comparison of the polarization performance of Ni electrode in pure and synthetic seawater towards HER is presented in Fig 2. On one hand, the calculated exchange current densities, obtained for seawater, are higher compared to the ones in the case of pure water except at 353 K. It should be noticed that the exchange current density is a measure of a reaction rate at the reversible potential, i.e. where the net current densities are zero. However, in reality it is possible that a reaction, having high value of  $j_0$ , shows a lower activity at current densities which are comparable to the ones, achieved in the industrial practice. On the other hand, the registered overpotential at a constant current density of 100 mA.cm<sup>-2</sup> is higher in the case of seawater, indicating lower electrocatalytic activity for HER. This could be only due to the presence of contaminants in the electrolyte, because all the other experimental conditions are the same as in the case of the pure water.

The experimental electrochemical impedance spectra (EIS) of Ni electrode in artificial seawater at four constant potentials, taken from the Tafel region are presented as complex-plane (Nyquist) plot on Fig. 3.

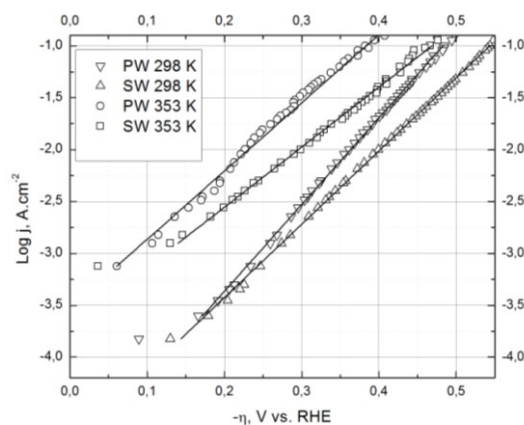


**Fig. 2.** iR corrected galvanostatic Tafel curves of pure water and seawater at 298K and 353K.

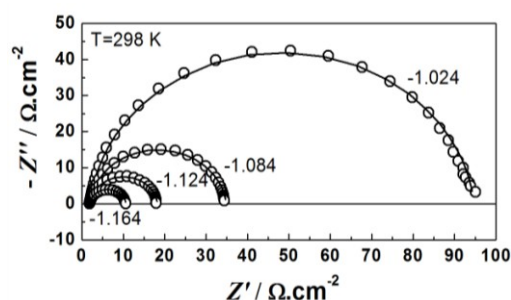


**Fig. 3.** Complex – plane plot of Ni electrode in artificial seawater – alkaline solution at constant temperature of 298 K and potentials -1,024; -1,084; -1,124; -1,164 V vs. RHE.

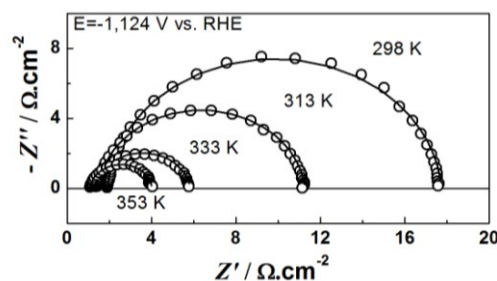


**Fig. 4.** Complex – plane plot of Ni electrode in artificial seawater – alkaline solution at constant potential of -1.124 V vs. RHE and four different temperatures.

One depressed capacitive loop is observed at all potentials under investigation. To analyze the experimental EIS data 1CPE equivalent circuit was used. It consists of a solution resistance  $R_s$  in serial connection with a constant phase element – CPE, which is in parallel connection with the charge transfer resistance  $R_{ct}$ . The CPE is used instead of a pure capacitor and it accounts for the inhomogeneities of the electrode surface. The double layer capacitance ( $C_{dl}$ ) can be calculated according to the relation [13, 14]:

$$C_{dl} = [T(R_s^{-1} + R_{ct}^{-1})^{-(1-a)}]^{1/a} \quad (1)$$

The charge transfer resistance is related to the kinetics of the HER. Fig. 3 confirms the charge transfer controlled kinetics and shows as expected a decrease of  $R_{ct}$  with increasing cathodic polarization.

Fig. 4 shows the complex-plane plot of the system at constant potential and different temperatures. As expected, a decrease of  $R_{ct}$  values with increasing temperature is observed which confirms that the HER proceeds faster at elevated temperatures.

**Table 3.** Values of the equivalent circuit elements obtained with the 1-CPE model on Ni in artificial seawater + 1 mol.dm<sup>-3</sup> KOH at T=298 K and five potentials (\* - values obtained in the case of pure water + 1 mol.dm<sup>-3</sup> KOH).

E, V vs. RHE	$R_s$ ( $\Omega \cdot \text{cm}^{-2}$ )	T, (F.s <sup>-1</sup> .cm <sup>-2</sup> ) $\times 10^{-4}$	a	$R_{ct}$ ( $\Omega \cdot \text{cm}^{-2}$ )	$C_{dl}$ (F.cm <sup>-2</sup> ) $\times 10^{-4}$
-0,984	1,88	1,51	0,93	180,24	0,818
-1,024	1,92	1,46	0,93	95,02	0,789
-1,084	1,91	1,30	0,94	32,52	0,761
-1,124	1,91	1,19	0,96	15,97	0,832
-1,164	1,89	1,06	0,97	8,38	0,809
-0,984*	1,87	10,08	0,87	211,38	3,95
-1,024*	1,94	5,91	0,91	73,13	3,02
-1,084*	1,94	3,73	0,95	21,55	2,53
-1,124*	1,96	3,43	0,96	11,03	2,51
-1,164*	1,97	3,70	0,95	6,27	2,49

Table 3 summarizes the values of the equivalent circuit elements, obtained by non-linear least squares (NLS) fitting. Values for the case of Ni in pure water are also listed for comparison. As it can be seen  $R_{ct}$  values in case of seawater are higher at more negative potentials where high current densities of practical use are reached, which is in good agreement with the results, obtained from the galvanostatic d.c. measurements. The lower values of the double layer capacitance, measured for seawater, and compared to pure water, are assumed to result from the fact that part of the electrochemically active surface is covered by adsorbed species from the electrolyte solution which lowered the available electrode surface for the HER.

Since Tafel analysis clearly indicated that the HER kinetics within the investigated potential region is charge transfer controlled, it was assumed that the  $\eta$ -log( $R_{ct}$ )<sup>-1</sup> relationship, presented in Fig. 5, will follow a linear trend, and will have a slope identical to the Tafel slope.

The obtained slopes,  $b_{ac}$  were found to be in accordance with those, derived from Tafel analysis of galvanostatic polarization curves.

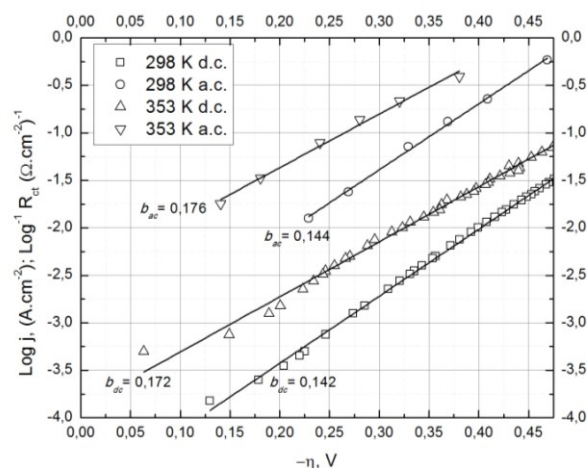
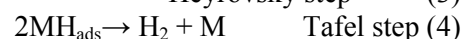
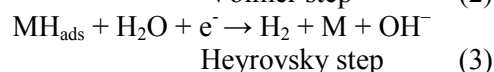
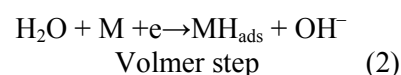


**Fig. 5.** Comparison of log j vs.  $\eta$  and log  $R_{ct}^{-1}$  vs.  $\eta$  and obtained Tafel slopes by d.c. polarization and a.c. impedance method for seawater at 298 and 353 K.

Generally, it is accepted that in alkaline solutions the HER proceeds through three steps [15–18]:



Consecutive combinations of Volmer-Tafel and Volmer-Heyrovsky steps, in which one of them is the rate-determining step (RDS), have been proposed for the HER mechanism on different cathodic materials [16, 19–21].

As discussed in details by Krstajic et al. [19], if we assume that the experimentally recorded current density is determined by the rate of Heyrovsky step in the potential region  $E < -1.2$  V vs. RHE, then the relation will hold:

$$V_h = k_h \theta \exp(-\alpha FE/RT) = i_{ss}/2F \quad (5)$$

where  $V_h$  is the rate of the Heyrovsky step,  $k_h$  [mol.cm<sup>-2</sup>.s<sup>-1</sup>] is the chemical rate constant for the rate controlling Heyrovsky step. Then, using the current density in the experimentally obtained potential region between 1.2 and 1.3 V vs. RHE and the transfer coefficient i. e. 0.42 at 298K, the average value of  $k_h = 2.42 \times 10^{-12}$  was calculated, assuming that the surface coverage by adsorbed hydrogen ( $\theta$ ) is  $\sim 1$ .

As shown, the experimentally calculated values of the Tafel slope by d.c. and a.c. techniques are higher than the theoretically expected if a proton discharge is assumed to be the RDS and  $\alpha = 0.5$ . If the Volmer step is fast and the Heyrovsky step is slow, the surface coverage  $\theta$  will approach unity and the Tafel slope will increase. Thus, the most likely mechanism for the HER under the present

conditions would be the Volmer-Heyrovsky

pathway in which the second step is the RDS.

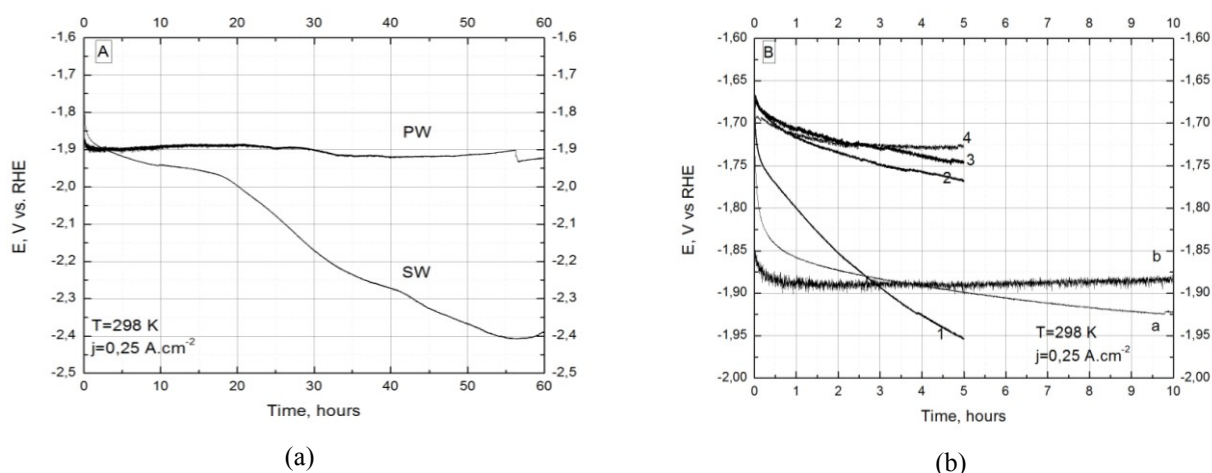


**Fig. 6** Stability test: A – 60 h at current density  $0,25 \text{ A.cm}^{-2}$  at 298 K; B – comparison of potential dependence after reversing the current for 10 min. – a and b are the first 10 h taken from A

Galvanostatic d.c. and a.c. impedance measurements could account only for short-term performance of the investigated system. From a practical point of view the long-term behavior is as important as its kinetics properties. For this reason a stability test at a constant current density of  $0,25 \text{ A.cm}^{-2}$  within 60 hours was performed. As shown in Fig. 6A, the potential of the Ni electrode in artificial seawater increased with time and after 60 hours reached a value of approximately  $\sim -2.4 \text{ V}$  vs. RHE at 298K. In the case of pure water the potential of the electrode also varied but in a very narrow range at around  $\sim -1.9 \text{ V}$  vs. RHE. Again, it is assumed that the increase of the electrode potential in synthetic seawater is due to the poisoning effect of the impurities towards the electrochemically active surface for the HER. It is known that poisons could be adsorbed irreversibly or reversibly [22]. In the latter case it is believed that they could be removed by oxidation reaction and in this way the electrode surface could be cleaned. To verify if this effect is applicable in the case of Ni electrode in synthetic seawater another test was performed. Under the same conditions as in the stability test after 5 hours cathodic polarization, the current was reversed for 10 minutes in the positive direction. This procedure was repeated 4 times and the obtained results are shown in Fig. 6B.

Obviously, switching the current to positive direction changes the surface state of the electrode. After each cycle the potential of the electrode decreased further and stayed lower even when compared with the one of pure water under the long-term test conditions. This could be explained with the fact that the part of the electrode surface, which was not poisoned, is also oxidized by

imposing it to the positive current. It is known from the literature [23] that the HER on oxide covered Ni electrode proceeds faster than on pure metallic Ni. This behavior confirms that the poisoning effect of the impurities in the electrolyte could be overcome to some extent by reversing the current in positive direction for a certain period of time.

## CONCLUSIONS

It can be concluded from the experimental results that the HER on Ni electrode in artificial seawater – an alkaline solution is charge transfer controlled. The obtained exchange current density is higher except at 353K, compared to the density in the case of the pure water. The overpotential at  $0,1 \text{ A.cm}^{-2}$  is also higher while the transfer coefficient is lower and varies little with the temperature. The high values of the Tafel slope lead to the conclusion that the reaction mechanism is a consecutive combination of the Volmer step followed by the Heyrovsky step, the latter being a rate-determining step at more negative potentials. Deactivation of the electrode performance is monitored under long-term tests most probably due to the blockage of the electrochemically available surface with impurities from the bulk electrolyte. Reversing the current for a short time proved to be efficient to some extent for cleaning the surface of the electrode.

## REFERENCES:

- 1 A. Temeev, V. Belokopytov, S. Temeev, *Renewable Energy*, **31**, 225, (2006)
- 2 J. Bokris, *Int. J. Hydrogen Energy*, **24**, 1, (1999)
- 3 L. Bareto, A. Makihira, K. Riahi, *Int. J. Hydrogen Energy*, **28**, 267, (2003)

- 4 L. Gandia, R. Oroz, A. Ursua, P. Sanchis, P. Dieguez, *Energy&Fuels*, **21**, 1699, (2007)
- 5 F. Barbir, *Solar Energy*, **78**, 661, (2005)
- 6 M. Julia, M. Belo, *Portugal. Electrochim. Acta*, **22**, 263, (2004)
- 7 D. Bergner, *J. Appl. Electrochem.*, **12**, 631, (1982)
- 8 J. Giz, M. Marengo, E. Ticianelli, E. Gonzales, *Ecletica Quimica*, **28/2**, 21, (2003)
- 9 A. Antozzi, C. Bargioni, L. Iacopetti, M. Musiani, L. Vazques-Gomez, *Electrochim. Acta*, **53**, 7410, (2008)
- 10 J. Bennet, *Int. J. Hydrogen Energy*, **5**, 401, (1980)
- 11 G. Kreysa, B. Hakansson, P. Ekdunge, *Electrochim. Acta*, **33/10**, 1351, (1988)
- 12 K. Hashimoto, M. Yamasaki, S. Meguro, T. Sasaki, H. Katagiri, K. Izumiya, N. Kumagai, H. Habazaki, E. Akiyama, K. Asami, *Corr. Science*, **44**, 371, (2002)
- 13 G. Brug, A. van den Eden, M. Sluyters-Rehback, J. Sluyters, *J. Electroanal. Chem.*, **176**, 275, (1984)
- 14 W. Mulder, J. Sluyters, *Electrochim. Acta*, **33/3**, 303, (1988)
- 15 E. Gonzalez, L. Avaca, G. Tremiliosi-Filho, S. Machado, M. Ferreira, *Int. J. Hydrogen Energy*, **19/1**, 17, (1994)
- 16 K. Hashimoto, T. Sasaki, S. Meguro, K. Asami, *Mat. Science&Engineering A*, **375-377**, 942, (2004)
- 17 M. Jafarian, O. Azizi, F. Gobal, M. Mahjani, *Int. J. Hydrogen Energy*, **32**, 1686, (2007)
- 18 D. Harrington, B. Conway, *Electrochim. Acta*, **32/12**, 1703, (1987)
- 19 N. Krstajic, M. Popovic, B. Grgur, M. Vojnovic, D. Sepa, *J. Electroanal. Chem.*, **512**, 16, (2001)
- 20 C. Hitz, A. Lasia, *J. Electroanal. Chem.*, **500**, 213, (2001)
- 21 N. Krstajic, B. Grgur, M. Zdujic, M. Vojnovic, M. Jaksic, *Electrochim. Acta*, **42/2**, 323, (1997)
- 22 K. Haga, Y. Shiratori, K. Ito, K. Sasaki, *J. Electrochem. Soc.*, **155/12**, B1233
- 23 A. Lasia, A. Rami, *J. Electroanal. Chem.*, **294**, 123, (1990)

## КИНЕТИКА НА РЕАКЦИЯТА НА ОТДЕЛЯНЕ НА ВОДОРОД ВЪРХУ НИКЕЛОВ ЕЛЕКТРОД В СИНТЕТИЧНА МОРСКА ВОДА – АЛКАЛЕН РАЗТВОР

Я. Петров<sup>1\*</sup>, Ж.-П. Шосгер<sup>2</sup>, Ф. де Бруийн<sup>3</sup>

<sup>1</sup>Институт по електрохимия и енергийни системи, Българска академия на науките,  
ул. 'Акад. Г. Бончев', бл. 10, 1113 София

<sup>2</sup>Институт по Енергия, Съвместен изследователски център, Вестердюнвех 3, 1175 ЛЕ  
Петен, Нидерландия

<sup>3</sup>Изследователски институт за устойчивост и енергия, Гронингенски университет,  
Нйенборг 4, 9747 АЕ Гронинген, Нидерландия

Постъпила на 12 ноември, 2010 г.; коригирана на 16 ноември, 2010 г.

(Резюме)

Изследвано е влиянието на замърсителите в синтетична морска вода - алкален разтвор, върху реакцията на електрохимично отделяне на водород от никелов електрод, в температурният диапазон 25-80° С. Кинетичните параметри на реакцията - Тафелов наклон, обменен ток и коефициента на пренос на заряд са изчислени въз основа на получените галваностатични поляризационни зависимости и електрохимични импедансни измервания. Проведени и анализирани са тестове за стабилност в продължение на 60 часа. Всички стойности са сравнени с резултати получени в алкален разтвор на чиста вода.

## Investigations of mixed oxides Mg/Ni/Al(O) from layered double hydroxides as catalyst support for proton exchange membrane water electrolysis

D. Kostadinova\*, G. Topalov, A. Stoyanova, E. Lefterova, I. Dragieva

*Institute of Electrochemistry and Energy Systems, Bulgarian Academy of Sciences, G. Bonchev St. Building 10, 1113 Sofia, Bulgaria*

Received: September 16, 2010; accepted: September 23, 2010

Various alternatives of electrocatalyst supports are being searched. The conformation of the multi-cationic Layered Double Hydroxides (LDHs) Mg/Ni/Al after calcination - mixed oxide Mg/Ni/Al(O) are proposed as advanced support for electrocatalysis. LDHs, a new class of basic mixed hydroxides exhibiting layered structure, proved to be good substrates to be loaded with noble metals and non noble metals, also having properties of electron donor promoters. The aim of this work is a characterization of the structure of Pt-catalysts appropriate for electrochemical water splitting. These catalysts are prepared by deposition of Pt on supports mixed oxides Mg/Ni/Al(O), obtained by calcination of multicationic LDH. These materials are characterized by means of structural (XRD, TEM) and electrochemical methods: cyclic voltammetry (CV) and steady-state polarization techniques, in view of their possible application as electrocatalytic support for oxygen evolution reaction in proton exchange membrane water electrolysis.

**Keywords:** catalyst support material, Pt\_Mg/Ni/Al(O), PEMWEs, oxygen evolution reaction, Pt

### 1. INTRODUCTION

The proton exchange membrane water electrolysis (PEMWEs) is efficient method to produce hydrogen with higher purity and it offers several advantages over the traditional technologies [1]. Even if the electrolyte and the membrane electrode assembly have been widely studied, degradation of the materials, especially the carbon supports of the electrode, and the high cost of the Pt loaded electrodes are now the new issues to overcome. Few researches have been carried out, aiming to replace the carbon support and decrease the Pt loading. It came out that using divers metal oxide powder as a support would significantly decrease the cost of the PEMWEs but also would increase its stability and thus the life time of the cell. Pt nanoparticles and their alloys are usually dispersed on porous carbon black (e.g., Vulcan XC-72) to function as PEMWEs anode and cathode catalysts, which are one of the most important and most expensive components in PEM water electrolysis. Suitable support materials must be electrically conductive and corrosion inert [2]. The big disadvantage of carbon is its lack of stability at high anodic potentials, where oxygen evolution takes place [3]. The stability of carbon support affects the loss of platinum surface area following

both, the platinum particle sintering and the platinum release from the carbon support [4]. Therefore, various alternatives of electrocatalyst supports are being searched. A good candidate as a catalyst support could be a material which manifests the stability and the specific property - strong metal-support interaction (SMSI) effect [5–7], which presumed the lower Pt loadings and the greater efficiency. This fort interaction between support and particles is due to intensive electronic transfer. Surprisingly, interaction and cooperation between nanosized metal particles and basic supports have been scarcely investigated. A recent review considering the metal-support interaction (“electron transfer”) and the metal-support cooperation (“metal-base bifunctional catalysis”) has shown the great potential of the layered double hydroxides (LDH) as precursors of the metal particles on basic supports with very unique properties [8, 9]. LDHs of the general formula of  $[M^{2+}_{1-x} M^{3+}_x(OH)_2][A^{n-}]_{x/n} \cdot mH_2O$  can contain different  $M^{2+}$  and  $M^{3+}$  metal cations in their brucite-like sheets, and various  $A^{n-}$  charge-compensating anions in their interlayer space. LDH compounds easily decompose into mixed oxides of the  $M^{2+}M^{3+}(O)$  type after calcination [10–12], these materials having both basic and redox functions as catalysts. Three general routes are available for synthesis of the LDHs precursors: first, the synthesis of the LDHs, containing  $M^{2+}$  and/or  $M^{3+}$  elements with redox behavior within the sheets;

\*To whom all correspondence should be sent:  
E-mail: dессie.kostadinova@gmail.com

second, the exchange with anionic metal precursors of the desired metal in the interlayer space of the LDHs; and third, the deposition or grafting of inorganic or organometallic precursors onto the calcined precursor LDH. The choice of this material is based on its properties of an electron donor promoter. [13]. It is known also that LDHs are good precursors for loading noble metals and non noble metals [14]. The aim of this research is to investigate the possible apply of the LDHs materials as a support material of metal catalysts, used in PEMWEs. In this work we use the conformation of multi-cationic Layered Double Hydroxides LDHs  $\text{NO}_3 - \text{Mg/Ni/Al}$  after calcination – mixed oxide  $\text{Mg/Ni/Al(O)}$  which are proposed as advanced Pt catalyst support for electrocatalysis.

## 2. EXPERIMENTAL

### 2.1. Catalyst synthesis

The initial multi-cationic structure  $\text{NO}_3 - \text{Mg/Ni/Al}$  was synthesized by coprecipitation at constant pH (~11) of suitable amounts of  $\text{Mg}(\text{NO}_3)_2 \cdot 6\text{H}_2\text{O}$  (0.2 M),  $\text{Al}(\text{NO}_3)_3 \cdot 6\text{H}_2\text{O}$  (0.1 M) and  $\text{Ni}(\text{NO}_3)_2 \cdot 6\text{H}_2\text{O}$  (0.05 M) with a solution of NaOH (2.0 M). The addition of the alkaline solution was controlled by using a pH-STAT Titrimo (Metrohm) apparatus to keep the pH constant. The suspension was stirred overnight at 80°C for 17 h, and then the solid was separated by centrifugation, washed thoroughly with distilled water, and dried overnight at 80°C. The support of mixed oxide  $\text{Mg/Ni/Al(O)}$  was obtained by calcination of multi-cationic LDH  $\text{NO}_3 - \text{Mg/Ni/Al}$ , at 450°C for 5 hours under air. One part of the sample was impregnated by platinum (II) acetylacetonate using the sol-gel method to prepare supported Pt catalysts. These samples were gradually heated in hydrogen atmosphere until the the temperature of 240°C was reached, than they were held for 2 h under these conditions, and gradually cooled. This first part of samples were hereafter labeled as  $\text{Mg/Ni/Al(O)} - \text{Pt}$ . Another part was kept without platinum impregnation, these samples were labeled as  $\text{Mg/Ni/Al(O)}$ .

### 2.2. Electrode preparation

The electrodes have a complex multilayered structure, consisting of gas diffusion layer, catalytic nanoparticle mixture layer, and a support of mixed oxide  $\text{Mg/Ni/Al(O)}$ . The last layer is made of a catalyst and support mixture, deposited on a thin carbon cloth, serving as a gas diffusion

layer. The catalytic layer is spread upon the carbon cloth at several steps. After each step the electrode was dried for 30 min at ambient temperature and weighted using an analytical microbalance. The procedure has been repeated until a metal loading of  $0.5 \text{ mg. cm}^{-2}$  was reached. Then the electrode was hot pressed onto the PEM. The hot pressing is performed stepwise in the regime of gradual temperature and pressure increase, starting at 50°C and  $6 \text{ kg. cm}^{-2}$ , and ending at 120°C and  $12 \text{ kg. cm}^{-2}$ , respectively.

### 2.3. Physical characterization

XRD patterns were recorded on a Bruker D8 Advance instrument using the  $\text{Cu K}\alpha_1$  radiation ( $\lambda = 1.542 \text{ \AA}$ , 40 kV, and 50 mA). TEM analysis of samples was performed using a JEOL 1200 EXII microscope, operated at 80 kV on samples, previously calcined at 450°C. Measurements of the reduced platinum particle sizes on several micrographs led to the determination of the mean particle sizes.

### 2.4. Electrochemical characterization

The catalysts under study are investigated as electrodes for the oxygen evolution reaction. The electrochemical tests were performed on membrane electrode assemblies (MEAs), using a Nafion 117 membrane as an electrolyte. The performance characteristics of thus prepared MEA were investigated in a self made laboratory PEM electrolytic cell. The electrochemical behavior of the prepared  $\text{Pt}_{\text{Mg/Ni/Al(O)}} - \text{composites}$  as catalysts for oxygen evolution reaction (OER) were studied and compared to that of the support  $\text{Mg/Ni/Al(O)}$  using the techniques of cyclic voltammetry and steady state polarisation. All electrochemical measurements were carried out with a commercial Galvanostat/ Potentiostat POS 2 Bank Elektronik, Germany.

## 3. RESULTS AND DISCUSSION

The XRD analyst show that the support corresponds to  $\text{Mg}(\text{Ni,Al})\text{O}$  periclase, (Figure 1a). The crystallite size is around 4.5 nm (Table 1). After the electrochemical test, the support partially reconstructed in layered structure of multicationic LDH (type hydrotalcite,  $\text{Mg}(\text{Ni}) - \text{Al}$ ). Figure 2 presents the XRD spectra of the samples with different Pt-content (10% and 20%), deposited on  $\text{Mg}(\text{Ni,Al})\text{O}$  periclase support. The average Pt-crystalline size on catalyst with 20% Pt is 14-17 nm, and the size does not change after electrochemical tests. For the sample with 10% Pt,

the crystalline sizes are of 10-11 nm (Table 1). After the electrochemical tests (Fig. 2b), the diffraction peak disappears at around 63 degree.

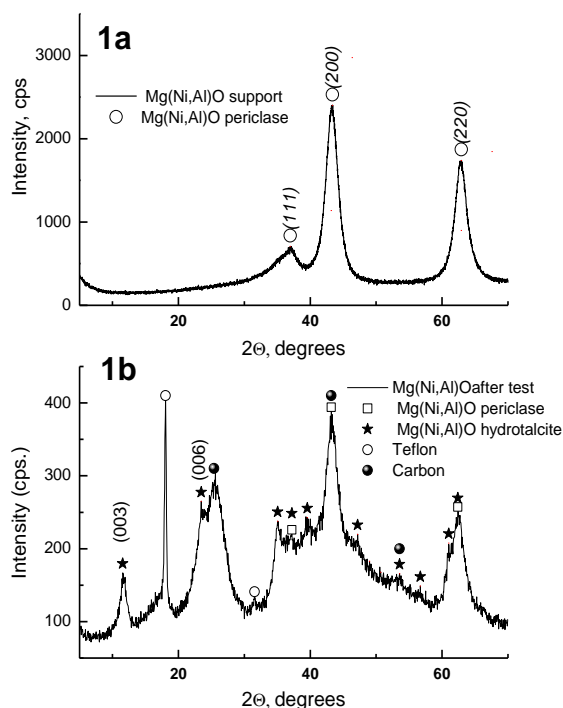


Fig. 1. XRD spectra of catalyst support: a) before electrochemical and b) after electrochemical test.

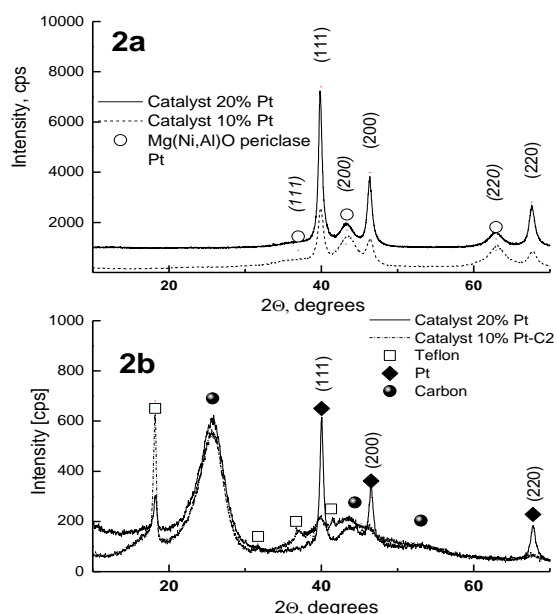


Fig. 2. XRD spectra of Pt catalyst a/ before and b/ after electrochemical test.

No intensive diffraction peaks were observed in the x-ray spectra of hydrotalcite. All this subjects the complementary analysis of the support structure after the electrochemical test. Our previous results showed that the CV-curves

of Mg/Ni/Al(O) – substrate (without Pt) was active up to the 30th cycle, and then its activity dropped down sharply.

Table 1. Crystallite size of the Mg(Ni,Al)O-support, and Pt/Mg(Ni,Al)O catalysts

Sample	Crystallite size, nm
Support	D <sub>(200)</sub> 4.00
	D <sub>(220)</sub> 5.00
Pt (20%)	D <sub>(111)</sub> D <sub>(200)</sub> 17.00
	D <sub>(220)</sub> 14.00
Pt (10%)	D <sub>(111)</sub> 11.00
	D <sub>(200)</sub> 10.00

This result is explained with the degradation of Mg/Ni/Al(O) or in other words, the reconstruction which was confirmed by the XRD patterns [15]. Similar effect was observed in the catalyst with 10% Pt. The anodic curves, corresponding to the oxygen evolution (Fig. 4), show that the catalytic activity of tested catalyst is lower. The best activity exhibits the electrode with a higher platinum content. This result may be associated with the XRD- results. The higher Pt-content prevents to a greater degree the reconstruction of the support. This may be due to the strong interaction between small Pt-particles and mixed oxide. The same results are observed for the Ni-catalyst based on LDH [16].

### TEM

The materials were characterized by TEM in order to compare the size distribution of the metal particles before and after the electrocatalytic test (Figure 3).

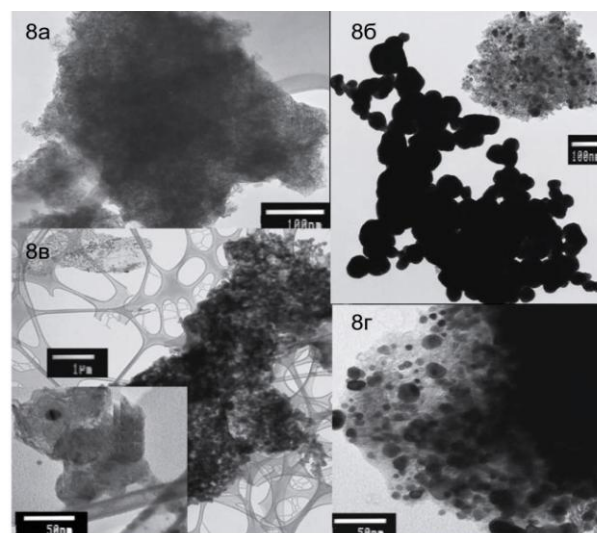


Fig. 3. TEM images: 1a – support of Mg(Ni,Al)O periclase; 1b – impregnated sample with Pt; 1c - the sample after electrode preparation before electrochemical test; 1d – the electrode after electrochemical test.

These observations on the catalyst Pt-loading sample ( $0.5 \text{ mg.cm}^{-2}$ ) showed the formation of different-sized Pt- particles on the mixed oxide support (3–15 nm), while the massive clusters of Pt (23–115 nm) were formed outside of the support.

These results suppose the excess of platinum. They also allow us to compare the TEM images of the samples of Pt-catalyst before and after work of the electrode. The results show that Pt particles remain of the same size. Again, the control of the metal dispersion state may be due to the fort interaction between the support and the small particles.

### 3.3. Electrochemical characterization

The cyclovoltammetric experiments have been performed in the whole potential range between the hydrogen and the oxygen evolution. Our previous results showed that the CV curve of the Pt\_Mg/Ni/Al(O) sample has the typical behavior of the monometallic platinum in regards to the hydrogen and the oxygen regions, and its character does not change with the cycling – it has clearly delineated the oxidation and the reduction peaks, and the double layer region. The CV-curves of Mg/Ni/Al(O) (without Pt) electrode have rather different profile, their peaks are not clearly defined. The electrode was active up to the 30<sup>th</sup> cycle, and then its activity dropped down sharply. This result can be explained with the degradation of Mg/Ni/Al(O) or in other words, with the reconstruction which was confirmed by the XRD patterns. In the presence of platinum, this effect is not observed and the electrode is stable [17].

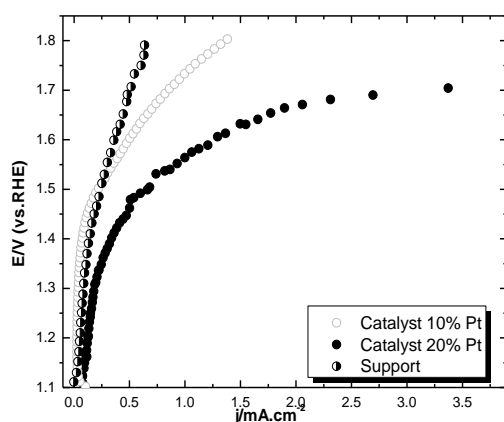


**Fig. 4.** Steady state polarisation curves at 80°C.

Figure 4 shows the polarization curves. The polarization test showed the OER proceeds with

a higher rate on the Pt\_Mg/Ni/Al(O), compared to the none-containing platinum electrode. The curve demonstrates a stable behavior of the catalyst, due to the endurance of the substrate by these anodic potentials.

## 4. CONCLUSIONS AND PERSPECTIVES

It was shown that the preparation of catalyst leads to small Pt particles, supported on a Ni/Mg/Al/O mixed oxide matrix. The Pt particles have the same mean size of 3–15 nm before and after operation of the electrode. The massive clusters of Pt (23–115 nm), which were observed outside the support, suppose the excess of platinum which can be reduced for further work, and thus decrease the quantity of the noble metal (Pt) in the catalyst. The use of oxide mixed in LDHs leads to solids, exhibiting higher metal dispersion, and to stability of the particle size distribution under the electrocatalytic test. The solid, obtained from co-precipitated Ni/Mg/Al LDH calcinated, and the non impregnated reveals the interesting result of 170 cycles before the reconstruction of its structure. These Ni-containing materials offer interesting outlooks for electrocatalytic applications due to their better stability and higher conductivity. The main hindrances for the application of the mixed oxide Mg/Ni/Al(O) are in the first place the low electronic conductivity and secondly the memory effect which lead to reconstruction in the HDL layered structure. There is also a possibility of reducing the quantity of noble metals used (Pt-catalyst) or replaced by a none-noble metal. Further modifications in the support composition reveal an opportunity to increase its conductivity and its stability. The investigations showed that the conformation oxide of LDHs Ni/Mg/Al, can be successfully applied as an electrocatalyst supporting material in PEM water electrolysis. It was observed that strong connections between the metal particles and the support are established. The support has a beneficial influence on the particle-size.

## REFERENCES

1. E. Rasten, G. Hagen, R. Tunold, *Electrochim. Acta*, **48**, 3945 (2003).
2. Lj. M. Vračar, N.V. Krastajić, V.R. Radmirović, M.M. Jakšić, *J. Electroanal. Chemistry*, **586**, 99 (2006).
3. E. Slavcheva, V. Nikolova, T. Petkova, E. Lefterova, I. Dragieva, T. Vitanov, E. Budevski, *Electrochim. Acta*, **50**, 5444 (2005).

4. E. Antolini, E.R. Gonzalez, *Solid State Ionics*, **180**, 746 (2009).
5. S.J. Tauster, S.C. Fung, R.L. Garten, *J. Am. Chem. Soc.*, **100**, 170 (1978).
6. F. Garin, *Catal. Today*, **89**, 255 (2004).
7. L.F. Liotta, A. Longo, A. Macaluso, A. Martorana, G. Pantaleo, A.M. Venezia, G. Deganello, *Applied Catalysis B: Environmental*, **48**, 133 (2004).
8. A. Vaccari, *Appl. Clay Sci.*, **14**, 161 (1999).
9. D. Tichit, B. Coq, *Cattech*, **7**, 206 (2003).
10. F. Cavani, F. Trifiro, A. Vaccari, *Catal. Today*, **11**, 173 (1991).
11. A. De Roy, C. Forano, K. El Malki, J. P. Besse, in: *Synthesis of Microporous Materials*; Occelli, M. L., Robson, H., (eds.), Van Nostrand Reinhold: New York, 1992.
12. V. Rives, *Layered Double Hydroxides: Present and Future*; Nova Science Publishers: New York, 2001
13. C. Gerardin, D. Kostadinova, N. Sanson, B. Coq, and D. Tichit; *Chem. Mater.*, **17**, 6473 (2005).
14. S. Narayanan, *Bull. Catal. Soc. India*, **2**, 107 (2003).
15. J.G. Nunan, R.G. Herman and K. Klier, *J. Catal.*, **116**, 222 (1989).
16. C. Gerardin, D. Kostadinova, B. Coq, D. Tichit, *Chem. Mater.*, **20**, 2086 (2008).
17. D. Kostadinova, G. Topalov, A. Stoyanova, Th. Cacciaguerra, C. Gerardin, D. Tichit, I. Dragieva, Proc. "Nanoscience & Nanotechnology"- Nanostructured Materials Applications and Innovation Transfer, Issue 10, E. Balabanova and I. Dragieva (eds.), "BPS" Ltd., Sofia, Bulgaria (2010), pp.109–112.

## Изследване на смесени оксиди Mg/Ni/Al(O) получени от двуслойни хидроксиди като каталитичен носител за ПЕМ водна електролиза

Д. Костадинова\*, Г. Топалов, А. Стоянова, Е. Лефтерова, И Драгиева

*Институт по електрохимия и енергийни системи – БАН  
ул. Акад. Г. Бончев бл. 10, 1113 София, България*

Постъпила на 16 септември, 2010 г.; приета на 23 септември, 2010 г.

(Резюме)

Търсени са различни алтернативи за електрокаталитични носители. Кристалната конформация смесен оксид Mg/Ni/Al(O), получен чрез калциниране на нитратна форма на мултикатионен двуслоен хидрооксид (ДСХ) Mg/Ni/Al-NO<sub>3</sub> - е разглеждан като перспективен носител за електрокатализа. ДСХ са клас от основни смесени хидрооксиди със слоестта структура, които се проявяват като добри носители за натоварване с благородни и неблагородни метали и притежават свойства на електронни донори. Целта на настоящата работа е охарактеризиране на структурата на Pt-катализатори, подходящи за електрохимично разлагане на вода. Тези катализатори са синтезирани чрез отлагане върху носители от смесени оксиди Mg/Ni/Al(O), получени при калциниране на мултикатионен ДСХ. Материалите са изследвани със структурни (XRD, TEM) и електрохимични методи: циклична волтаметрия (CV) и стационарна поляризационна техника, с оглед евентуалното им приложение като електрокаталитични носители по отношение на реакцията на отделяне на кислород при ПЕМ водна електролиза.

\*To whom all correspondence should be sent:

E-mail: [dessie.kostadinova@gmail.com](mailto:dessie.kostadinova@gmail.com)

# BULGARIAN CHEMICAL COMMUNICATIONS

## Instructions about Preparation of Manuscripts

**General remarks:** Manuscripts are submitted in English by e-mail or by mail (in duplicate). The text must be typed double-spaced, on A4 format paper using Times New Roman font size 12, normal character spacing. The manuscript should not exceed 15 pages (about 3500 words), including photographs, tables, drawings, formulae, etc. Authors are requested to use margins of 3 cm on all sides. For mail submission hard copies, made by a clearly legible duplication process, are requested. Manuscripts should be subdivided into labelled sections, e.g. **Introduction, Experimental, Results and Discussion, etc.**

**The title page** comprises headline, author's names and affiliations, abstract and key words.

Attention is drawn to the following:

a) **The title** of the manuscript should reflect concisely the purpose and findings of the work. Abbreviations, symbols, chemical formulas, references and footnotes should be avoided. If indispensable, abbreviations and formulas should be given in parentheses immediately after the respective full form.

b) **The author's** first and middle name initials, and family name in full should be given, followed by the address (or addresses) of the contributing laboratory (laboratories). **The affiliation** of the author(s) should be listed in detail (no abbreviations!). The author to whom correspondence and/or inquiries should be sent should be indicated by asterisk (\*).

**The abstract** should be self-explanatory and intelligible without any references to the text and containing not more than 250 words. It should be followed by key words (not more than six).

**References** should be numbered sequentially in the order, in which they are cited in the text. The numbers in the text should be enclosed in brackets [2], [5, 6], [9–12], etc., set on the text line. References, typed with double spacing, are to be listed in numerical order on a separate sheet. All references are to be given in Latin letters. The names of the authors are given without inversion. Titles of journals must be abbreviated according to Chemical Abstracts and given in italics, the volume is typed in bold, the initial page is given and the year in parentheses. Attention is drawn to the following conventions:

a) The names of all authors of a certain publications should be given. The use of “*et al.*” in

the list of references is not acceptable.

b) Only the initials of the first and middle names should be given.

In the manuscripts, the reference to author(s) of cited works should be made without giving initials, e.g. “Bush and Smith [7] pioneered...”. If the reference carries the names of three or more authors it should be quoted as “Bush *et al.* [7]”, if Bush is the first author, or as “Bush and co-workers [7]”, if Bush is the senior author.

**Footnotes** should be reduced to a minimum. Each footnote should be typed double-spaced at the bottom of the page, on which its subject is first mentioned.

**Tables** are numbered with Arabic numerals on the left-hand top. Each table should be referred to in the text. Column headings should be as short as possible but they must define units unambiguously. The units are to be separated from the preceding symbols by a comma or brackets.

Note: The following format should be used when figures, equations, *etc.* are referred to the text (followed by the respective numbers): Fig., Eqns., Table, Scheme.

**Schemes and figures.** Each manuscript (hard copy) should contain or be accompanied by the respective illustrative material as well as by the respective figure captions in a separate file (sheet). As far as presentation of units is concerned, SI units are to be used. However, some non-SI units are also acceptable, such as °C, ml, l, etc.

The author(s) name(s), the title of the manuscript, the number of drawings, photographs, diagrams, etc., should be written in black pencil on the back of the illustrative material (hard copies) in accordance with the list enclosed. Avoid using more than 6 (12 for reviews, respectively) figures in the manuscript. Since most of the illustrative materials are to be presented as 8-cm wide pictures, attention should be paid that all axis titles, numerals, legend(s) and texts are legible.

The authors are asked to submit **the final text** (after the manuscript has been accepted for publication) in electronic form either by e-mail or mail on a 3.5” diskette (CD) using a PC Word-processor. The main text, list of references, tables and figure captions should be saved in separate files (as \*.rtf or \*.doc) with clearly identifiable file names. It is essential that the name and version of

the word-processing program and the format of the text files is clearly indicated. It is recommended that the pictures are presented in \*.tif, \*.jpg, \*.cdr or \*.bmp format, the equations are written using "Equation Editor" and chemical reaction schemes are written using ISIS Draw or ChemDraw programme.

The authors are required to submit the final text with a list three individuals and their e-mail addresses that can be considered by the Editors as potential reviewers. Please, note that the reviewers should be outside the authors' own institution or organization. The Editorial Board of the journal is not obliged to accept these proposals.

## EXAMPLES FOR PRESENTATION OF REFERENCES

### REFERENCES

1. D. S. Newsome, *Catal. Rev.–Sci. Eng.*, **21**, 275 (1980).
2. C.-H. Lin, C.-Y. Hsu, *J. Chem. Soc. Chem. Commun.*, 1479 (1992).
3. R. G. Parr, W. Yang, *Density Functional Theory of Atoms and Molecules*, Oxford Univ. Press, New York, 1989.
4. V. Ponec, G. C. Bond, *Catalysis by Metals and Alloys* (Stud. Surf. Sci. Catal., vol. 95), Elsevier, Amsterdam, 1995.
5. G. Kadinov, S. Todorova, A. Palazov, in: *New Frontiers in Catalysis* (Proc. 10th Int. Congr. Catal., Budapest, 1992), L. Guzzi, F. Solymosi, P. Tetenyi (eds.), Akademiai Kiado, Budapest, 1993, Part C, p. 2817.
6. G. L. C. Maire, F. Garin, in: *Catalysis. Science and Technology*, J. R. Anderson, M. Boudart (eds), vol. 6, Springer-Verlag, Berlin, 1984, p. 161.
7. D. Pocknell, *GB Patent 2 207 355* (1949).
8. G. Angelov, PhD Thesis, UCTM, Sofia, 2001.
9. JCPDS International Center for Diffraction Data, *Power Diffraction File*, Swarthmore, PA, 1991.
10. *CA* **127**, 184 762q (1998).
11. P. Hou, H. Wise, *J. Catal.*, in press.
12. M. Sinev, private communication.
13. <http://www.chemweb.com/alchem/articles/1051611477211.html>.

## CONTENTS

Academician Evgeni B. Budevski - In Memoriam.....	5
EDITORIAL, National Conference "Sofia Electrochemical Days 2010" (SED 2010).....	6
<i>B.I. Banov, H.C. Vasilchina</i> , Environmentally friendly cathode materials for Li-ion batteries.....	7
<i>N. D. Dimcheva, E. G. Horozova, T. M. Dodevska</i> , Direct electrochemistry of myoglobin immobilized on non-modified and modified graphite.....	17
<i>E. A. Matter, S.V. Kozhukharov, M.S. Machkova</i> , Effect of preliminary treatment on the superficial morphology and the corrosion behaviour of AA2024 aluminum alloy.....	23
<i>G. S. Spasov, C. Popov</i> , Auger analysis of plasma treated ultrananocrystalline diamond films.....	31
<i>G. Hodjaoglu, I. Ivanov</i> , Zinc recovery from sulphate electrolytes, containing copper and ferrous ions..	37
<i>Y.D. Milusheva, R.I. Boukoureshitlieva, S.M. Hristov, A.R. Kaisheva</i> , Environmentally-clean Mg-air electrochemical power sources .....	42
<i>K. Ignatova, D. Stoykova</i> , Study of the influence of nitrite anions on the electrode processes in ammonium electrolyte for Ag-Cu deposition.....	48
<i>D.I. Ivanova, L.B. Fachikov</i> , Phosphating of zinc surfaces in zinc-calcium solutions.....	54
<i>M.L. Petrova, M.S. Bojinov, I.H. Gadjov</i> , Electrodeposition of molybdenum oxides from weakly alkaline ammonia-molybdate electrolytes.....	60
<i>V. P. Pashova, L. G. Mirkova, M. H. Monev, P. Nowak, G. Nawrat</i> , Ni/Re-Co as electrocatalytic material for hydrogen evolution reaction in alkaline solution.....	64
<i>G. M. Raichevski, L. Lutov, N. S. Boshkov</i> , Corrosion characterization and protective ability of the LR-3 rust converter.....	69
<i>P. Paunović, D. Stoevska Gogovska, O. Popovski, I. Radev, E. Lefterova, E. Slavcheva, A. T. Dimitrov, S. Hadži Jordanov</i> , Non-platinum electrode materials for hydrogen evolution: effect of catalyst support and metallic phase.....	74
<i>R.I. Boukoureshitlieva, S.M. Hristov, Y.D. Milusheva, P.B. Atanassov, A.R. Kaisheva</i> , Mediated enzyme electrodes.....	81
<i>S. L. Nineva, Ts. V. Dobrovolska, I. N. Krastev</i> , Electrodeposition of silver-cobalt coatings. Electrolytes.....	88
<i>S. L. Nineva, Ts. V. Dobrovolska, I. N. Krastev</i> , Electrodeposition of silver-cobalt coatings. The cyanide-pyrophosphate electrolyte.....	96
<i>K. Petrov, I.Nikolov, V. Nikolova, P. Iliev, D.Uzun, T. Vitanov</i> , Electrolytic cell for hydrogen and sulfuric acid production.....	105
<i>S.M. Hristov, R.I. Boukoureshitlieva, Y.D. Milusheva</i> , Experimental metal hydride-air fuel cell.....	111
<i>V. D. Bachvarov, M. H. Arnaudova, R. St. Rashkov, A. Zielonka</i> , Electrochemical deposition of alloys based on Ni-Fe-Co, containing W,P, and their characterization for hydrogen evolution reaction.....	115
<i>M. P. Slavova, D. E. Vladikova, M. Z. Krapchanska, G. S. Raikova, Z. B. Stoynov</i> , Differential impedance analysis of BaCe <sub>0,85</sub> Y <sub>0,15</sub> O <sub>2,925</sub> .....	120
<i>M. Mladenov, N. Petrov, T. Budinova, B. Tsyntsarski, T. Petrov, D. Kovacheva, R. Raicheff</i> , Synthesis and electrochemical properties of the electrode materials for supercapacitors.....	125
<i>G. Raikova, D. Vladikova, Z. Stoynov</i> , Differential impedance analysis of the cathode compartment in dual membrane fuel cell.....	133
<i>E.D. Lefterova, A.E. Stoyanova, G.R. Borisov, E.P. Slavcheva</i> , Physical characterization of Pt-M binary electrocatalysts for water splitting.....	138
<i>I. G. Angelov, Chr. A. Girginov, E. Klein</i> , Growth and dissolution of anodic antimony oxide in oxalic acid electrolytes.....	144
<i>D. Guergova, E. Stoyanova, D. Stoychev, I. Avramova, G. Atanasova, P. Stefanov</i> , Corrosion stability of stainless steel, modified electrochemically with Ce <sub>2</sub> O <sub>3</sub> -CeO <sub>2</sub> films, in 3.5% NaCl media.....	150
<i>Y. Petrov, J.-P. Schosger, F. de Bruijn</i> , Kinetics of the hydrogen evolution reaction on Ni electrode in synthetic seawater – an alkaline solution.....	158
<i>D. Kostadinova, G. Topalov, A. Stoyanova, E. Lefterova, I. Dragieva</i> , Investigations of mixed oxides Mg/Ni/Al(O) from layered double hydroxides as catalyst support for proton exchange membrane water electrolysis.....	164
INSTRUCTIONS TO THE AUTHORS.....	169

СЪДЪРЖАНИЕ

IN MEMORIAM , В памет на академик Евгени Будевски.....	5
Редакционна: Национална конференция “Софийски електрохимични дни-2010 (SED 2010).....	6
<i>Бр.И. Банов, Хр.К. Василчина</i> , Екологично-съвместими катодни материали за литиево-йонни батерии.....	16
<i>Н.Д. Димчева, Е.Г. Хорозова, Т.М. Додевска</i> , Директни електрохимични отнасяния на миоглобин, имобилизиран върху немодифициран и модифициран графит .....	22
<i>Е.А. Матер, С.В. Кожухаров, М.С. Мачкова</i> , Ефект на предварителната подготовка върху повърхностната морфология и корозионното поведение на алуминиева сплав АА 2024.....	30
<i>Г.С. Спасов, К. Попов</i> , Оже-анализ на плазмено третиранни ултрананокристални диамантени слоеве.....	36
<i>Г. Ходжаоглу, Ив. Иванов</i> , Извличане на цинк от сулфатни електролити, съдържащи медни и феройони.....	41
<i>Й.Д. Милушева, Р.И. Букурецилиева, С.М. Христов, А.Р. Каишева</i> , Екологични електрохимични източници на енергия магнезий – въздух.....	47
<i>К. Игнатова, Д. Стойкова</i> , Изследване на влиянието на нитритни аниони в амонячен електролит за отлагане на Ag-Cu .....	53
<i>Д. И. Иванова, Л.Б. Фачиков</i> , Фосфатиране на цинкови повърхности в цинк-калциеви препарати.....	59
<i>М.Л. Петрова, М.С. Божинов, И.Х. Гаджов</i> , Електрохимично отлагане на молибденови оксиди из слабо алкални електролити, съдържащи амониев молибдат.....	63
<i>В. Пашова, Л. Миркова, М. Монеv, П. Новак, Г. Наврат</i> , Ni/Re-Co като електрокаталитичен материал за отделяне на водород в алкален разтвор.....	68
<i>Г.М. Райчевски, Л. Лютов, Н.С. Божков</i> , Охарактеризиране на корозията и защитните свойства на преобразувател на ръжда LR-3 .....	73
<i>П. Паунович, Д. Стоевска-Гоговска, О. Поповски, И. Радев, Е. Кефтерова, Е. Славчева, А.Т. Димитров, С. ХаджиЙорданов</i> , Не-платинови електродни материали за добиване на водород: ефект на подложката на катализатора и на металната фаза .....	80
<i>Р.И. Букурецилиева, С.М. Христов, Й.Д. Милушева, П.Б. Атанасов, А.Р.Каишева</i> , Медиаторни ензимни електроди.....	87
<i>С.Л. Нинева, Цв.В. Доброволска, Ив. Н. Кръстев</i> , Електролитно отлагане на сребърно-кобалтови покрития. Електролити.....	95
<i>С.Л. Нинева, Цв.В. Доброволска, Ив. Н. Кръстев</i> , Електро-отлагане на сребърно-кобалтови покрития из цианидно-пирофосфатен електролит.....	104
<i>К. Петров, И. Николов, В. Николова, П. Илиев, Дж. Узун, Т. Витанов</i> , Електролизна клетка за получаване на водород и сярна киселина.....	110
<i>С.М. Христов, Р.И. Букурецилиева, Й.Д. Милушева</i> , Експериментален горивен елемент метален хидрид-въздух.....	114
<i>В. Бъчваров, М. Арнаудова, Р. Рашков, А. Цилонка</i> , Електрохимично отложени сплави на основа Ni-Fe-Co, съдържащи W, P и тяхното охарактеризиране за реакцията на отделяне на водород.....	119
<i>М.З. Кръпчанска, Д.Е. Владикова, Г.С. Райкова, М.П. Славова, З.Б. Стойнов</i> , Диференциален импедансен анализ на $BaCe_{0,85}Y_{0,15}O_{2,925}$ .....	124
<i>М. Младенов, Н. Петров, Т. Будинова, Б. Цинцарски, Т. Петров, Д. Ковачева, Р. Райчев</i> , Синтез и електрохимични свойства на електродни материали за суперкондензатори.....	132
<i>Г. Райкова, Д. Владикова, З. Стойнов</i> , Диференциален импедансен анализ на катодния елемент на двойно- мембранна горивна клетка.....	137
<i>Е.Д. Лефтерова, А.Е. Стоянова, Г.Р. Борисов, Е.П. Славчева</i> , Физично охарактеризиране на Pt-M двумкомпонентни електрокатализатори за разлагане на вода.....	143
<i>И. Г. Ангелов, Кр. А. Гиргинов, Е. Клайн</i> , Образуване и разтваряне на аноден антимонов оксид в разтвори на оксалова киселина.....	149

<i>Д. Гергова, Е. Стоянова, Д. Стойчев, И. Аврамова, Г. Атанасова, П. Стефанов</i> , Корозионна устойчивост на неръждаема стомана, модифицирана електрохимично с $\text{Ce}_2\text{O}_3\text{-CeO}_2$ филми, в среда от 3,5 % NaCl.....	157
<i>Я. Петров, Ж.-П. Шосгер, Ф. де Бруийн</i> , Кинетика на реакцията на отделяне на водород върху никелов електрод в синтетична морска вода – алкален разтвор.....	163
<i>Д. Костадинова, Г. Топалов, А. Стоянова, Е. Лефтерова, Й. Драгиева</i> , Изследване на смесени оксиди Mg/Ni/Al(O) получени от двуслойни хидроксиди като каталитичен носител за ПЕМ водна електролиза.....	168